MEASUREMENTS, MODELING, AND SIMULATION OF SEMICONDUCTOR/GATE DIELECTRIC DEFECTS USING RANDOM TELEGRAPH SIGNALS

by

MOHAMED NOUR

Presented to the Faculty of the Graduate School of

The University of Texas at Arlington in Partial Fulfillment

of the Requirements

for the Degree of

DOCTOR OF PHILOSOPHY

THE UNIVERSITY OF TEXAS AT ARLINGTON

December 2015

Acknowledgments

I would like to express my deep appreciation to my advisor Professor Zeynep Çelik-Butler for her great support, mentoring, and close guidance during the last 3 years. Professor Çelik-Butler always gives enough time to discuss any issues or challenges regarding the research and always encourages and motivates me to explore new ideas. This helps me to develop great foundations in my field and encourages me to think out of the box. Networking with industry and professional community is one of several blessings that I had during my graduate years. I would like to thank Professors Donald Butler, Samir Iqbal, Dereje Agonafer, and Ali Davoudi for serving as my committee members. Also I want to thank the former and current lab-mates Dr. MD Iqbal, Dr. Moinuddin, Rouf, Sohel, Sajeeb, Tousif, and Yi-Li for their help and fruitful discussions. I cannot forget the staff and the academic advisors in the electrical engineering department at the University of Texas at Arlington for their support and help. I want to thank Fan-Chi Hou, Shaoping Tang, Arif Sonnet, Guru Mathur, Luigi Colombo, and Rick Wise from Texas Instruments Inc. for providing several wafers to conduct my research and investigate the phenomenon of random telegraph noise. Also I want to thank the Semiconductor Research Corporation for their partial financial support.

Finally, I would like to express my great gratitude to my family. Everything I have is due to their special prayer which sustained me thus far. All mercy on my Dad and Mom and may Allah accept them and grant them the paradise. I would like to thank all of my brothers and sisters who inspired and encouraged me to come through this successful journey. My special thanks to my dear respected wife Khadija who spent sleepless nights helping and praying for me.

October 10, 2015

Abstract

Measurements, Modeling, and Simulation of Semiconductor/Gate Dielectric Defects Using Random Telegraph Signals

Mohamed Nour, Ph.D.

The University of Texas at Arlington, 2015

Supervising: Zeynep Çelik-Butler

Constructing an effective statistical model and a simulation tool that can predict the phenomenon of random telegraph signals (RTS) is the objective of this work. The continuous scaling down of metal oxide – semiconductor field effect transistors (MOSFETs) makes charging/discharging traps(s) located at the silicon/silicon dioxide interface or deep in the oxide bulk by mobile charge(s) a more pronounced problem for both analog and digital applications. The intent of this work is to develop an RTS statistical model and a simulation tool based on first principles and supported by extensive experimental data. The newly developed RTS statistical model and its simulation tool should be able to replicate and predict the RTS in time and frequency domains.

First, room temperature RTS measurements are performed which provide limited information about the trap. They yield the extraction of some trap and RTS characteristics such as average capture and emission times associated with RTS traces, trap position in the oxide with respect to the Si/SiO_2 interface and along the channel with respect to the source, capture cross section, and trap energies in the Si and SiO_2 band – gaps. Variable temperature measurements, on the other hand, yield much more valuable information. Variable temperature RTS measurements from room temperature down to 80 K were performed, with the MOSFET biased from threshold voltage to strong inversion, in the linear and saturation regions. Variable temperature RTS measurements yield the

extraction of trap characteristics such as capture cross – section prefactor, capture and emission activation energies, change in entropy and enthalpy, and relaxation energy associated with a trap from which the nature and origin of a defect center can be identified.

The newly developed Random Telegraph Signals Simulation (RTSSIM) is based on several physical principles and mechanisms e.g. (1) capturing and emitting a mobile charge from and to the channel is governed by phonon- assisted- tunneling, (2) traps only within a few k_BT of the Fermi energy level are considered electrically active, (3) trap density is taken as U – shaped in energy in the silicon band-gap, (4) device scalability is accounted for, (5) and temperature dependence of all parameters is considered. RTSSIM reconstructs the RTS traces in time domain from which the power spectral density (PSD) is evaluated. If there is 20 or more active traps, RTSSIM evaluates the PSD from the superposition of the RTS spectra. RTSSIM extracts RTS and trap characteristics from the simulated RTS data and outputs them to MS Excel files for further analyses and study.

The novelty of this work is: (1) it is the first time quantum trap states have been accurately assigned to each switching level in a complex RTS corresponding to dependently and independently interacting traps, (2) new physics-based measurement-driven model and simulation tool has been developed for RTS phenomenon in a MOSFET, (3) and it is the first time a species in SiO_2 responsible for RTS has been identified through time-domain measurements and extensive analysis using four trap characteristics at the same time.

Table of Contents

List of Figures

List of Tables

List of Symbols

a	exponent of the direct current in the Hooge formula
A_{gD}	slope of g_D vs. V_{GS} (A/V)
a_{ll}	lower limit of average tunneling time interval (s)
a_{lu}	upper limit of average tunneling time interval (s)
A_{ntAA}	average number of active traps of two dependent acceptors in a device
A_{ntSA}	average number of active traps of a single acceptor in a device
A_{ntSD}	average number of active traps of a single donor in a device
C_{GC}	gate–channel capacitance (F/cm^2)
$C_{GC_{inv}}$	gate–channel capacitance in the inversion layer (F/cm^2)
$C_{GC_{ov}}$	overlap gate–channel capacitance in the accumulation layer (F/cm^2)
C_{ox}	gate oxide capacitance (F/cm^2)
E_A	ionization energy depends on the dopant type in the semiconductor (eV)
E_C	Si conduction band–edge (eV)
E_{Cox}	conduction band-edge of the SiO_2 (eV)
E_F	Fermi energy level (eV)
E_{Fn}	Fermi energy level for electrons (eV)
E_{Fp}	Fermi energy level for holes (eV)
E_G	energy band-gap for Si (eV)
E_{ij}	the electron energy in the j^{th} energy sub-band in the i^{th} valley of the

	inversion layer (eV)
E_R	relaxation energy (eV)
E_T	trap energy level in the oxide (eV)
E_V	Si valence band-edge (eV)
E_y	electric field along the channel (V/cm)
f	frequency (Hz)
f_0	corner frequency in a Lorentzian spectrum (Hz)
F_m	forward mode when drain-source voltage is varied
F_{nb}	number of the switching event within each histogram bin
F_S	sampling frequency (Hz)
F_{Surf}	effective surface electric field (V cm^{-1})
f_t	trap occupancy by the Fermi-Dirac distribution
g	degeneracy factor of trap
g_A	degeneracy factor for holes
g_d	channel output conductance (Ω^{-1})
$g_{D\text{int}}$	Intercept of g_D vs. V_{GS} (Ω^{-1})
g_m	MOSFET channel transconductance (Ω^{-1})
h	Planck’s constant (J. s)
$\hbar$	reduced Planck constant (J. s)
I_{DC}	direct current (A)

I_{DS}	drain–source current (A)
I_{sh}	shot noise current (A)
k	wave vectors
k_B	Boltzmann’s constant (J K^{-1})
$k_{1/f}$	ratio of the Hooge parameter to number fluctuators
L	drawn channel length of a MOSFET (µm)
L_{cap}	Length of the MOS capacitor (µm)
L_D	Debye length (nm)
L_{eff}	effective channel length of a MOSFET (µm)
L_{halo}	halo implanted region length (µm)
m_n^*	electron effective mass (kg)
m_0	effective mass of electron in the vacuum (kg)
m_{ox}^*	electron effective mass in the oxide (kg)
m_p	effective mass of hole mass (kg)
N	number of fluctuators that generates 1/f noise (cm^{-2})
n	charge carrier concentration (cm^{-3})
N_A	substrate doping concentration in nMOS (cm^{-3})
N_A^-	ionized acceptor concentration (cm^{-3})
$N_{Aavg_{eff}}$	average effective doping concentration along the channel (cm^{-3})
N_{Ahalo}	halo doping concentration for p-type or (cm^{-3})

n_b	bin number used in the histogram of the average time analysis
N_b	total number of bins used in the histogram of the average time analysis
N_C	conduction band effective density of states (cm^{-3})
N_{dev}	number of devices
N_{Dhalo}	halo doping concentration for n-type (cm^{-3})
N_{Fcont}	number fluctuation contributions
N_{fdev}	number of fingers per device
n_i	intrinsic carrier concentration in equilibrium (cm^{-3})
N_{inv}	inversion channel carrier density (cm^{-2})
N_L	number of RTS levels
n_0	majority carrier concentration in equilibrium for electrons (cm^{-3})
N_{sub}	sub channel doping concentration (cm^{-3})
N_t	number of occupied trap per unit area (cm^{-2})
N_{tA}	areal trap density of single acceptor trap (cm^{-2})
N_{tAA}	areal trap density of single double acceptor traps (cm^{-2})
$N_{t_{active}}$	total number of active traps in a simulated device
$N_{tA_{active}}$	number of active traps in a simulated device for a single acceptor species
$N_{tAA_{active}}$	number of active traps in a device for two dependent acceptor species
$N_{tD_{active}}$	number of active traps in a simulated device for a single donor species
N_{tD}	areal trap density of single donor trap (cm^{-2})

$N_t(E,x,y,z)$	distribution of the traps in the gate dielectric (cm^{-3} eV^{-1})
$N_T(E_F)$	volumetric trap density per energy (cm^{-3} eV^{-1})
N_V	valance band effective density of states (cm^{-3})
p	a random number can be chosen from a uniform distribution on logarithmic time scale
$p(t)$	probability of electron transition from one level to others
p_0	majority carrier concentration in equilibrium for holes (cm^{-3})
p_{x_t}	probability of the trap position in the oxide (nm^{-1})
q	electronic charge (C)
Q_{inv}	total inversion charge in the channel MOSFET (C/cm^2)
Q_{ox}	gate oxide interface charge (C)
R	resistance or the real part of impedance (Ω)
R_C	radius of the capture cross- section for a trap (nm)
R_m	reverse mode when drain-source voltage is varied
S	Huang and Rhys parameter corresponds to the number of emitted phonon
$S_{\Delta I_{DS}}$	power spectral density of the local current fluctuations (A^2/Hz)
$S_{\Delta N_t}$	power spectral density of the mean square fluctuation in the number of occupied traps over the area $W\Delta y$ (Hz^{-1})
S_I	power spectral density of the flicker noise (A^2/Hz)

$S_{I_{DS}}$	power spectral density of drain–source current in a MOSFET (A^2/Hz)
$S_{I_{sh}}$	power spectral density of the shot noise (A^2/Hz)
S_V	power spectral density of the thermal noise (V^2/Hz)
$S_{V_{DS}}$	drain–source voltage noise power spectral density (V^2/Hz)
$S_{V_{fb}}$	power spectral density of the flat band voltage (V^2/Hz)
$S_{Q_{ox}}$	power spectral density of the oxide interface charge (C^2/Hz)
T	temperature (K)
t_{inv}	inversion layer thickness (nm)
t_{nb}	duration time of the histogram bin (s)
T_{ox}	gate oxide thickness (nm)
V_C	channel voltage (V)
V_{DS}	drain–source voltage (V)
$V_{DS_{F\max}}$	drain-source voltage in the forward mode where the maximum of $\left(\bar{\tau}_c/\bar{\tau}_e\right)$ versus V_{DS} is observed (V)
$V_{DS_{R\max}}$	drain-source voltage in the reverse mode where the maximum of $\left(\bar{\tau}_c/\bar{\tau}_e\right)$ versus V_{DS} is observed (V)
V_{FB}	flat band voltage (V)
V_{GS}	gate–source voltage (V)
V_{ox}	voltage across the gate oxide (V)
V_{SB}	source-body voltage (V)

V_{th}	threshold voltage of (V)
V_{thTD}	slope of threshold voltage vs. temperature (V/K)
$\bar{v}_{th}$	average thermal velocity of the channel carriers (cm/s)
W	drawn channel width of a MOSFET (µm)
W_{cap}	width of the MOS capacitor (µm)
x	coordinate axis along the oxide depth from the Si/SiO$_2$ interface (nm)
x_t	trap position in the oxide with respect to the Si/SiO$_2$ interface (nm)
$\bar{x}_t$	average trap position for a trap species (nm)
$\bar{x}_{tAA}$	average trap position for two dependent acceptor traps (nm)
$\bar{x}_{tSA}$	average trap position for a single acceptor trap (nm)
$\bar{x}_{tSD}$	average trap position for a single donor trap (nm)
x_{tAA}	generated trap position for two dependent acceptor traps (nm)
x_{tSA}	generated trap position for a single acceptor trap (nm)
x_{tSD}	generated trap position for a single donor trap (nm)
y	coordinate axis along the channel length (µm)
y_t	trap location along the channel with respect to the source (µm)
z	coordinate axis along the channel width (µm)
α	Coulomb screened scattering coefficient (V s)
α_H	Hooge’s parameter
α_{lat}	scattering coefficient due to the lattice scattering mechanism

$\delta\Delta N_{inv}$	channel carrier fluctuations (cm^{-2})
$\delta\Delta N_t$	occupied trap fluctuations (cm^{-2})
ΔE_B	capture activation energy (eV)
ΔE_{CT}	change in Gibbs free energy (eV)
Δf	system frequency band width (Hz)
ΔH	trap binding enthalpy (eV)
δI_{DS}	drain-source current fluctuations (A)
$\Delta\mu$	mobility fluctuations (cm^2/V s)
$\delta\overline{\mu}_c$	average channel carrier mobility fluctuations (cm^2/V s)
ΔN	number fluctuations
ΔN_{inv}	charge density in the channel within $W\Delta y$ area (cm^{-2})
ΔN_{ox}	change in the number of gate oxide charges (cm^{-2})
ΔN_t	number of occupied traps in the oxide within $W\Delta y$ area (cm^{-2})
δQ_{ox}	gate oxide charge fluctuations (C)
ΔS	change in entropy (eV/K)
ΔV_{DS}	random telegraph signal amplitude (V)
δV_{fb}	flat band voltage fluctuations (V)
ε_0	permittivity of free space (F/cm)
ε_{Si}	permittivity of Si (F/cm)
ε_{SiO_2}	permittivity of SiO_2 (F/cm)

ϕ_0	electron affinity difference between the Si and SiO_2 (eV)
ϕ_F	Fermi energy with respect to the intrinsic energy level in the Si bulk (eV)
γ	frequency exponent in the power spectral density of flicker noise
λ	electron wave attenuation coefficient (cm^{-1})
$\overline{\mu}_c$	effective channel carrier mobility in the linear *or* in the saturation region (cm^2/V s)
μ_{eff}	channel carrier effective mobility (cm^2/V s)
μ_{Fcont}	mobility fluctuation contributions
μ_{imp}	mobility due to impurity scattering (cm^2/V s)
$\overline{\mu}_l$	effective channel carrier mobility in the linear region (cm^2/V s)
μ_{lat}	mobility due to lattice scattering (cm^2/V s)
μ_n	channel carrier mobility (cm^2/V s)
μ_{oth}	mobility due to other mechanisms (cm^2/V s)
μ_{ox}	mobility limited by the gate oxide charge scattering (cm^2/V s)
$\overline{\mu}_s$	effective channel carrier mobility in the onset of saturation (cm^2/V s)
σ	capture cross-section (cm^2)
σ_n	conductivity (S/cm)
σ_0	trap capture cross section prefactor (cm^2)
ψ_s	band bending at the source side and channel voltage (eV)
ψ_{s_0}	band bending at the source side (eV)
ω	angular frequency (rad/s)

ω_p	phonon radian frequency (rad/s)
$\bar{\tau}$	average time constant (s)
τ_0	electron tunneling constant from the Si/SiO_2 interface to the trap (s)
$\bar{\tau}_c$	average capture time (s)
$\bar{\tau}_e$	average emission time (s)

Chapter 1 Introduction

1.1 Preface and Inspiration

Metal Oxide Semiconductor Field Effect Transistors (MOSFETs) have been considered the back-bone for most technological advancements in microelectronics industry. This great leverage of MOSFETs has allowed billions of devices to be integrated on one chip, which drives the price per device to drop down, enables less power consumption, and provides higher computational speed. The remarkable properties of silicon (Si) and silicon dioxide (SiO_2) materials are considered the major source for the success of MOSFETs in analog and digital applications. However, highly scaled devices have exhibited serious reliability problems and threatened the integrated circuit performance and stability. One of these problem is noise.

In this research work, we focus on Random Telegraph Signals (RTS) which are mainly due to the capture and emission of mobile charges by defect(s) at the Si/SiO_2 interface and in the oxide bulk. This phenomenon becomes more important when device channel lengths go below 45 nm [1, 2, 3]. It impacts analog and RF applications in advanced CMOS technologies [4]. Thus, low-frequency noise in a highly scaled device becomes dominated by RTS which sets the limit for the minimum detectable signal and the sensitivity for a device [5]. Moreover, in RF and microwave applications significant phase noise due to up-converted low-frequency noise is observed [4]. In addition, in digital applications bit error ratio (BER) increases suddenly around the noise level where 1's and 0's become indiscernible. Low frequency noise may strongly affect the quality of the image for CMOS imagers that use transistors in the sub – micron range [6, 7]. Therefore, RTS can be used as a non-destructive tool to investigate the trap characteristics in the gate oxide and to provide insightful information about the nature and the origin of the defects.

There are several reasons behind this research such as significant waste of wafer real estate and simulation-device design cycle time due to lack of effective physics-based statistical device model that can accurately predict trap characteristics in the gate oxide. It was noticed in 2000s that modeling RTS phenomenon based on a simple modulation of stationary signal as a source for the noise produces inaccurate noise estimation [5, 8]. In addition, most of the current studies for RTS phenomenon are done using frequency domain in order to extract some RTS and trap characteristics [9, 10, 11, 12]. Moreover, most of the current studies are based on physics or experimental data but not necessary both. Furthermore, the improper implementation of some statistical techniques in some of the RTS simulator e.g. hidden Markov model (HMM), time lag plot (TLP), or two stage L-shaped RC circuit (LSRCC) [2, 13,14, 15, 16, 17]. The concerns have been raised about the direct use of HMM, TLP, and LSRCC without major enhancements, such as limitation of RTS amplitude (ΔV_{DS}) extraction due to one or two active traps in a particular device [2, 15]. Extraction of ΔV_{DS} , average capture ($\bar{\tau}_c$) and emission ($\bar{\tau}_e$) times is done independently without being interrelated which may lead to inaccurate results. LSRCC does not relate the simulated RTS waveforms or *1/f* noise spectrum to the physical mechanisms of trap species that are causing the noise in highly scaled devices. In fact, this will generate only a random waveform that looks like an RTS but does not represent or reflect the real cause of the noise.

The aforementioned issues and challenges regarding the RTS and its simulation tools have been taken into account in this work. The newly developed RTS statistical model and its simulation tool are based on first principles and supported by extensive measured data. ΔV_{DS} , $\bar{\tau}_e$, and $\bar{\tau}_c$ are interrelated when RTS and trap characteristics are analyzed and extracted. The newly developed RTS simulation (RTSSIM) can reconstruct RTS in time domain for up to 19 active traps from which the power spectral density (PSD) is evaluated. In the case of 20 or more active traps, RTSSIM switches to $1/f$ noise mode and evaluates the PSD based on the superposition of the RTS spectra without computing time traces first.

RTSSIM reconstructs the RTS in time and frequency domains according to the electrical properties associated with the identified defect center. Some of these mechanisms and assumptions are: (1) a trap is assumed to be electrically active if its energy is within few $k_B T$ of the Fermi energy level where k_B is the Boltzmann's constant and T is the absolute ambient temperature [18], (2) capturing and emitting a mobile charge from and to the channel are done through phonon – assisted tunneling [18, 19], (3) number of the traps at a specific device follows Poisson distribution [2, 13], (4) and the trap density as a function of energy is taken as U–shaped [20, 21]. In addition, doping concentration along the channel is considered to be non – uniform, and the effect of linear and saturation regions of operation is included. A trap is treated as neutral or charged prior to the capturing, remote Coulomb scattering effect and number fluctuation theory are utilized [22], and all traps are assumed to be empty at time zero.

As it is known, there are many defects located at the Si/SiO$_2$ interface or in the oxide bulk. However, not all of the traps are electrically active. Therefore, being able to determine the number of active traps in a highly scaled device is important for prediction of the type of noise resulting from these traps. RTS can be used as a diagnostic tool to study the energy and spatial distribution of gate oxide traps. RTS is based on real-time electron switching events in the drain – source current or voltage. Thus, it is used to probe active traps individually at the proper bias and temperature conditions. Here, the RTS is used as a method to study the variability of traps and other electrically active defects within the same process technology and to study the multi-level fluctuations caused by independent or correlated traps.

Using the RTS tool to investigate the gate oxide defects has shown superior advantages in many aspects over other techniques such as charge pumping or deep – level transient – spectroscopy (DLTS). For example, studying the surface states of Si/SiO_2 based on MOS capacitor measurements is applicable primarily for channel lengths > 20 µm [23]. The DLTS measurements require sensing of small transient capacitance values, which might lead to errors [23]. Charge pumping technique reaches the limit as a tool capable of characterizing the gate oxide traps due to the increase of leakage current in highly scaled devices [24]. On the other hand, RTS measurements can be performed on highly scaled devices < 45 nm and can provide accurate information about the gate oxide traps in real time. RTS is also considered to be a nondestructive diagnostic tool for gate oxide characterization [25].

In general, investigating the charge carrier trapping/detrapping physical phenomenon in time domain has several advantages over the frequency method. RTS measurements lead to the extraction of the trap type and nature of the defect that causes the disturbance in the V_{DS} signals [26]. Therefore, developing a physics-based statistical model supported by extensive experimental data and a simulation tool that can reconstruct this phenomenon in time and frequency domains is an urgent matter for the CMOS technology.

1.2 Electronic Noise in Semiconductor Devices

Electronic noise is a stochastic process that can be defined as any unwanted signal interfering with or disturbing the desired signal [27]. The fluctuations in the voltage or the current signals are due to the change in the amplitude and/or the phase of the signal frequency. Noise can be categorized into two groups: first group is external noise due to sources other than the device such as electromagnetic signals, photon, and radio signals [27]. Second group is internal sources either fundamental to physics of the device or resulting from a defect. This defect might be in the bulk of the semiconductor or at the interface of two different materials.

In this thesis, primarily one type of the internal noise sources is considered. This type of noise is mainly from defects located at the Si/SiO_2 interface in MOSFET devices or in the oxide bulk. This implies that several noise mechanisms exist for an internal noise sources i.e. thermal noise, shot noise, flicker noise or $1/f$ noise, generation recombination noise, and RTS. The significance of the electronic noise in circuit design is the ability to show the minimum signal that can be detected and processed by a device. It is not true that any small signal can be amplified by higher amplification system. If a transmitted signal is masked with a noise signal, it will be hard to differentiate between the two signals. Thus, it will be difficult to reconstruct the desired signal and that may lower the quality and resolution of the output signal [27, 28, 32]. Noise level in a circuit has a trade - off between the power consumption and speed [29]. In general, the effect of noise in large–area devices is less than in small–area devices. Noise can be used as a tool to study many physical phenomena in semiconductor devices such as capture and emission of mobile charges by defect centers in the MOSFET gate oxide. Having said that, the effect of electronic noise should be taken into account during circuit design to improve circuit precision.

1.2.1 *Thermal Noise*

Thermal noise results from the random motion of charge carriers (electron or hole) in a conductor at temperatures above zero Kelvin. Thus, thermal noise exists even with the absence of bias. This noise was discovered for the first time in 1926 by John B. Johnson and later during that year explained by Harry Nyquist [30, 31]. The observed thermal noise in MOSFETs is due to the channel resistance which decreases with the increase of gate-source voltage (V_{GS}). Increasing V_{GS} in a MOSFET would increase the inverted carrier density in the channel. This leads to the reduction in the channel resistance which in turns decreases the thermal noise. In addition, thermal noise is considered temperature dependent. If device temperature increases the thermal noise would increase linearly. The PSD of the thermal noise is evaluated as [27, 32]:

$$S_v(f) = 4k_B TR \,. \tag{1-1}$$

Here, k_B = 1.38 x10^{-23} J/K, and *R* is the resistance or the real part of a conductor impedance. The PSD of thermal noise is frequency independent. It has a uniform power distribution with respect to the frequency. This noise is also called white noise by analogy to white light which has a uniform distribution in the optical band [28].

1.2.2 *Shot Noise*

Shot noise is the time dependent fluctuations of an electronic current caused by the discreteness of the charges arrival at a potential barrier. It can be observed in a vacuum tube, diode, or transistors. Therefore, shot noise cannot be seen in a simple conductor due to the absence of barrier [27, 33]. In addition, shot noise requires a DC current in order to be seen [34]. This noise was seen for the first time back in 1918 by Walter Schottky while he was working on vacuum tubes [27, 28, 32]. The shot noise can be calculated from:

$$I_{sh} = \sqrt{2qI_{DC}\Delta f} \,. \tag{1-2}$$

Here, q is the electronic charge (1.602 x10^{-19} c), I_{DC} is the direct current in amperes, and Δf is the system's noise bandwidth in (Hz). Typically Δf is evaluated at very low frequency

~ 1 (Hz). PSD of the shot noise can be extracted from the expression [27, 28]:

$$S_{I_{sh}}(f) = 2qI_{DC} \,. \tag{1-3}$$

It is hard to distinguish the shot noise form the thermal noise on the spectrum analyzer due to its flat nature with respect to frequency. However, shot noise depends on DC current level and is temperature independent. In MOS transistors, shot noise is due to the leakage current between the substrate and the channel or between the gate and the channel especially when the gate oxide is very thin [35, 36].

1.2.3 *Generation and Recombination Noise*

Generation and recombination (G-R) noise exists in semiconductor devices when a charge carrier (a hole or an electron) is trapped and detrapped randomly and spontaneously by a defect in the bulk or at the interface of two materials. Trapping a carrier will fluctuate the voltage or the current signals due to the loss and gain of carriers for transport. In addition, a trapped charge may modulate mobility of the carriers, space charge region width, and local electric field [27, 32, 37]. The defect within the forbidden band - gap is considered a trap center if it is close either to the conduction or valance band - edge. On the other hand, if the trap is close to the middle of Si band – gap energy, then it acts as a generation recombination center. The power spectral density of the fluctuations in the number of charge carriers can be expressed as [27, 32]:

$$S_N(f) = \frac{4\overline{\Delta N}^2 \bar{\tau}}{1+\left(2\pi f \bar{\tau}\right)^2} \,, \tag{1-4}$$

where, $\bar{\tau}$ is the average time constant for a random signal switching between two states, and ΔN is the change in number of carriers due to trapping and detrapping phenomenon.

1.2.4 *Random Telegraph Signals*

Random telegraph signals have been studied and investigated for over two decades [38, 39, 40, 41, 42]. RTS is a special case of G-R noise which originates from the consecutive capture and emission events of a single or multiple mobile charge carriers located in the channel by defect center(s) at the Si/SiO$_2$ interface or in the oxide bulk (Figure 1-1) [42, 43]. The probability of capturing an electron or a hole from the channel by a defect in the gate dielectric will be less if the trap energy in the SiO$_2$ band - gap goes beyond a few $k_B T$ of the Fermi energy level. This affects the probability of observing an RTS in a device. The probability of finding a trap to be occupied in the gate oxide or at the interface can be evaluated based on the Fermi - Dirac distribution [37, 44]:

$$f_t(E) = \frac{1}{1 + g e^{(E - E_F)/k_B T}} , \tag{1-5}$$

where, E_F is the Fermi energy level, and g is the degeneracy factor of a trap which is typically taken as 1. On the other hand, the probability of finding a trap empty is (1- $f_t(E)$). Figure 1-2 demonstrates the probability profile of a trap occupancy and the regions where a trap can communicate with the channel carriers and cause fluctuations in the V_{DS}. It is

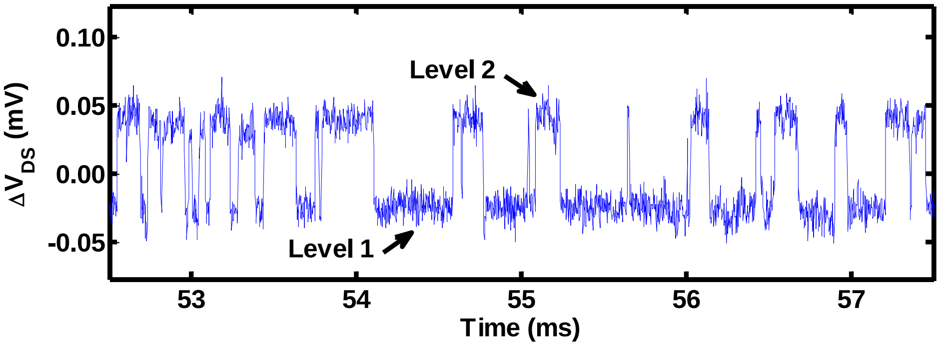

Figure 1-1 An example of small window for two level RTS measured on a 3.3 V nMOS device biased at V_{GS} = 1.40 V and V_{DS} = 0.50 V at temperature of 190 K.

inferred from Figure 1-2 if a trap is filled, it will be impossible to capture another charge due to the Pauli Exclusion Principle [37]. Thus, a trap should be empty and reside within a few $k_B T$ from the Fermi energy level to be able to communicate with the channel carries.

RTS can be observed in MOS devices with a typical gate area less than 1 μm^2 [45, 46]. If there is one active trap, most likely there will be two level RTS where the drain-source voltage is switching between two states as shown in (Figure 1-1). This assumes the trap is stable. Determining the number of active traps in a complex RTS is not straight forward. Some literature suggest that the number of active traps can be extracted from the number of RTS levels using: ceil($\log_2(N_L)$) [2]. Here, ceil(N) is the ceiling function which rounds up N to the nearest integer value, and N_L is the number of RTS levels. In some complicated RTS traces, there are 4 discrete states or levels as shown in Figure 1-3, according to ceil($\log_2(4)$), there should be 2 active traps. In fact, we identified three traps are responsible for causing this complicated RTS.

The drain voltage noise PSD $S_{V_{DS}}$ for the same RTS trace in Figure 1-1 is depicted in Figure 1-4. Here, the corner frequency is $f_0 = 1/\bar{\tau} = 1/\bar{\tau}_e + 1/\bar{\tau}_c$, and $S_{V_{DS}}$ can be expressed in terms of the RTS amplitude as [42]:

$$S_{V_{DS}}(f) = \frac{4\left(\Delta V_{DS}\right)^2}{\left(\bar{\tau}_c + \bar{\tau}_e\right)\left[\left(1/\bar{\tau}_c + 1/\bar{\tau}_e\right)^2 + \left(2\pi f\right)^2\right]} . \tag{1-6}$$

Here, $\bar{\tau}_c$ and $\bar{\tau}_e$ are the average capture and emission time constants associated with a trap. As the device area gets larger, more and more traps are sampled with different time constants. If one considers the device area to be partitioned into individual units: the conductance of each unit is locally modulated only by the trapping center contained within it. The current noise power spectral density summed over all traps is in $1/f$ form.

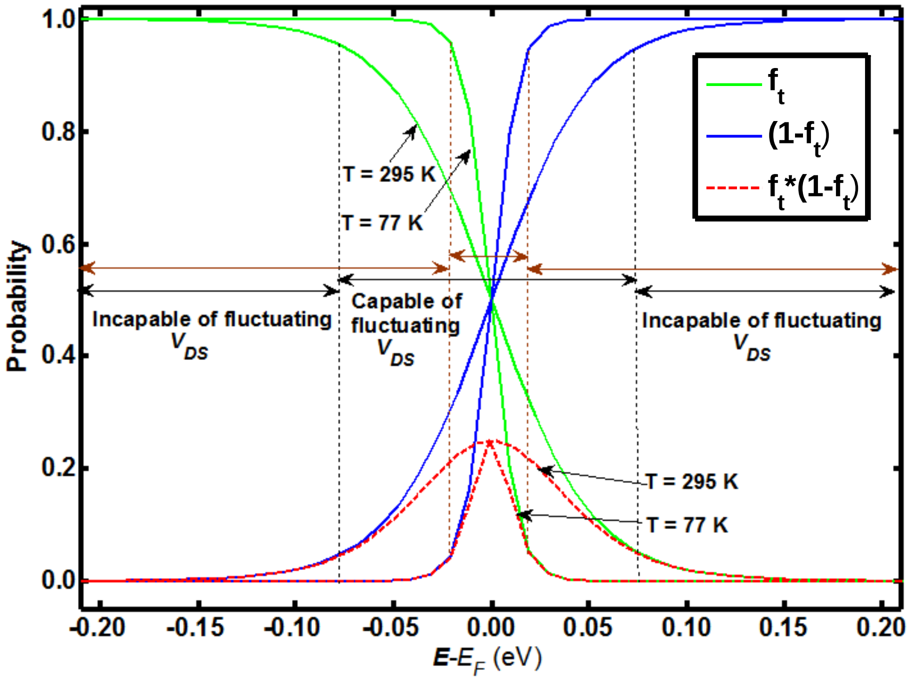

Figure 1-2 The probability of trap occupancy at two temperatures. The product of the probability of the trap to be empty and the probability of the electron to exist in a nearby energy level to be trapped $\left[f_t(E)\left(1-f_t(E)\right)\right]$ looks like a delta function at low temperature.

1.2.5 *Flicker Noise or* $1/f^{\gamma}$

Flicker noise is distinguished based on the nature of the frequency domain noise power spectra e.g. $(1/f)$ noise. It occurs in all electronic devices regardless of the materials (whether conductor, semiconductor etc.). Also $1/f$ noise can be seen in some biological and financial systems as well as in some natural phenomena [47, 48, 49]. The mechanisms and origin of $1/f$ noise in all these systems are not the same. Several models have been suggested to study the $1/f$ noise in semiconductor devices such as MOSFETs. One of these models is the Unified Number –Mobility (UNM) fluctuations model. It is one

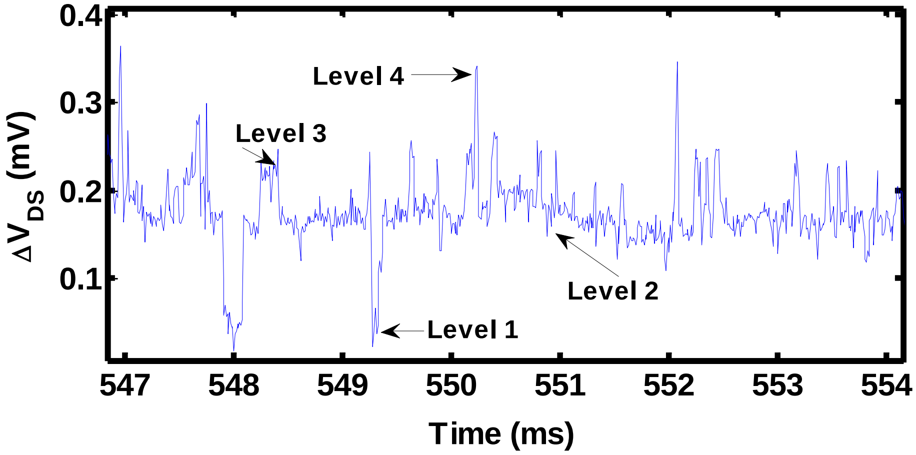

Figure 1-3 An example of 4 Level RTS measured on a 3.3 V nMOS device. V_{GS} = 1.40 V and V_{DS} = 0.50 V where temperature is 295 K.

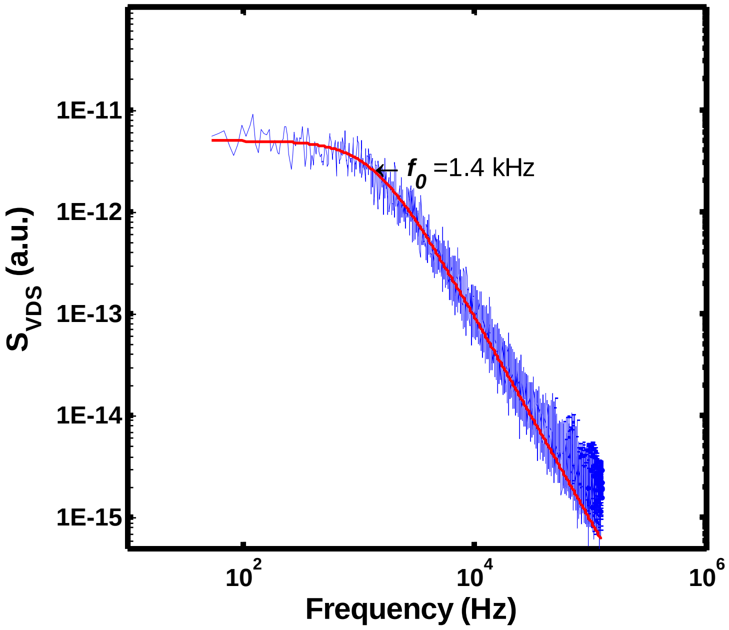

Figure 1-4 Lorentzain power spectral density corresponds to the two-level RTS noise waveform in Figure 1-1 shows corner frequency 1.4 kHz. V_{GS} = 1.4 V and V_{DS} = 0.5 V at 190 K.

of the most accepted models that can provide a satisfactory elucidation of the flicker noise in large–area of MOSFET devices [22]. In a MOSFET, the flicker noise is observed due to the interference of several traps located close to the Si/SiO$_2$ interface with the channel carriers. In large devices, when several channel carriers captured by traps nearby the Si/SiO$_2$ interface over a wide range of tunneling times, local channel conductivity changes randomly due to the loss of channel carriers. In addition, the occupied traps become electrically active centers capable of modulating the channel carrier mobility [22, 28].This process occurs spontaneously and randomly between the channel carriers and the defect centers.

Flicker noise PSD is proportional to $1/f^{\gamma}$ where γ is in the range of 0.7 and 1.3. The current spectral density can be expressed by Hooge empirical formula, McWhorter's model, Unified Number-Mobility fluctuations model etc. In this section, a brief discussion of the Hooge empirical formula is introduced. In Chapter 2, more details about this theory can be found. The Hooge empirical formula of the drain current noise generated by the fluctuations in the channel carrier mobility can be expressed by [22, 27, 32]:

$$S_I = \frac{\alpha_H I_{dc}^{a}}{N f^{\gamma}} = \frac{K_{1/f} I_{dc}^{a}}{f^{\gamma}} . \tag{1-7}$$

Here, *N* is the number of the fluctuators that generates the $1/f$ noise, a and γ depend upon the relevant physical process where $a = 2$ and $0.5 < \gamma < 1.5$ [32, 50], α_H is the Hooge parameter which depends on the material quality. It was observed that for a high quality material, α_H is lower by 2-3 orders of magnitude than the suggested value of 2x10^{-3} [51]. When the MOS devices are heavily downsized, the number of the fluctuators per unit area decreases. Thus, making the $1/f$ noise a definite problem for the microelectronic industry. Further shrinking to the device geometry produces new noise mechanisms that dominate the internal noise sources at low frequency such as the RTS phenomenon.

1.3 Summary

The main focus of this thesis is to provide a comprehensive study about the gate oxide defects in MOSFETs using measured RTS data and construct a new RTS statistical model and simulation tool. The newly developed RTS statistical model and its simulation tool are constructed based on the first principles and supported by extensive measured data. A review of the sources and mechanisms for the electronic noise has been provided. Motivations and reasons behind this research are highlighted.

This thesis has been arranged and divided into several chapters. In Chapter 2, the focus is on the origin of the low frequency noise in MOSFETs, specifically bulk mobility fluctuations, number fluctuations, and oxide trap generated correlated number – mobility fluctuations. The effect of device scalability and the variability on $1/f$ noise and RTS are explained and discussed. State–of–the-art in RTS noise model is expounded in great detail.

In Chapter 3, experimental measurement setup and techniques on acquiring RTS data are shown for variable temperatures. The current – voltage and capacitance – voltage measurement procedures are outlined. RTS data were acquired on fresh devices as well as on stressed devices. The advantages of using variable temperatures in investigating the gate oxide defects are explained and supported with relevant literature. Specifications of the –used devices in this thesis are discussed.

In Chapter 4, RTS analyses in time and frequency domains are performed to extract the RTS and trap characteristics from the measured data. Trap position in 2D is calculated. Trap energies in SiO_2 band –gap energy, capture, emission, and relaxation energies are extracted. Trap type and species causing the fluctuations in the V_{DS} are studied on several devices. Neutral oxygen vacancy deficient center is found to be the origin of the RTS noise.

In Chapter 5, the adopted mechanisms and principles for reconstructing the new RTS statistical model are discussed. This chapter explains all equations that are utilized to reconstruct the RTS in time and frequency domains.

In Chapter 6, transformation of the new RTS statistical model into an interactive program using MATLAB as a platform has been implemented. User-provided parameters to run the simulation are described and listed. Output results of the RTSSIM are compared with the measured RTS data at the same criteria for the purpose of validation.

Chapter 7 summarizes the aim, importance, and major contributions of this work in the area of random telegraph noise in CMOS technology. In addition, this chapter outlines the future possible work can be done and added to diversify the functionality of the RTSSIM.

Chapter 2 Low Frequency Noise in MOSFETS

2.1 Introduction

Accelerated demands of scaling down MOSFETs have raised many issues and opportunities for low frequency noise (LFN). Scaling down MOSFETs provides high integration of devices on one chip, reduces power consumption, and increases the device speed [52]. On the other hand, maintaining integrity and reliability of a thin film of SiO_2 are one of the key factors to keep the miniaturized MOSFETs usable in integrated circuits with reliable performance. Hundreds of millions of MOSFETs are constructed in a single chip which is used in microprocessor, memories, and other devices. This highly dense integrated circuit dictates the highest thoroughness and quality control to ensure that the electrical properties of the silicon dioxide films are preserved and well maintained. In addition, scaling down the devices impacts the signal to noise ratio.

The number of channel carriers in MOSFETs decreases as the device volume scales down. In this case, the nature of LFN is quite different from LFN in larger-area devices. This suggests the 1/*f* noise is replaced by another mechanism which is known as random telegraph signals [43, 52]. Down-scaling results in variability of many device characteristics including LFN and RTS. This variation may reach several orders of magnitude within the same technology [52, 20].

In some applications, LFN can be reduced by turning ‘Off’ the MOSFET for some time before is turned ‘On’ [8, 52, 53, 54, 55]. This implies that the LFN does not depend only on the current bias point but also depends on the previous history of the bias [52]. In addition, switching the MOSFET to the accumulation region when the device is not contributing to the circuit helps to save power and reduce noise [8]. This technique might be used to reduce the 1/*f* noise in large–area devices. However, in highly scaled devices, RTS due to a single or a few trapped electrons cannot be reduced effectively [54].

Several mechanisms of LFN have been suggested. However, no definite theory has explained and modeled the origin of RTS in highly scaled devices yet. Understanding the cause and origin of LFN in large – area devices paved the way to understanding the RTS. Two schools of thought among these several proposed theories are considered the most popular ones. These two schools of thought suggest that the physical origin of 1/f noise in MOSFETs is the mobility and number fluctuations of the channel carriers [52]. Hooge showed in 1969, semiconductor samples suffer from 1/f noise which later was explained and related to mobility fluctuations $(\Delta\mu)$ [56]. According to the second perspective, 1/f noise is due to the fluctuations in the channel carriers (ΔN). This perspective was explained by McWhorter in 1957 [57]. According to J. Chang *et al.* [58], the data taken on several pMOSFETs showed behavior that can be explained by $\Delta\mu$ theory where, the measured data on nMOSFETs behave according to ΔN perspective. In 1992, K. Hung *et al*. suggested a combined model that correlates both perspectives which is known as the Unified Number – Mobility Fluctuations (UNMF) model [22]. The UNMF model produces excellent results and provides a good explanation for LFN in large-area MOSFETs [52]. From this introduction, there are three mechanisms responsible for the LFN in large–area devices which are $\Delta\mu$, ΔN, and correlated $\Delta\mu$ and ΔN.

2.2 Number Fluctuations

Low frequency noise in electronic devices can be related to the modulation of the conductivity $\sigma_n = q\mu_n n$, where n and μ_n are the charge carrier density and average carrier mobility, respectively. From this relation we cannot determine exactly whether n, μ_n, or both are causing the modulation in σ_n. It is hard to tell which parameter is dominating as

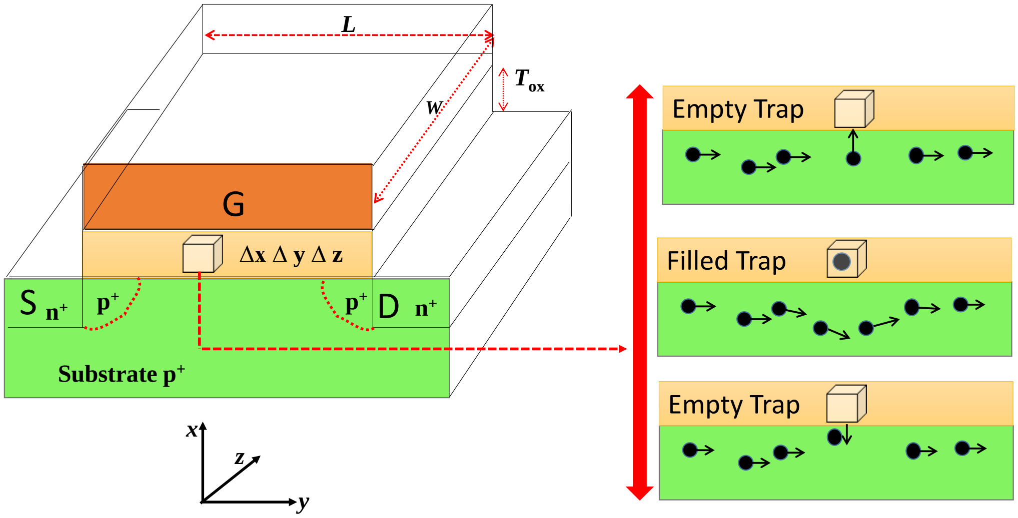

Figure 2-1 Single electron trapping/detrapping events in MOSFETs. Capturing electron(s) by trap(s) located in the gate oxide would remotely modulate the channel carrier mobility and decrease the local conductivity of the channel.

a source of noise. Therefore, looking at the contribution of each parameter as a function of V_{GS} is essential.

The noise contribution from the number fluctuations in MOSFETs can be related to the interactions between the defects that are located close to the Si/SiO$_2$ interface with the channel carriers (Figure 2-1). If the trap is located within a few $k_B T$ of the Fermi energy level and it is empty, then it has a probability to dynamically exchange an electron with the channel (Figure 1-2). Number fluctuation depends on the total active traps and on the availability of the carriers in the channel. When an active trap captures an electron from the channel, the total charge in the oxide changes by (δQ_{ox}). This small change in the Q_{ox} leads to fluctuations in the flat band voltage (δV_{FB}). The spectral density of these two quantities can be related as: $S_{V_{fb}} = S_{Q_{ox}} C_{ox}^2$ [32, 59]. The noise spectral density due to capture and emission of an electron by one trap in the oxide can be evaluated as [32]:

$$S_{Q_{ox}} = \frac{4q^2\overline{\Delta N_{ox}^2}}{W^2L^2}\frac{\overline{\tau}}{1+\left(\omega\overline{\tau}\right)^2}\ . \tag{2-1}$$

Here, ΔN_{ox} is the change in the number of oxide charges, and $\omega = 2\pi f$. From the probability of trap occupancy, $\overline{\Delta N_{ox}}$ is computed according to the Fermi - Dirac distribution (Eq. 1-5) Then, $\overline{\Delta N_{ox}^2} = \left(1 - f_t(E)\right) f_t(E)$. In a typical device, there could be several traps distributed around the Si/SiO2 interface or in the oxide bulk. In order to include the total noise due to all active traps, the corresponding PSD due to each active trap should be added up. However, the exact number of the active traps is not known. Therefore, a uniform trap density distribution in volume and energy is considered and can be integrated to find the total active traps in a particular device. The fluctuation in the $S_{Q_{ox}}$ due to all active traps is computed using [32]:

$$S_{Q_{ox}} = \int_{E_V}^{E_C}\int_0^{T_{ox}}\int_0^{L}\int_0^{W}\frac{4q^2N_t\left(E,x,y,z\right)(1-f_t(\mathrm{E}))f_t(E)}{W^2L^2}\left(\frac{\overline{\tau}}{1+\omega^2\tau^2}\right)dzdydxdE\ . \tag{2-2}$$

Here, E_C is the Si conduction band – edge, E_V is the Si valance band – edge, T_{ox} is the oxide thickness, and $N_t\left(E,x,y,z\right)$ is the distribution of the traps over the energy and space. Here, the oxide defects are assumed a uniform spatial distribution which makes $N_t\left(E,x,y,z\right) = N_t\left(E\right)$. The integration of Eq. 2-2 along the width and length of the channel is:

$$S_{Q_{ox}} = \frac{4q^2}{WL}\int_{E_V}^{E_C}\int_0^{T_{ox}} N_t\left(E\right)(1-f_t(\mathrm{E}))f_t(E)\left(\overline{\tau}/1+\omega^2\tau^2\right)dxdE\ . \tag{2-3}$$

The product of $(1-f_t(\mathrm{E}))f_t(E)$ equals to: $-k_BT\,\partial f(E)/\partial E$ and it acts like a delta function around the Fermi energy level. Then, the integration of Eq. 2.3 is:

$$S_{Q_{ox}} = \frac{4k_B T q^2}{WL} \int_0^{T_{ox}} N_t\left(E_F\right)\left(\overline{\tau}/1+\omega^2\tau^2\right)dx . \tag{2-4}$$

Direct tunneling is the assumed mechanism of charging and discharging an electron by a trap in the oxide. One of the concerns about this approach that it does not consider the capture and emission of an electron or a hole as a thermally activated process (phonon–assisted tunneling) but takes it as an equi-energy process. Thus, the average elastic tunneling time is [10, 60]:

$$\overline{\tau} = \tau_0 e^{\lambda x} , \tag{2-5}$$

where, the electron wave attenuation coefficient $\left(\lambda\right)$ can be evaluated using Wentzel – Kramers – Brillouin (WKB) approximation: $\lambda = 4\pi/h\sqrt{2qm_{ox}{}^{*}\phi_0}$ [10, 60]. Here, ϕ_0 is the electron affinity difference between the Si and SiO$_2$, and m_{ox}^{*} is the electron effective mass in the oxide. The derivative of Eq. 2-5 with respect to *z* is $dx = d\tau/\lambda\tau$. This result can be substituted in Eq. 2.4 and integrated between 0 and ∞. If the gate oxide thickness is large enough and the tunneled electron cannot reach the gate electrode/oxide interface, the electron keeps bouncing between the channel conduction band and the defect. Therefore, an electron sees T_{ox} as an infinite depth. Thus, the upper limit of T_{ox} is replaced by ∞. The final expression of the power spectral density due to the fluctuations in the Q_{ox} is:

$$S_{Q_{ox}} = \frac{k_B T q^2 N_t\left(E_F\right)}{\lambda W L f^{\gamma}} . \tag{2-6}$$

Since we assumed the distribution of the traps in the oxide is uniform, then the exponent $\left(\gamma\right)$ of the frequency in Eq. 2-6 is 1. The power spectral density of MOSFET drain – source current $\left(S_{I_{DS}}\right)$ can be related to the flat – band voltage fluctuation in terms of the transconductance $\left(g_m\right)$ [59]:

$$S_{I_{DS}}(f)=\frac{k_B T q^2 N_t\left(E_F\right)}{\lambda W L f C_{ox}^2} g_m^2 . \tag{2-7}$$

In general, $g_m = \partial I_{DS} / \partial V_{GS}$ in the linear or in the saturation regions. In the linear region, the transconductance is evaluated based on the I_{DS} in the linear region [61]:

$$g_m = \mu_n C_{ox}\left(\frac{W}{L}\right) V_{DS} . \tag{2-8}$$

Here, $S_{I_{DS}}$ in the linear region depends strongly on the V_{DS} but is independent of V_{GS}.

2.3 Mobility Fluctuations

Hooge model has been utilized to extend the explanation of 1/f noise in MOSFETs. Hooge empirical formula for 1/*f* noise (Eq. 1-7) suggests the fluctuations in the drain – source current is mainly due to the bulk mobility fluctuations [22, 62]. Hooge parameter $\left(\alpha_H\right)$ is related to the effective mobility $\left(\mu_{eff}\right)$ which is due to two mechanisms: the mobility due to lattice $\left(\mu_{lat}\right)$ and impurity $\left(\mu_{imp}\right)$ scattering [62]. Hooge did not consider other mechanisms that may affect the carrier mobility fluctuations in the channel such as surface roughness or remote Coulomb scattering due to active gate oxide traps. Hooge assumed lattice scattering mechanism produces 1/*f* noise where impurity scattering had no major contribution to the noise [62]. It is assumed that μ_{lat} and μ_{imp} are acting independently and have the same energy dependence. Thus, the effective channel carrier mobility is evaluated using Matthiessen's rule [62]:

$$\frac{1}{\mu_{eff}}=\frac{1}{\mu_{lat}}+\frac{1}{\mu_{imp}} . \tag{2-9}$$

The Hooge parameter is then evaluated [62]

$$\alpha_H = \left(\frac{\mu_{eff}}{\mu_{lat}}\right)\alpha_{lat}\,, \tag{2-10}$$

where, α_{lat} is the scattering coefficient due to the lattice scattering mechanism. From Eq. 1-7 we can infer that the flicker noise depends on the charge carrier density in the channel which increases with the increase of V_{GS}. In addition, $S_{I_{DS}}$ ccording to Hooge theory is proportion to α_{lat}. In general, regardless of the scattering mechanisms, if the scattering effect increases, the carrier mobility decreases. When T is increased, mobility fluctuation corresponding to the lattice scattering decreases due to the increase of lattice vibrations. However, the opposite effect is observed when temperature is increased, average carrier mobility increases for a certain point before lattice scattering starts to dominate (Figure 2-2) [63, 64].

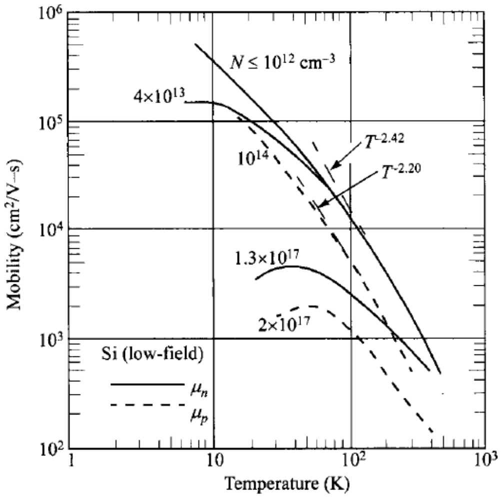

Figure 2-2 Mobility of electrons and holes as a function of temperature (Reprinted with permission), [63, 64].

Ghibaudo *et al.* has combined both mobility and number fluctuations in one compact model to evaluate the $S_{I_{DS}}$ [59, 65]. Trapping a mobile charge by a gate oxide defect may cause a charged scattering center, affecting the mobility of the remaining channel carriers. This suggests, the fluctuations in the drain – source current could be due to the fluctuation in the flat – band voltage and effective channel carrier mobility [59]:

$$\delta I_{DS} = \frac{\partial I_{DS}}{\partial V_{fb}} \delta V_{fb} + \frac{\partial I_{DS}}{\partial \mu_{eff}} \frac{\partial \mu_{eff}}{\partial Q_{ox}} \delta Q_{ox} . \tag{2-11}$$

According to Ghibaudo *et al.* [59], $\partial I_{DS} / \partial V_{fb} = -\partial I_{DS} / \partial V_{GS} = -g_m$ which can be substituted in Eq. 2-11. This yields the evaluation of the I_{DS} fluctuation in the linear region which includes the effect of channel carrier mobility fluctuation:

$$\delta I_{DS} = -g_m \delta V_{fb} + \frac{I_{DS}}{\mu_{eff}} \frac{\partial \mu_{eff}}{\partial Q_{ox}} \delta Q_{ox} . \tag{2-12}$$

From Eq. 2-12, the scattering parameter is used to link the variation in the oxide charge to the fluctuation in the channel carrier mobility $\alpha = \left(1/\mu_{eff}^2\right)\left(\partial \mu_{eff} / \partial Q_{ox}\right)$. When α is substituted in Eq. 2-12, the fluctuation in I_{DS} becomes: $\delta I_{DS} = -g_m \delta V_{fb} + \mu_{eff} \alpha I_{DS} \delta Q_{ox} \rightarrow \delta I_{DS} = -g_m \delta V_{fb} + \mu_{eff} \alpha I_{DS} \delta V_{fb} C_{ox}$. The power spectral density of the drain – source current is [59]:

$$S_{I_{DS}} = S_{V_{fb}} \left(-g_m + \mu_{eff} \alpha I_{DS} C_{ox}\right)^2 . \tag{2-13}$$

One of the concerns about this approach is the sensitivity of the mobility to the gate oxide charge which is weak. In this case, the mobility can be independent of the interface charge. On the other hand, if α is high, then $\left(S_{I_{DS}} / I_{DS}^2\right)$ may not be well correlated to $\left(g_m^2 / I_{DS}^2\right)$ because the mobility fluctuation term dominates [59].

2.4 Unified Number – Mobility Fluctuation Theory

Scaling down MOSFETs has allowed scientists to study LFN which is generated by single or a few traps. Hung *et al.* in 1990 [22], suggested a unified model for 1/*f* noise based on the carrier concentration fluctuations per unit area in the channel and surface carrier mobility fluctuations. The UNMF model considers the total inversion charge along the width of the channel constant. On the other hand, the inversion charge density along the channel length may change due to the capture and emission of mobile charge by the trap(s) in the oxide. A drain – source current in the linear region in a MOSFET biased with a small drain-source voltage can be expressed as [22]

$$I_{DS} = qW\bar{\mu}_l N_{inv} E_y \,. \tag{2-14}$$

Here, $\bar{\mu}_l$ is the average channel carrier mobility in the linear region, N_{inv} is the inversion channel carrier density per unit area, and E_y is the electric field along the channel. If there is one active trap capable of capturing an electron or a hole from the channel, a fractional change in the local current can be observed [22]. This fractional change in the local current can be translated mathematically as [22]:

$$\frac{\delta I_{DS}}{I_{DS}} = -\left(\frac{1}{\Delta N_{inv}}\delta\Delta N_{inv} \pm \frac{1}{\bar{\mu}_c}\delta\mu_c\right). \tag{2-15}$$

K. K. Hung *et al.* [22], linked number of occupied traps to the number of trapped carriers through: $\delta\Delta N_{inv}/\delta\Delta N_t$ where $\Delta N_{inv} = W\Delta y N_{inv}$ and $\Delta N_t = W\Delta y N_t$ (Figure 2-1). This implies, if only one electron is captured, there is one trap filled up. Thus, at the strong inversion the ratio $\delta\Delta N_{inv}/\delta\Delta N_t = 1$ and that is known as the coupling coefficient. When $\delta\Delta N_t/\delta\Delta N_t$ is multiplied with $\delta I_{DS}/I_{DS}$, this leads to new expression:

$$\frac{\delta I_{DS}}{I_{DS}} = -\left(\frac{1}{\Delta N_{inv}}\frac{\delta\Delta N_{inv}}{\delta\Delta N_t} \pm \frac{1}{\bar{\mu}_c}\frac{\delta\mu_c}{\delta\Delta N_t}\right)\delta\Delta N_t \,. \tag{2-16}$$

From the ratio $\delta\mu_c/\delta\Delta N_t$, Eq. 2-16 can be simplified further. The UNMF model assumes the average channel carrier mobility is governed by two mechanisms. The effective surface mobility is dominated by the Coulomb scattering by the trapped charge in the oxide, screened by the channel carriers. Matthiessen's rule is used to utilize the evaluation of the average channel carrier mobility [22]:

$$\frac{1}{\bar{\mu}_c} = \frac{1}{\mu_{oth}} + \frac{1}{\mu_{ox}} \rightarrow \frac{1}{\mu_{oth}} + \alpha N_t \,. \tag{2-17}$$

From Eq. 2-17 $\mu_{ox} = 1/\alpha N_t$. Here, μ_{ox} is the mobility limited by the gate oxide charge scattering where μ_{oth} is the mobility limited by other mechanisms such as surface roughness, impurity scattering, lattice scattering etc. [66]. Fluctuations in the number of occupied traps cause fluctuations in the channel carrier mobility and that can be expressed as:

$$\frac{\delta\bar{\mu}_c}{\delta N_t} = \frac{-\alpha\mu_{oth}^2}{\left(1+\alpha N_t \mu_{oth}\right)^2} = -\alpha\bar{\mu}_c^2 \rightarrow \delta\bar{\mu}_c = -\alpha\bar{\mu}_c^2 \delta N_t \,. \tag{2-18}$$

Substituting $\delta\Delta N_{inv}/\delta\Delta N_t = 1$ for strong inversion, $\delta\Delta N_t = W\Delta y \delta N_t$ and Eq. 2-18 in Eq. 2-16 :

$$\frac{\delta I_{DS}}{I_{DS}} = -\left(\frac{1}{W\Delta y N_{inv}} \pm \alpha\bar{\mu}_c \frac{1}{W\Delta y}\right)\delta\Delta N_t \rightarrow \frac{\delta I_{DS}}{I_{DS}} = -\left(\frac{1}{N_{inv}} \pm \alpha\bar{\mu}_c\right)\frac{\delta\Delta N_t}{W\Delta y} \,. \tag{2-19}$$

The power spectral density of $\delta I_{DS}/I_{DS}$ in term of the power spectral density of average fluctuations in the number of occupied gate oxide traps $\left(S_{\Delta N_t}\right)$ is [22]:

$$S_{\Delta I_{DS}} = \left(\frac{I_{DS}}{\Delta N_{inv}}\left(\frac{1}{N_{inv}} \pm \alpha\bar{\mu}_c N_{inv}\right)\right)^2 S_{\Delta N_t} \,. \tag{2-20}$$

From the number fluctuation theory, $S_{\Delta N_t}$ can be evaluated using the same procedure in section 2.2 [22]:

$$S_{\Delta N_t} = 4\int_{E_V}^{E_C}\int_0^W\int_0^{T_{ox}} N_t\left(x,y,z,E\right)(1-f_t(\mathrm{E}))\,f_t(E)\Delta y\left(\frac{\overline{\tau}}{1+\omega^2\tau^2}\right)dxdzdE\ . \tag{2-21}$$

Assumptions are made in order to evaluate the integration. First, it is assumed that the trap density close to the Si/SiO$_2$ interface is uniformly distributed and varied only with energy. Second, the probability of a charge carrier penetrating into the oxide decreases exponentially as expressed in Eq. 2-5. The trap occupancy is computed using Eq. 1-5. From Figure 1-2, $f_t\left(E\right)\left(1-f_t\left(E\right)\right)$ acting like a delta function around the quasi Fermi energy level. This implies the major contribution to the integration comes from the traps whose energy is close to the Fermi level. Evaluating the integration of Eq. 2-21 leads to the power spectral density due to the occupied gate oxide traps [22]:

$$S_{\Delta N_t} = N_t\left(E_F\right)\frac{k_B T W \Delta y}{\lambda f}\ . \tag{2-22}$$

According to the UNMF model, the average noise power of I_{DS} due to the fluctuations in the I_{DS} can be evaluated using [67]:

$$S_{I_{DS}} = \frac{1}{L^2}\int_0^L S_{\Delta I_{DS}}\Delta y dy\ . \tag{2-23}$$

From Eqs.20–2.23, the total power spectral density of I_{DS} is [22]:

$$S_{I_{DS}} = \frac{k_B T I_{DS}^2}{\lambda f W L}\left(\frac{1}{N_{inv}} \pm \alpha\bar{\mu}_c\right)^2 N_t(E_F)\ . \tag{2-24}$$

The sign of the mobility fluctuation term in Eq.2-24 depends on the trap type. If the trap is neutral when is empty, ‘+’ sign is used. If the trap is attractive when is empty, ‘-’ sign will be used. Implementation, comparisons with other methods, and further discussions of UNMF theory will be in the next chapters.

2.5 State-of-the-art in RTS

The continuous scaling of electronic devices has shown discrete switching in the V_{DS} due to the capture and emission of mobile charge carriers by an individual defect located in the bulk oxide or at the Si/SiO_2 interface. Studying RTS at variable temperatures can provide insightful information about the nature and the origin of the defect. RTS might be considered an alternative technique for studying the microscopic origin of LFN. RTS has the ability to probe on an individual trap in real time from which several trap characteristics are extracted and studied.

RTS is a stationary signal where its statistical properties are constant e.g. the average and the standard deviation of a stationary signal are time independent. The common approach for acquiring and studying RTS data is to use steady state biasing conditions. Based on the Poisson distribution of occurrence for each RTS level and from the V_{GS}, V_{DS}, and temperature dependence, RTS and trap characteristics are extracted. In this work, we are adopting this method for analyzing and modeling the RTS.

On the other hand, RTS can be evaluated based on the cyclo-stationary excitation where the MOSFET is not biased at steady state but is switched periodically [68]. Under cyclo–stationary excitation RTS is evaluated through the calculation of the RTS autocorrelation and the implementation of the Wiener – Khinchin formula [68]. The cyclo-stationary approach yields the analytical formulation of the RTS spectrum.

Zero crossing statistics is a method used to analyze the RTS data [69]. This approach can track any fluctuations in the V_{DS} due to the capture and emission of an electron from and to the channel. The RTS data are divided into constant width of intervals and the number of crossing events in each window is examined. This approach may work fine and lead to good results and analysis for well-defined RTS-levels. However, if the RTS levels are overlapped, zero crossing approach cannot differentiate between the levels and that may populate the data in the wrong group. Zero crossing method does not link the crossing events to the electron transition and to the state of the trap (whether a trap is filled or empty). Therefore, extraction of the average capture and emission times in a complex RTS is associated with high risk and that may end up with erroneous calculation of the RTS characteristics.

RTS is also modeled through Markov process which can describe single trap transitions between two discreet states (0 and 1) at different times (t_1 and t_2) as shown in Figure 2-3 [70]. Using this model without major enhancements limits the applicability of the analysis to one or two active traps. Furthermore, RTS amplitude, average capture, and emission times are extracted independently which may lead to inaccurate results [2, 15].

Time lag plot (TLP) is known by a lag scatter plot used to analyze the RTS autocorrelation in time-series data [2, 13]. The TLP constructs the date on two -dimensional graph where the data sampled at i_{th} time interval (t_i) is plotted on the x–axis. The data sampled at [time interval +1] (t_i +1) is plotted on the y–axis. Each RTS level appears on the TLP as a diagonal cluster. This method is considered an impractical way to analyze a large amount of RTS data as well as a complex RTS. This is due to the absence of a clear method that allows the extraction of the number of RTS levels. In addition, strong presence of the thermal or 1/*f* noise might cause the RTS levels to overlap. In this case, it will be

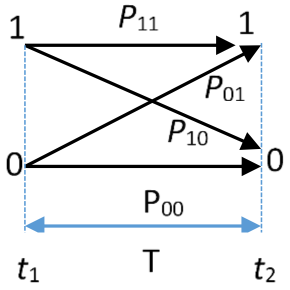

Figure 2-3 Description of single trap transitions between two states using Markov method.

hard to differentiate between the RTS levels. However, using an enhanced TLP technique may allow the analysis of large RTS data even with the presence of additional noise. According to Realov *et al.* [2], the frequency of each point in the TLP is transformed into a two–dimensional histogram from which the number of the RTS levels is extracted [2].

Another way to model the effect of RTS is using compact models based on the two–stage L–shaped resistance–capacitance (RC) circuits [17]. According to this method, generation of the RTS traces can be done by integrating a white noise source with a L–shaped circuit connected to a comparator as shown in Figure 2-4 [17]. The RC values are set based on the RTS characteristics. However, this model does not consider the characteristics of the trap species that are responsible for the fluctuations in the V_{DS} signals. Moreover, it does not incorporate the trap position in the oxide and along the channel. In addition, this approach makes the construction of the complex RTS due to several active traps impractical. Reconstructing a complex RTS through L-shaped RC circuit does require several stages connected in parallel where each stage can handle a single trap.

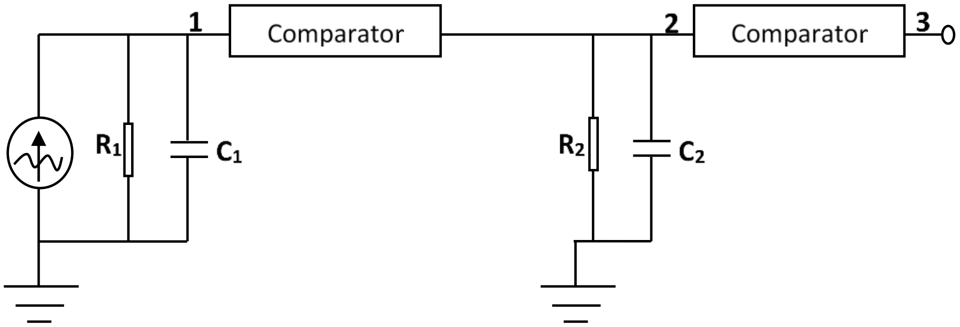

Figure 2-4 Two-stage L–shaped circuit for generating RTS traces for single active trap.

2.6 Low Frequency Noise Scaling and Variability

In highly scaled devices, the free carrier number is less than 10^4 where the LFN is dominated by RTS noise [71, 72]. The LFN in these small – area devices are impacted with the effect of a single or a few active traps. On the other hand, in large –area devices several active traps may yield the ensample averaged 1/*f* noise. The RTS amplitude has been shown to increase with decreasing device dimensions. The RTS amplitude depends on several other factors such as: bias conditions, trap position in the oxide, remote Coulomb scattering effect, and the substrate doping concentration especially when there is a halo implanted region by the source and drain in the MOSFET channel [70]. Based on Eq. 2-24, both number and mobility fluctuations are proportional to $1/\sqrt{WL}$, which raises serious concerns for future device scaling.

The LFN level changes from device to device. For large-area devices the change in LFN level is small which is less than one order of magnitude [73, 52]. However, for small–area devices the variability in LFN level can reach 3 to 4 orders of magnitude [73, 52]. The increase in the variability of RTS magnitude with down-scaling has been shown to be much greater than that introduced by random dopant fluctuations [74]. RTS amplitude at the 22 nm node is large enough to push the variability of noise sources above the minimum supply voltage [75]. This negatively impacts the design margin where RTS is considered the fastest growing contributor to design margin degradation [75].The magnitude of the RTS increases as $1/WL$ which is considered a rate faster than other sources of variability [74, 75].

In pointing out the main differences between the RTS in large and small devices one can think the RTS trace in time domain in highly scaled devices is a discrete signal switching between two or more states. The equivalent PSD of this discrete signal is a

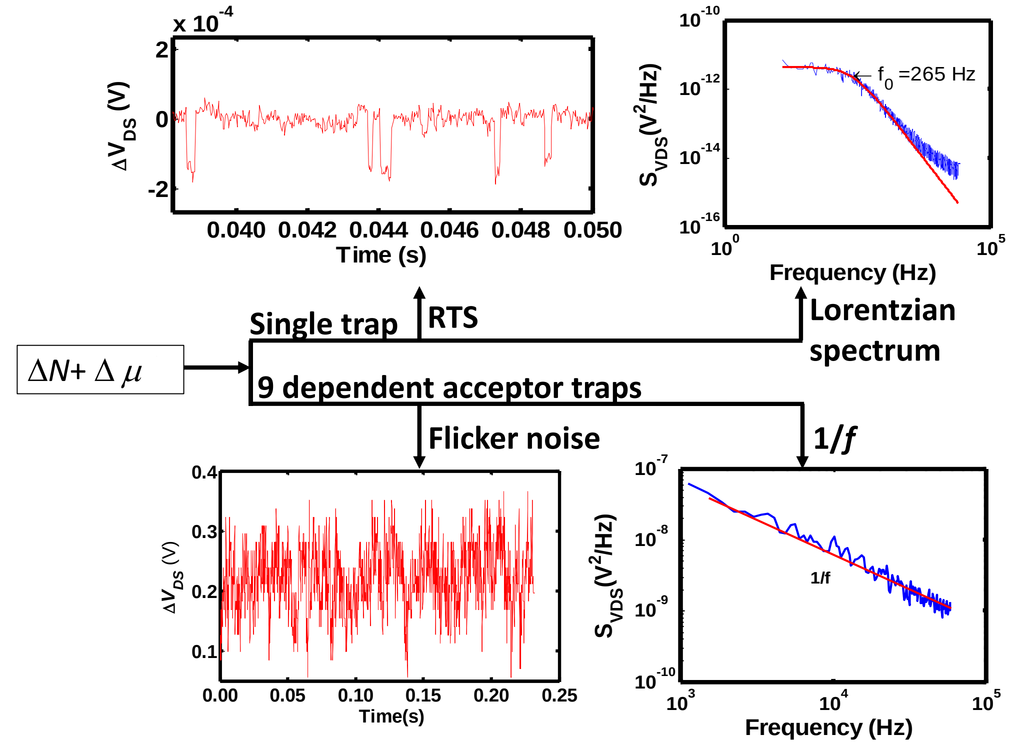

Figure 2-5 The effect of mobility and number fluctuations on the drain–source voltage signal due to single and multiple active traps in time and frequency domains.

Lorentzian shape. In large-area devices, the RTS in time domain is a continuous signal where the corresponding PSD is $1/f^{\gamma}$ noise (Figure 2-5). If *WL* is large, then the effect of a single trap is smeared out, while in small–area devices the effect of a single trap becomes more pronounced and more influential.

2.7 Summary

A brief review on the development of low frequency noise has been provided. Several key concepts are shown which provide a basic understanding of the origin of LFN. LFN can be related to the channel carrier number fluctuations which may dominate the $S_{V_{DS}}$ amplitude and the fluctuations in the V_{DS} signal in large–area devices, while in the small–area devices the mobility fluctuation becomes more pronounced. State–of–the-art in the RTS analysis has been reviewed and several RTS models are discussed. Analyzing and reconstructing the RTS in time and frequency domains based on the SRH and Poisson statistics is shown to be the best approach. The method based on the first principles takes into account the actual physical species causing the fluctuations in the V_{DS}. In addition, several other physical mechanism can be incorporated through this method.

Chapter 3 Experimental Measurement Setup and Techniques

3.1 Introduction

Conducting accurate, vigorous, and repeatable measurements is essential to predicting and modeling the low frequency noise. Noise measurement is a sensitive process which requires extra caution. The acquired signal should result from the targeted device, not from extrinsic interferences such as RF or other source of electronic signals. Therefore, shielding and grounding of extraneous noise are essential. A nondestructive procedure is adopted to investigate the low frequency noise in several MOS devices. Wafer level measurements at room temperature were performed to verify the IV characteristics and to select certain devices for further investigation at various temperatures. MicroManipulator 8600 series probe station is used for this purpose after the proper connections and settings are made. After certain devices were identified and selected, wafer was diced into several modules and packaged to be placed inside the cryostat (Figure 3-1).

In order to protect the device from electrostatic discharge (ESD), a known voltage should be maintained on its leads at all times while the device is not under test. For the purpose of eliminating the noise from the bias circuit, we have used two sets of rechargeable batteries connected in series (Figure 3-2). This low-noise biasing circuitry is used to provide the necessary current to bias the gate-source and the drain-source terminals. A resistive voltage divider is utilized along with the batteries to provide a continuous flow of current. Once the device is biased, the measured drain-source AC voltage signals are amplified through EG&G PAR113 pre-amplifier. This low noise pre-amplifier was set to operate at the frequency range of DC-300 kHz with a voltage gain of 10,000. The output of the amplifier is then connected either to the oscilloscope to record the RTS in time domain or to the dynamic signal analyzer to evaluate the RTS spectrum.

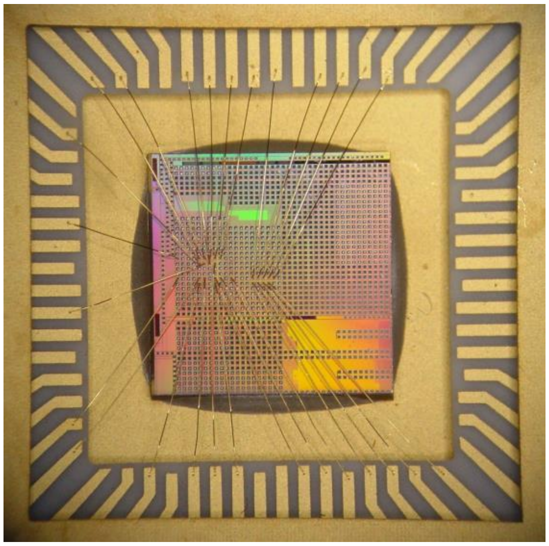

Figure 3-1 Bonded chip shows several devices connected to the external leads to be used inside the cryostat.

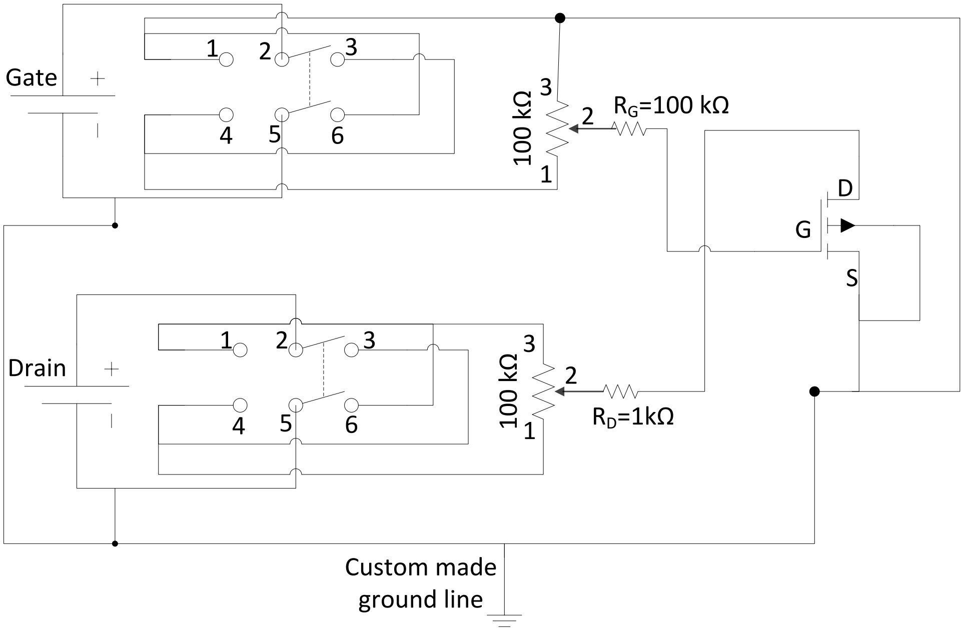

Figure 3-2 DC bias circuit used in the RTS measurements. The source of the MOSFET and negative terminal of the batteries are connected to custom made ground line.

60 Hz power line effect on the RTS signals is observed while the device is under test inside the shielded room. This problem can be completely treated by making sure the source and substrate terminals of the nMOS device are shorted and connected to real ground line that is connected outside the building. Relying on the battery box virtual ground to minimize the effect of 60 Hz is not an effective solution. Therefore, RTS cannot be observed and measured if we do not eliminate the effect of 60 Hz and its harmonics. All equipment including oscilloscope, dynamic single analyzer, precision semiconductor parameter analyzer, precision impedance analyzer, temperature controller, and vacuum pump are kept outside the shielded room to minimize the effect of 60 Hz or any external noise pick-up. Having the AC equipment outside the shielded room helps to track, observe, and record the RTS traces. Consequently, the quality and the credibility of the acquired RTS data are improved (Figure 3-3).

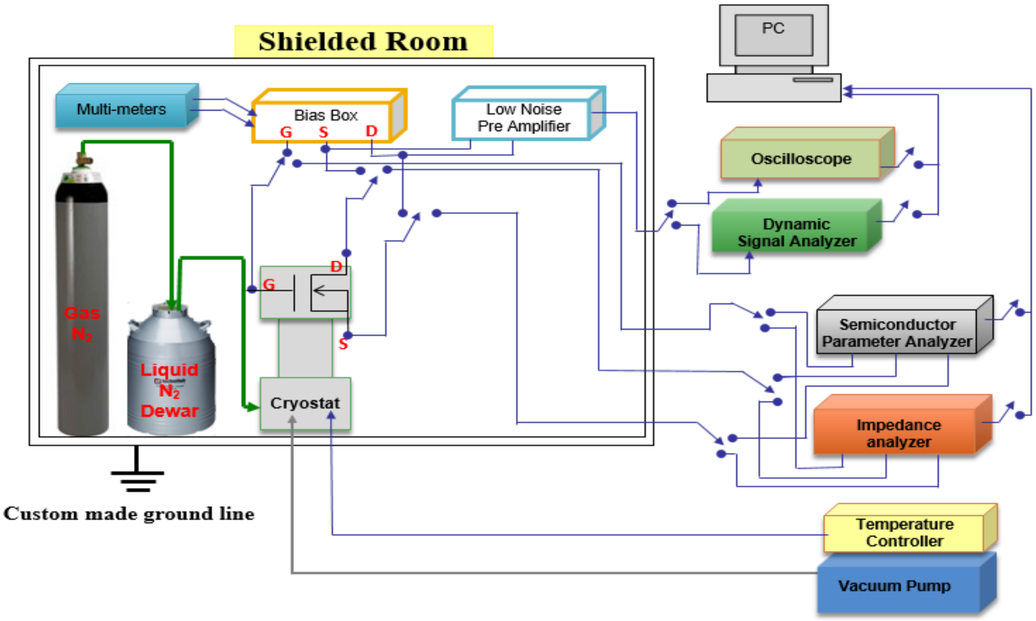

Figure 3-3 Variable temperature RTS measurement setup using a passive continuous flow, open cycle cryogenic system that does not require any power. All equipment inside the shielded room are battery-operated to minimize 60 Hz and environmental noise pick-up. All equipment on AC power are kept outside the shielded room.

3.2 Advantages of Variable Temperature RTS Measurements

In general, variable temperature RTS measurements provide more perceptive information about the defect responsible for the RTS than room temperature RTS measurements. It is essential to vary the temperature to study the thermally activated processes and to extract the associated activation energies such as: relaxation energy associated with a trap in the oxide, capture activation energy, and emission activation energy. In addition, capture cross section prefactor can be evaluated from which the capture cross section is computed. Moreover, the nature and origin of a defect can be studied and might be identified through the RTS measured data.

Lowering the ambient sample temperature has several advantages over heating up the device. If we are to identify the defects responsible for the RTS, there is simply a wider temperature range below room temperature than above to go to and still maintain safe and reliable operation of the MOSFET without changing the defect inherent characteristics. Other reasons for taking low temperature measurements are: (1) as only traps within a few $k_B T$ of the Fermi level are active, lowering the temperature allows us to pinpoint individual traps without interference from other active ones with close energies (Figure 1-2) [42, 43, 76, 77], (2) less thermal noise helps us pick up faster RTS signals with lower magnitude, (3) and ability to track the interactions and trapping/detrapping events between the traps within the time scale of the measurement, since switching slows down. Heating up the device may stress or activate several traps *or* may lead to two-state systems capable of producing discreet events looking like capture and emission of a carrier but in fact originating from an unstable scattering center induced by the increased temperature [77].

3.3 Device Specifications

Several nMOSFETs were investigated with a channel area of 0.36-0.55 µm^2. RTS was measured from room temperature down to 80 K. Gate-source voltage was varied from the threshold voltage into strong inversion while drain-source voltage was kept between 0.20 and 0.50 V. The voltage rating of the investigated devices was 3.3 V. All investigated devices were provided and fabricated by Texas Instruments Inc. The investigated devices were based on two different technologies. The first group has higher doping concentration and thinner oxide thickness than the second group. MOS–capacitor structures with an area range of 1,400 and 10,800 µm^2 were used to measure the CV data at the same temperatures that the RTS was observed.

3.4 Current- Voltage and Capacitance – Voltage Measurements

DC measurements are the first step in the noise analysis. DC characterizations were performed to extract the threshold voltage and current – voltage (IV) characteristics as a function of V_{GS} and V_{DS} (Figure 3-4 and 3.5). Once the RTS was observed at different temperatures, the DC measurements were repeated for the same temperature range to extract V_{th} as a function of temperature. In addition, the channel output conductance (g_d) was extracted from the DC measurements as a function of V_{GS} for the calculation of the channel carrier mobility in the linear and in the onset of saturation region.

The threshold voltage was evaluated from the square root and the derivative of the square root of drain – source current with respect to gate – source voltage. From the maximum of $\partial\sqrt{I_{DS}}/\partial V_{GS}$ a straight line was dropped down to intercept with $\sqrt{I_{DS}}$ curve at point A (Figure 3-6). From the intercept of point A and the slope of $\partial\sqrt{I_{DS}}/\partial V_{GS}$ curve, V_{th} was determined from the intercept with V_{GS} - axis at point B.

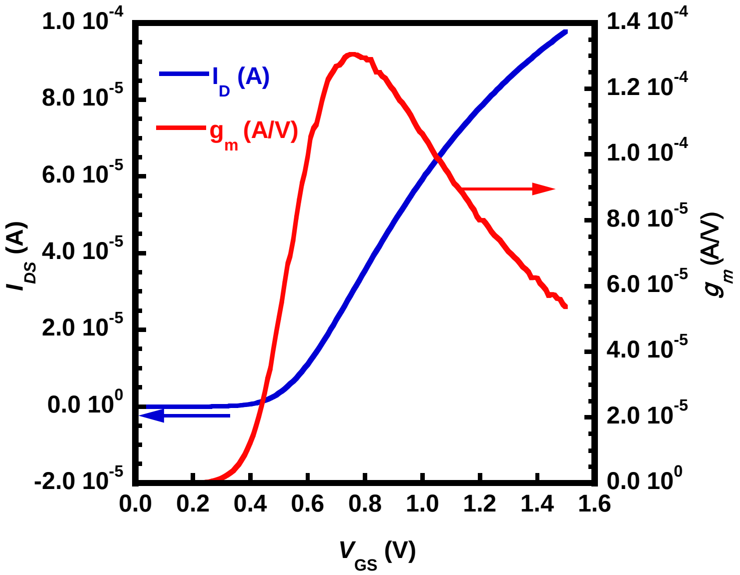

Figure 3-4 Typical drain current and channel output conductance characteristics as a function of V_{GS} for a 3.3 V nMOS device.

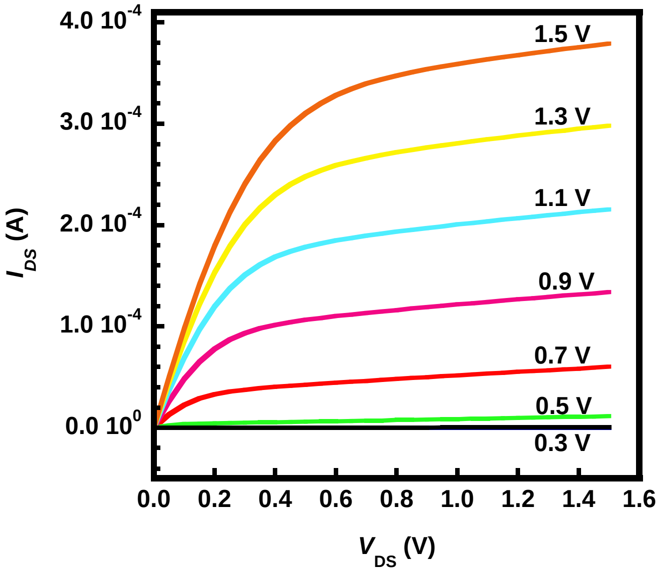

Figure 3-5 An example of measured drain – source current at various gate – source voltage for a 3.3 nMOS device. The drain – source current curves show the device behave normally where short channel effect is not observed.

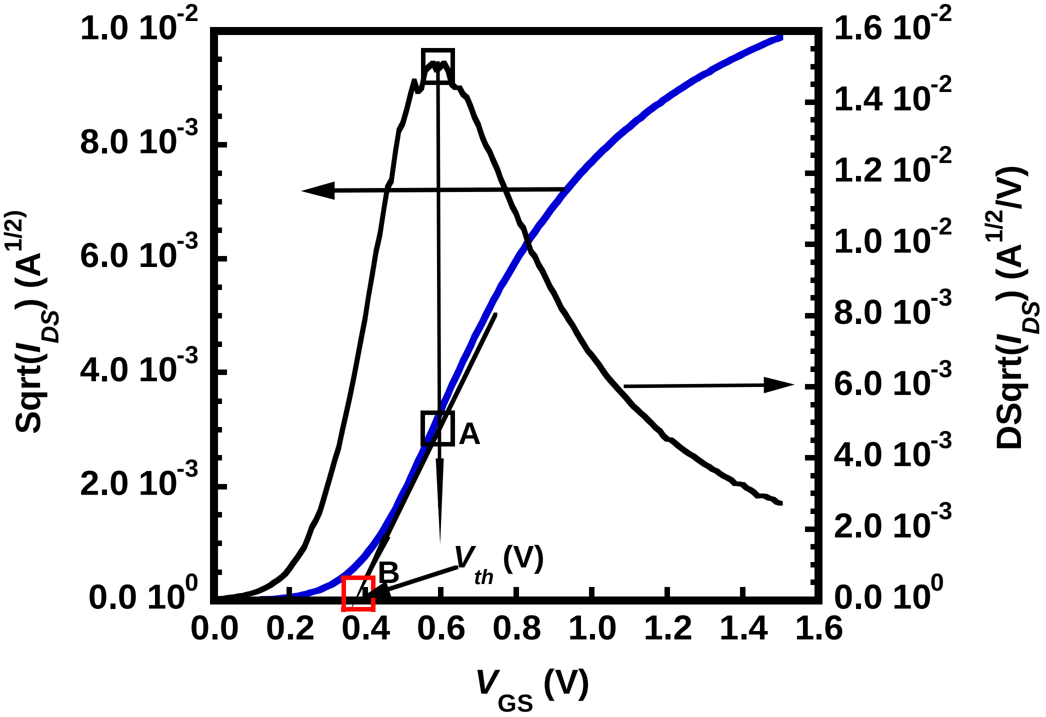

Figure 3-6 Extraction of the threshold voltage from the square root of drain – source current and the derivative of the square root of drain–source current with respect to gate – source voltage.

Capacitance–voltage (CV) measurements were taken at the same temperatures that the RTS was observed. The CV measurements were performed between the gate and channel (C_{GC}) after the proper connections were made as depicted in Figure 3-7. The outer conductor of all coaxial cables used was connected together with the guard terminal of the Agilent precision impedance analyzer 4294A (Figure 3-8). In addition, all ground lines of the probe-tips were connected with the guard terminal of Agilent 4294A. This helped to prevent a ground loop effect which may add a stray capacitance and mutual inductance to the measured CV data. Providing a return path to the induced current through the outer conductor in opposite direction to the injected current improved the measured CV

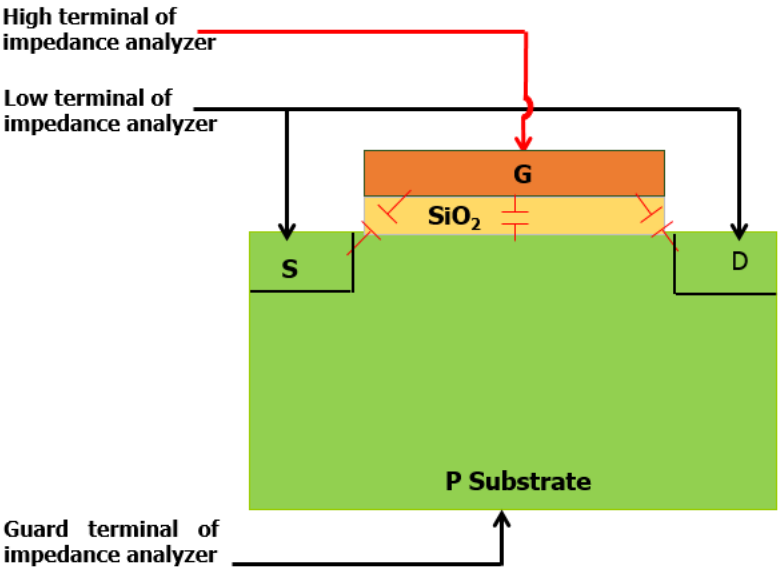

Figure 3-7 Gate-channel capacitance measurement setup for nMOS device using Agilent 4294A precision impedance analyzer.

data.

From the experimental CV data, charge carrier concentration per unit area was extracted as a function of V_{GS}. The total inversion charge (Q_{inv}) was evaluated from the integrated area under the gate-channel capacitance curve after the overlap capacitance in the accumulation layer was subtracted from the entire C_{GC} curve (Figure 3-9). This leads to the evaluation of the carrier density in the inversion layer (N_{inv}) [37]:

$$N_{inv} = \frac{Q_{inv}\left(V_{GS}\right)}{q} = \frac{1}{q}\int_{V_{GS\min}}^{V_{GS\max}} C_{GC}\left(V_{GS}\right) dV_{GS} \,. \tag{3-1}$$

The effective channel length (L_{eff}) was extracted from the C_{GC} curve using [37]:

$$L_{eff} = L\left(1-\frac{C_{GC_{ov}}}{C_{GC_{inv}}}\right), \tag{3-2}$$

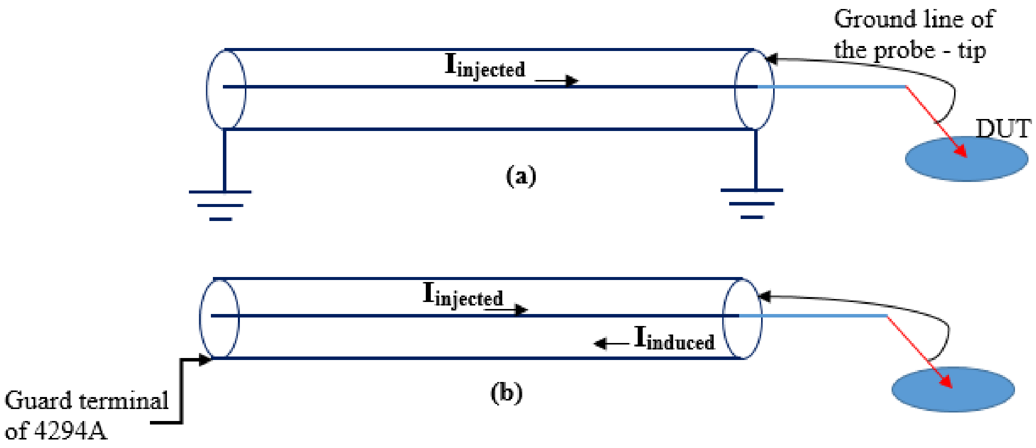

Figure 3-8 (a) A ground loop effect is observed when the outer conductor of the coaxial cable is grounded on both ends. This connection may create a stray capacitance. (b) Connecting one end of the outer conductor to the probe ground helps decrease the noise.

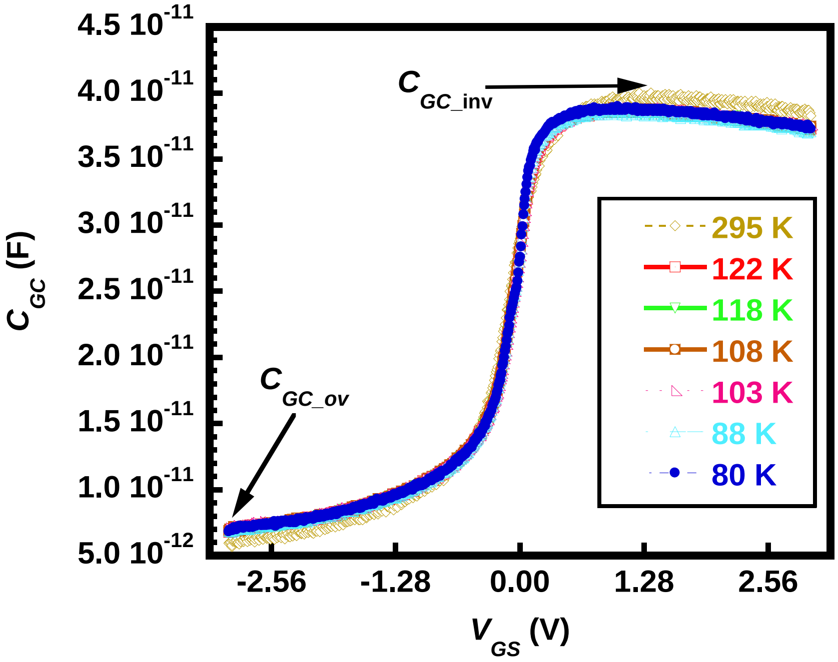

Figure 3-9 Raw data of the gate-channel capacitance at variable temperatures for an nMOS-capacitor.

where L is the drawn channel length in a MOSFET, C_{GC} is the overlap gate-channel capacitance in the accumulation region, and the $C_{GC_{inv}}$ is the gate-channel capacitance in the inversion region. C_{GC} data was used to extract the oxide thickness as a function of temperature where, $T_{ox} = \varepsilon_0 \varepsilon_{SiO_2} / C_{ox}$. Here, C_{ox} is the corrected $C_{GC_{inv}}$, ε_0 and ε_{SiO_2} are permittivity of free space and SiO_2, respectively. From Figure 3-9, the gate–channel capacitance does not change with temperature, which allowed us to provide one CV curve to the RTS simulation to calculate the N_{inv} and L_{eff}. Further discussion and use of CV data can be found in Chapters 4 and 5.

3.5 RTS Noise Measurement Setup and Procedure

Performing the DC measurements and verifying if the RTS was observed at room temperature was the first step in the procedure of the RTS data acquisition. If the RTS was not observed at room temperature, we lowered down the sample ambient temperature until the switching in the V_{DS} signal was observed (Figure 3-10). Once the RTS was picked up on the oscilloscope, the RTS measurements were taken at that temperature for 10 to 15 different bias points by varying the V_{GS} and keeping the V_{DS} at a constant value. For variable V_{DS} measurements, we fixed the V_{GS} and varied the V_{DS} at several bias points between the linear and saturation regions (please see section 4.3.4).

Once the packaged device is attached to the cold finger inside the cryostat chamber, all leads of the device under test (DUT) were shorted with 4 miniGrabber test clips to eliminate the effect of ESD and provide a known voltage at its leads (Figure 3-11(a)). Then, the DUT leads were disconnected from the outer - frame of the package. Four custom made pin socket connectors were used to connect the DUT leads with the

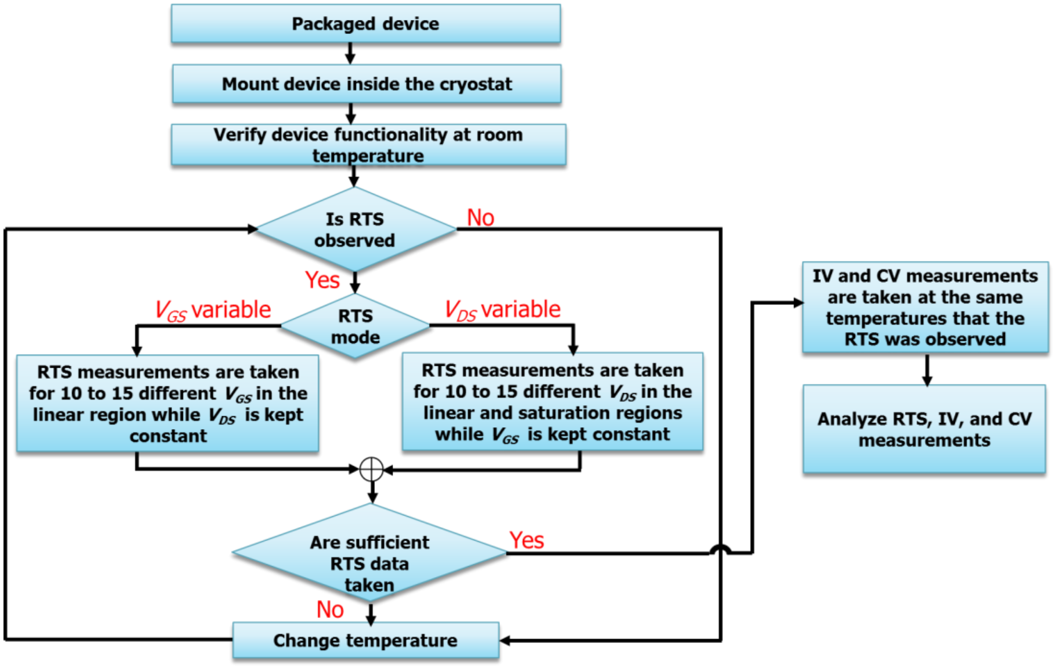

Figure 3-10 A procedure is set to acquire RTS data, CV and IV measurements at variable temperatures and bias conditions.

BNC connectors in the cryostat (Figure 3-11(b)). As soon as the device was shorted and the interface with the BNC connectors was done, DUT connection with the RTS measurement setup was completed. Before device was biased, the four miniGrabber test clips were taken out. Typically, the device was biased at low $V_{DS} \sim 0.2$ V while V_{GS} was varied from threshold voltage to strong inversion searching for RTS. If RTS was not seen, V_{DS} was increased and V_{GS} was varied again.

The cryostat (RC 102) pressure was lowered to below 65 mTorr using mechanical pump. DUT temperature was set to the desired value using a LakeShore 330 temperature controller. The proportional-integral-derivative (PID) gain loop was set to 350, 50, and 0, accordingly to have optimal temperature control [78]. Once the desired vacuum level was reached, liquid and gas nitrogen nozzles were gradually opened to avoid overflow of liquid nitrogen. Temperature of the cryogenic system was monitored on the temperature

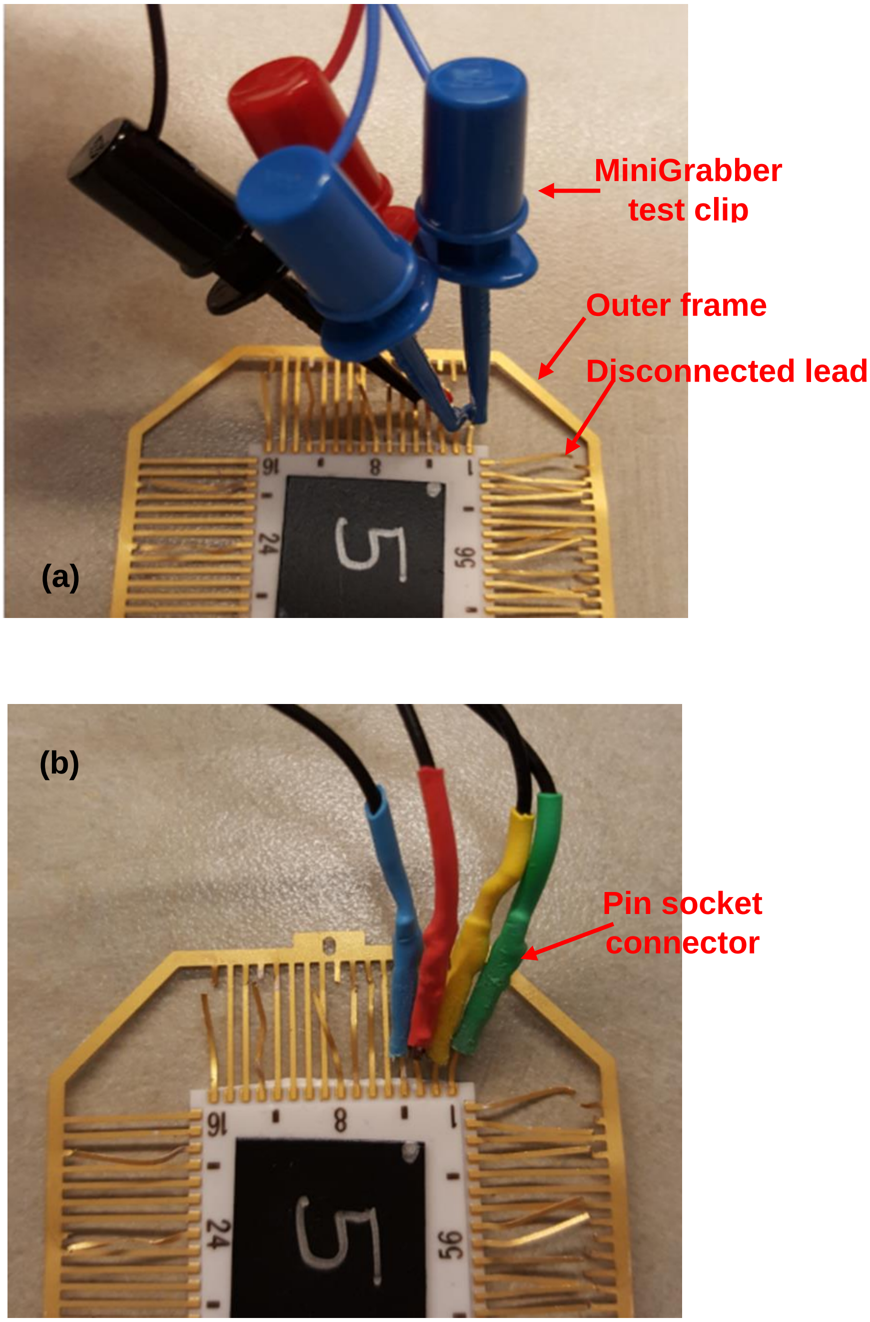

Figure 3-11 (a) Leads of the investigated device are shorted using miniGrabber test clips. (b) DUT is connected through pin socket connectors to the BNC connectors in the cryostat.

controller display. Once the desired temperature was reached, the flow of the liquid nitrogen was slowed down and the nitrogen gas cylinder pressure gauge was set between 8 and 12 psi to maintain a fixed-continuous flow of the liquid nitrogen. This helped the controller to keep the cryostat temperature at the desired value.

There were two temperature sensors inside the cryostat. First one was located under the stage close to the wire wound heater nozzle where the second one was placed behind the cold finger. Both temperature sensors were connected to two different channels in the LakeShore 330. The first sensor was connected to channel A and the second one was connected to channel B. We typically consider the sample temperature that was measured by the second sensor (Channel B), since it is located close to DUT. Channel A was used to provide feedback to the temperature controller.

Sampling frequency of the oscilloscope was adjusted according to the DUT temperature and the speed of communication of the trap with the channel carriers. High DUT temperature results in fast transitions of electrons between the channel conduction band and the bound state at the defect site, since capture and emission of an electron are thermally activated processes. For this reason, high sampling frequency in the range of 0.5-1 MS/s was used to capture all of the transitions. Otherwise, sampling frequency was decreased since the carriers communicate much more slowly with the traps as the temperature was decreased.

In some cases, a trap was found to be communicating very slowly with the channel carriers. Thus, not enough transitions were observed between the RTS levels within the observation window for meaningful statistical analyses. If there are 600 to 1000 transitions between two states in an RTS trace for 60,000 to 100,000 readings, the Poisson statistical analysis would be more realistic. However, if there are less than 200 transitions for 20,000 points in two - level RTS trace, the statistical analysis most likely will be invalid. Therefore, more RTS traces were acquired and stitched together at the same bias and temperature conditions to ensure adequate transitions. For the convenience of the stitched RTS analysis, sampling frequency, and the total number of acquired points, and the total recording time were kept the same for all RTS traces that were stitched together.

HP-3562A is used along with computer interface to perform the fast Fourier transform on the time domain V_{DS} signals which produces the PSD. The number of averages was set up to 28 and overlap sampling window to 75%. The spectrum analyzer AC power cord is connected to an outlet surge protection where its earth – grounding line is connected directly to outside building. This helps to minimize the effect of 60 Hz on the PSD.

3.6 Device Stressing

The idea behind stressing MOSFET devices is to analyze the DC-stress-induced trap(s) in the Si/SiO_2 interface and compare it with the process-induced trap characteristics. As it is known, devices degrade over time. Thus, tracking the RTS effect as a function of operation time is important for prediction of the lifetime of a device. RTS was searched and scanned in a fresh device before it was stressed. Agilent-4156C was used to stress the device for 60 second at the conditions shown in *Table 3-1*. The device was then tested in

Table 3-1 Stressing and testing conditions for a 3.3 V nMOS device.

Stressing conditions			
Gate terminal (V)	Drain terminal (V)	Source and body terminals (V)	Temperature (K)
2.1	3.0	0.0	295
Testing conditions (V)			
Gate terminal (V)	Drain terminal (V)	Source and body terminals (V)	
0.0-2.5	0.1	0.0	

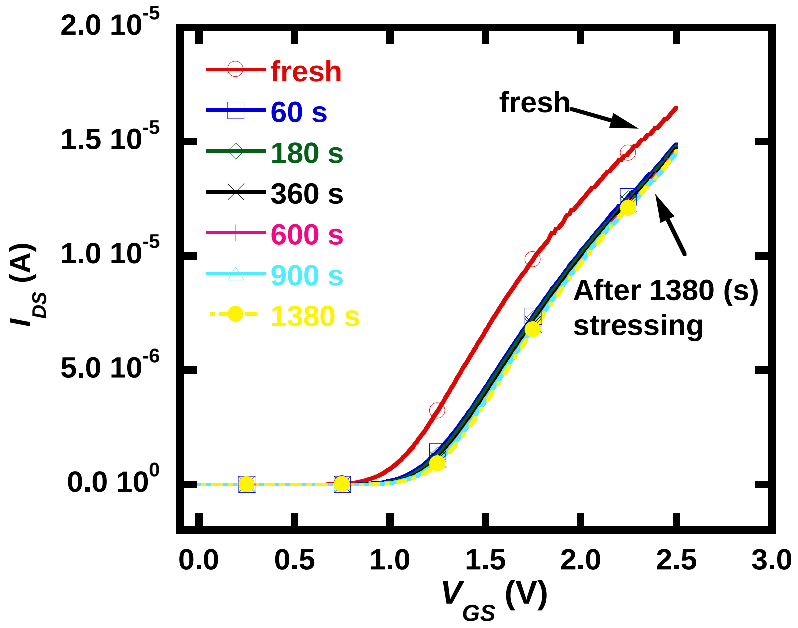

Figure 3-12 I_D as a function of V_{GS} for a 3.3 NMOS device before and after stressing. Major shift in the I_D value occurs at the first 60 seconds then minor shift is observed for the rest of the 1320 seconds.

the linear region for variable V_{GS} up to 2.5 V with V_{DS} = 0.1 V. IV characteristics and V_{th} were recorded (Figure 3-12). The device was scanned again for any RTS presence after the stressing. If the RTS was observed, the RTS measurement procedure was repeated (Figure 3-10). Cumulative stressing of 120, 360, 600, 900, 1380 seconds was performed all at room temperature. It was noticed that the major shift in V_{th} occurred in the first 60 seconds and after that the change was much less as depicted in Figure 3-13. On the other hand, observing a major shift in the V_{th} does not necessarily produce an RTS in a device. This implies that a process- or stress-induced trap may be permanently filled with a carrier, producing a fixed charge in the gate oxide which changes the electrical property of the dielectric material. This might be the reason behind the shift in the threshold voltage without any accompanying RTS fluctuations.

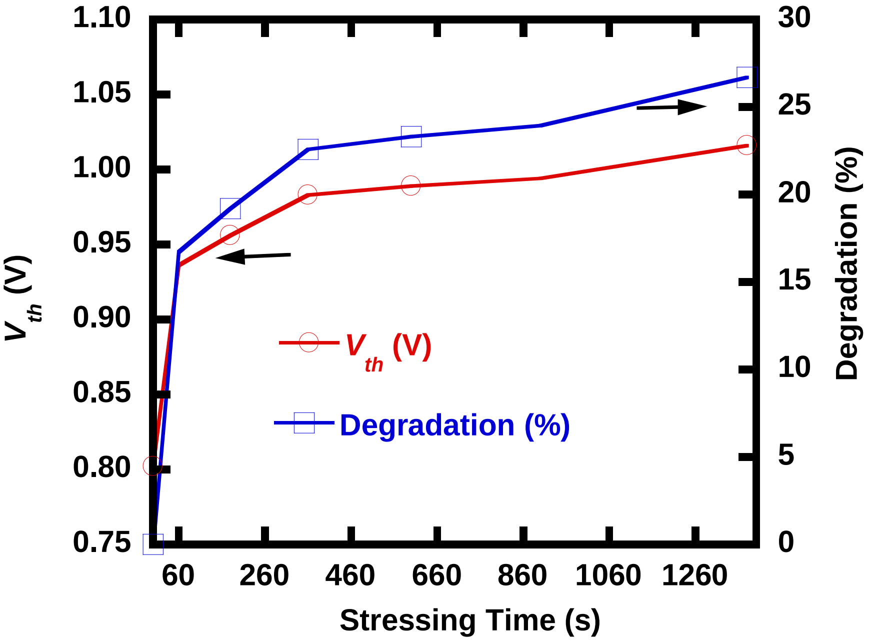

Figure 3-13 Threshold voltage and its degradation percentage as a function of stressing time range between 0 and 1380 seconds. The first 60 seconds V_{th} degraded 16 % and after 1320 seconds it degraded 10 %.

In general, a fixed charge could not cause additional number fluctuations. However, it might cause additional mobility fluctuations depending on the location of the induced charge. In addition, stressing a device may induce a trap capable of capturing and emitting an electron from and to the channel. One of the investigated devices showed no RTS before stress. However, after it was stressed for 1460 seconds, two – level RTS was observed at the temperature range of 186 and 228 K.

3.7 Summary

Variable temperature RTS measurement setup is outlined. Extraction of the threshold voltage procedure from the IV curve is shown. Evaluating the total charge in the inversion layer from the measured CV data is explained. For variable temperature measurements the advantages of cooling down the investigated devices over heating them up are discussed. The procedures for obtaining IV characteristics and threshold voltage for stressed and fresh nMOSFETs are described. From the IV and RTS data of the stressed devices, shift in the threshold voltage does not necessarily lead to switching in the V_{DS}.

Chapter 4 RTS Analysis in Time and Frequency Domains

4.1 Introduction

The availability of deep-submicrometer MOSFETs has provided an opportunity to study the noise generated by individual gate oxide traps. It is possible to have one oxide trap or a few active traps in the vicinity of surface Fermi level over the entire channel [41]. RTS originates from the consecutive capture and emission events of a single or multiple electrons by defect center(s) at the Si/SiO$_2$ interface or in the gate oxide bulk [42]. RTS can be used as a diagnostic tool to study the energy and spatial distribution of gate oxide traps. However, existing techniques assumed a uniform trap distribution and neglected variation of trap characteristics. RTS is based on real-time electron switching events in the drain current or voltage. Therefore, it is used to probe active traps individually. RTS plays major role in determining the future limitations of highly scaled devices [43]. RTS method is adopted to study the variability of traps and other electrically active defects within the same process technology and to study the multi-level fluctuations caused by independent or correlated traps.

In this chapter, the results and analyses of simple two-level and multilevel RTS as well as RTS due to fast and slow traps are presented. RTS is statistical in nature and may vary between different devices with the same geometry and technology or different geometries on the same wafer. Therefore, RTS was investigated on a variety of MOSFETs and technologies at different operational voltages and in a wide range of temperatures to obtain sufficient statistical data that can be used to construct a meaningful statistical model.

Identifying and characterizing of gate oxide defects with high resolution and nondestructively are essential for the reliability of MOSFETs and digital memory devices. Investigating the gate oxide defects using RTS is considered to be a powerful tool for studying the oxide trap characteristics in real time, although, there are several trap characteristics that cannot be extracted from room temperature RTS measurements alone. These are the trap capture cross section prefactor (σ_0), capture activation energy (ΔE_B), change in entropy (ΔS), trap binding enthalpy (ΔH), emission energy $\Delta E_B + (\Delta H - T\Delta S)$, and relaxation energy (E_R) (Figure 4-1). On the other hand, room temperature RTS measurements are sufficient for the extraction of trap position (x_t) in the oxide with respect to the Si/SiO2 interface, trap location along the channel with respect to the source (y_t), and the trap energy in the SiO2 band–gap $\left(E_{C_{ox}} - E_T\right)$. Therefore for complete characterization of the oxide traps and accurate simulation of the resultant RTS traces, variable temperature measurements, analyses and modelling were done in this work.

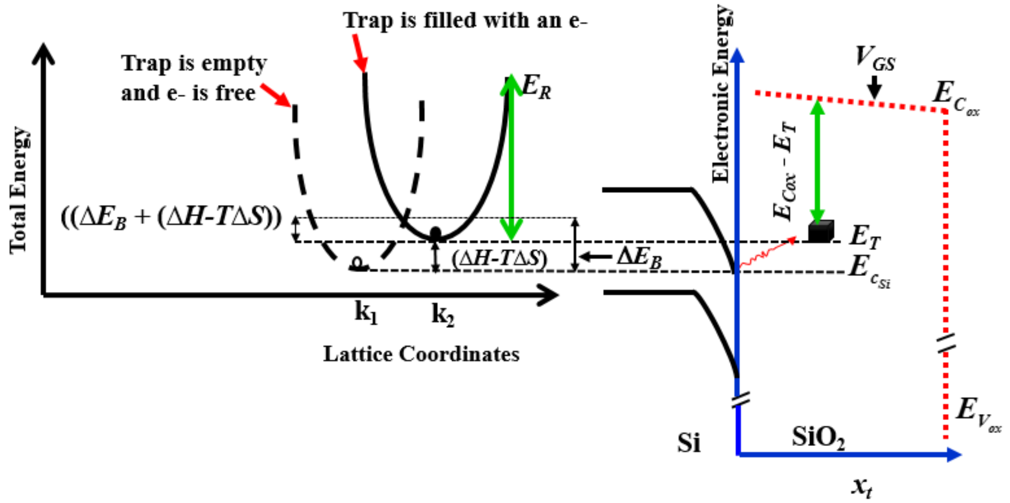

Figure 4-1 Configuration coordinate diagram denotes two electron states. Dashed curve corresponds to the empty trap and the electron is free in the channel. The solid curve corresponds to the trap filled with an electron. ΔE_B and ΔH are temperature independent. However, the energy needed to release a trapped electron from the defect site increases with the decrease of temperature. In this particular diagram, $\Delta H - T\Delta S < 0$.

4.2 RTS Analysis in Time Domain

In the time domain, RTS traces are characterized by three major parameters. First, RTS amplitude (ΔV_{DS}) is computed from the Gaussian histograms of the RTS data. Second, average time constant associated with the empty state $(\bar{\tau}_c)$ is extracted from the RTS waveforms (Figure 4-2). Third, average time constant associated with the filled state $(\bar{\tau}_e)$ is calculated from the RTS waveforms as depicted in Figure 4-2. MATLAB code was developed to track $\bar{\tau}_c$ and $\bar{\tau}_e$ associated with each trap and calculate the RTS amplitude corresponding to each trap. An example of RTS acquired on a 3.3 V nMOSFET with the channel area of 0.36 μm^2 is shown in Figure 4-2. The three-level RTS in Figure 4-2 are due to two dependent traps, since all transitions to level 3 occur from level 2. A minimum of 200 transitions between different RTS levels and 20,000 readings were obtained for each time-trace. The corresponding time associated with the empty state of trap A (Figure 4-2) is recorded until the state changes. Once the transition is realized, the recording time associated with the empty state of trap A stops. Meanwhile, the recording time associated with the full state of trap A begins until the state changes. Same procedure was used to run the time analysis associated with trap B. In general, when a trapped carrier moves from one state to another, one of the average time constants associated with the trap is stopped recording and others continued to be recorded or reset as illustrated clearly in Figure 4-2.

After setting the upper and the lower limits for each level on the RTS signal, then the distribution of time spent in each level was investigated. The time was divided into bins (t_{nb}) in seconds and the frequency of occurrence of each time duration (F_{nb}) was counted. Thus, the average time constant associated with each RTS level was computed as:

$$\bar{\tau}_{c,e} = \sum_{1}^{N_b} t_{n_b} \left|F_{n_b}\right| \Big/ \sum_{1}^{N_b} \left|F_{n_b}\right| . \tag{4-1}$$

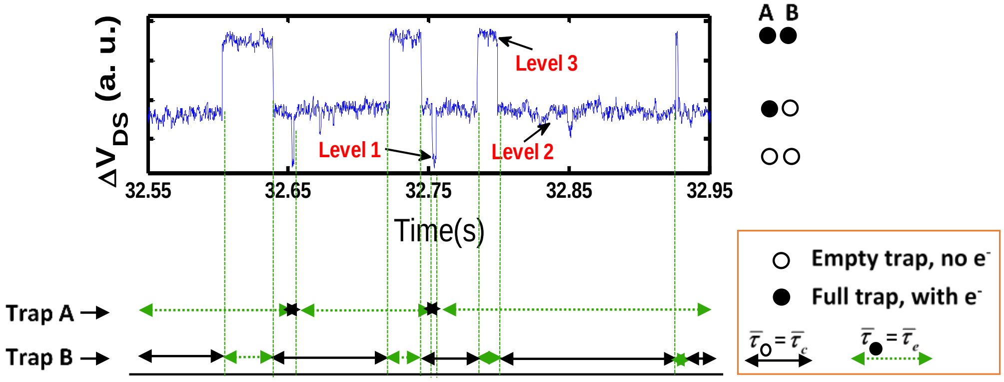

Figure 4-2 Time analysis for measured RTS traces for two dependent acceptor traps. Trap B is active only when trap A is full.

Here, n_b is the bin number used in the histogram, and N_b is the total number of bins used in the histogram.

4.3.1 *Average Time Constants Associated with Each RTS Level*

The discussion here will be confined to two-, three-, and four-level RTS in two different nMOSFETs. For transistor A (TA), two level-RTS was seen at low temperatures between 80 and 122 K for V_{GS} = 1.50-1.74 V with V_{DS} = 0.25 V (Figure 4-3). Also three-level RTS was observed in TA at T=80-88 K for V_{GS} = 1.62-1.74 V (Figure 4-4). In transistor B (TB), four-level RTS due to fast and slow traps switching was seen at temperature range of 263 and 300 K for V_{GS} = 1.00–1.90 V while V_{DS} kept at 0.30 V (Figure 4-5(a)). Due to the complexity of this RTS waveform and difficulty to differentiate between the RTS levels, RTS was acquired at two different sampling frequencies in an attempt to capture the fast and slow transitions at two different traces. Therefore, RTS measurements due to the fast trap were taken at V_{GS} between 1.00 and 1.45 V with sample frequency 1 MSample/s. RTS data due to the slow trap were acquired at low sampling frequency $\sim$ 1 KSample/s for V_{GS} range of 1.50–1.90 V. At lower temperature (217–263) K, the slow trap became quiet and only RTS due to the fast trap was seen.

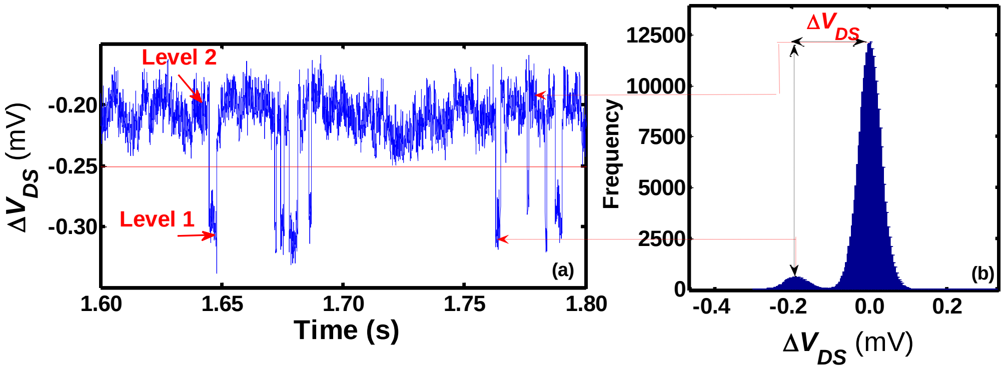

Figure 4-3 (a) Two-level RTS corresponding to one active trap measured on an nMOS device. (b) Histogram of the time domain RTS data from which the RTS amplitude was extracted. V_{GS}=1.5 V, V_{DS} = 0.25 V, and DUT temperature 88 K.

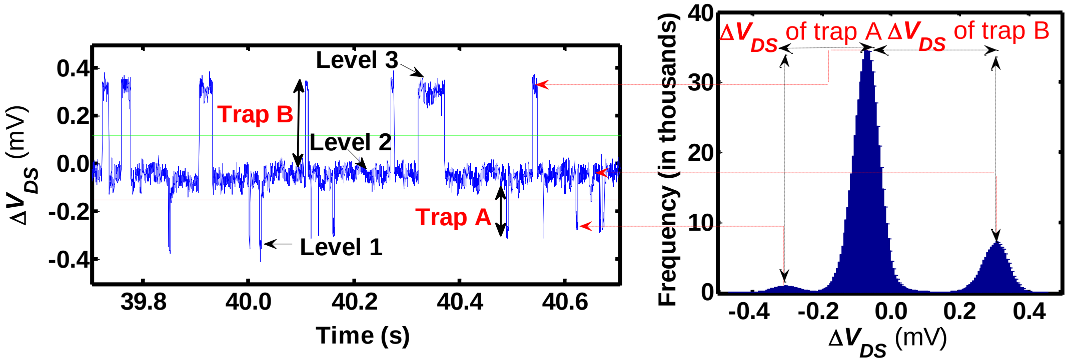

Figure 4-4 Three-level RTS corresponding to two active traps along with the RTS amplitude to the right. Traps A and B were dependent where B was active only when A was full. V_{GS}=1.7 V, V_{DS} = 0.25 V at DUT temperature 88 K.

The Poisson distribution for the switching events of the two RTS samples in Figure 4-3(a) and Figure 4-4(a) is shown in Figure 4-6 and Figure 4-7, respectively. The extracted average times associated with the observed RTS in TA as a function of V_{GS} and T are depicted in Figure 4-8. The fluctuations in the V_{DS} due to the fast trap represent two-level

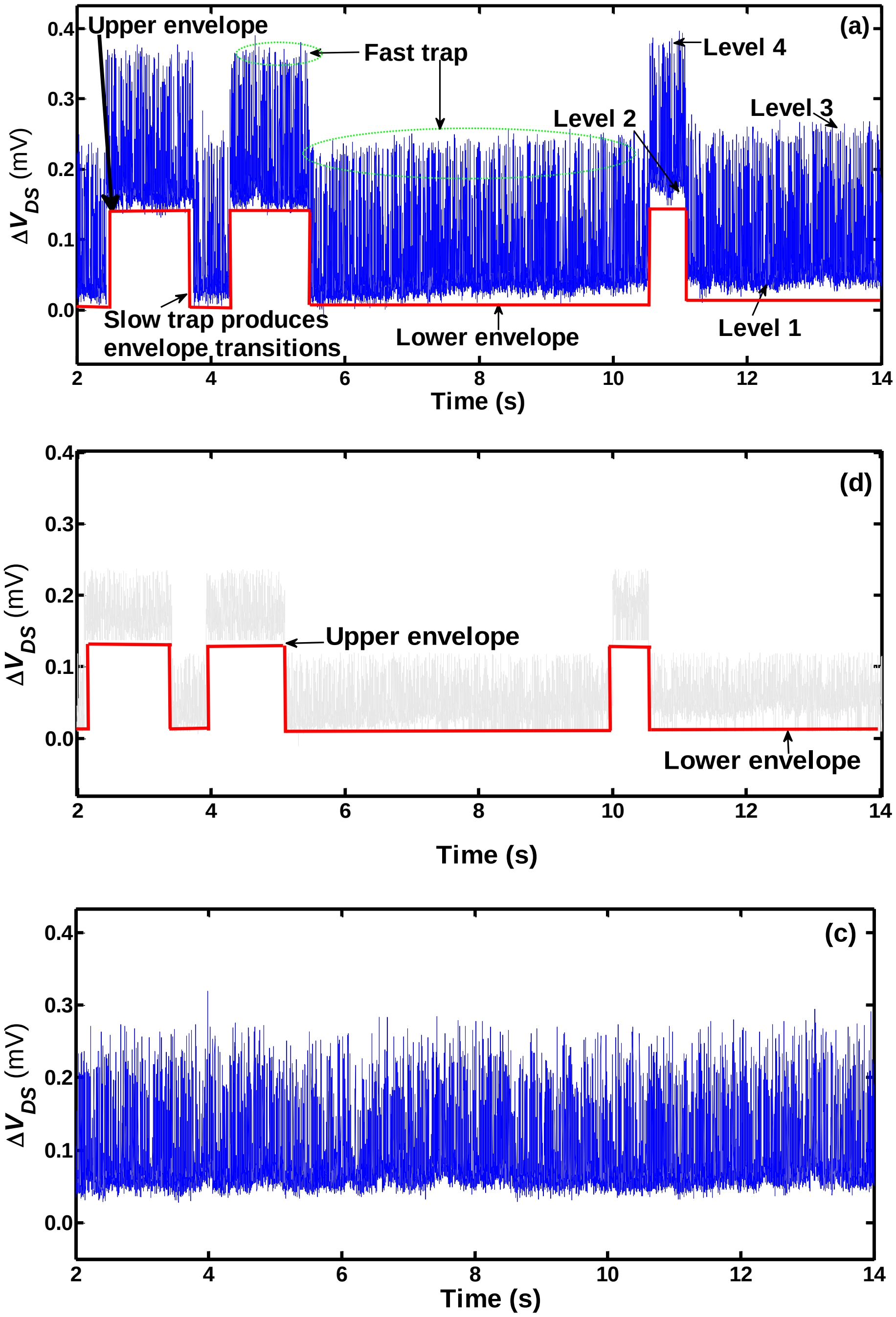

Figure 4-5 Sample of four level RTS obtained on a 3.3 nMOS transistor due to fast and slow traps. (b) The separated two–level RTS due to the slow trap. (c) The separated two–level RTS due to the fast trap. V_{GS} = 1.90 V, V_{DS} = 0.30 V where temperature is 263 K.

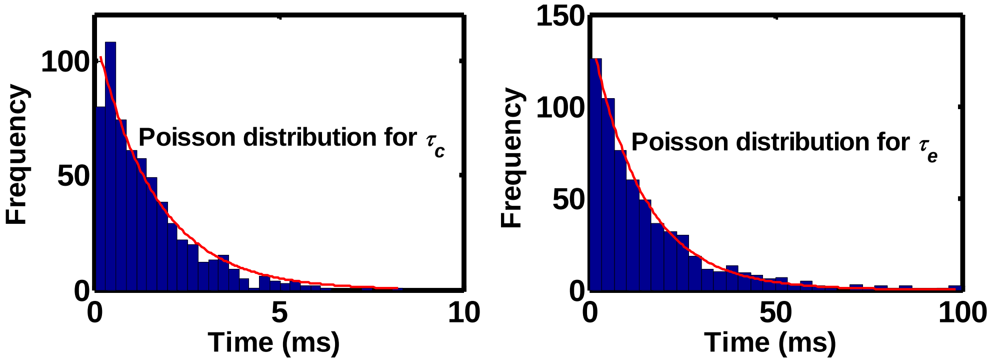

Figure 4-6 Time events distribution with Poisson fitting corresponds to the RTS waveform in Figure 4-3(a). $\bar{\tau}_c$ =1.9, $\bar{\tau}_e$ = 25.6 ms. V_{GS} = 1.5 V, V_{DS} = 0.25 V and DUT temperature 88 K.

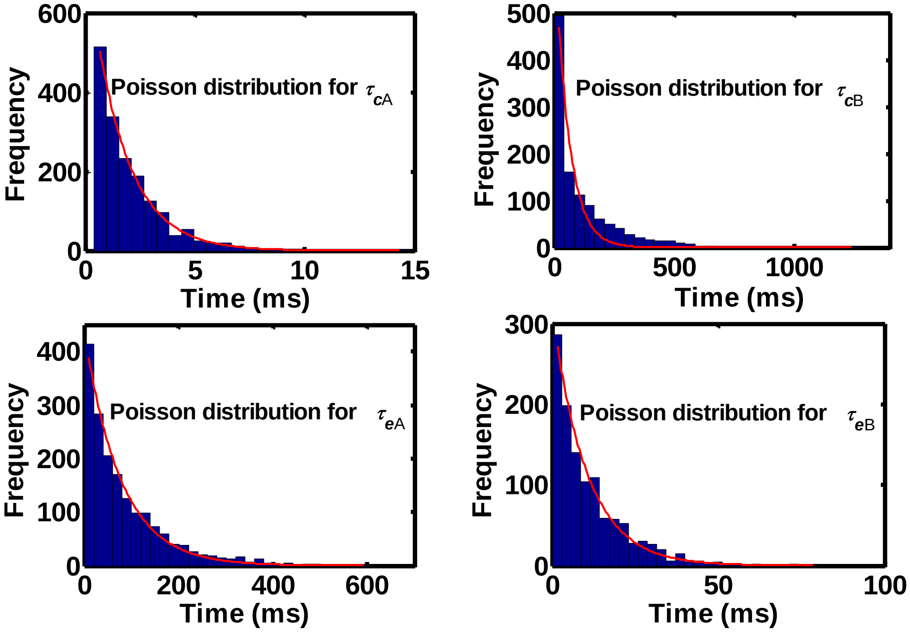

Figure 4-7 Time events distribution with Poisson fitting corresponds to the RTS waveform in Figure 4-4. The data were taken at bias conditions of V_{GS} = 1.7 V where V_{DS} = 0.25 V at temperature 88 K. $\bar{\tau}_{cA}$ = 2.2, $\bar{\tau}_{eA}$ = 87.5, $\bar{\tau}_{cB}$ = 121.0, and $\bar{\tau}_{eB}$ = 22.6 ms.

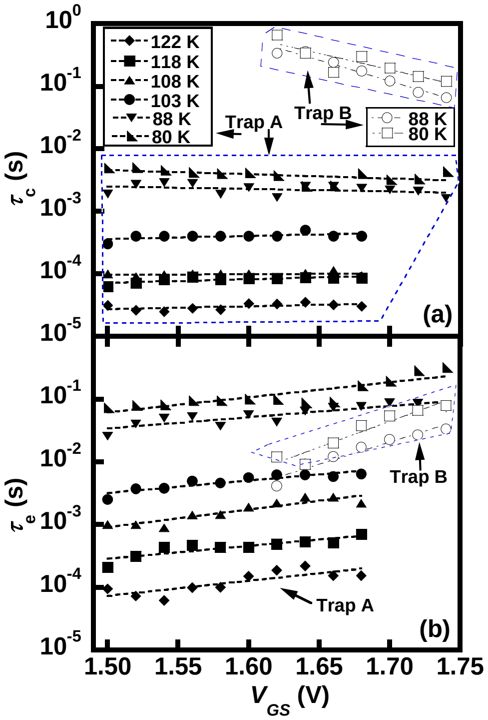

Figure 4-8 Average capture (a) and emission (b) times computed from the RTS time trace at each bias condition and temperature for TA. V_{DS} = 0.25 V.

RTS. Extraction of the average times associated with each trap was done after the separation between the overlapped levels had been completed. From Figure 4-5(a), level 2 is overlapped with level 3. Thus, level 3 was shifted below level 2 without affecting or changing the integrity of level 2 (appendix A). The separated waveform looks like the one in Figure 4-5(b). The separated RTS data due to the fast trap is shown in Figure 4-5(c). The separated RTS data (Figure 4-5(c)) due to the fast trap were not used in the analysis of time constants. This is due to the fact that these data looked like spikes in this time scale. The histogram of the RTS shown in Figure 4-5 is illustrated in Figure 4-10. From Figure 4-10(c), the V_{DS} fluctuations are not strictly Gaussian distribution. Thus, only the extracted data due to the slow trap were considered and used in the analysis of time constants when RTS was acquired at low sampling frequency. For TB, the average times associated with slow and fast traps are plotted in Figure 4-9. It is noted that at a specific gate bias average time constants increase as the temperature is decreased. This is due to the reduction in the lattice temperature. And since the mechanism of capture and emission of an electron is phonon–assisted, we expect the average times to increase when DUT temperature falls down.

To show the relative importance of trap A and B in TA, we looked at the progression of the RTS in time domain with bias. The DUT temperature was fixed at 88 K while V_{DS} kept at 0.25, then V_{GS} was varied between 1.62 and 1.72 V. Figure 4-11 shows trap A was more active at lower V_{GS} with higher number of transitions, and became less active at higher V_{GS}. On the other hand, trap B was active at high V_{GS} which can be inferred from the RTS histograms amplitude in Figure 4-12.

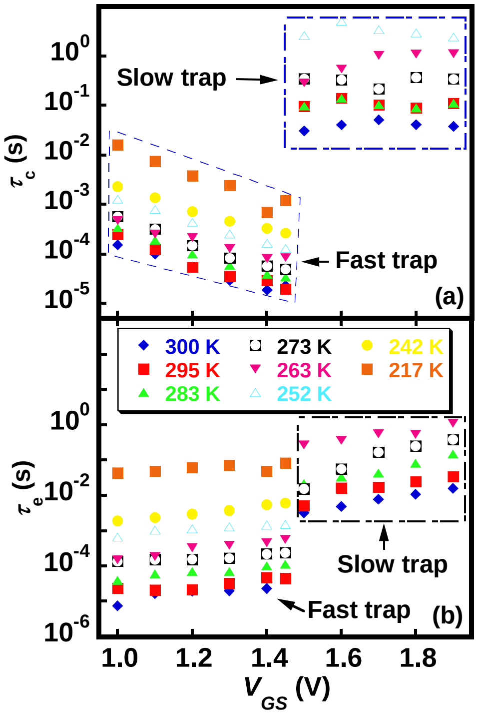

Figure 4-9 Average capture (a) and emission times (b) associated with the fast and slow traps for TB. V_{DS} = 0.30 V.

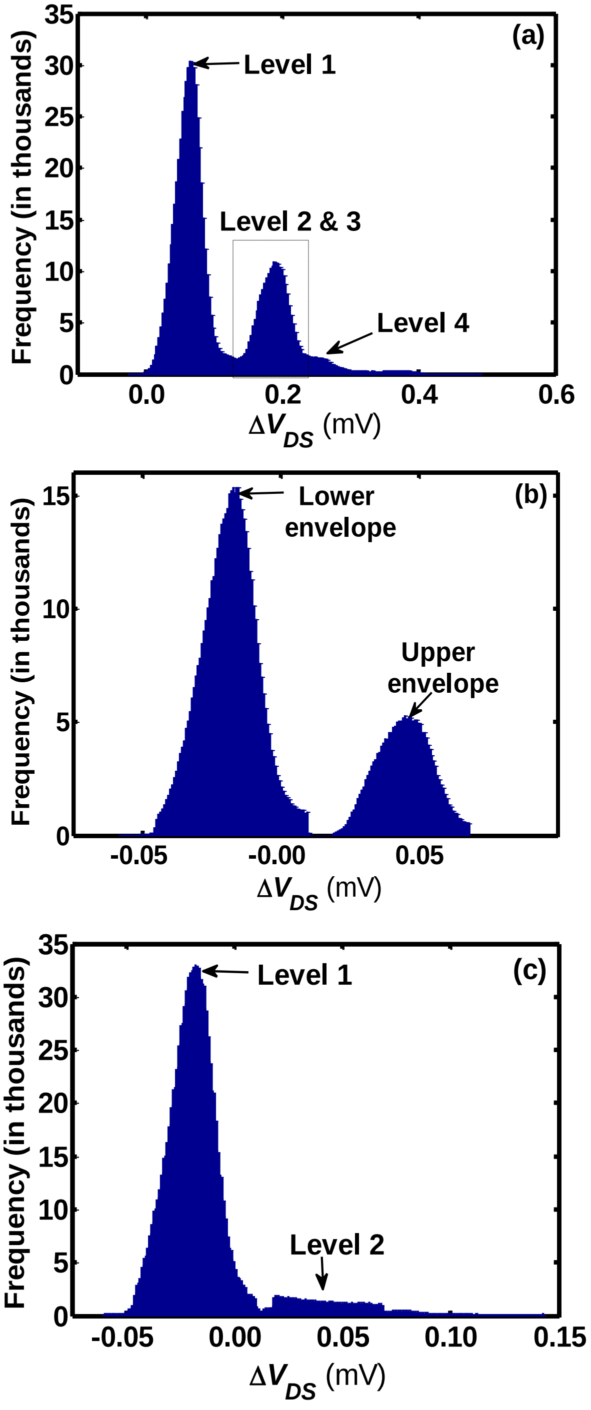

Figure 4-10 (a) Histogram of the time domain RTS data for both traps before separation. (b) Histogram of RTS data for the slow trap after separation from which the RTS amplitude due to the slow trap is extracted. (c) Histogram of RTS data due to the fast trap which does not represent a Gaussian distribution for level 2.

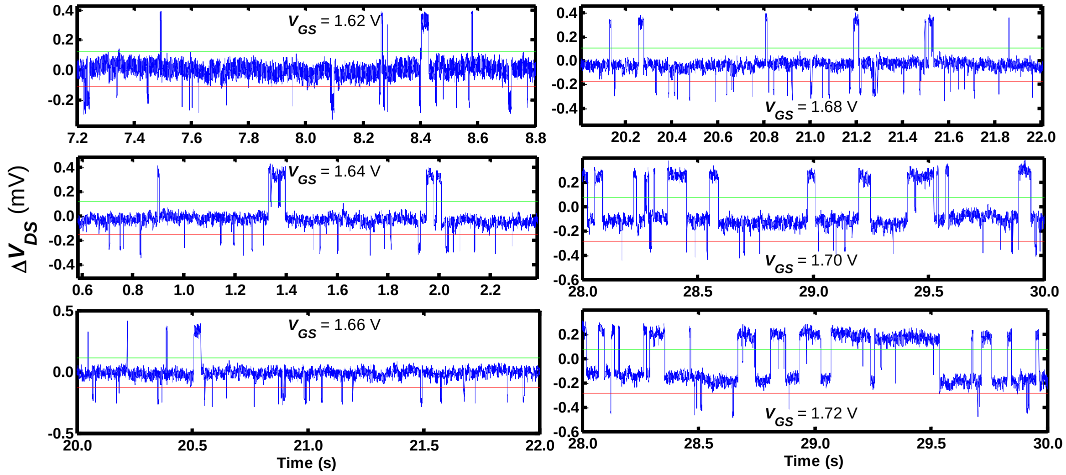

Figure 4-11 Three-level RTS shows the relative influence of trap A and B on the V_{DS} signals in TA. Trap B became more active and pronounced at higher V_{GS}, while channel communications with trap A started to diminish.

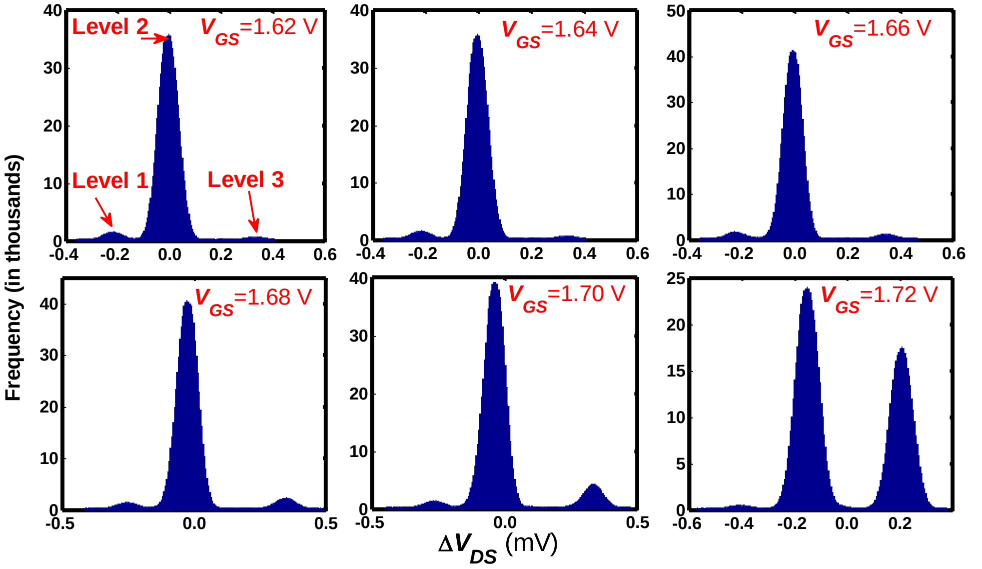

Figure 4-12 RTS histogram amplitude for the RTS waveforms in Figure 4-11 for V_{GS} range between 1.62 and 1.72 V at V_{DS} = 0.25 and temperature 88K. Level 1 started to diminish as V_{GS} was increased and level 3 started to become more pronounced.

4.3.2 Determination of Average Capture and Emission Times for a Trap

Average capture time can be defined as the time it takes the trap to capture an electron from the channel provided the state of that trap is initially empty (if the trap is an acceptor type) (Figure 4-13). On the other hand, average emission time represents the average confinement time for a carrier in the defect center before is released back to the channel.

From the V_{GS} dependence of the extracted average times associated with each trap, the average capture and emission time constants were identified. If a trap is an acceptor and the channel carriers are electrons, the average time associated with level 1 (Figure 4-3(a)) decreases as the V_{GS} is increased, and that is corresponding to $\bar{\tau}_c$ (Figure 4-8(a) and Figure 4-9(a)). However, the average time constant associated with level 2 (Figure 4-3(a)) increases as a function of V_{GS}, which represents $\bar{\tau}_e$ (Figure 4-8(b) and Figure 4-9(b)). In addition, the ratio $\bar{\tau}_c/\bar{\tau}_e = (1-f_t)/f_t$ decreases due to the increase of the trap occupancy [42]. Here, f_t is the trap occupancy function. The trap responsible for the switching events in this device was identified to be an acceptor type. Acceptor defects in nMOS are neutral centers prior to the capturing of an electron and negatively charged after they are filled with an electron. On the other hand, donor defects are neutral when filled and positively charged when empty.

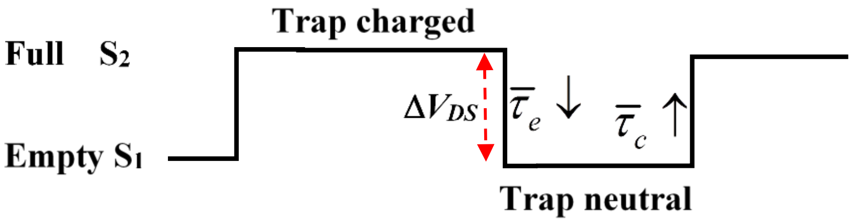

Figure 4-13 (a) Two-state drain-source voltage switching in an nMOSFET device, where the lower state corresponds to the trap when empty and the upper state corresponds to the trap when full with an electron.

4.3.3 Extraction of Trap Position in the Oxide

For an electron to be captured by a defect in the oxide, it needs to overcome the potential barrier due to the conduction band-edge offset between the Si and SiO_2. From the energy band diagram of the Si/SiO_2 system in an nMOS device (Figure 4-14), an expression for the trap position $\left(x_t\right)$ in the oxide with respect to Si/SiO_2 interface can be derived as [79]:

$$E_1+\left(E_{Cox}-E_T\right)+\left(E_T-E_{Fn}\right)=E_2+\phi_0\,. \tag{4-2}$$

From the ratio of the two shaded triangles as shown in Figure 4-14, E_1 energy can be defined as:

$$E_1/qV_{ox}=x_t/T_{ox}\Rightarrow E_1=qx_t/T_{ox}\left(V_{GS}-V_{FB}-\psi_s\right), \tag{4-3}$$

where V_{FB} is the flat band voltage, and V_{ox} is the voltage across the oxide. At the same time $E_2+q\psi_s=E_C-E_{Fn}$ where, $qV_C=E_{Ep}-E_{Fn}\Rightarrow E_{Fn}=E_{Ep}-qV_C$. Thus, E_2 is:

$$E_2=\left(E_C-E_{Fp}\right)+qV_C-q\psi_s\,. \tag{4-4}$$

Here, E_{Fp} is the Fermi energy level for holes, E_{Fn} is the Fermi energy level for electrons, and V_C is the channel voltage. Equations (4-4) and (4-3) are substituted in Eq. (4-2):

$$\left(E_T-E_{Fn}\right)=\left(E_C-E_{Fp}\right)+qV_C-q\psi_s+\phi_0-qx_t/T_{ox}\left(V_{GS}-V_{FB}-\psi_s\right)-\left(E_{Cox}-E_T\right). \tag{4-5}$$

Based on the Shockley-Read-Hall (SRH) statistics and for linear region of MOSFET operation, the trap occupancy can be expressed in terms of the ratio of the average capture to emission times as [42]:

$$\frac{\overline{\tau}_c}{\overline{\tau}_e}=ge^{\left(E_T-E_{F_n}\right)/k_BT}\,. \tag{4-6}$$

Equation (4-5) is substituted in $\ln\left(\overline{\tau}_c/\overline{\tau}_e\right)=\left(E_T-E_{F_n}\right)/k_BT$. Therefore, $\ln\left(\overline{\tau}_c/\overline{\tau}_e\right)$ can be shown as:

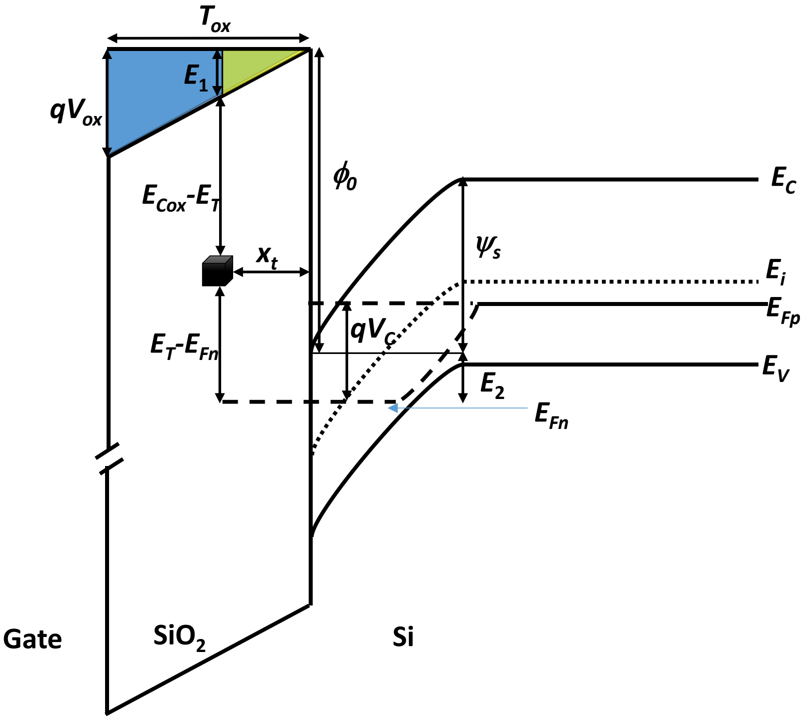

Figure 4-14 A schematic energy band diagram for Si/SiO$_2$ system in an nMOSFET device at a specific position along the channel.

$$\ln\left(\frac{\bar{\tau}_c}{\bar{\tau}_e}\right)=-\frac{1}{k_BT}\left[\left(E_{Cox}-E_T\right)-\left(E_C-E_{Fp}+qV_C\right)+q\psi_s-\phi_0+qx_t/T_{ox}\left(V_{GS}-V_{FB}-\psi_s\right)\right]. \qquad (4\text{-}7)$$

Trap position in the oxide from the Si/SiO$_2$ interface was evaluated using the slope of $\ln\left(\bar{\tau}_c/\bar{\tau}_e\right)/\partial V_{GS}$ [79 ,80, 81]:

$$x_t=\frac{T_{ox}\left[\frac{\left(k_BT/q\right)\partial\ln\left(\bar{\tau}_c/\bar{\tau}_e\right)}{\partial V_{GS}}+\frac{\partial\psi_S}{\partial V_{GS}}\right]}{\left(\partial\psi_S/\partial V_{GS}-1\right)}. \qquad (4\text{-}8)$$

The surface potential was computed from N_{inv} (Eq. (3-1)) as a function of V_{GS} and T [82]:

$$N_{inv}=A\left(\sqrt{\left(u+\mathrm{e}^{-u_s}-1\right)+\frac{n_0(T)}{p_o(T)}\left(\mathrm{e}^{u_s}-u_s-1\right)}-\sqrt{u_s}\right). \qquad (4\text{-}9)$$

$u_s = q\psi_s(T)/k_B T$, $A = \sqrt{2}\varepsilon_{Si} k_B T / q^2 L_D(T)$, and L_D is the Debye length which is evaluated from $\sqrt{\varepsilon_{Si} k_B T / q^2 p_0(T)}$ [82]. Here, p_0 is the carrier concentration for holes in equilibrium. All temperature dependent parameters were evaluated at the same temperatures that the RTS was observed. The temperature dependent parameters used in all aspects of the RTS calculations and analyses were [37, 63, 82]:

- $\bar{v}_{th}(T) = \sqrt{\frac{8k_B T}{\pi m_n^*}}$, the average thermal velocity of the channel carriers.
- $m_n^*(T) = m_0(1.053 + 0.00012T)$, the electron effective mass.
- $E_G(T) = 1.166 - \frac{4.730x10^{-4} T^2}{(T + 636)}$, Energy band-gap of Si.
- $N_C(T) = 2\left(\frac{2\pi m_n k_B T}{h^2}\right)^{3/2}$, the conduction band effective density of states.
- $N_V(T) = 2\left(\frac{2\pi m_p k_B T}{h^2}\right)^{3/2}$, the valance band effective density of states,
- $n_i(T) = \sqrt{N_C N_V} e^{-E_G/(2k_B T)}$, intrinsic carrier concentration in equilibrium.

Charge density per unit volume (n) in the inversion layer was evaluated based on the surface potential $\psi_s(x)$ from the interface down to the silicon bulk through [37, 63, 82]:

$$n(T) = n_0(T) e^{q\psi_s/k_B T} , \tag{4-10}$$

where $n_0(T) = n^2{}_i(T)/p_0(T)$. Here, n_0 is the carrier concentration for electrons in equilibrium. From the charge neutrality we derived an expression to calculate the hole concentration per unit volume as a function of temperature. Typically, at low temperatures the hole concentration does not equal to the background concentration (N_A) (for nMOSFET). This is due to the carrier freeze-out effect. The majority carrier concentration in equilibrium as a function of temperature is: $p_0(T) = N_A^-(T)$ where, $p_0(T) = N_V(T)\exp\left((E_V - E_F)/k_B T\right)$, and N_A^- is the ionized acceptor concentration which can be expressed as [37, 63, 82]:

$$N_A^-(T) = \frac{N_A}{1 + g_A e^{\frac{(E_A - E_F)}{k_B T}}} . \tag{4-11}$$

Here, E_A is the ionization energy that depends on the dopant type in the semiconductor, and g_A is the degeneracy factor for holes which is typically taken as 4 for Si. After substitution of p_0 and $\left(E_A - E_F\right) = \left(E_A - E_V\right) + \left(E_V - E_F\right)$ in Eq. (4-11), we have an expression for p_0 as:

$$p_0(T) = \frac{-1 \pm \sqrt{1 + 4\left[\left(\frac{g_A}{N_V(T)}\right) e^{\frac{(E_A - E_v)}{k_B T}}\right] N_A}}{2\left[\left(\frac{g_A}{N_V(T)}\right) e^{\frac{(E_A - E_v)}{k_B T}}\right]} . \tag{4-12}$$

The trap position values in the oxide that are obtained from Eq. (4-8) exhibit a large error if change in surface potential with respect to V_{GS} is ignored [80, 81].

Ratio of the average capture to emission times for the measured RTS data on TA and TB are plotted in Figure 4-15. Table 4-1 shows the values of x_t thus obtained following the procedure outlined above for traps in TA and TB. In general, bias dependence of the capture time constant depends on the trap positon in the oxide with respect to the Si/SiO$_2$ interface. Based on the principle of detailed balance, $\bar{\tau}_e$ may increase, decrease or stay constant with gate voltage. This behavior is highly affected by the trap location in the oxide

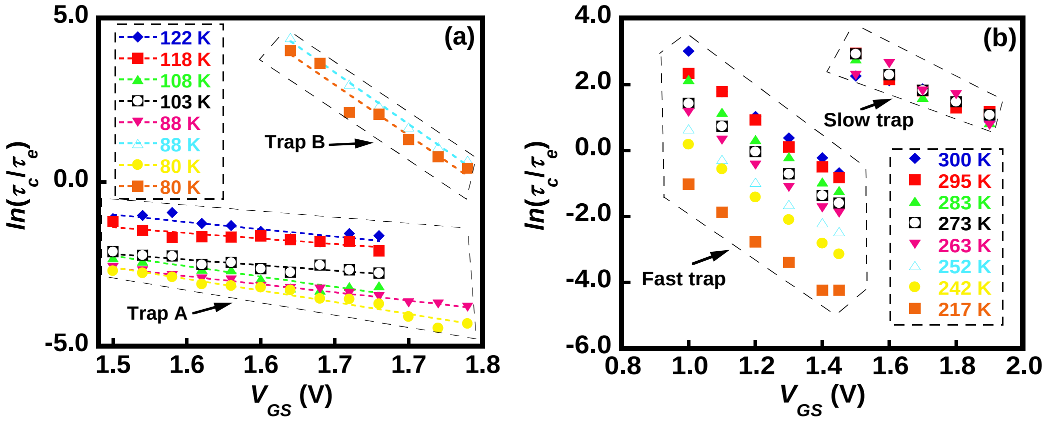

Figure 4-15 Ratio of the natural log of average capture to emission times for TA (a) and TB (b) from which the trap position in the oxide was calculated.

from the Si/SiO2 interface. As V_{GS} increases, band bending will also increase which will push the furthest trap from the interface down below the Fermi level at a higher rate compared to the trap closer to the interface. This makes the exponent of $\bar{\tau}_e/\bar{\tau}_c = 1/g\,\exp-\left(E_T - E_{F_n}/k_BT\right)$ to dominate, causing an increase with gate bias. Traps closer to the interface, however, might not experience much change with gate bias in their emission times or capture time as illustrated in Figure 4-15 for the trap A in TA and the slow trap in TB. Weak V_{GS} dependence of the average time constants can be found in

Table 4-1 Summary of the trap position in the oxide with respect to the Si/SiO2 interface in TA and TB.

TA		TB	
Trap	x_t (nm)	Trap	x_t (nm)
A	0.26	Fast	1.50
B	1.66	Slow	0.86

these references [24, 83, 84].

4.3.4 Extraction of Trap Position along the Channel

The drain-source voltage dependence of the ratio of the average capture to emission times was utilized to extract the trap location along the channel with respect to the source. Since the DUT is symmetrical, the source and drain can be switched. The possible orientations of the device are shown in or forward (F_m) and reverse (R_m) modes. We measured the RTS data as a function of V_{DS} in Figure 4-16 the strong inversion from linear to saturation region (Figure 3-10). Figure 4-17 depicts that the $(\bar{\tau}_c/\bar{\tau}_e)$ versus V_{DS} increases in the linear region and decreases in the saturation region. Based on the SRH statistics, average capture times can be expressed in terms of capture cross-section (σ), average thermal velocity, and charge carrier density as [42]:

$$\bar{\tau}_c = \frac{1}{\bar{v}_{th}\sigma n} \,. \tag{4-13}$$

For small V_{DS}, the linear channel approximation was assumed where the quasi-Fermi level for electrons varied linearly between the source and drain. Thus, the charge carrier density per unit volume can be evaluated from the gradual channel approximation [61, 85]:

$$n = \frac{C_{ox}\left(V_{GS} - V_{th} - V_C\right)}{qt_{inv}} \,, \tag{4-14}$$

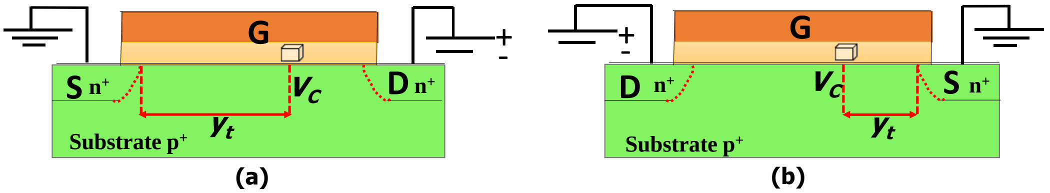

(a) **(b)**

Figure 4-16 Schematic diagram of two nMOSFET orientations showing the trap location along the channel with respect to the source for forward (a) and reversed (b) modes.

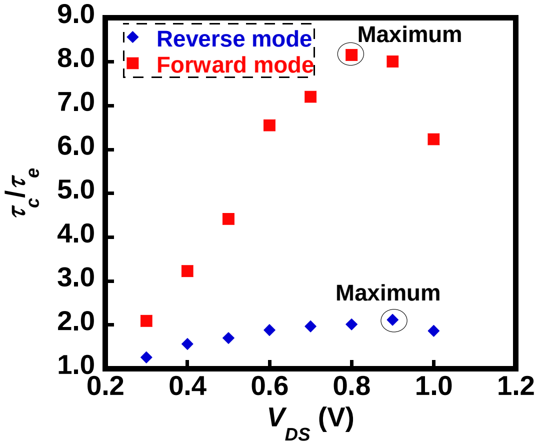

Figure 4-17 Ratio of the average capture to emission times as a function of drain-source voltage for the slow trap in TB. V_{GS} = 1.20 V and DUT temperature was 295 K.

where, t_{inv} is the inversion layer thickness. At y_t , the channel voltage is [79]:

$$V_C = \frac{y_t V_{DS}}{L}. \tag{4-15}$$

When V_{DS} was increased in the linear region, V_C increased which in turned decreased n. If the charge density near the drain region decreased, $\bar{\tau}_c$ would be expected to increase slightly. However, when the DUT operated in the saturation region, the average velocity of channel carrier exceeded $\bar{v}_{th}$ which was affected by the high electric field. At the same time n in the saturation region did not change that much. This made $\bar{\tau}_c/\bar{\tau}_e$ to decrease in the saturation region as shown in Figure 4-17.

In the forward mode, Eqs. (4-7), (4-15), and $\psi_s = \psi_{s_0} + V_C$ were utilized to compute trap location along the channel with respect to the source. Here, ψ_{s_0} is the band bending at the source side [79, 86]. Thus, the ratio of $\ln\left(\bar{\tau}_c/\bar{\tau}_e\right)_{F_m}$ can be expressed as:

$$\ln\left(\frac{\bar{\tau}_c}{\bar{\tau}_e}\right)_{F_m} = -\frac{1}{k_B T}\begin{bmatrix} \left(E_{Cox}-E_T\right)-\left(E_C-E_{Fp}\right)-\dfrac{q y_t V_{DS_{F\max}}}{L}+q\psi_{s_0}+\dfrac{q y_t V_{DS_{F\max}}}{L}-\phi_0+ \\ \dfrac{q x_t}{T_{ox}}\left(V_{GS}-V_{FB}-q\psi_{s_0}-\dfrac{q y_t V_{DS_{F\max}}}{L}\right) \end{bmatrix}$$

. (4-16)

In the reverse mode, $V_C = \left(1-y_t\right)V_{DS}/L$ and $\psi_s = \psi_{s_0} + \left(1-y_t\right)V_{DS}/L$ were substituted in Eq. (4-7) which resulted in $\ln\left(\bar{\tau}_c/\bar{\tau}_e\right)_{R_m}$:

$$\ln\left(\frac{\bar{\tau}_c}{\bar{\tau}_e}\right)_{R_m} = -\frac{1}{k_B T}\begin{bmatrix} \left(E_{Cox}-E_T\right)-\left(E_C-E_{Fp}\right)-\dfrac{q\left(1-y_t\right)V_{DS_{R\max}}}{L}+q\psi_{s_0}+\dfrac{q\left(1-y_t\right)V_{DS_{R\max}}}{L} \\ -\phi_0+\dfrac{q x_t}{T_{ox}}\left(V_{GS}-V_{FB}-q\psi_{s_0}-\dfrac{q\left(1-y_t\right)V_{DS_{R\max}}}{L}\right) \end{bmatrix}. \quad (4\text{-}17)$$

Eq. (4-17) was subtracted from Eq. (4-16) which yielded the trap position along the channel:

$$\frac{y_T}{L} = \frac{\left(\dfrac{k_B T T_{ox}}{q x_t}\right)\ln\left[\dfrac{(\bar{\tau}_c/\bar{\tau}_e)_{F_\mathrm{m}}}{(\bar{\tau}_c/\bar{\tau}_e)_{R_\mathrm{m}}}\right]+V_{DS_{R\max}}}{V_{DS_{F\max}}+V_{DS_{R\max}}}. \quad (4\text{-}18)$$

Here, $V_{DS_{F\max}}$ and $V_{DS_{R\max}}$ are the drain-source voltages in the forward and reverse modes, respectively at which the maximum interaction between the trap and the channel carriers can be observed (Figure 4-17). The maximum $\bar{\tau}_c/\bar{\tau}_e$ versus V_{DS} depends on the location of the trap along the channel. Therefore, the extracted y_t/L for the fast trap in TB is 0.66 which suggests the trap is located closer to the drain than to the source. However, we could not extract the trap location for the slow trap in TB. We acquired RTS as a function of V_{DS} in the forward mode but we did not see any RTS in the reverse mode. This might be due to location of the slow trap being much closer to the drain side than to the source side in the forward mode. Therefore, if the trap is located near the source side and capable of capturing an electron from the channel, most likely the effect of losing an electron on the local conductivity *or* the effect of Coulomb scattering on the channel carriers will be smeared out by the presence of large number of charge carriers near the source and their screening effect.

4.3.5 *Extraction of the Trap Electrical Properties*

Understanding the microscopic processes by which charge carrier trapping occurs by gate oxide defects in MOSFETs is essential in identifying the physical origin of these defects and taking precautionary measures to minimize them. In our analysis, first principles were used to study the capture and emission of a mobile charge carrier by defects in the oxide. Kirton and Uren developed trapping model and standard MOSFET analysis where the average capture and emission time constants are given by [42]:

$$\bar{\tau}_c(T) = \frac{1}{n(T)\sigma_0 \bar{v}_{th}(T)} \mathrm{e}^{(\Delta E_B/k_B T)} \,. \tag{4-19}$$

$$\bar{\tau}_e(T) = \frac{1}{g\left(8k_B T/\pi m^*(T)\right)^{1/2} N_C(T)\sigma_0 \, \mathrm{e}^{(\Delta S/k_B)}} e^{\left((\Delta E_B+\Delta H)/k_B T\right)} \,. \tag{4-20}$$

From the V_{GS} and temperature dependence of $\bar{\tau}_c$ and $\bar{\tau}_e$ several trap properties were extracted. The following section will highlight these parameters.

4.3.5.1. Capture Cross – Section

The capture cross section of a trap depends on the depth of the trap in the oxide (the tunneling, $\propto \exp(-x_t/\lambda)$) and the lattice relaxation upon capture of an electron in an

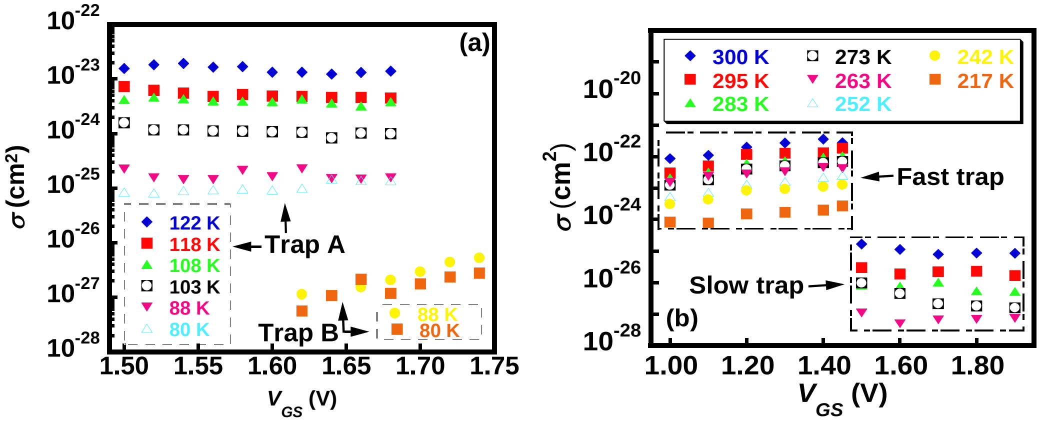

Figure 4-18 Capture cross-section of the probed traps in TA (a) and TB (b).

nMOS device [84]. The tunneling component does not change with respect to temperature. The latter component, however, depends exponentially on temperature. Capture cross-section can be expressed in terms of capture activation energy and capture cross-section prefactor as [42]:

$$\sigma = \sigma_0 \exp(-\Delta E_B / k_B T) . \tag{4-21}$$

Capture cross-section was evaluated based on Eq. (4-13). The obtained values of σ as a function of V_{GS} and temperature are shown in Figure 4-18.

The change in the capture cross section with respect to temperature is primarily determined by the ΔE_B and the temperature range measured. In general, there are three

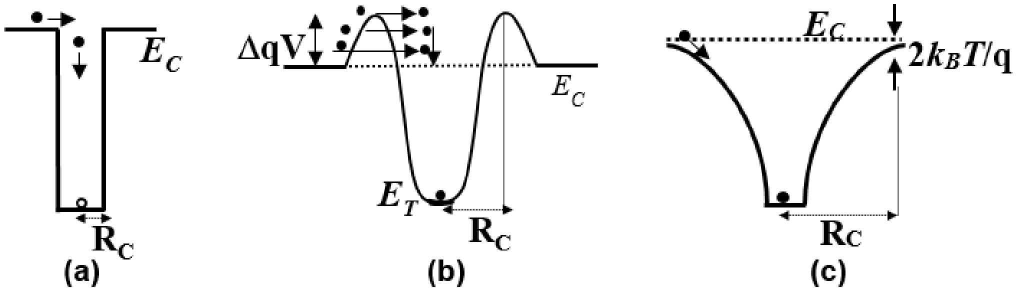

Figure 4-19 Three type of capture cross sections where (a) is neutral, (b) is the Coulombic repulsive, and (c) is the Coulombic attractive center.

different defect centers in the oxide: The capture cross section for a neutral center is weakly dependent on the electric field and highly dependent on the temperature. Capture cross section for a neutral center increases when temperature is increased (Figure 4-19(a)) [87, 88, 89]. The second type is the Coulombic repulsive defect center, whose capture cross-section increases when V_{GS} and T are increased (Figure 4-19(b)) [87, 88, 89]. The third type is the Coulombic attractive center. The capture cross section for the Coulombic attractive center decreases when temperature is increased and increases when V_{GS} is increased Figure 4-19(c)) [87,88, 89]. According to these three defect centers and from the values of capture cross section which are extracted from the RTS data, the results suggest that the defect responsible for the drain-source voltage fluctuations in our case is a neutral center which looks like an acceptor that becomes negatively charged after capturing an electron.

Small capture cross sections lead to the trap being mostly empty and therefore hard to detect by methods other than RTS. According to [90, 91, 92], the small capture cross-section values of negatively charged oxygen vacancy is difficult to detect and identify experimentally. However, using the RTS technique to probe on electrically active trap would resolve the short average capture times from which capture cross-section of a trap is computed. This yielded the extraction of σ for a negatively charged center. In addition, taking long-time RTS data would allow the measurement of a small capture cross-section. This can be done through several acquired RTS traces which can be stitched together to provide enough transitions between the RTS levels.

4.3.5.2. Capture Activation Energy

Capture activation energy of defects in the gate oxide in a MOSFET is an important parameter that can be utilized to evaluate $\overline{\tau}_c$, relaxation energy, and energy needed to

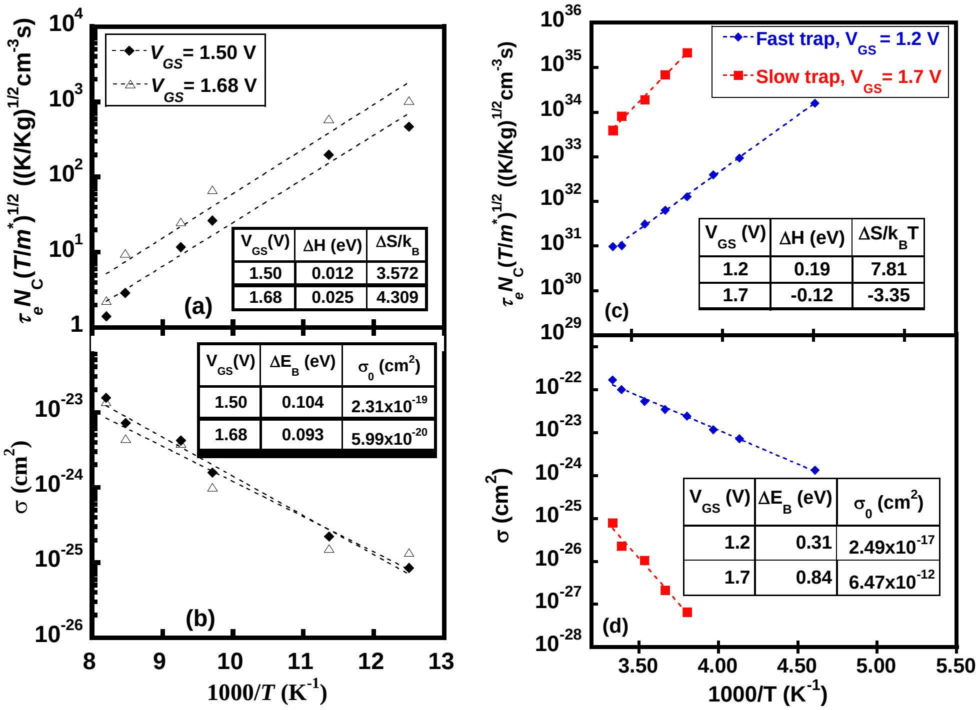

V_{GS}(V)	ΔH (eV)	$\Delta S/k_B$
1.50	0.012	3.572
1.68	0.025	4.309

V_{GS}(V)	ΔE_B (eV)	σ_0 (cm^2)
1.50	0.104	$2.31\text{x}10^{-19}$
1.68	0.093	$5.99\text{x}10^{-20}$

V_{GS} (V)	ΔH (eV)	$\Delta S/k_B T$
1.2	0.19	7.81
1.7	-0.12	-3.35

V_{GS} (V)	ΔE_B (eV)	σ_0 (cm^2)
1.2	0.31	$2.49\text{x}10^{-17}$
1.7	0.84	$6.47\text{x}10^{-12}$

Figure 4-20 Arrhenius plot of the normalized emission time constant for trap A in TA (a) and the two traps in TB (c).The Arrhenius plot of capture cross–section for trap A in TA (b) and the fast and slow traps in TB (d).

release the trapped carrier back to the channel. As discussed earlier, the mechanism of capturing an electron from the channel by a defect at the Si/SiO_2 interface or deep in the oxide is phonon-assisted tunneling. This means an electron needs to overcome the barrier energy between the trap level and the Si conduction band edge in order to be captured (Figure 4-1). Before capturing an electron, the trap center would go under thermal vibrations around the equilibrium position close to the silicon conduction band-edge. This is accompanied by large lattice vibrations. This phenomenon facilitates the capture of electrons from the channel [93].

From the Arrhenius plots of σ (Eq. (4-13), ΔE_B and σ_0 in Eq. (4-21) were extracted for all traps in TA and TB as illustrated in Figure 4-20. The extracted capture

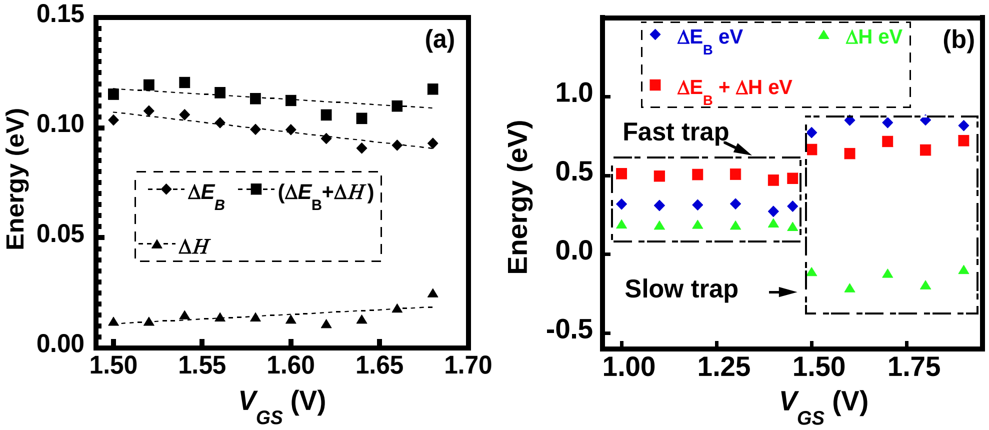

Figure 4-21 The gate voltage dependence of the extracted capture activation energy, emission energy, and change in enthalpy for trap A in TA (a) and the fast and slow traps in TB (b). The drain-source voltage in TA and TB kept at 0.25 and 0.30 V, respectively.

activation energy of the defects in TA and TB are plotted in Figure 4-21. The extracted ΔE_B associated with the trap A ranges from 0.092 to 0.103 eV (in TA). In general, the average capture time depends exponentially on ΔE_B. Here, the extracted ΔE_B values agree with the previously reported ones [42, 94]. Capture activation energy of the fast trap $\left(\Delta E_{B_{Fast}}\right)$ n TA was in the range of 0.27-0.32 eV. Similar ΔE_B values have been reported in the literature [42, 90, 93]. On the other hand, capture activation energy of the slow trap $\left(\Delta E_{B_{Slow}}\right)$ is bigger than capture activation energy of the fast trap. $\Delta E_{B_{Slow}}$ was between 0.77 and 0.82 eV. This high capture activation energy reveals the reason behind the long times to exchange a mobile charge between the channel and the defect(s). In addition, the high capture activation energy reflects on the relaxation energy associated with the defect. This can be inferred from the relation between ΔE_B and E_R as it will be shown in section 4.3.5.6.

Capture cross section prefactors for trap A in TA were found in the range of

4.29x10^{-20}-3.34x10^{-19} cm^2 where capture cross-section prefactor of the fast trap $\left(\sigma_{0_{Fast}}\right)$ in TB was found between 6.73x10^{-18} and 4.07x10^{-17} cm^2. These values agree with the previously reported ones [42, 95]. The extracted capture cross-section prefactor of the slow trap $\left(\sigma_{0_{Slow}}\right)$ was found on the range between 8.72x10^{-13} and 1.17x10^{-11} cm^2. $\sigma_{0_{Slow}}$ was larger than $\sigma_{0_{Fast}}$ with 5-6 orders of magnitude. The values of $\sigma_{0_{Slow}}$ are close to the ones that have been reported before [96]. If we did not incorporate trap entropy component in Eq. (4-20), the capture cross-section prefactor values obtained from Eq. (4-19) would be one to two orders of magnitude smaller than those obtained from Eq. (4-20). Therefore, σ_0 in Eq. 4-20 is not the capture cross-section prefactor but the capture cross-section prefactor multiplied with $e^{\Delta S/k_B}$, which accounts for the discrepancy between σ_0 values extracted from Eqs. (4-19) and (4-20).

4.3.5.3. Emission Activation Energy

Upon capturing an electron the defect binding force is assumed to increase. Consequently, lattice oscillations increase [97]. The raise of phonon energy works to restore the defect structure very quickly to the state prior to the trapping (empty state) by emitting the trapped electron back to the channel. The energy needed to release a trapped electron from the defect $\left(\Delta E_B + \Delta H\right)$ and the constant $C = \left(g\sqrt{8k_B T/\pi m^*(T)}N_C(T)\sigma_0\,\mathrm{e}^{(\Delta S/k_B)}\right)^{-1}$ (Eq. 4-20) can be read out from the Arrhenius plot of $\bar{\tau}_e(T)N_C(T)\left(T/m^*(\mathrm{T})\right)^{1/2}$ as denoted in Figure 4-20(a) and (c). The obtained values of $\left(\Delta E_B + \Delta H\right)$ associated with trap A in TA and the fast and slow traps in TB are shown in

Figure 4-21.

4.3.5.4. *Change in Enthalpy*

Change in the system enthalpy is highly impacted with the delocalization of the remaining bound carriers to the defect [98]. Higher value of ΔH corresponds to deeper trap level within the SiO$_2$ band gap. However, our data in TA show small values of ΔH = 12 -25 meV which were within the range of the reported values (Figure 4-21(a)) [93, 94]. Change in enthalpy due to the fast trap (TB) was found to be between 180 and 200 meV. These values reveal the emission of a trapped electron back to the channel is an endothermic-process that absorbs energy in the form of heat. Change in enthalpy due to the slow trap lies in the range of -0.21 to -0.10 eV. This indicates the emission of a trapped electron by the slow trap is an exothermic-process where a heat is generated upon releasing the trapped electron.

4.3.5.5. *Change in Entropy*

Change in entropy was computed from the constant C (as previously defined in section 4.3.5.3) which was read out from the Arrhenius plots of the normalized average capture times. Change in entropy due to trap A in TA was 6.00–9.00. A typical value of $\Delta S/k_B$ is 5-8 for Si/SiO$_2$ system, while values as high as 11.8 and as low as 2.2 have also been reported [42]. The increase in the entropy comes from the contribution of the electron freed from the trap and the structural relaxation of the remaining defect. Change in entropy due to the fast trap $(\Delta S/k_B)_{Fast}$ in TB was in the range of 6.15 and 9.34. These values are consistent with other extracted values through RTS measurements [42, 93, 94]. Change in entropy due to the slow trap $(\Delta S/k_B)_{slow}$ was between -6.08 and -1.64. The negative change in entropy may show that the trapped electron was shared between the defect atom and the surrounding lattice. As a consequence, the interactions between the neighboring atoms increased and the energy separation between the trap and the ground state energy level of the electron in the conduction ban-edge would be small [99]. This would soften the lattice in the immediate vicinity of the defect (when the trap is full) which decreases the vibrational frequency [42]. Similarly, when the trapped electron was emitted, a negative change in enthalpy was observed which showed heat was transformed to the lattice. Transferring heat to the lattice would increase the vibrational frequency which in turn increases the binding force and leads to less entropy (when the trap is empty). To our knowledge, this is the first time change in entropy due to the emission of a trapped electron to the channel resulted in negative ΔS values based on the RTS analysis. Again, this might reveal that the local environment within the vicinity of the defect in the oxide was more disordered when the trap was filled with an electron than when was empty.

4.3.5.6. Geometric Relaxation Energy

The relaxation energy was used as one of the four trap characteristics to identify the trap species that causes the fluctuations in the drain-source voltage. ΔE_B, ΔH, and

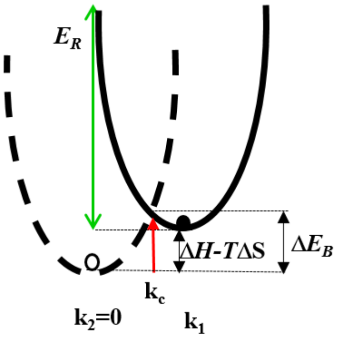

Figure 4-22 Configuration coordinate diagram. The dashed curve corresponds to the empty trap and the electron is free in the conduction band-edge where, solid the curve represents the trap state when is filled with an electron.

ΔS were used to evaluate E_R as a function of V_{GS} and temperature. According to Figure 4-22, E_R was computed from the potential barrier between the initial and the final state of the total system energy and the trap energy level with respect to the silicon conduction band-edge. The change in Gibbs free energy was considered to perfect the RTS analysis. The change in Gibbs free energy can be expressed in terms of the trap binding enthalpy and entropy as [42]:

$$\Delta E_{CT} = \Delta H - T\Delta S\,. \tag{4-22}$$

Here, $\Delta E_{CT} = E_{C_{Si}} - E_T$. As we discussed before, the mechanism of trapping/detrapping of channel carriers is phonon-assisted tunneling. Therefore, when a carrier is trapped, it will relax to the trap energy level by emitting several phonons and that determines the E_R value. The relaxation energy associated with the defect center in the gate oxide was derived from the energy and wave vector (*k*) relation [84]. We equated the two parabolic curves (Figure 4-22) as:

$$Ak^2 = A\left(k - k_1\right)^2 + b\,. \tag{4-23}$$

Here, A is a constant, $b = \Delta E_{CT} = \Delta H - T\Delta S$, and we are assuming that the effective mass of the electron does not change between the free and the trapped state. The value of $\left(\Delta H - T\Delta S\right)$ can be positive where the trap energy is below the Si conduction band edge, or it can be negative if the trap energy is above the Si conduction band edge. k_c was evaluated at the intercept point:

$$Ak_c^{\,2} = A\left(k_c - k_1\right)^2 + b \Rightarrow Ak_c^{\,2} = Ak_c^{\,2} - 2Ak_ck_1 + Ak_1^{\,2} + b \Rightarrow k_c = \frac{Ak_1^{\,2} + b}{2Ak_1}\,. \tag{4-24}$$

From Figure 4-22, we defined $E_{\mathrm{R}} = Ak^2{}_1$, $\Delta E\ {}_B = Ak_c^{\,2}$, and substituted them in Eq. 4-24:

$$\Delta E_B = A\left[\frac{E_R/A + b/A}{2 \pm \sqrt{\frac{E_R}{A}}}\right]^2 = \frac{\left(E_R + b\right)^2}{4E_R}. \tag{4-25}$$

$$\therefore \Delta E_B = \frac{\left(E_R + b\right)^2}{4E_R}. \tag{4-26}$$

Thus, the derived relaxation energy in terms of Gibbs free energy and capture activation energy is [84]:

$$\Delta E_B = \frac{\left(E_R + \left(\Delta H - T\Delta S\right)\right)^2}{4E_R}. \tag{4-27}$$

The extracted relaxation energy associated with trap A in TA and the fast and slow traps in TB were on the average of 0.60, 1.24, and 3.19 eV, respectively. These values were compared with several relaxation energies associated with a variety of possible defect configurations in the silicon dioxide. E_R values of trap A in TA and the fast trap in TB showed that the electron was trapped by an unrelaxed neutral oxygen deficiency center (V^0 ODC II) where, the origin of the slow trap was unclear to us [90, 91, 100]. According to Kimmel *et al*. [91], The geometric relaxation energy associated with the oxygen neutral vacancy depends on the local environment of the vacancy which can lower the total energy system by 0.8 - 2.1 eV, causing dispersion in E_R. These values were found by using *embedded cluster method*, which is used to study point defects in various charge states along with their relaxation and polarization effects [101]. The wide range of relaxation energy could lead to inaccurate conclusion. Therefore, we used three more trap characteristics ($E_{Cox} - E_T$, ΔE_B, and σ) to deduce the nature and origin of the defect in the gate oxide. The study was repeated on several nMOSFETs at various T and V_{GS} ranges to verify the results (Table 4-2) and (Figure 4-23).

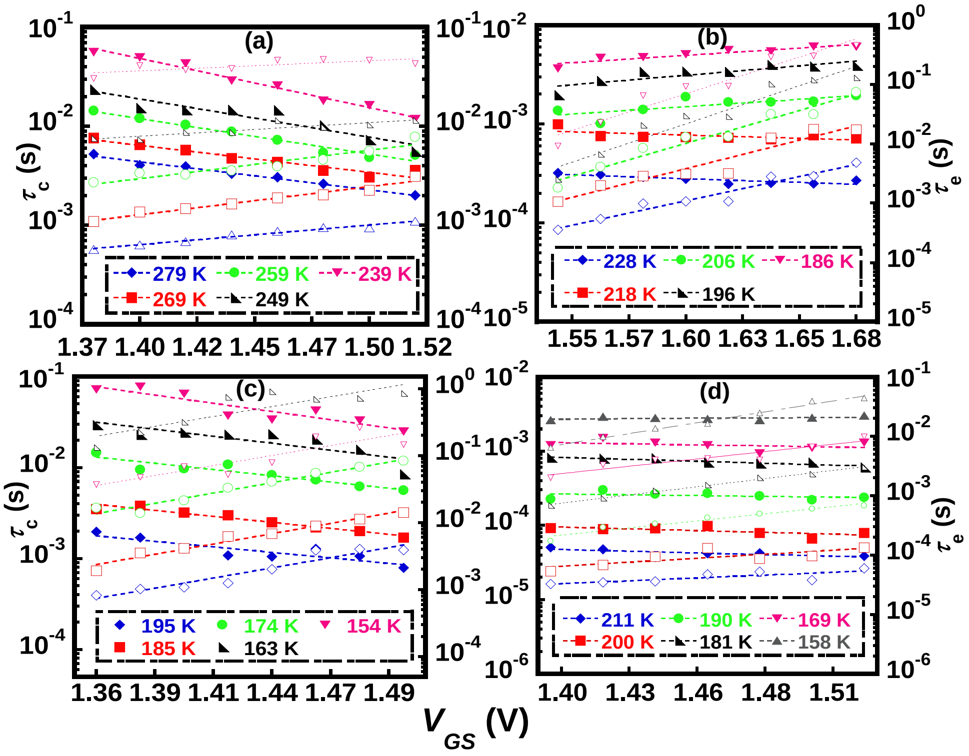

Figure 4-23 Average capture (solid symbols) and emission (open symbols) time constants measured on several nMOSFETs. (a) Device 1, (b) device 2, (c) device 3, and (d) device 4.

Table 4-2 ΔE_B, E_R, $(E_{Cox}-E_T)$ values extracted from the measured RTS data on six nMOSFETs at various V_{GS} and T ranges.

Device	V_{GS} (V)	T (K)	ΔE_B (eV)	E_R (eV)	(E_{Cox}-E_T) (eV)
1	1.38-1.48	239-279	0.35	1.63	2.98
2	1.54-1.68	186-228	0.28	1.14	2.88
3	1.36-1.50	154-195	0.23	0.89	2.89
4	1.40-1.52	158-211	0.24	0.90	3.00
5	1.50-1.68	80-122	0.10	0.60	3.09
6	1.00-1.45	217-300	0.31	1.25	3.00

There are no assumptions made in the process of identifying the trap nature. In fact, all results and analysis were based on experimental RTS data from which the average capture and emission time constants were extracted. From the V_{GS} and temperature dependence of $\bar{\tau}_c$ and $\bar{\tau}_e$, energies associated with a trap were extracted. This gives the RTS some advantages over other methods by looking instantaneously at the trap characteristics in real time within one measurement setup.

4.3.5.7. *Trap Energy in the SiO_2 Band-Gap*

The trap energy with respect to the SiO_2 conduction band-edge $\left(E_{Cox}-E_T\right)$ was evaluated as a function of V_{GS} and temperature using Eq. 4-7. The values shown in Figure 4-24 would make the trap to be relatively deep in the SiO_2 band-gap. Moreover, these values indicate that the trap center responsible for the fluctuations in the V_{DS} signal was a neutral oxygen vacancy which becomes a negatively charged center upon capturing an electron [11, 90]. According to [102], the negatively charged oxygen vacancy center has an energy level of 3.3 eV with respect to the SiO_2 conduction band-edge. This result was

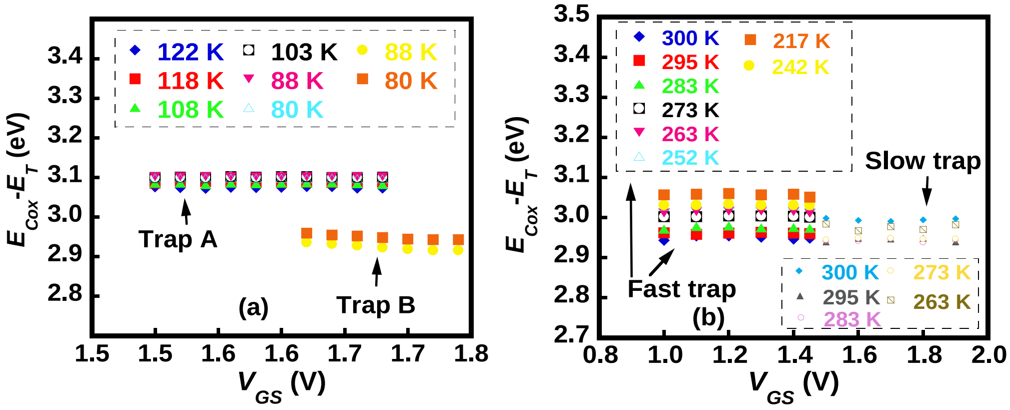

Figure 4-24 The trap energy level with respect to the SiO_2 conduction band-edge for TA (a) and TB (b).

found through spin unrestricted time–dependent density functional theory approach in agreement with our values, which are extracted from the RTS.

4.3.6 RTS Amplitude

The RTS amplitude was experimentally obtained from the histogram of the RTS data after the peak of each Gaussian was identified as shown in Figure 4-3(b) and Figure 4-4(b). The RTS amplitude was evaluated as function of V_{GS} and temperature due to each active trap in TA and TB and plotted in Figure 4-25. Remote Coulomb scattering effect of the charged trap was considered for mobility fluctuations of the channel carriers in addition to the carrier number fluctuations due to trapping/detrapping. This is the essence of UNMF model [22]. According to UNMF model, the fluctuations in the drain-source voltage can be written as the summation of carrier number and correlated mobility fluctuations from which the RTS amplitude is computed as [22]:

$$\frac{\Delta V_{DS}}{V_{DS}} = -\frac{1}{WL}\left[\frac{1}{N_{inv}} \pm \alpha\bar{\mu}_c\right]. \tag{4-28}$$

The RTS amplitude was utilized to compute the screened scattering coefficient using Eq.

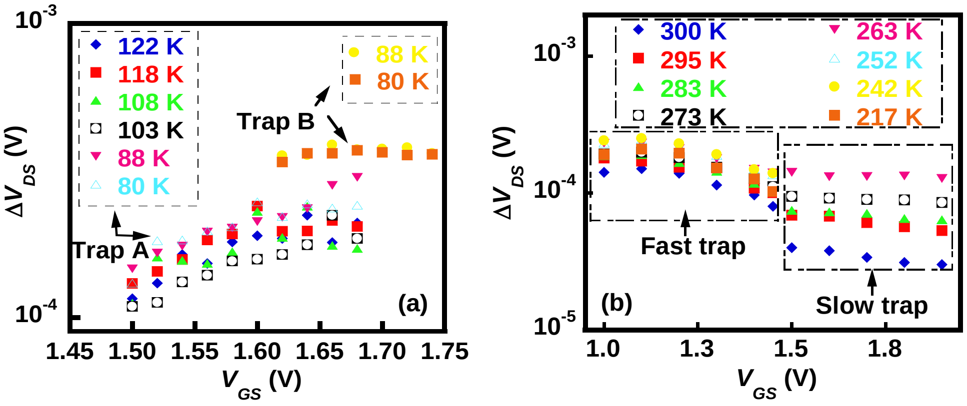

Figure 4-25 RTS amplitude extracted from the measured RTS data. V_{DS} = 0.25 and 0.30 V for TA (a) and TB (b), respectively.

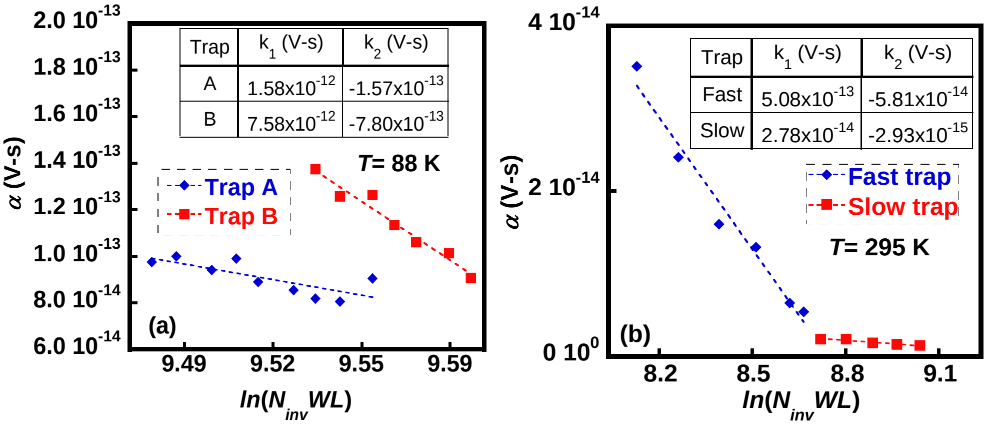

Figure 4-26 Screened scattering coefficient as a function of natural log of charge carrier number in the inversion layer for TA (a) and TB (b).

4-28 (Figure 4-26). From the linear regression of α versus $\ln\left(N_{inv}WL\right)$, remote Coulomb scattering coefficients k_1 and k_2 were identified through this empirical formula [22]:

$$\alpha = k_1 + k_2 \ln\left(N_{inv}WL\right). \tag{4-29}$$

Here, k_1 and k_2 are constants where, $k_2 < 0$. The extracted k_1 and k_2 as a function of temperature associated with the active traps in TA and TB are denoted in Table 4-3. The values of α thus obtained agree with the previously reported ones [41, 93,103]. The screened scattering coefficient indicates the effectiveness of the trap in causing mobility fluctuations in the channel carriers. When gate oxide thickness is decreased, and V_{GS} is increased, the surface channel carrier density increases. Since k_2 < 0, and with the increase of N_{inv}, the screening effect would increase which decreases the screened scattering coefficient as illustrated in Eq (4-29) (Figure 4-26).

The effective channel carrier mobility for the linear region ($\bar{\mu}_l$) was computed from the channel conductance g_d (Figure 4-27) and the total charge $\left(Q_{inv} = qN_{inv}\right)$ as [44]:

$$\bar{\mu}_l = g_d/(W/L)Q_{inv} . \tag{4-30}$$

The obtained values of $\bar{\mu}_l$ are plotted in Figure 4-28. The effective channel carrier mobility in the onset of saturation region ($\bar{\mu}_s$) can be obtained using [44]:

$$\bar{\mu}_s = \bar{\mu}_l \left(1 - \frac{1}{\sqrt{1 + \frac{2\left(2\phi_F + V_{SB}\right)C_{ox}^2}{qp_0\varepsilon_{Si}}}} \right), \tag{4-31}$$

where, ϕ_F is the Fermi energy level with respect to the intrinsic energy level in the Si bulk, and V_{SB} is the source-body voltage.

The relative contribution of the number and mobility fluctuations to the RTS amplitude was extracted as a function of V_{GS} and temperature (Figure 4-29). As depicted in Figure 4-29(c)-(d), the number fluctuations in TA and TB as well as the mobility

Table 4-3 The extract Coulomb scattering coefficients k_1 and k_2 associated with the identified traps in TA and TB as a function of temperature.

TA				
	Trap A		Trap B	
T (K)	k_1 (V-s)	k_2 (V-s)	k_1 (V-s)	k_2 (V-s)
122	$1.14\text{x}10^{-12}$	$-1.12\text{x}10^{-13}$		
118	$2.05\text{x}10^{-12}$	$-2.08\text{x}10^{-13}$		
108	$2.51\text{x}10^{-12}$	$-2.55\text{x}10^{-13}$		
103	$5.88\text{x}10^{-13}$	$-5.44\text{x}10^{-14}$		
88	$1.58\text{x}10^{-12}$	$-1.57\text{x}10^{-13}$	$7.58\text{x}10^{-12}$	$-7.80\text{x}10^{-13}$
80	$2.40\text{x}10^{-12}$	$-2.43\text{x}10^{-13}$	$6.39\text{x}10^{-12}$	$-6.56\text{x}10^{-13}$
Average	$1.71\text{x}10^{-12}$	$-1.71\text{x}10^{-13}$	$6.99\text{x}10^{-12}$	$-7.18\text{x}10^{-13}$
TB				
	Fast trap		Slow trap	
T (K)	k_1 (V-s)	k_2 (V-s)	k_1 (V-s)	k_2 (V-s)
300	$4.50\text{x}10^{-13}$	$-5.03\text{x}10^{-14}$	$9.44\text{x}10^{-16}$	$-1.05\text{x}10^{-16}$
295	$5.08\text{x}10^{-13}$	$-5.81\text{x}10^{-14}$	$2.78\text{x}10^{-14}$	$-2.93\text{x}10^{-15}$
283	$5.85\text{x}10^{-13}$	$-6.69\text{x}10^{-14}$	$2.17\text{x}10^{-14}$	$-2.18\text{x}10^{-15}$
273	$6.32\text{x}10^{-13}$	$-7.22\text{x}10^{-14}$	$3.28\text{x}10^{-14}$	$-3.23\text{x}10^{-15}$
263	$7.72\text{x}10^{-13}$	$-8.84\text{x}10^{-14}$	$7.09\text{x}10^{-14}$	$-7.16\text{x}10^{-15}$
252	$8.47\text{x}10^{-13}$	$-9.69\text{x}10^{-14}$		
242	$8.62\text{x}10^{-13}$	$-9.89\text{x}10^{-14}$		
217	$8.50\text{x}10^{-13}$	$-9.75\text{x}10^{-14}$		
Average	$6.88\text{x}10^{-13}$	$-7.86\text{x}10^{-14}$	$3.08\text{x}10^{-14}$	$-3.12\text{x}10^{-15}$

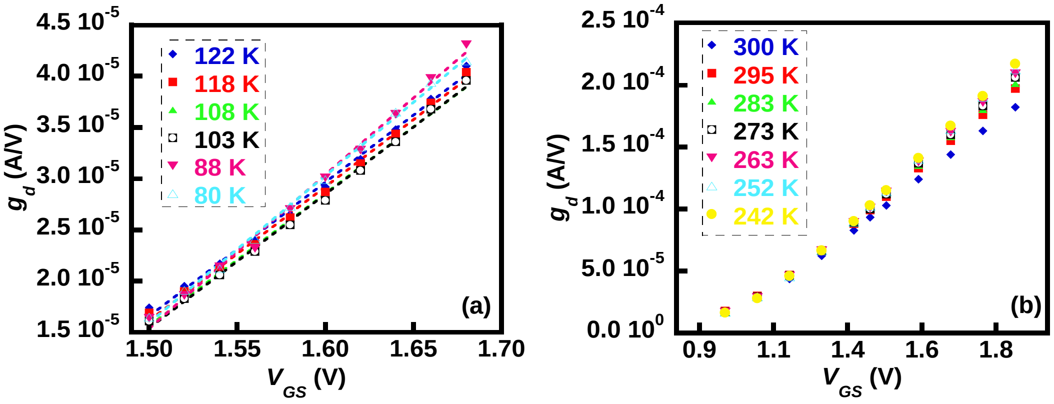

Figure 4-27 Channel conductance for TA (a) and TB (b) devices showed linear relation with V_{GS}. V_{DS} for TA and TB were 0.25 and 0.30 V, respectively.

fluctuations in TB decreased with the increase of V_{GS} and temperature. In contrary to that, mobility fluctuations contribution in TA increased as V_{GS} and T were increased. This might be due to the weak effect of α on the channel carriers (T=80-122). In addition, the average mobility increased with the increased of V_{GS} which in turn dominated the mobility fluctuation term. Number and mobility fluctuations almost had the same influence on the V_{DS} in TB. In case of large oxide thickness, the effect of $\ln(N_{inv}WL)$ and the values of k_1 and k_2 on the mobility fluctuations were insignificant [93]. Therefore, the contributions of number and

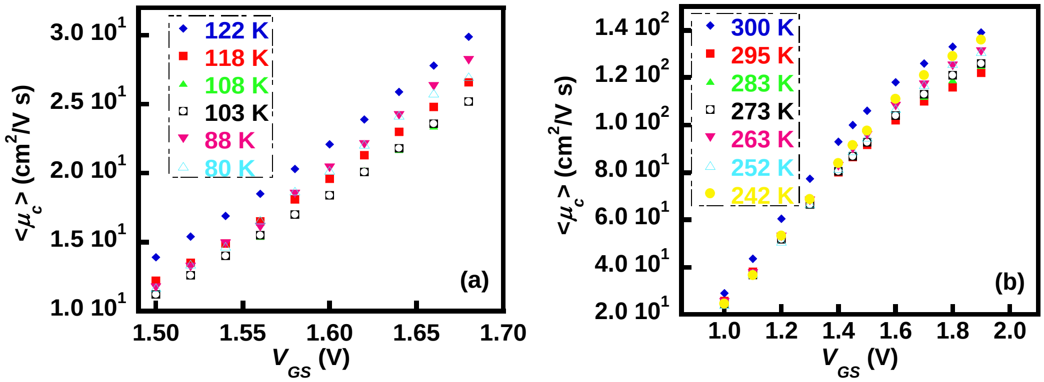

Figure 4-28 Average channel carrier mobility in TA (a) and TB (B). Drain-source voltage were 0.25 and 0.30 V for TA and TB, respectively

mobility fluctuations to the RTS noise were comparable. However, mobility fluctuations in TA dominated over number fluctuations.

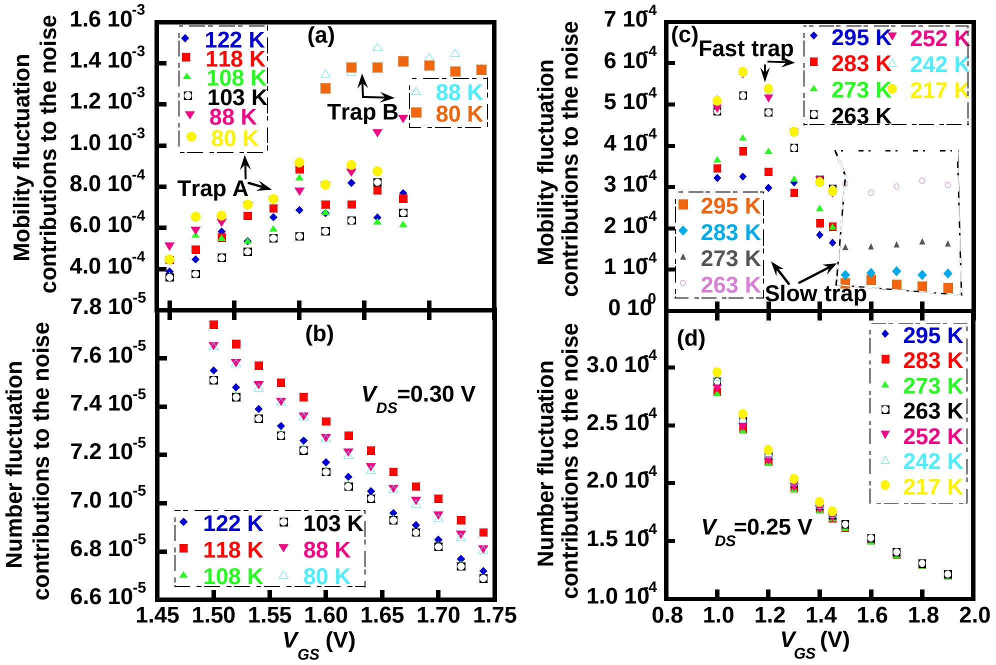

Figure 4-29 Number (a and c) and mobility (b and d) fluctuations contribution to the RTS as a function of gate-source voltage where V_{DS} = 0.25 and 0.30 V for TA and TB, respectively.

4.3.7 RTS Analysis in time domain before and after Electrical Stressing

Characteristics of DC-stress-induced traps were investigated in the gate dielectric oxide on 3.3 V-rated nMOSFETS with the channel area of 0.36 µm^2. RTS measurements were performed in the same device (TA) before and after electrical stress, from which the trap characteristics were extracted. Trap species responsible for the fluctuations in the drain-source voltage were identified and found to be due to unrelaxed oxygen deficiency center before DC stress (DCS) and after DCS.

DCS was performed to intentionally create defect centers in the gate oxide and compare it to the process-induced trap characteristics. First, RTS and IV measurements were taken on a fresh device as a function of V_{GS} and temperature. Two level and three level RTS were observed and recorded at the temperature range of 80 to 122 K. Subsequently, the same device was stressed at V_{GS} = 2.1 V and V_{DS} = 3.0 V for 60, 120, 180, 220, 350, and 480 s at room temperature. After each stressing, IV measurements were repeated. The device was scanned again for any RTS presence. It was observed that the RTS quieted down after 60 s of stressing, while degradation in the threshold voltage V_{th} was noted. Even after, 1410 s of stressing time, no RTS was observed. This implies that a stress-induced or a process-induced trap may be filled with a carrier during stress, producing a fixed charge in the gate oxide which shifts V_{th} (Figure 4-30).

Next, the temperature was lowered down to 80 K in small increments. Two-level RTS was observed on the stressed device at the temperature range of 239 to 279 K for V_{GS} =1.38-1.52 V with V_{DS}=0.25 V. Although before DCS, two-level RTS was seen for T=80-122 K, and three-level RTS was present for T= 80 and 88 K (Figure 4-4), after stressing, only two level RTS was present for T= of 239 to 279 K. The data were analyzed

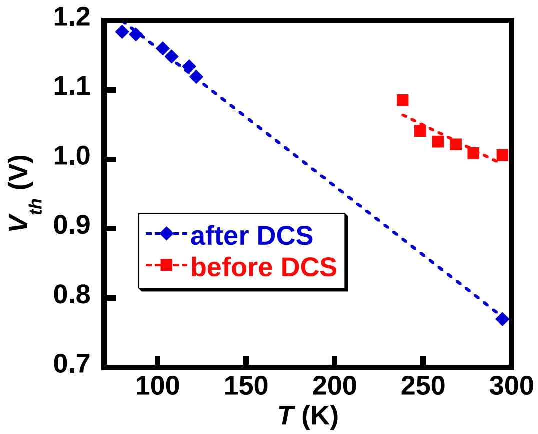

Figure 4-30 Threshold voltage on TA before and after DC stress.

to extract the trap properties responsible for the switching events in each case. Carrier freeze-out statistics and the temperature dependence of all device parameters were taken fully into account. The traps responsible for RTS before DCS are referred as A and B, while the identified trap after DCS is called trap C.

Figure 4-31 depicts the average capture and emission time constants computed using the described technique in section 4.3.2. Trap position of trap C from the Si/SiO_2 interface was calculated using Eq. 4-8 and found to be on the average of 1.83 nm. The stress-induced trap C was found deeper in the oxide than the process-induced trap A, inducing slower switching. This is an unusual result for hot-electron stressing. However, the temperatures where each trap is active are different.

The RTS amplitude after stressing as a function of V_{GS} and temperature are plotted in Figure 4-32. From the measured RTS amplitude, the computed inversion carrier density and mobility, and the relative contributions of mobility and number fluctuations were determined (Figure 4-33). α for trap A is smaller than α for trap C where α for trap B is the largest (Figure 4-34). Therefore, trap B has the highest influence on the fluctuations

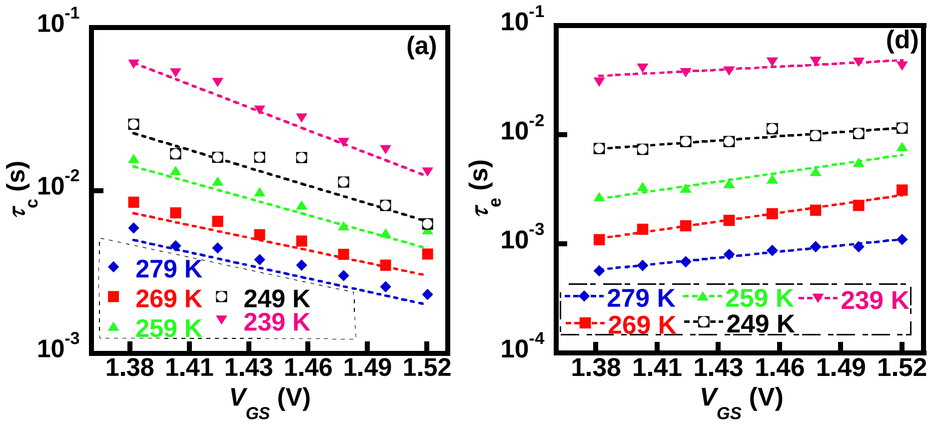

Figure 4-31 (a) Average time associated with empty state of trap C after DCS. (b) Average time associated with filled state of trap C after DCS.

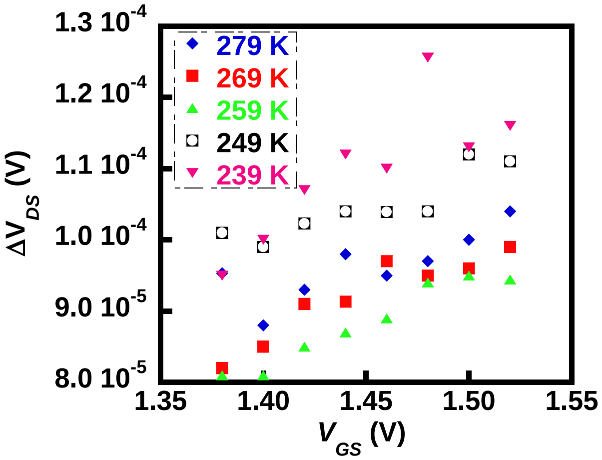

Figure 4-32 RTS amplitude due to trap C after stressing of TA. V_{DS} =0.25 V

compared to traps A and C.

The capture energy, change in the trap enthalpy, change in the trap entropy, and capture cross section prefactor were extracted for traps A, B, and C as shown in the Table 4-4. ΔE_B and ΔH values after stress are three and 13 times larger than the values before stress, respectively (Table 4-5). Based on the extracted relaxation energy, the trap species responsible for RTS before and after DCS were identified to be an unrelaxed neutral oxygen deficiency where trap stability after DCS is more than before DCS.

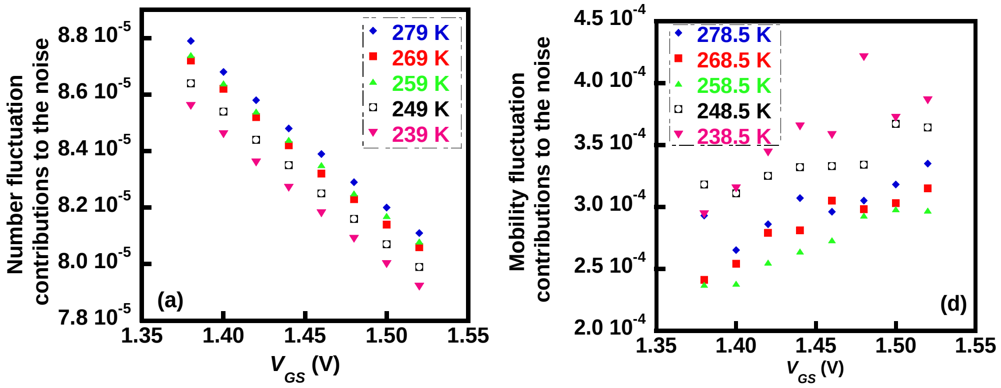

Figure 4-33 (a) Number fluctuations due to trap C after stressing. (b) Mobility fluctuations due to trap C after stressing

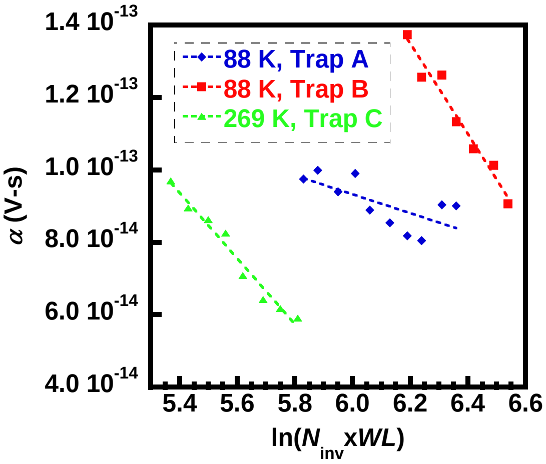

Figure 4-34 Screened scattering coefficients as a function of charge carriers in the inversion layer for trap A, B, and C. Again, trap B causes the largest scattering.

The extracted capture cross-section values as a function of V_{GS} and temperature were evaluated and shown in Figure 4-35. The capture cross-section of the potential well for a neutral center is highly dependent on the temperature and weakly dependent on the V_{GS} (Figure 4-19(d)) [4]. This seems consistent with the data we have in Figure 4-18(a) and Figure 4-35 for before and after DCS. σ did not change much with the increase of V_{GS} while it increased one order of magnitude as the temperature was increased. In contrast, if the trap were a Coulombic attractive center, it should have behaved in the exact opposite manner (Figure 4-19(c)). It is possible that trap A had been annealed after stress due to an electron tunneling from the channel to a neutral center. Putting an extra electron on a neutral Si atom would generate a dipole. The positive and the negative end of the dipole attracted each other. True annealing was then obtained by reforming the bond between the two neighboring Si atoms. If the bond between the two Si atoms was reformed, then the trap configuration might change to a more stable one [104].

Table 4-4 E_R and $E_{Cox}-E_T$ were evaluated at different temperatures where V_{GS} = 1.62 and 1.38 V before and after DCS, respectively.

	Before Stressing		After Stressing			
	Trap A		Trap B	Trap C		
T (K)	E_R (eV)	$E_{Cox}-E_T$ (eV)	$E_{Cox}-E_T$ (eV)	T (K)	E_R (eV)	$E_{Cox}-E_T$ (eV)
122	0.464	3.08		279	1.20	2.80
118	0.461	3.09		269	1.22	2.79
108	0.456	3.09		259	1.24	2.78
103	0.453	3.10		249	1.27	2.85
88	0.444	3.10	2.98	239	1.29	2.86
80	0.439	3.10	3.00			

Table 4-5 ΔE_B, ΔH, $\Delta S/k_B$, and σ_0 were extracted from the measured RTS data before and after stressing as a function of V_{GS} at V_{DS} = 0.25 V. $\Delta S/k_B$ was evaluated at 122 K and 279 K before and after stress, respectively. The rest of the parameters are temperature independent as expected.

Before stressing					After stressing				
V_{GS} (V)	ΔE_B (eV)	ΔH (eV)	$\Delta S/k_B$	σ_0 (cm^2)	V_{GS} (V)	ΔE_B (eV)	ΔH (eV)	$\Delta S/k_B$	σ_0 (cm^2)
1.50	0.103	0.012	3.55	$2.31\text{x}10^{-19}$	1.38	0.394	0.130	11.3	$7.33\text{x}10^{-19}$
1.52	0.108	0.012	3.48	$3.38\text{x}10^{-19}$	1.40	0.396	0.137	11.3	$9.55\text{x}10^{-19}$
1.54	0.106	0.015	3.77	$2.72\text{x}10^{-19}$	1.42	0.388	0.129	10.8	$7.56\text{x}10^{-19}$
1.56	0.102	0.014	3.48	$1.67\text{x}10^{-19}$	1.44	0.366	0.131	9.60	$3.24\text{x}10^{-19}$
1.58	0.099	0.014	3.51	$1.28\text{x}10^{-19}$	1.46	0.373	0.143	11.0	$4.90\text{x}10^{-19}$
1.60	0.099	0.013	3.31	$1.14\text{x}10^{-19}$	1.48	0.341	0.156	11.3	$1.44\text{x}10^{-19}$
1.62	0.095	0.011	2.88	$7.82\text{x}10^{-20}$	1.5	0.338	0.152	11.0	$1.48\text{x}10^{-19}$
1.64	0.091	0.013	3.17	$4.29\text{x}10^{-20}$	1.52	0.286	0.164	11.1	$1.52\text{x}10^{-20}$
1.66	0.092	0.018	3.70	$5.09\text{x}10^{-20}$					
1.68	0.093	0.025	4.31	$5.79\text{x}10^{-20}$					

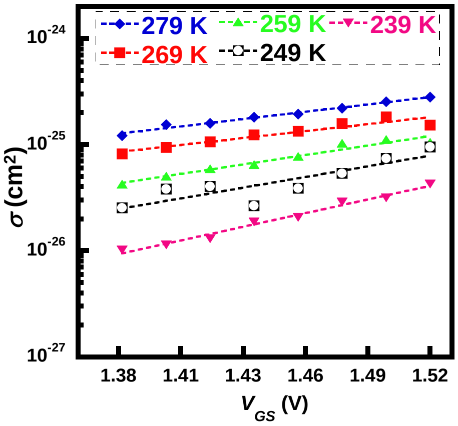

Figure 4-35 Capture cross-section of trap C after stressing.

4.3 RTS Analysis in Frequency Domain

As was discussed in section 1.2.4, the drain-source voltage power spectral density of random telegraph signals can be expressed as [42]:

$$S_{V_{DS}}(f) = \frac{4(\Delta V_{DS})^2}{(\bar{\tau}_c + \bar{\tau}_e)\left[(1/\bar{\tau}_c + 1/\bar{\tau}_e)^2 + (2\pi f)^2\right]}. \tag{1-6}$$

Here, ΔV_{DS} is evaluated using Eq. 4-28. PSD for RTS follows a Lorentzian spectrum where its amplitude is constant up to a corner frequency (f_0). f_0 is evaluated for each trap based on the average time constant for an RTS $(\bar{\tau})$, where $1/\bar{\tau} = 1/\bar{\tau}_c + 1/\bar{\tau}_e$ and $f_0 = 1/(2\pi\bar{\tau})$. The amplitude of the RTS PSD can be then described as:

$$k = \frac{4\bar{\tau}^2 \Delta V_{DS}^2}{(\bar{\tau}_c + \bar{\tau}_e)}. \tag{4-32}$$

The total PSD of all active traps $\left(N_{t_{active}}\right)$ in a particular device is then calculated from the summation of the individual Lorentzian spectrum associated with each active trap [42, 105]:

$$S_{V_{DS}}(f)=\sum_{i=1}^{N_{tactive}}\frac{k_i}{1+\left(f/f_{0i}\right)^2}\,. \qquad (4\text{-}33)$$

The parameters k_i and f_{0i} are the PSD magnitude and corner frequency due to the i^{th} trap, accordingly. Further discussions of Eq. 1-6 will be in Chapter 6.

4.4 Trap Nature and Origin

Oxygen vacancy is one of the different kinds of defects responsible for RTS in MOSFETs [90, 106]. Oxygen vacancy has manifested in several structural configurations due to the variation in local bonding [106]. Each type of oxygen vacancy exhibits a different structural relaxation energy from which the trap species can be identified [91, 106]. Here, we show that electron switching RTS was caused by an unrelaxed neutral oxygen deficiency center (V^0 ODC II) that was transformed into a negatively charged vacancy (V^-). This is the first time V^0 ODC II center was confirmed to be the source of electron switching through RTS.

Unrelaxed neutral oxygen deficiency centers in SiO_2 had been identified as the cause of random telegraph signals in 75% of the investigated devices here. The novelty of this study lies in the fact that four trap characteristics: relaxation energy, trap energy in the SiO_2 band-gap, capture activation energy, and capture cross-section were extracted from the RTS data and used together as identification markers to study the nature and origin of the gate oxide defects. In general, the electrical properties (E_R, ΔE_B, and $E_{Cox}-E_T$) associated with a trap in the gate oxide show a wide range of values. For this reason, some of the electrical properties of several oxide defects were studied and summarized in Table 4-6.

Table 4-6 The electrical properties of some defects in the oxide. The corresponding energy level of different trap states ($^+/0$, $0/^+$, $0/^-$, and $^-/0$) with respect to the SiO_2 conduction band-edge. The first and the second signs denote the charge state of the defect before and after capture of a charge carrier (e^- or h^+), respectively.

Trap species	E_R (eV)	ΔE_B (eV)	$E_{Cox} - E_T$ (eV)	
V^0 ODC II	0.8-2.1 [91] capturing an e^-	0.1-0.5 [90]	0/- 3.3 [102]	
Nitrogen defect		0.9 [107]	2.5-2.87 [108, 109, 110, 111]	
Hydrogen bridge with Si atoms	1.9-3.1 [112] capturing an e^-	1.5 [113]	+/0	3.9-4.1
			0/+	8.1-8.7
			0/-	4.6-5.8
			-/0	7.8-8.1 [114]
E’$_\gamma$	0.3-0.4 [115, 116] capturing a h^+	0.1-.4 [115, 116]	+/0	4.9-5.1 [114]
			0/+	6.6-6.9 [114]
			0/-	-
			-/0	-
E’$_\delta$	0.6-1.6 [117] Capturing a h^+	1.2 [106]	+/0	5.4-7.3 [114]
			0/+	8.5-8.7 [114]
Fluorine		0.5-1.0 [107]	0/+	1.0 [107]

4.5 Summary and Conclusions

Extraction of average time constants associated with each RTS level based on the Poisson statistics was shown. A procedure to determine the capture and emission time constants associated with each trap was described. A methodology to locate the trap in the oxide with respect to the Si/SiO_2 interfaces and along the channel was presented. Some of the electrical properties associated with the traps were extracted from the gate-source and temperature dependence. From the extracted energies associated with the traps, the origin of the three defects was identified to be unrelaxed neutral oxygen deficiency center. However, the origin of the slow trap could not be found due to the narrow temperature range that this trap was active.

Chapter 5 RTS Modeling

5.1 Introduction

Current circuit and device designs are based on worst scenarios resulting in significant waste of wafer real estate. This is due to lack of physics-based statistical device models that can accurately: (1) predict gate dielectric defect levels and all active defects. (2) Compute trapping/detrapping characteristics of traps at time zero and as a function of operational time. (3) Correlate the effect of charge carrier number and mobility fluctuations due to trapping/detrapping. (4) Calculate trap position in the oxide and along the channel. (5) Evaluate the effectiveness of the active trap(s) on the drain-source voltage. Thus, experimental and analytical procedures were developed to lay down the foundations for these statistical models. This is an improvement over the current statistical models for RTS, which are either experimentally-oriented *or* physics-based, but not necessarily both. RTS is statistical in nature and may vary between different devices with the same geometry and technology or different geometries on the same wafer. Therefore, RTS is investigated at a variety of devices and at different operational conditions to obtain sufficient statistical data that can be used to construct meaningful statistical models. Moreover, most of the current RTS statistical models concentrate on the prediction of the noise PSD in frequency domain, but neglect RTS trace [9, 118]. Although, some RTS model were developed to predict the RTS at room temperature but not as a variable of temperatures. This limits the extraction of RTS and trap characteristics to a few parameters such as: RTS amplitude, average capture and emission times, screened scattering coefficient, and capture cross-section [15, 26, 105]. In our model, we incorporated some of the physical properties associated with a trap (ΔE_B , $E_{Cox} - E_T$, and x_t) from which the average capture and emission times are computed. In addition, our newly developed RTS model capable of reconstructing the RTS in time and frequency domains as a function of gate-source voltage, drain-source voltage, and temperature from which several RTS and trap characteristics can be extracted as was earlier discussed in section 4.1.

5.2 Mechanism and Principles

A stand-alone, comprehensive, variable-temperature, single-to-multi-trap scalable RTS model has been developed based on first principles and supported by experimental data. The model is governed by the following principles: (1) non-radiative multiphonon-assisted tunneling is known to be the mechanism for trapping/detrapping of the channel carriers by the oxide traps, leading to the switching events observed as RTS in the drain voltage in a MOSFET [18, 19, 42]. (2) Traps only within a few $k_B T$ of the Fermi energy level are considered electrically active. This helps to identify and quantify the gate oxide traps that are capable of communicating with the channel carriers at each bias point and temperature [18, 42]. (3) The number of traps at a specific device follows a Poisson distribution [2, 13, 15, 119]. (4) The trap density as a function of energy is taken as a U–shaped in energy in the silicon band-gap [20, 21]. (5) Doping concentration along the channel is considered non-uniform, allowing for channel implants for halo doping etc. (6) The effect of linear and saturation regions on the channel carrier distribution and on the RTS is included. (7) A trap is treated as either neutral or charged prior to the capturing, becoming charged or neutral upon capture, respectively [120, 121]. (8) UNMF model is adopted to compute the RTS amplitude [22]. (9) Only one electron can be trapped by an electronic trap in the oxide [42]. (10) Trap can be located at any distance from the Si/SiO$_2$ interface up to T_{ox}. The probability of finding the trap at a location in the oxide was assumed to be exponentially decreasing from the Si/SiO$_2$ interface to the oxide bulk. (11) Temperature dependence of all parameters is considered.

5.3 Developing the Statistical Model

Several RTS statistical models had been developed that can describe charge carrier trapping/de-trapping at the MOS semiconductor/dielectric interface and in the dielectric [1, 15, 26, 40]. Novelty of this newly developed RTS statistical models lies in the fact that it: (1) is based on first principles of charge carrier conduction, (2) is measurement driven, (3) incorporates the effects of selected process variations, (4) takes into account the temperature dependence of all parameters, (5) generates simultaneously a time- and frequency-domain output directly usable by the engineers, (6) is fully scalable from single electron switching to ensemble averaged 1/*f* noise, (7) can be used for n- or p-MOS with different gate oxide materials, (8) and incorporates the electrical parameters of the physical species of the oxide trap.

The parameters of the newly developed statistical model are computed based on the extracted physical properties associated with the identified trap. This relies upon accurate determination of the trap characteristics (ΔE_B, $E_{Cox} - E_T$, x_t, k_1, and k_2) for a particular technology. RTS is a Poisson process governed by the average capture, emission time constants, and RTS amplitude. These parameters are described in terms of the physical device parameters (W, L, T_{ox}, etc.), and bias and temperature conditions. The RTS statistical models were developed in time and frequency domains. In this section, we will show these models respectively.

5.3.1 Time Domain

The capture and emission of a mobile charge is a stochastic processes describable by their average values. The average capture time was computed based on the SRH statistics using Eq. (4-19) where, the average emission time was evaluated according to Eq. (4-20) [42]. $\bar{v}_{th}$, N_c, n, and $m*$ in Eqs. (4-19) and (4-20) were computed as shown in section 4.3.3. From Eqs. (4-7), (4-19), and (4-20), the change in Gibbs free energy is extracted as:

$$\left(\Delta H - T\Delta S\right) = \left(k_B T\right)\left[\ln\left(\frac{g\left(8k_B T/\pi\, m^*(T)\right)^{1/2} N_C(T)}{n(T)\bar{v}_{th}(T)}\frac{\bar{\tau}_e(T)}{\bar{\tau}_c(T)}\right)\right]. \tag{5-1}$$

Equation (5-1) in conjunction with the active capture energy is used to compute the relaxation energy associated with a defect in the oxide. The capture cross-section prefactor in Eq. (4-19) was given by [18], 122]:

$$\sigma_0 = \sqrt{\frac{E_{ij}}{S\hbar\omega_p}}\left(\frac{\pi^2}{2}\right)\left(\frac{\hbar}{2m^*(T)k_B T}\right), \tag{5-2}$$

where, E_{ij} is the electron energy in the *jth* energy sub-band in the *ith* valley of the inversion layer, $S\hbar\omega_p$ is the relaxation energy where, S is the Huang and Rhys parameter corresponding to the number of emitted phonons, $\hbar$ is the reduced Planck constant, and ω_p is the radian frequency of the phonon. E_{ij} is computed as [18]:

$$E_{ij} = \left(\frac{\hbar^2}{2m^*}\right)^{1/3}\left[\frac{3}{2}\pi q F_{Surf}\left(j+\frac{3}{4}\right)\right]^{2/3}. \tag{5-3}$$

Here, F_{Surf} is the effective surface of electric field which is obtained from [61]:

$$F_{Surf} = \frac{qN_A X_d}{\varepsilon_0\varepsilon_{Si}}. \tag{5-4}$$

Here, X_d is length of the space-charge region and is given by [61]:

$$X_d = \sqrt{\frac{2\varepsilon_0\varepsilon_{Si}\psi_s}{qN_A}}. \tag{5-5}$$

N_A is evaluated according to Eq. (4-12) where the temperature dependence is accounted for. E_{10} is typically taken as 0.06 (eV) [122]. The relaxation energy in Eq. (5-2) is evaluated from Eq. (4-27). Capture cross-section as a function of V_{GS} and T of a trap is computed from Eqs. (4-19) and (5-2). The capture cross section prefactor in Eq. (5-2) is not a constant as a function of V_{GS}. Therefore, it is assumed to vary with the change of V_{GS}. However, σ_0 shows no explicit dependence on the V_{GS}.

The newly developed RTS model and its simulation tool evaluate the channel carrier density in the inversion layer from one of the three provided options. First, full CV data of the gate-channel capacitance (C_{GC}) can be uploaded. Second, discrete CV values (C_{GC1}, C_{GC2}, C_{GC3}) of C_{GC} for three points at different regions can be provided (Figure 5-1) from which the full CV curve can be reconstructed as a function of V_{GS}. Third, the gate oxide thickness. Accurate inversion layer carrier density can be computed from either of the first two cases by integrating under the corrected curve (Figure 5-1) divided by q, while

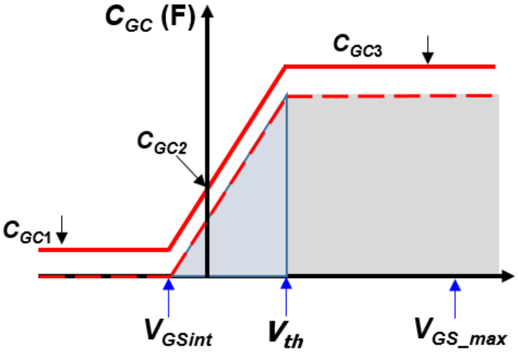

Figure 5-1 The CV curve for the gate-channel capacitance which can be extracted from three regions (in the accumulation (C_{GC1}), at V_{GS}=0 (C_{GC2}), and in the strong inversion (C_{GC3})). The solid line is the gate-channel capacitance as measured. The dashed line is the corrected C_{GC} with overlap capacitance subtracted. Shaded area represents qN_{inv}.

for the last option, N_{inv} is estimated through:

$$N_{inv} = \frac{C_{ox}\left(V_{GS} - V_{th}\right)}{q} = \frac{\varepsilon_o \varepsilon_{ox}\left(V_{GS} - V_{th}\right)}{qT_{ox}}. \quad (5\text{-}6)$$

Here, C_{GC1} is the overlap capacitance, C_{GC2} is the gate-channel capacitance at $V_{GS} = 0$, and C_{GC3} is the gate-channel capacitance in the strong inversion. In Figure 5-1, the overlap capacitance is subtracted from the raw values of the three discreet C_{GC} as: $C_{GC1_{Cor}} = C_{GC1} - C_{GC1}$, $C_{GC2_{Cor}} = C_{GC2} - C_{GC1}$, $C_{GC3_{Cor}} = C_{GC3} - C_{GC1}$ where, $C_{GC1,2,3cor}$ is the corrected C_{GC} values at the three regions as shown in Figure 5-1.

From the IV measurements, V_{th} and g_d are extracted as a function of T and V_{GS}, respectively. From the linear relation of V_{th} vs. temperature, the slope $\left(V_{thTD}\right)$ and the intercept $\left(A_{gD}\right)$ of the fitting equation in Figure 4-30 can be read out. Knowing V_{th} as a function of temperature allowed the extraction of flat band voltage as a function of temperature and is given by [44, 61]:

$$V_{FB} = V_{th} - 2\phi_F + \frac{\sqrt{4q\varepsilon_0 \varepsilon_{Si} p_0 \phi_F}}{C_{ox}}. \quad (5\text{-}7)$$

Here, C_{ox} is the same as $C_{GC3_{Cor}}$. Flat band voltage was used in Eq. (4-7) to evaluate the ratio of the average capture to emission times.

In our model, we assumed g_d is independent of temperature, since the standard deviation of g_d in a wide range of temperatures is less than 3%. Then, average charge carrier mobility in the inversion layer is computed using Eqs. 4-30 and 4-31 for the linear and saturation regions, respectively. After RTS amplitude is calculated using the UNMF model (Eq. (4-28)), the contributions of number $\left(N_{Fcont}\right)$ and mobility $\left(\mu_{Fcont}\right)$ fluctuations to the noise were extracted as (Figure 4-29):

$$N_{Fcont} = \frac{1}{WL}\left(\frac{1}{N_{inv}}\right). \tag{5-8}$$

$$\mu_{Fcont} = \frac{1}{WL}\left(\alpha\bar{\mu}_c\right). \tag{5-9}$$

The effect of remote Coulomb scattering on the channel carrier and number fluctuations are utilized to evaluate the RTS amplitude. The screened scattering coefficient is calculated based on Eq. (4-29) after the total channel carrier concentration in the inversion layer was calculated.

5.3.2 Frequency Domain

Welch's power spectral density (WPSD) method is used to evaluate the corresponding PSD of the measured and generated RTS traces [123]. WPSD method estimates the discrete time signal vector V_{DS}(t) through fast Fourier transform function (FFT). The V_{DS}(t) sequence is multiplied by a Hanning window before the FFT is applied [124]. In addition, the V_{DS}(t) data are divided into 16 sections with 50% overlap. The sampling frequency (F_S) of a measured or generated RTS trace is provided to WPSD function. The implementation of WPSD function along with the extraction of f_0 and PSD amplitude from the fitted PSD data are shown in appendix A.

An example of RTS PSD with a Lorentzian fitting using WPSD model is shown in Figure 1-4. The corner frequency is extracted and displayed on the graph (Figure 1-4). In general, the PSD of two level RTS can be evaluated as a function of frequency using Eq. (1-6), since the average capture, emission times, and RTS amplitude are known. In the case of several active traps, RTS PSD is estimated using the superposition of RTS spectra as depicted in Eq. (4-33). Examples of superposition of RTS spectra are presented in Chapter 6.

5.4 Summary

Mechanism and principles of the newly developed RTS model and its simulation tool were presented and discussed. RTS model is constructed in time and frequency domains based on first principles. In addition, the electrical characteristics associated with trapping defects are defined and explained. A methodology to determine the change in Gibbs free energy due to the capture and emission of an electron from and to the channel was presented. Computing of the channel carrier concentration in the inversion layer from the gate-channel capacitance and the gate oxide thickness was shown.

Chapter 6 RTS Simulation

6.1 Introduction

Several RTS simulation techniques have been developed to predict and reconstruct RTS in time and frequency domains [1, 15, 26,40, 71, 75, 105, 118, 125, 126]. The number of active traps per device and the location of these traps in the oxide and along the channel are statistical events affecting the resultant RTS trace. Although the trap position along the channel has been mostly taken into account, many have assumed the traps to be at the Si/SiO_2 interface [1, 26, 40, 126] or uniformly distributed in the oxide [105, 125]. In this work, we consider an experimentally verified, exponentially decreasing probability distribution in the oxide from the interface for the traps [21].

Random Telegraph Signals Simulation (RTSSIM) tool can reconstruct accurate multi-trap time traces and PSD for variable gate-source voltage (V_{GS}), drain-source voltage (V_{DS}), and temperature (T) in less than 15 minutes. The RTSSIM is capable of producing smooth transition from RTS to 1/f noise. RTSSIM takes into account device scalability. There is no limit to the number of traps simulated. In addition, RTSSIM can be used as means for training those who have no prior experience with RTS. RTSSIM might be linked or integrated with circuit simulator although this has not be done yet.

The RTSSIM was constructed using MATLAB as a platform. RTS phenomenon is a Poisson process governed and controlled by the calculated $\bar{\tau}_c$ and $\bar{\tau}_e$. The RTSSIM computes $\bar{\tau}_c$ and $\bar{\tau}_e$ based on the extracted electrical properties associated with a trap then reconstructs RTS traces from which PSD is evaluated. Based on our experimental data, RTSSIM is set to recognize three different trap species: (1) single acceptor (SA) [93, 103, 120], (2) two dependent acceptors (AA) [13, 103, 127, 128, 129], (3) and single donor (SD) [43, 103, 121].

6.2 Principles

RTSSIM has been constructed based on the aforementioned models and principles which were discussed in chapter 5. RTSSIM computes and reconstructs RTS traces and the corresponding PSD that originates from MOSFET gate-oxide defects, once these defect types are inputted to the program along with some of their electrical properties as it will be discussed latter in this chapter. After $\bar{\tau}_c$ and $\bar{\tau}_e$ are computed, probabilities of the electron transition from one level to others are evaluated. A Poisson process is executed at each interval time which is governed by the average capture, emission time constants, and sampling frequency. Duration time for each Poisson process is tracked and fed into the probability equations after each iteration. Once the probability is computed and the decision is made for the next transition, another Poisson process occurs and time is tracked and fed back into the probability equations. After RTS is generated, all RTS and trap characteristics are extracted from the V_{GS} and temperature dependence.

6.2.1 Computation of the Electron Transitions Probabilities

Once the device and RTS parameters (section 4.3.3, and Eqs. (4-19)-(4-28)) are computed for each temperature and bias point, the switching time trace is constructed (section 6.4.3). The following description pertains to an acceptor trap resulting in two level switching $S1$ and $S2$ ($\tau_1 = \tau_c$, $\tau_2 = \tau_e$). All traps are assumed to be empty at time zero. The accessibility probability of a trap by a channel carrier is computed based on previously calculated $\bar{\tau}_c$, and $\bar{\tau}_e$ (section 5.3.1). If V_{DS} goes from empty to filled trap state, $S1 \rightarrow S2$ or stays for some time at $S2 \rightarrow S2$ (Figure 4-13) and then goes back to $S1$, then a trap is considered to be electrically active. If V_{DS} stays all the time at $S1$, then the trap is assumed to be inactive. The probability of charge transition from the channel to the trap is

$P_{12}(1 \rightarrow 2) = dt/\overline{\tau}_1 = dt/\overline{\tau}_c$. Similarly, the probability of the transition from the trap back to the channel is $P_{21}(2 \rightarrow 1) = dt/\overline{\tau}_2 = dt/\overline{\tau}_e$. Therefore, the probability of a trap to be occupied as a function of time is computed based on the probability of the transition $S1 \rightarrow S2$ [20, 42]:

$$P_{12}\left(t\right) = \frac{\overline{\tau}_2}{\left(\overline{\tau}_1 + \overline{\tau}_2\right)}\left(e^{-\left(1/\overline{\tau}_1 + 1/\overline{\tau}_2\right)t} - 1\right). \tag{6-1}$$

Probability that an electron will remain within the vicinity of the defect site for a period of time is calculated using [20, 42]:

$$P_{22}\left(t\right) = \frac{\overline{\tau}_2}{\left(\overline{\tau}_1 + \overline{\tau}_2\right)} e^{-\left(1/\overline{\tau}_1 + 1/\overline{\tau}_2\right)t} + \frac{\overline{\tau}_1}{\left(\overline{\tau}_1 + \overline{\tau}_2\right)} . \tag{6-2}$$

Complete derivation of Eqs. (6-1) and (6-2) are shown in appendix B.

In a complex RTS, there are two or more active traps at the same time for which the trap occupancy might depend on one another. In this case, the probability of the electron transition from one level to all others is evaluated first to find the highest probability transition e.g. if there is a three level RTS and the V_{DS} signal is at level 2, then the probabilities of electron transition will be evaluated before the next transition is made. Thus, if the transition probability to level 3 is higher than to level 1, then electron transition proceeds to level 3.

6.3 Features of the RTSSIM

In this section, features and operational requirements of RTSSIM are discussed. RTSSIM is equipped with a friendly user interface and an easily understandable manual. RTSSIM was built based on several modules which are known as functions. These functions are connected and linked to each other to run the calculations, produce RTS traces, extract RTS and trap characteristics, and output results to MS Excel files. RTSSIM has the capability to output all generated figures for each active trap at each bias and temperature condition. In addition, RTSSIM transfers all provided parameter values as well as all generated RTS data and the extracted parameters to MS Excel files as it will be shown in the upcoming sections.

6.3.1 Operational Requirements

RTSSIM was constructed using MATLAB as a platform. RTSSIM requires MATLAB R2013 or newer version which includes symbolic variables and functions solver (sym). This function is used to solve several equations that are embedded inside the RTSSIM program. In addition, *Ezyfit* 2.42 toolbox needs to be downloaded in order to enable RTSSIM to fit the Poisson distribution of the set frequencies of time events associated with each RTS level. After *ezyfit* is downloaded, user needs to select (Set Path) which is available in the *home- tab* in MATLAB R2013**.** Moreover, RTSSIM requires MS Excel program (2007 or newer versions) to export all generated RTS data in time and frequency domains. Please see section 6.4.5 about the output results for more information.

6.3.2 User Interface

RTSSIM possesses friendly user interface environment that allows users to input all device, trap characteristics, bias, and temperature conditions in a sequential manner with pop-up windows for different menu and utility. Figure 6-1 is the flow chart diagram of the RTSSIM program. From the flowchart, RTSSIM is divided into three stages:

- User interface.
- Calculations and generation of RTS characteristics and RTS traces, respectively.
- Output results and figures.

Once user provides all device and trap parameters that are necessary to activate RTSSIM (section 6.3.3), the program automatically starts: calculating the new RTS statistical model

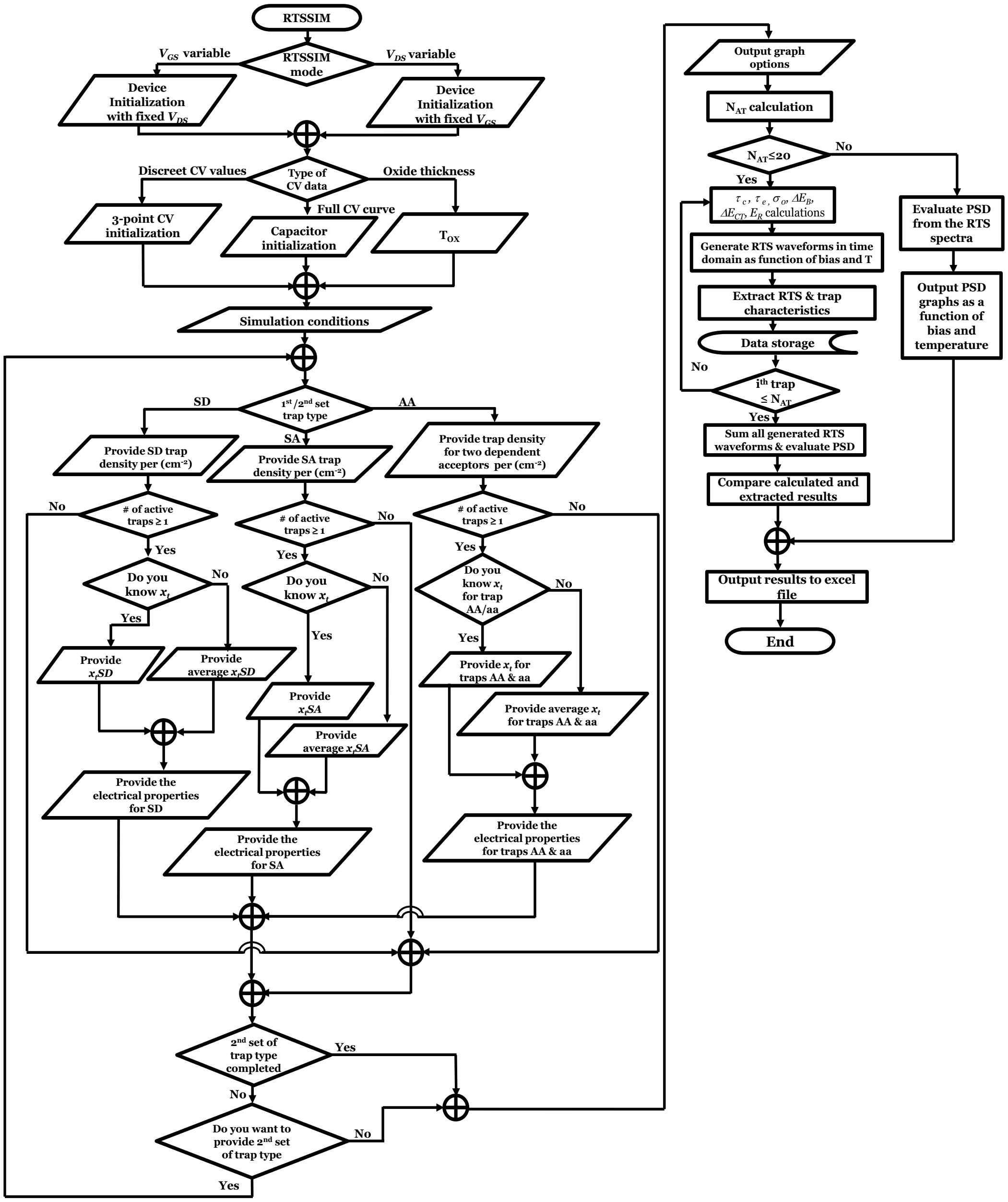

Figure 6-1 RTSSIM flow chart starts with two modes that user can choose. The user needs to initialize the device and provide the prompted trap characteristics to reconstruct the RTS in time and frequency domains. RTS and trap characteristics are extracted from the generated traces. All user-provided and extracted parameters are exported automatically to MS-Excel files for further analysis.

parameters, generating RTS traces in time and frequency domains, and outputting the results. RTSSIM does not disrupt ongoing activities on the computer. However, user can stop the process of simulation by manually interrupting the program using “Ctrl+C” in MATLAB command window.

6.3.3 Parameters Input and Initialization

The aim of RTSSIM is to provide a realistic reconstruction of RTS traces which is based on the extracted physical properties of a trap. Therefore, specific trap parameters need to be provided to the RTSSIM as shown in Table 6-1. From these provided parameters, RTSSIM calculates the rest of the RTS model parameters which leads to the RTS traces and its corresponding PSD. In addition, the provided trap characteristics are extracted again from the simulated RTS waveforms for comparison purposes and evaluation of the predicted trap characteristics. Table 6-1 also shows the parameters needed to initialize the simulated device in order to activate the RTSSIM. Based on the device dimensions and characteristics provided by the user, the MOSFET is initialized and the equilibrium electron n_0 and hole p_0 carrier concentrations are computed for the V_{GS} and V_{DS} bias ranges and the temperature range requested by the user (section 4.3.3). Carrier freeze-out is fully taken into account. The units for the user interface are adopted in terms of convenience, such as µm for lateral dimension of the device, nm for vertical dimensions, and trap position in the oxide etc. Some of the device parameters such as V_{th}, g_d , and doping concentration can be extracted from the IV and CV measurements and then entered into the simulation (sections 3.4, 4.3.6, and 4.3.7). This helps to provide realistic conditions which are similar to those in a real measured device.

Table 6-1 User-provided and calculated RTSSIM parameters.

User Input		Calculated by RTSSIM	
Device	Trap	Device	Trap
Channel L and W (µm)	ΔE_B (eV)	p_0 (cm^{-3})	ΔH (eV)
Halo implanted region length, L_{halo} (µm)	x_t *or* $\bar{x}_t$ (nm)	n_0 (cm^{-3})	$\Delta S/k_B$
Doping concentration N_A or N_D (cm^{-3})	$E_{Cox} - E_T$ (eV)	n (cm^{-3})	$E_T - E_F$ (eV)
Halo doping concentration N_{Ahalo} or N_{Dhalo} (cm^{-3})	k_1 (V-s) & k_2 (V-s)	ψ_s (eV)	ΔE_{CT} (eV)
V_{GS} range (V)		C_{ox} (F/cm^2)	σ_0 (cm^2)
V_{DS} range (V)		N_{inv} (cm^{-2})	E_R (eV)
Temperature range (77-350) (K)		$\bar{\mu}_c$ (cm^2/V s)	$\bar{\tau}_c$ & $\bar{\tau}_e$ (s)
Threshold voltage at room temperature, V_{th} (V)		T_{ox} (nm)	ΔV_{DS} (V)
Slope of threshold voltage vs. temperature, V_{thTD} (V/K)		L_{eff} (µm)	ΔE_B (eV)*
Slope of g_D vs. V_{GS}, A_{gD} (A/V^2)			x_t (nm)*
Intercept of g_D vs. V_{GS}, g_{Dint} (A/V)			$E_{Cox} - E_T$ (eV)*
CV curve or T_{ox}			y_t (µm)
Areal trap density, N_{tA}, N_{tAA}, and/or N_{tD} (cm^{-2})			$N_{tA_{active}}$, $N_{tAA_{active}}$, and $N_{tD_{active}}$

*For verification of the input parameters only.

6.3.4 Output Choices

User has the leverage to control the output of the generated graphs. User can choose to display or suppress the generated graphs by selecting the desired graph(s) from the drop-down menu as shown in Figure 6-2. If there are several active traps at the same time, the contribution of each trap can be outputted or by selecting “Over all output only”, the total RTS and PSD can be outputted (Figure 6-2). RTSSIM generates several graphs

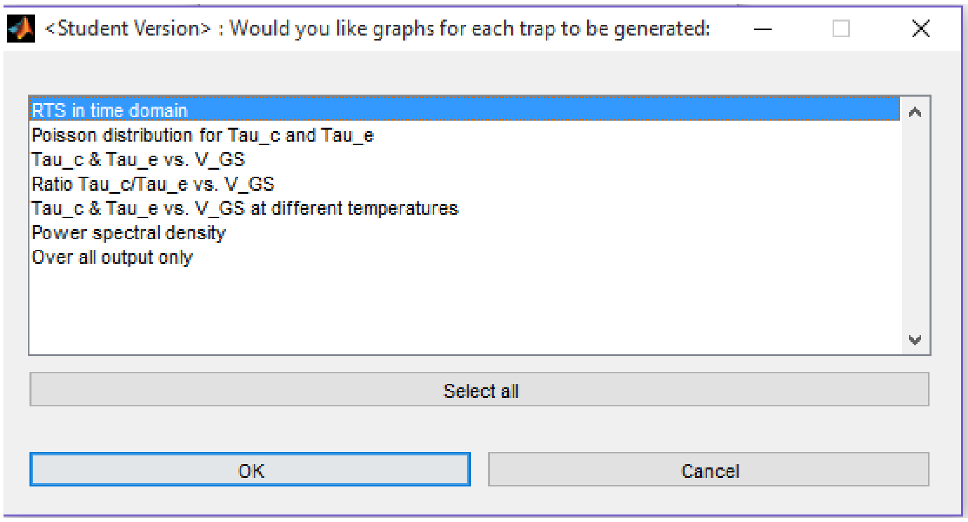

<Student Version> : Would you like graphs for each trap to be generated:

- RTS in time domain
- Poisson distribution for Tau_c and Tau_e
- Tau_c & Tau_e vs. V_GS
- Ratio Tau_c/Tau_e vs. V_GS
- Tau_c & Tau_e vs. V_GS at different temperatures
- Power spectral density
- Over all output only

Figure 6-2 Graph output options where user can choose to output All/Some of the options.

in the same run. Thus, RTSSIM tracks and displays the following marks on each generated graph:

- Title of the graph.
- Simulated trap type whether single acceptor (SA), two dependent acceptors (AA), or single donor (SD).
- Trap set:
  - First set
  - Second set.
- The simulated trap number.
- Simulated gate and/or drain bias conditions.
- Simulated temperature.
- Forward mode (FM) or reveres mode (RM).

When several bias and temperature conditions are set to simulate RTS, the expected number of generated graphs is large. Therefore, user can select the “over all output only” option rather than the individual figures.

All user provided parameters come with default values and an allowed range. In case user provides a value outside of this range, the program terminates and generates error message "*Please check your value and keep it within the range*". Simultaneously, another window pops-up showing the inputted and corrected range values for that provided parameter. For example, if the user has entered 15 µm for the channel length, then an error message will be invoked and the program will terminate, since maximum channel length is set to be 11 µm (Table 6-2). At the same time, the correct range values will be displayed as [0.02 -11] µm. User can change the range of any input by modifying `getrangerror` function parameters. `getrangerror` function is shown in appendix C.

6.4 RTSSIM Procedures

Random telegraph signals simulation starts first with two simulation modes. These simulation modes are: V_{GS} mode which simulates RTS at various V_{GS} while V_{DS} is constant, and V_{DS} mode which keeps V_{GS} constant and varies the V_{DS} between the minimum and maximum bias conditions. User can choose only one simulation mode to be simulated in each run. Thus, user cannot simulate both modes at the same time. From the V_{GS} mode, RTSSIM extracts the RTS and trap characteristics as shown in Table 6-3. On the other hand, V_{DS} mode yields the extraction of a trap position along the channel. Once the simulation mode is selected, the program prompts user to the next user input window to initialize the simulated device. The user-input device and trap parameters are shown in Table 6-1. User needs to know some information about the simulated device such as:

- ➢ Length and width of the channel which are the nominal values. RTSSIM calculates the effective channel length from the nominal value and the CV data (Eq. (3-2))

Table 6-2 Ranges of minimum-maximum of each user-provided parameter.

User Input		
Parameter	Min. Value	Max. value
Channel length, L (µm)	0.02	11.00
Channel width, W (µm)	0.10	11.00
Halo doping concentration, N_{Ahalo} (cm^{-3})	0	1x10^{20}
Halo implanted region length, L_{halo} (µm)	0.00	5x10^{-3}
Sub channel doping concentration, N_{sub} (cm^{-3})	1x10^{15}	9x10^{19}
Threshold voltage at room temperature, V_{th} (V)	0.10	1.50
Slope of threshold voltage vs. temperature, V_{thTD} (V/K)	-0.09	-1x10^{-4}
Slope of g_D vs. V_{GS}, A_{gD} (A/V^2)	1x10^{-7}	9x10^{-1}
Intercept of g_D vs. V_{GS}, g_{Dint} (A/V)	-9x10^{-3}	-1x10^{-6}
Length of the MOS capacitor, L_{cap} (µm)	0.10	10.00
Width of the MOS capacitor, W_{cap} (µm)	1.00	60.00
Number of fingers per device, N_{fdev}	1.00	300.00
Number of devices, N_{dev}	1.00	20.00
Overlap gate-channel capacitance, C_{GCov} (F)	0.00	1x10^{-11}
Gate-channel capacitance at V_{GS} =0, C_{GC0} (F)	1x10^{-13}	1x10^{-10}
Gate-channel capacitance in the inversion region, C_{GCinv} (F)	1x10^{-13}	1x10^{-8}
Oxide thickness, T_{ox} (nm)	3.00	200.00
Minimum V_{GS}, $V_{GS\,min}$ (V)	0.15	5.00
Maximum V_{GS}, $V_{GS\,max}$ (V	0.15	10.00
Minimum V_{DS}, $V_{DS\,min}$ (V)	0.15	5.00
Maximum V_{DS}, $V_{DS\,max}$ (V)	0.15	10.00
Number of V_{GS} points, V_{GSinc}	1.00	10.00
Minimum temperature, T_{min} (K)	77.00	350.00
Maximum temperature, T_{max} (K)	77.00	350.00
Number of temperature points, T_{inc}	1.00	10.00
Areal trap density for SA, AA, SD are N_{tSA}, N_{tAA}, and N_{tSD} (cm^{-2}), respectively.	1x10^{3}	1x10^{15}
Capture activation energy, ΔE_B (eV)	0.001	1.50
Energy difference between conduction band edge of the SiO$_2$ and trap, $E_{Cox}-E_T$ (eV)	2.00	4.00
Remote Coulomb scattering constant, k_1 (V-s)	1x10^{-14}	1x10^{-10}
Remote Coulomb scattering constant, k_2 (V-s)	-1x10^{-10}	-1x10^{-15}
Trap position from the Si/SiO$_2$ interface, x_t (nm)	0.20	T_{ox}
Average trap position from the Si/SiO$_2$ interface, x_{tAvg} (nm)	0.20	T_{ox}

Table 6-3 RTS and Trap characteristics are extracted from V_{GS} and V_{DS} modes.

Extracted parameters from V_{GS} mode	Extracted parameters from V_{DS} mode
ΔH (eV)	Maximum and minimum of $\bar{\tau}_c/\bar{\tau}_e$ in forward and reverse mode
$\Delta S/k_B$	V_{DS} values where maximum and minimum $\bar{\tau}_c/\bar{\tau}_e$ is observed
$E_{Cox} - E_T$ (eV)	y_t (µm)
ΔE_{CT} (eV)	
σ_0 (cm^2)	
E_R (eV)	
$\bar{\tau}_c$ & $\bar{\tau}_e$ (s)	
ΔV_{DS} (V)	
ΔE_B (eV)	
x_t (nm)	

(if user provides the CV curve or three discrete values of C_{GC} (5.3.1)).

- Length of a halo implanted region. This does not always exist in all devices, it depends on the size of a MOSFET. If there is no halo implant, 0 is entered.
- If there is a halo implantation in a device, user needs to provide the doping concentration for this region (either *p*- or *n*- type dopant).
- Background doping concentration needs to be provided whether for acceptor (N_A) or donor (N_D).
- RTSSIM takes into account the non-uniformity of doping concentration along the channel. Doping concentration along the channel is divided into three regions (Figure 6-3):
  - ☐ A: Halo implant near the source.
  - ☐ B: Sub channel.
  - ☐ C: Halo implant near the drain.

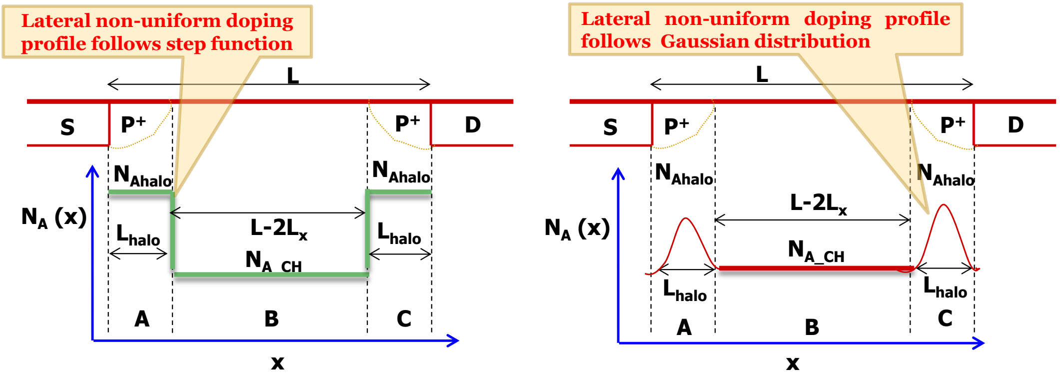

Figure 6-3 Non uniform-doping concentration along the channel.

RTSSIM takes the lateral non–uniform of doping profile along the channel as a step function. As the channel length becomes shorter, lateral non-uniform doping causes the threshold voltage to increase. RTSSIM computes the average effective doping concentration along the channel $\left(N_{Aavg_{eff}}\right)$ as [37]:

$$N_{Aavg_{eff}} = \frac{N_{A_{sub}}\left(L-2L_{halo}\right)+N_{A_{halo}}\left(2L_{halo}\right)}{L}. \tag{6-3}$$

- Threshold voltage information as a function of temperature needs to be provided (Figure 4-30).
- The V_{GS} dependence of the channel output conductance (A_{gD}) needs to be provided. The intercept of the channel output conductance versus V_{GS} ($g_{D\text{int}}$) also is one of the provided parameters. From A_{gD} and $g_{D\text{int}}$, the output conductance can be reconstructed as a function of V_{GS} from which the average mobility of the channel carriers is evaluated (Eqs.(4-30) or (4-31)).

6.4.1 Variation of Bias and Temperature Conditions

RTSSIM generates the RTS traces in time domain as a function of gate–source voltage, drain-source voltage, and temperature from which the trap characteristics are extracted. Typically, RTS is observed at certain V_{GS} and T ranges (Table 4-2*).* Therefore, V_{GS} range can be selected from the strong inversion up to the rated voltage of a device at a wide range of temperatures. User can run the RTSSIM for only one V_{GS} and T by providing the V_{GS} and temperature increments (V_{GSinc} and T_{inc}) to be 1. However, the extracted RTS and trap characteristics will be invalid because number of variable V_{GS} and temperature are insufficient to extract the dependences. Therefore, user can choose number of variable of V_{GS} and T to be at least 3 at wide ranges of bias and temperature conditions.

When V_{DS} dependence is selected from the simulation mode options, the interface window of the simulation conditions allows user to vary the V_{DS} instead of V_{GS}. This mode yields the generation of RTS traces as a function of V_{DS} in the forward and reverse mode from which the trap location along the channel is extracted using Eq. (4-18).

6.4.2 Simulation of Different Trap Types

The effect of the trap type (attractive or repulsive) on RTS has been neglected in simulations. Here we consider both attractive (positively charged when empty and neutral when full, donor) and repulsive trapping centers (neutral when empty and negatively charged when full, acceptor) for electrons in NMOS. When the trap type window pops-up, user can choose one trap type from the drop list menu to be simulated. The trap type interface window pops–up twice during user interface stage. RTSSIM is designed to handle a complex RTS. Thus, combination of two different or similar species is essential to produce complex RTS traces. AA choice would lead to three-level RTS but not necessarily

Table 6-4 Trap type options that user can choose for RTSSIM.

First choice options	Second choice options	Permutation of two trap species
SA1	SA2	SA1 and SA2
AA1	AA2	SA1 and AA2
SD1	SD2	SA1 and SD2
Null	Null	AA1 and SA2
		AA1 and AA2
		AA1 and SD2
		SD1 and SA2
		SD1 and AA2
		SD1 and SD2

to a complex RTS. User can choose a single species or one of the 9 permutations of the two trap species as shown in Table 6-4 to simulate RTS.

RTSSIM statistically calculates the number of active traps in a device, based on trap density and device area. There is no limit to the number of traps simulated. Areal trap density for each simulated trap type is provided to the RTSSIM. Areal trap density is identified from the experimental data. The average number of active traps for a selected species such as single acceptor $\left(A_{ntSA}\right)$ is calculated as:

$$A_{ntSA} = N_{tSA}WL \,. \tag{6-4}$$

Here, N_{tSA} is the areal trap density of a single acceptor. Equation (6-4) is also used to calculate the average number of traps in a device for two dependent acceptors $\left(A_{ntAA}\right)$ and single donor $\left(A_{ntSD}\right)$. However, N_{tSA} would be replaced by N_{tAA}, and N_{tSD}, respectively. The average number of traps in a simulated device goes through a statistical process from which number of active traps is computed. Number of active traps in a specific device follows Poisson distribution [2, 13,16, 119]. Thus, number of active traps in a device for a single acceptor species $\left(N_{tA_{active}}\right)$ is computed as:

$$N_{tA_{active}} = poissrnd\left(A_{ntSA}\right). \tag{6-5}$$

Again, number of active traps in a device for two dependent acceptor traps $\left(N_{tAA_{active}}\right)$ and single donor $\left(N_{tD_{active}}\right)$ can be evaluated using Eq. (6-5).

As soon as the actual active trap number is generated, trap position interface window pops-up. User has the options to provide either the trap position $\left(x_t\right)$ for each trap species *or* the average trap position $\left(\overline{x}_t\right)$ for a trap species. If user chooses to provide $\overline{x}_t$, then a trap position for each species can be assigned based on an exponential decreasing distribution from the Si/SiO$_2$ interface to the oxide bulk [21]. It is known from the 1/f noise statistics that trap density decreases exponentially from the Si/SO$_2$ interface to the oxide bulk [21]. Thus, the probability of a trap position in the oxide $\left(p_{x_t}\right)$ can be expressed as:

$$p_{x_t}\left(x\right) = a_0 e^{-bx}. \tag{6-6}$$

Here, a_0 and b are constants. Assuming $T_{ox} \to \infty$, then integration of Eq. (6-6) from 0 to ∞ is 1. Thus,

$$\int_0^\infty a_0 e^{-bx} dx = 1 \to a_0 = b. \tag{6-7}$$

The ensemble average of x_t can be calculated as:

$$\overline{x}_t = \int_0^\infty x p_{x_t}\left(x\right) dx = \frac{-\left[e^{-bx}\left(a_0 x + 1\right)\right]_0^\infty}{a_0} = \frac{1}{a_0}. \tag{6-8}$$

Hence, the probability of a trap position can be expressed in term of average trap position as:

$$p_{x_t}\left(x\right)=\frac{1}{\overline{x}_t}e^{-x/\overline{x}_t}\ . \tag{6-9}$$

RTSSIM generates trap position from $\overline{x}_t$ as:

$$x_{tSA}=\exp rnd\left(\overline{x}_{tSA}\right). \tag{6-10}$$

Here, x_{tSA} and $\overline{x}_{tSA}$ are the position and average position for a single acceptor species, respectively. Equation (6-10) is used to compute the trap position for AA $\left(x_{tAA}\right)$ and SD $\left(x_{tSD}\right)$ from the average trap position $\left(\overline{x}_{tAA}\right)$ and $\left(\overline{x}_{tSD}\right)$, respectively. The provided average trap position cannot exceed oxide thickness. Therefore, RTSSIM limits the generated trap position for each individual active trap by the oxide thickness.

The electrical properties (ΔE_B, $E_{Cox}-E_T$, x_t, k_1, and k_2) do not change for the same kind of species e.g. if there are three active SA species, then RTSSIM utilizes one time entry of the inputted electrical properties. Form the experimental data, capture activation energy and $\left(E_{Cox}-E_T\right)$ do not change with the change of V_{GS} [42], meanwhile they are temperature independent. RTSSIM takes into account the effect of number and mobility fluctuations on the V_{DS} signal according to UNMF model. RTSSIM computes the RTS amplitude from the provided screened scattering coefficients k_1 and k_2 (Eqs. (4-28) and (4.29)). In the case of AA species, RTSSIM allows the provided electrical properties for each dependent trap to be sequentially entered.

6.4.3 Generating RTS Traces

RTSSIM is activated by providing certain parameters at the level of device and trap as shown in Table 6-1. The provided $\left(E_{Cox}-E_T\right)$ and x_t are utilized to evaluate Eq. (4-7). If x_t is unknown, the average trap position can be provided from which x_t is evaluated using Eq. (6-10). The position of the trap along the channel (y_t) is randomly chosen with equal probability. After $\ln(\bar{\tau}_c/\bar{\tau}_e)$ is evaluated, $(\Delta H - T\Delta S)$ is calculated using Eq. (5-1). Providing ΔE_B leads to the evaluation of the relaxation energy as expressed in Eq. (4-27) where in turn the relaxation energy is used to compute the capture cross section prefactor (Eq. 5-2). ΔE_B from the experimental results does not show distinguishable change with the increase of V_{GS} [42, 105]. Thus, it is assumed to remain constant and is temperature independent.

$\bar{\tau}_c$, $\bar{\tau}_e$, and ΔV_{DS} are considered to be the foundation of the newly developed RTS model and its simulation tool. Having ΔE_B as one of the user-provided parameter allows RTSSIM to calculate $\bar{\tau}_c$ through Eqs. (4-19) and (5-2) (section 5.3.1). Then ΔE_B and $(\Delta H - T\Delta S)$ are used to evaluate $\bar{\tau}_e$ as described in Eq. (4-20) (section 5.3.1). RTSSIM evaluates the channel carrier density in the inversion layer from one of the three provided options as discussed and shown in section 5.3.1. Number of active traps in a simulated device is calculated using Eq. (6-5). Number of active traps is proportional to the *WL* of a MOSFET channel. Number of active traps reflects on the generated RTS and its power spectral density. RTS PSD might be closer to $1/f$ noise, if there is a large number of active traps in the simulated device.

RTSSIM generates RTS samples using Poisson statistics in time domain for each active trap. RTSSIM generates a sequence of samples for each interval of time by updating the value of the current random variable with a new sample generated number. The random variable is generated based on: the ceiling function, uniformly distributed pseudorandom numbers $(rand)$, average capture *or* emission times, and sampling

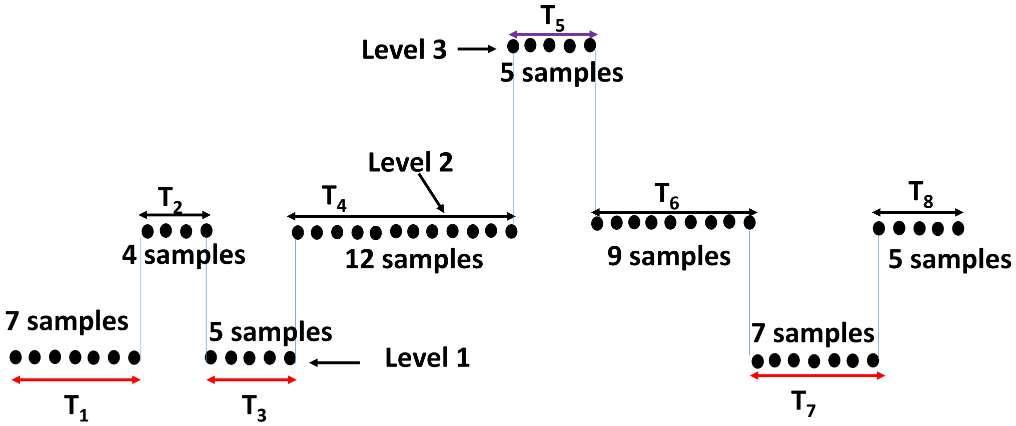

Figure 6-4 An example of generated RTS sample using Poisson process which occurred between interval one (T_1) to interval 8 (T_8). The duration time for each interval was tracked and fed back to the probability equations. If signal is at level 2, the probability of electron transition is evaluated first before next transition is made. The highest probability determines the direction of the next transition.

frequency (F_S) as expressed [130]:

$$ceil\left(-\log\left(rand\right)\overline{\tau}_{c,e}F_s\right). \tag{6-11}$$

Here, the sampling frequency is set to be three times larger than the reciprocal average time $\left(F_S = 3\left(1/\overline{\tau}_c + 1/\overline{\tau}_e\right)\right)$ to ensure all transitions are captured. From Figure 6-4, Poisson process generated 7 samples at T_1 and 4 samples at T_2 etc. The duration time for each interval is: $number\ of\ samples/F_S$. After the RTS trace was generated, the time events distribution with Poisson fitting (Eq. (4-1)) was utilized to compute the average time associated with each level. Again, the processes of generating RTS samples in level 2 and level 3 were repeated. In appendix C, the complete code for generating two level RTS trace (`get1LARTS`) is shown.

6.4.4 Extraction of RTS and Trap Properties from the Simulated RTS Data

To our knowledge, RTSSIM is the first simulation that incorporates the electrical properties of the identified trap in order to reconstruct RTS traces and its PSD as a function of V_{GS}, and temperature from which the trap characteristics are extracted. RTSSIM extracts the average capture and emission times for each generated RTS traces using Eq (4-1) (if number of active traps in a simulated device is <20). Once the average capture and emission times are populated in matrices as a function of V_{GS} and T, trap characteristics are extracted using the same procedures that were discussed in chapter 4. RTSSIM evaluates the RTS amplitude for each bias and temperature conditions according to the UNMF model using Eqs. (4-9), (4-28), and (4-29).

If number of active traps in a simulated device is less than 20, trap position in the oxide as a function of temperature is extracted using Eq. (4-8). Capture activation energy and capture cross-section prefactor are read out from the Arrhenius plots of capture cross-section (Eq. 4-21). Emission energy and change in trap entropy are extracted from the Arrhenius plots of the normalized average emission times (Eq. 4-20). Then the relaxation energy and $E_{Cox} - E_T$ are calculated using Eqs. (4-27) and (4-7), respectively. In addition, the corner frequency of a Lorentzian spectrum is evaluated for each RTS traces as: $1/\bar{\tau} = 1/\bar{\tau}_c + 1/\bar{\tau}_e$ where $f_0 = 1/(2\pi\bar{\tau})$. Welch's PSD density is utilized to evaluate the RTS PSD for each generated RTS traces and the overall of PSD due to the resultant RTS [123].

6.4.5 Output results

RTSSIM is designed to handle high volume of data. It is capable of transferring all generated RTS and its PSD data to MS Excel files. This allows the user to conduct further analyses of the generated data and results. RTSSIM generates the following MS Excel files upon completion of the simulation:

- **RTSresult.xls** contains the RTS and trap properties that have been extracted from the simulated RTS data. In this file, the workbook is divided into several sheets such as:
  - User-provided parameter.
  - Random generator output.
  - Calculated and extracted RTS and trap characteristics. This sheet is labeled as depicted in Figure 6-5 which includes the following information:

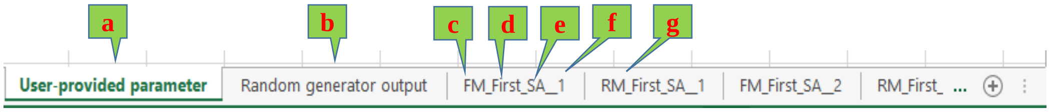

Figure 6-5 (a) User provided parameter sheet. (b) Random generator output sheet. (c) The simulation is taken in forward mode. (d) Calculated and extracted RTS and trap characteristics are resulted from the first set option where the trap is a single acceptor (e). (f) The simulated trap number is 1. (g) The extracted RTS results in the reverse mode. The expected parameters in each sheet are shown in Tables 6-5 and 6-6.

    - Simulation mode (forward (FM) or reverse (RM)).
    - Trap set option order (First or Second).
    - Trap type (SA, AA, or SD).
    - The simulated trap number.

The expected parameters in the user provided parameter sheet, random generator output sheet, calculated and extracted RTS and trap characteristics sheet are shown in Table 6-5, and Table 6-6, respectively.

- **OutputRTSData.xls** includes the generated RTS data in time domain for each bias, temperature, and active trap.
- **OutputPSD.xls** includes PSD data for each bias, temperature, and active Trap.
- **OverAllOutputRTSData.xls** contains the resultant RTS data due to all active traps

Table 6-5 The expected parameters in the user-provided parameter and random generator output (MS Excel sheets).

The expected parameters in the user-provided parameter sheet	The expected parameters in the random generator output sheet
Channel L and W (µm)	Number of active traps
Halo implanted region length, L_{halo} (µm)	generated x_t (nm) and y_t (µm) for each active trap
Doping concentration N_A or N_D (cm^{-3})	
Halo doping concentration N_{Ahalo} or N_{Dhalo} (cm^{-3})	
V_{GS} range (V)	
V_{DS} range (V)	
Temperature range (K)	
Threshold voltage at room temperature, V_{th} (V)	
Slope of threshold voltage vs. temperature, V_{thTD} (V/K)	
Slope of g_D vs. V_{GS}, A_{gD} (A/V^2)	
Intercept of g_D vs. V_{GS}, $g_{D\text{int}}$ (A/V)	
MOS capacitor information and 3-point CV discrete values	
Areal trap density (cm^{-2})	
ΔE_B (eV)	
$E_{Cox} - E_T$ (eV)	
T_{ox} (nm)	
k_1 and k_2 (V-s)	

Table 6-6 The expected parameters in the calculated and extracted (MS Excel sheet).

Parameter	Versus V_{GS}	Versus temperature
$\bar{\tau}_c$ & $\bar{\tau}_e$ (s)	✓	✓
ΔE_B (eV)	✓	
$\Delta S/k_B$	✓	✓
$E_{Cox} - E_T$ (eV)	✓	✓
σ_0 (cm^2)	✓	
E_R (eV)	✓	✓
ΔV_{DS} (V)	✓	✓
f_0 (Hz)	✓	✓
x_t (nm)		✓

for each bias and temperature conditions.

- **OverAllOutputPSDData.xls** encompasses the corresponding PSD data for the resultant RTS for each bias and temperature conditions.

6.4.6 Evaluation RTS PSD

Welch's power spectral density method is used to calculate the corresponding PSD for the generated RTS traces (section 5.3.2). In the case of 20 or more active traps, RTSSIM proceeds automatically to $1/f$ noise mode without generating RTS time traces. RTSSIM evaluates the total PSD for 20 or more active traps in a specific device based on the summation of the RTS Lorentzian spectra using Eq. (4-33). In this case, the average capture and emission times are evaluated as [42]:

$$\overline{\tau}_c = 10^p \left(1 + e^{-((E_T - E_F)/k_B T)}\right). \tag{6-12}$$

$$\overline{\tau}_e = 10^p \left(1 + e^{((E_T - E_F)/k_B T)}\right). \tag{6-13}$$

Here, p is a random number with a range between -5 and 1. This range is set based on the experimental data for different technologies. In addition, p can be related to $\overline{\tau}$ as: $p = \log(\overline{\tau})$. According to Kirton *et al.* [42], $\overline{\tau}$ of RTS can be chosen from a uniform distribution on logarithmic time scale. Thus, p is randomized with equal probability between lower (a_{ll}) and upper (a_{lu}) limit of average tunneling time interval as depicted in this relation:

$$p = \left(a_{ll} + rand\left(1, N_{t_{active}}\right)\left(a_{lu} - a_{ll}\right)\right), \tag{6-14}$$

where, $N_{t_{active}}$ is the number of the total active traps in a simulated device. $(E_T - E_F)$ also is randomized with equal probability between ±3 eV values. This ensures that only the traps existing within $\pm 3k_BT$ of the Fermi energy level are simulated. Therefore, $(E_T - E_F)$ is randomized as:

$$(E_T - E_F) = \left(-2 + rand\left(1, N_{t_{active}}\right)(4)\right), \tag{6-15}$$

The total PSD due to all active traps in a specific device is then calculated by adding the individual RTS spectrum associated with each active trap [42, 105]: Again, the RTS amplitude in Eq. 4-32 reflects on the PSD amplitude which is calculated from the first principles using Eqs. (4-9), (4-28), and (4-29).

6.5 Validation of RTSSIM

In this section, we are comparing simulated RTS data to measured RTS data taken on three nMOS transistors (TA, TB, and TC) at different ranges of V_{GS} and T with different dimensions and oxide thickness($WxL \leq 0.55$) µm^2. Measured RTS data on TA and TB were shown in Chapter 4. In TC, two level RTS was seen at the temperature range of 154-195 K for V_{GS} = 1.36-1.50 V and V_{DS} = 0.20 V. A sample window of measured two-level RTS waveforms in TB is shown in Figure 6-6. Following the same procedure in sections 4.3.1 and 4.3.2, the average time constants associated with each RTS level were extracted from the measured RTS data. Figure 6-7 depicts the computed average capture and emission times associated with each active trap as a function of V_{GS} and T for three transistors. In addition, RTS amplitude was extracted from the difference between the corresponding ΔV_{DS} of the two peaks of the RTS Gaussian-distribution as shown in Figure 6-6(b). The values of the RTS amplitude are displayed in Figure 6-8 for TC.

Experimental, simulated RTS and trap characteristics were compared to verify the newly develop RTS statistical model and its simulation tool. The values of the user provided

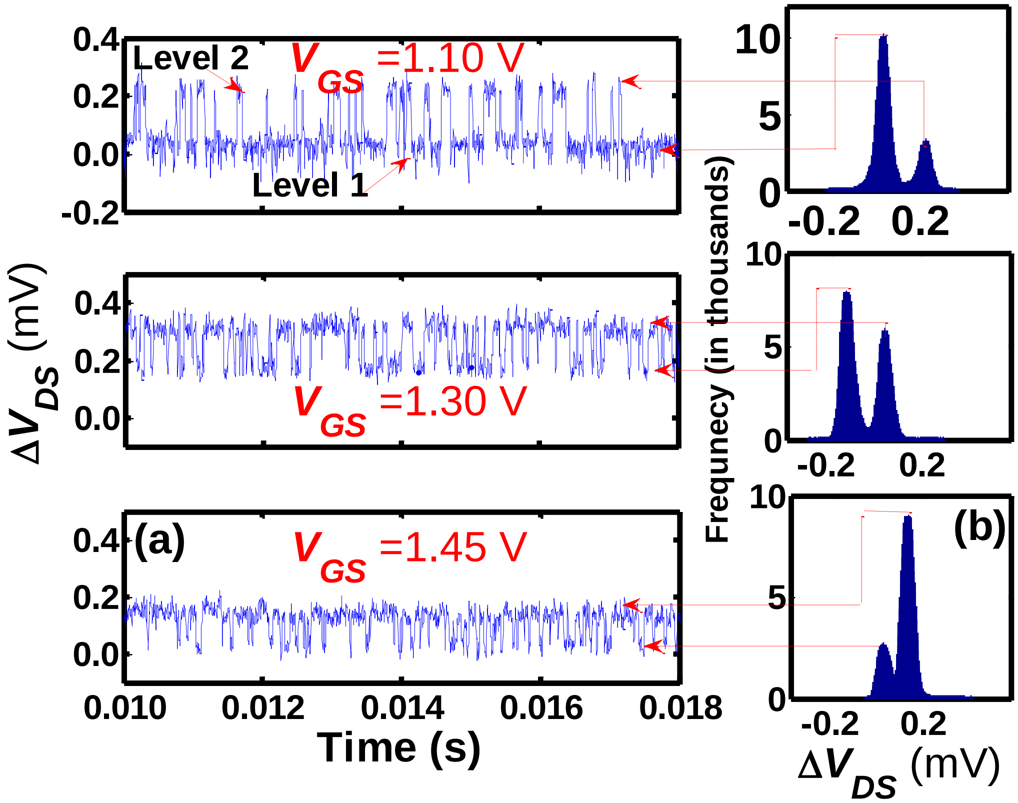

Figure 6-6 (a) A small two-level RTS time trace (b) RTS histogram amplitude. RTS was measured on TB. V_{DS} = 0.30 V. T = 283 K.

parameters at the level of trap are listed in Table 6-7 for TA, TB, and TC. Then RTSSIM calculates the rest of the RTS model parameters. The areas of the three simulated nMOSFETs were ≤ 0.55 µm^2. The extracted ΔE_B, ΔS, and ΔH from the measured and simulated RTS data for TB and TC are shown in Table 6-9. Table 6-8 shows the normalized values of x_t thus obtained from the measured RTS data, with respect to Si/SiO$_2$ interface as a function of T for both traps in TB and TC. The variation with respect to T represents a 10 %, and 9% error in extracting the trap location in TB and TC, respectively.

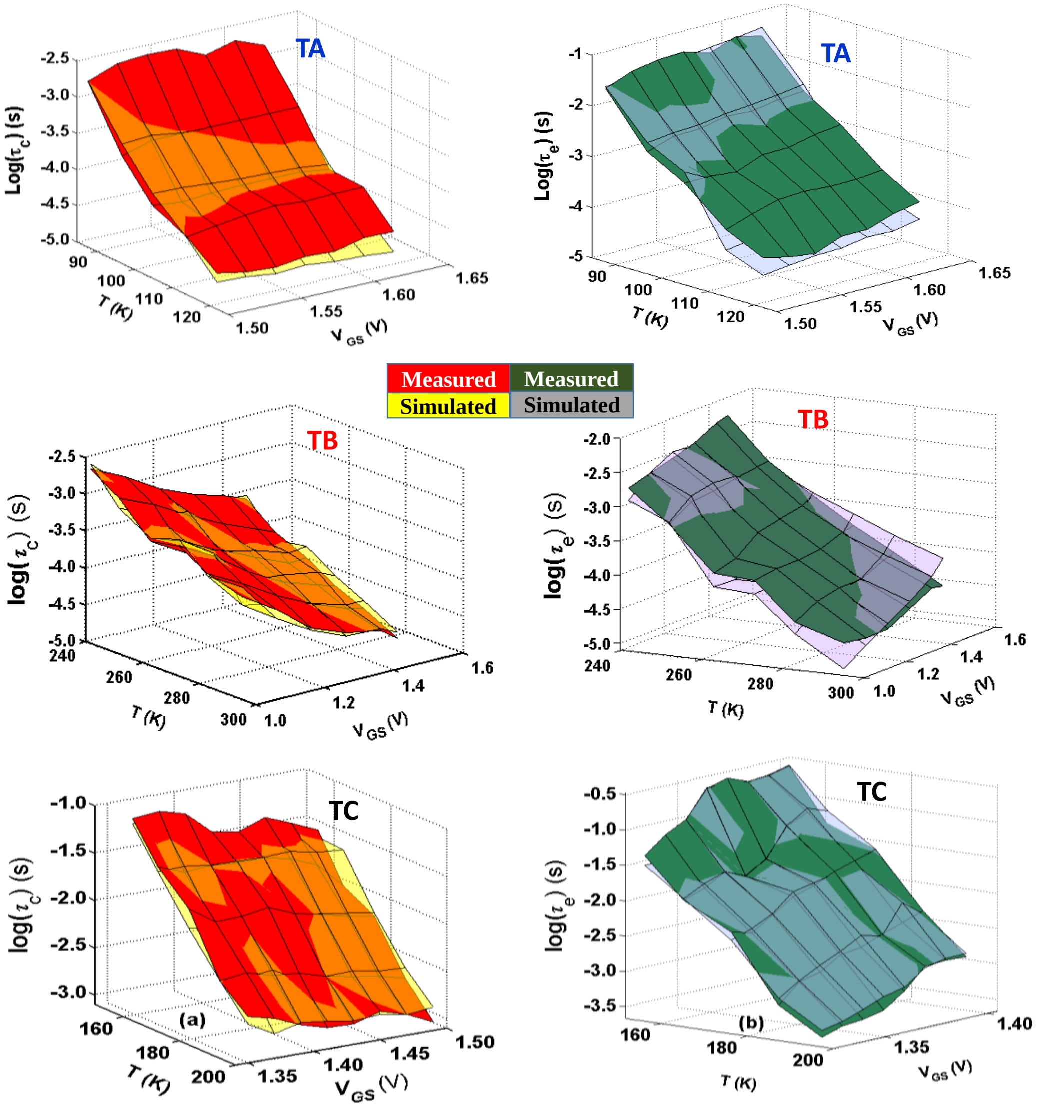

Figure 6-7 Measured and simulated mean capture (a) and emission (b) times for nMOS devices TA, TB, and TC. V_{DS} = 0.25, 0.30, and 0.20 V, for TA, TB, and TC, respectively.

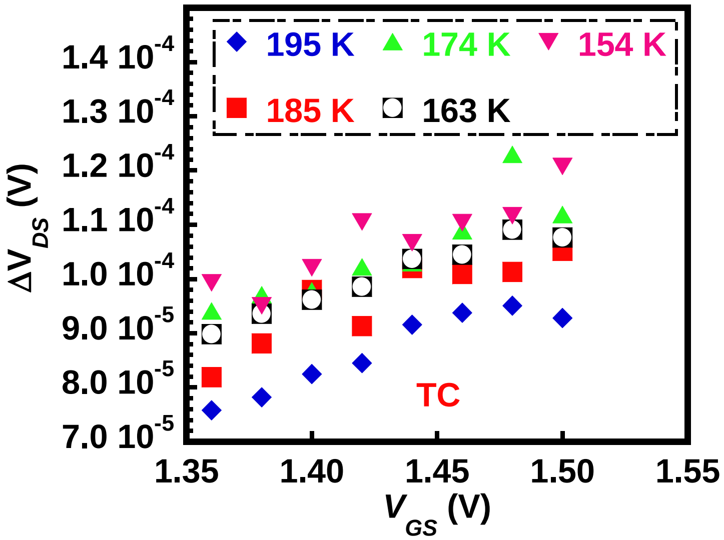

Figure 6-8 RTS amplitude extracted from the measured RTS data for TC. V_{DS} = 0.20 V.

Table 6-7 Simulation conditions and user–provided parameters for three nMOS devices.

Device	V_{GS} (V)	V_{DS} (V)	T (K)	ΔE_B (eV)	$E_{Cox} - E_T$ (eV)	x_t / T_{ox}	k_1 (V-s)	k_2 (V-s)
TA	1.50-1.62	0.25	88-122	0.240	3.10	0.061	$1.58\text{x}10^{-12}$	$-1.57\text{x}10^{-13}$
TB	1.00-1.45	0.30	242-295	0.308	3.00	0.134	$6.88\text{x}10^{-13}$	$-7.86\text{x}10^{-14}$
TC	1.36-1.50	0.20	154-195	0.234	2.87	0.310	$3.56\text{x}10^{-12}$	$-1.20\text{x}10^{-13}$

Table 6-8 The normalized values of the trap position in the oxide with respect to the Si/SiO$_2$ interface in TB and TC. Average provided x_t/T_{ox} to the RTSSIM were 0.134, and 0.310 for TB and TC, respectively.

	TB		TC		
T (K)	Measured x_t/T_{ox}	Simulated x_t/T_{ox}	*T* (K)	Measured x_t/T_{ox}	Simulated x_t/T_{ox}
295	0.150	0.166	195.0	0.354	0.342
283	0.146	0.181	185.0	0.351	0.335
273	0.127	0.151	174.0	0.335	0.295
263	0.123	0.146	163.0	0.312	0.280
252	0.116	0.139	154.0	0.297	0.293
242	0.124	0.140			

Table 6-9 ΔE_B, $\Delta S/k_B$, and ΔH extracted from the measured and simulated RTS data in TB and TC devices. User–provided ΔE_B was 0.308 and 0.234 eV for TB and TC, respectively. V$_{DS}$ was kept constant at 0.30 and 0.20 in TB and TC, respectively.

	TB						TC						
	Measured			Simulated				Measured			Simulated		
V_{GS} (V)	ΔE_B (eV)	ΔH (eV)	$\Delta S/k_B$	ΔE_B (eV)	ΔH (eV)	$\Delta S/k_B$	V_{GS} (V)	ΔE_B (eV)	ΔH (eV)	$\Delta S/k_B$	ΔE_B (eV)	ΔH (eV)	$\Delta S/k_B$
1.00	0.319	0.193	9.34	0.299	0.143	6.92	1.36	0.236	0.060	6.78	0.222	0.065	7.23
1.10	0.310	0.187	8.39	0.309	0.163	7.24	1.38	0.240	0.064	6.64	0.218	0.070	7.27
1.20	0.314	0.192	7.81	0.289	0.173	7.17	1.40	0.250	0.073	6.87	0.223	0.075	7.23
1.30	0.322	0.187	7.28	0.292	0.171	6.52	1.42	0.230	0.110	8.91	0.221	0.084	7.55
1.40	0.273	0.199	7.26	0.312	0.192	6.90	1.44	0.232	0.104	8.11	0.221	0.082	7.04
1.45	0.305	0.178	6.15	0.305	0.192	6.36	1.46	0.235	0.070	5.53	0.221	0.091	7.31
							1.48	0.230	0.076	5.58	0.221	0.096	7.30
							1.50	0.216	0.080	5.54	0.217	0.098	7.05

The experimental and simulated RTS traces are shown in Figure 6-9. Experimental and simulated RTS and trap characteristics were compared to verify RTSSIM. From Figure

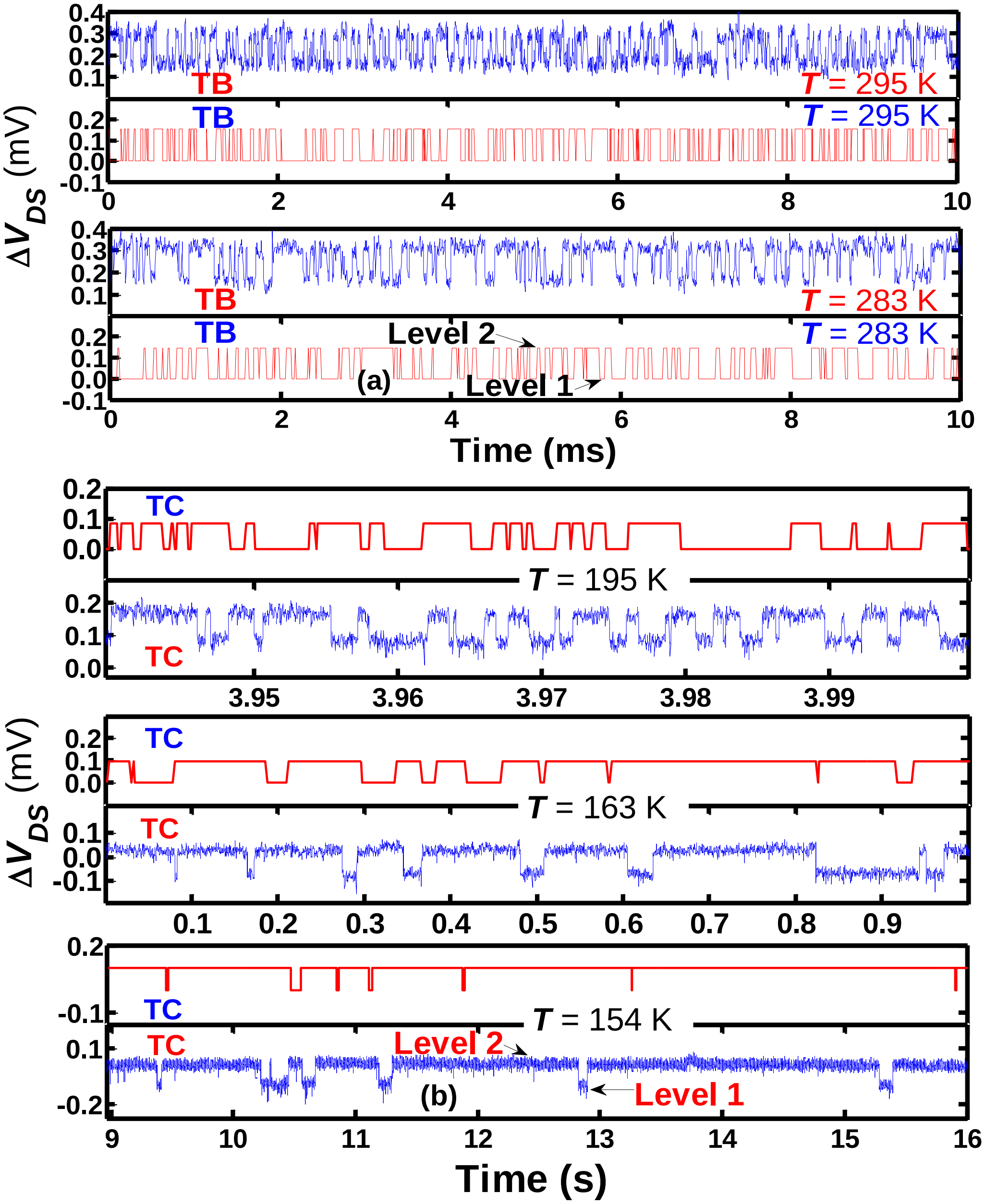

Figure 6-9 A An example time window for two-level measured and simulated RTS traces on devices TB (a) and TC (a). V_{DS}= 0.30, V_{GS}= 1.30 for TB. V_{DS}= 0.20, V_{GS}= 1.42 for TC.

6-9, channel carrier communication with the defect site slows down as temperature is decreased. This is due to the reduction in phonon energy which confirms the charging/discharging defect by an electron is phonon–assisted tunneling. The RTS amplitudes from the measured and simulated RTS agree well. The corresponding PSD for the RTS waveforms in Figure 6-9 are shown in Figure 6-10. Corner frequency and PSD

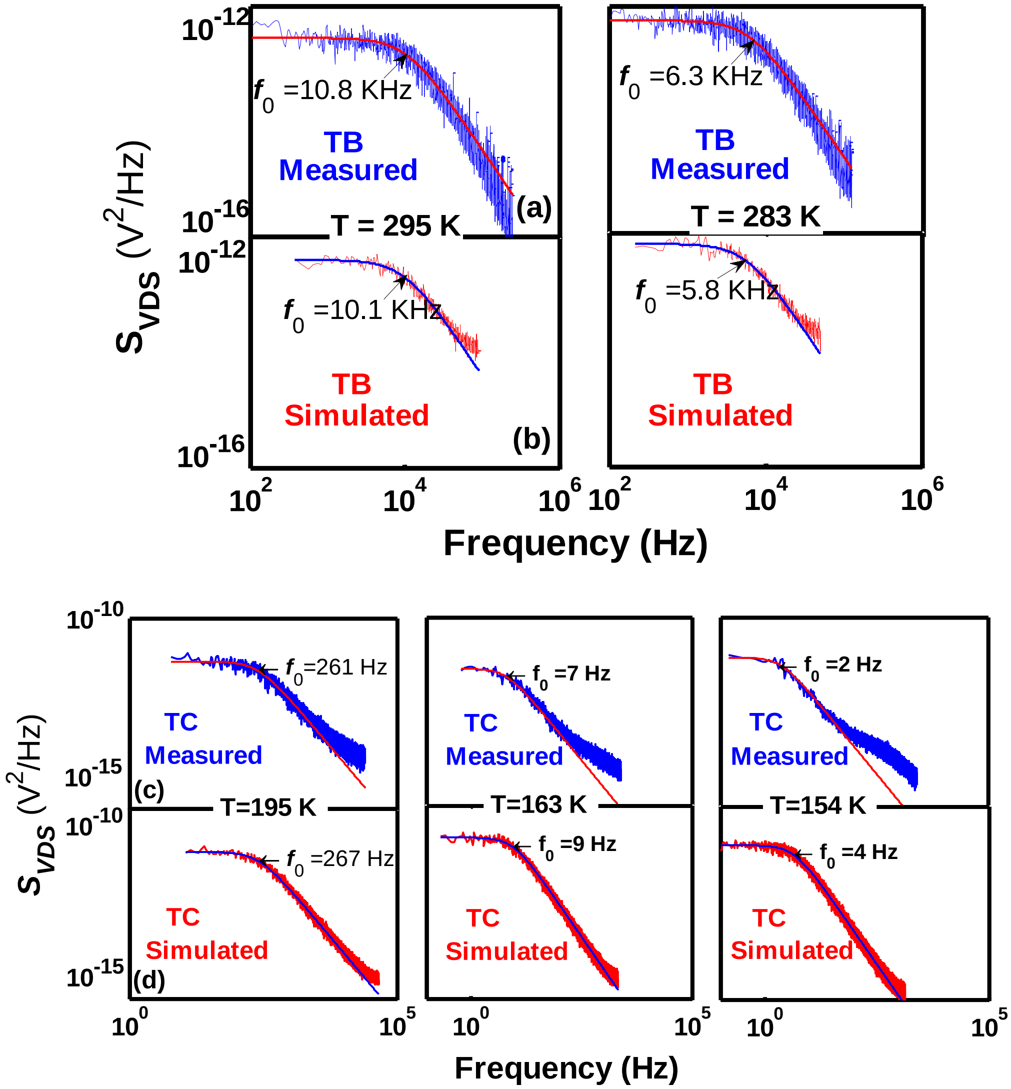

Figure 6-10 PSD corresponding to the two-level measured and simulated RTS in Figure 6-9 for TB ((a) and (b)), and for TC ((c) and (b)) with corresponding Lorentzian fitting.

amplitudes from the measured and simulated RTS data agree although there is some variation (18%) in the corner frequencies due to the cumulative effect of individual variances in $\overline{\tau}_c$ and $\overline{\tau}_e$.

The extracted ΔE_B, ΔH, and $\Delta S/k_B$ from the measured and simulated RTS data for TC show an average variation of 3%, 6%, and 8%, respectively (Table 6-8). Meanwhile, we observed an average of 6% variation between the simulated and the measured x_t (Table 6-8). For TB, the percentage variation between the measured and simulated ΔE_B, ΔH, $\Delta S/k_B$, and x_t are 2%, 9%, 11%, and 13%, respectively. RTS simulation was repeated at the same conditions for 22 times. The standard deviation of obtained $\overline{\tau}_c$, $\overline{\tau}_e$, E_R, $E_{Cox}-E_T$, ΔE_B, σ_0, and x_t were found to be 3%, 4%, 1%, 0.1%, 15%, 1%, and 2%, respectively.

The effectiveness in simulating three level RTS was also verified. Figure 6-11(a) shows a sample trace for a three-level RTS, where two acceptor traps whose occupancy depends on each other are responsible for the switching [127]. As can be seen from Figure

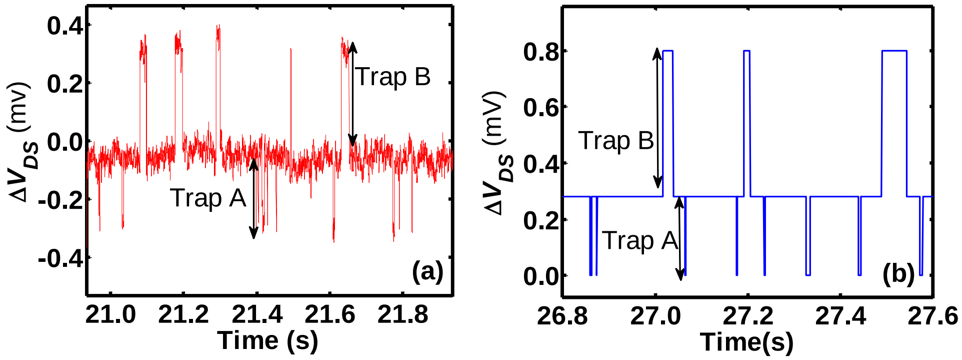

Figure 6-11 Measured (a) and simulated (b) RTS data for two active dependent acceptor traps. V_{GS} = 1.66 V, V_{DS} = 0.25 V, and T = 88 K where W x L = 0.6 x 0.6 µm^2. Measured: Measured: $\overline{\tau}_{cA} = 2.5ms$ $\overline{\tau}_{eA} = 74ms$ $\overline{\tau}_{cB} = 240ms$ $\overline{\tau}_{eB} = 12ms$. Simulated: $\overline{\tau}_{cA} = 1.6ms$ $\overline{\tau}_{eA} = 52ms$ $\overline{\tau}_{cB} = 337ms$ $\overline{\tau}_{eB} = 11ms$.

6-11 (b), RTSSIM is capable of reproducing the trace.

Smooth transition from RTS to 1/f noise was confirmed by checking the scalability of the model and agreement with the UNMF noise model [42]:

$$S_{V_{DS}} = \frac{k_B T V_{DS}^2}{\lambda f W L_{eff}} \left(\frac{1}{N_{inv}} \pm \alpha \bar{\mu}_c\right)^2 N_T(E_F)\,. \tag{6-16}$$

Here, L_{eff} is computed as described in section 5.3.1. α and $\bar{\mu}_c$ are evaluated as shown in section 4.3.6. λ is calculated as expressed in section 2.2. And $N_T(E_F)$ is the volumetric trap density per energy which is computed from the areal trap density and the average trap position as: $N_T(E_F) = N_t / \left(3k_BT(2\bar{x}_t)\right)$ (cm^{-3} eV^{-1}), assuming only traps within $3k_BT$ energy are active, and uniform trap distribution up to $2\bar{x}_t$ with an average distance $\bar{x}_t$. The estimated PSD according to the RTSSIM and UNMF model in large-area nMOSFETs show a good agreement (Figure 6-12).

Another example of a complex simulated RTS is shown in Figure 6-13 (a) due to five active traps in an nMOS device. The simulation conditions for this example are shown

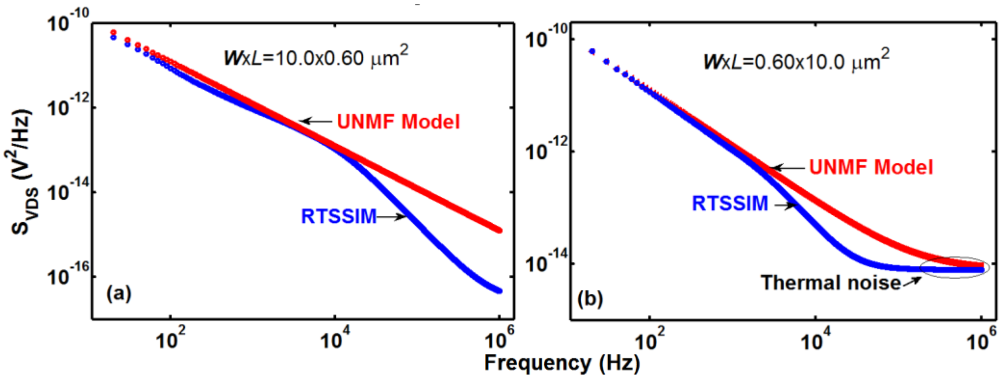

Figure 6-12 Simulated PSD using two approaches (RTSSIM and UNMF model) in nMOSFETs with the same area but two different widths and lengths which shows 35 and 39 active single acceptors for (a) and (b), respectively. V_{GS} = 1.52 V, V_{DS} = 0.25 V, T = 295 K, k_1 = 4.56x10^{-13} V-s, k_2 = -3.02x10^{-14} V-s, N_{tA} = 6.00x10^{8} cm^{-2}, and $\bar{x}_t$ = 1.00 nm.

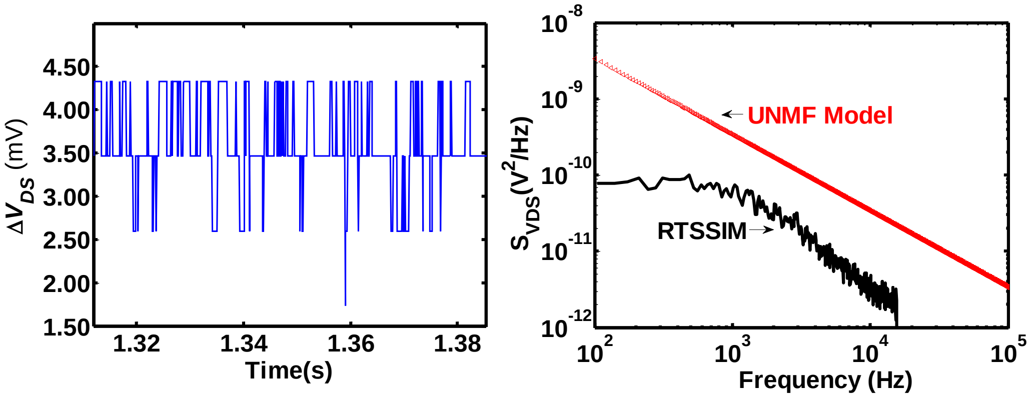

Figure 6-13 (a) Multilevel simulated RTS due to five single acceptor traps and its corresponding PSD (b). V_{GS} = 1.52 and V_{DS} = 0.25 V. T = 280 K.

in Table 6-10. The corresponding PSD for this complex RTS is shown in Figure 6-13(b) based on two different approaches, the RTSSIM model is predicting $1/f^{\gamma}$ more realistically than the UNMF model. This confirms that RTSSIM is capable of predicting the RTS and its corresponding PSD at various areas of MOSFETs with a different number of active traps (Figure 6-14). The simulation conditions for this example (Figure 6-14) are shown in Table 6-11. From Figure 6-14, RTSSIM scales from Lorentzian to $1/f$ noise PSD as the device area scales up. Figure 6-15 shows the simulated PSD for different trap densities with fixed device area (0.50 μm^2). Again, RTSSIM agrees with the UNMF model for $1/f$ noise. The

Table 6-10 Simulation conditions and user-provided parameters for an nMOSFET in Figure 6-13

Used parameters	Value
W (μm)	0.60
L (μm)	0.60
V_{GS} (V)	1.52
V_{DS} (V)	0.25
T (K)	280
N_{tA} (cm^{-2})	8.00x10^9
$\bar{x}_t$ (nm)	0.80
k_1 (V-s)	4.56x10^{-13}
k_2 (V-s)	-3.02x10^{-14}
ΔE_B (eV)	0.26
$E_{Cox} - E_T$ (eV)	3.09

simulation conditions used to demonstrate Figure 6-15 are depicted in Table 6-12.

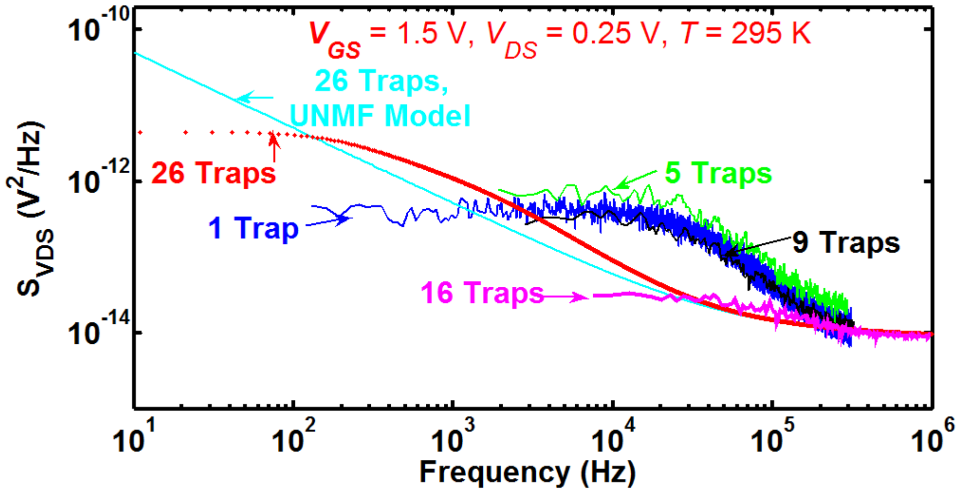

Figure 6-14 Progression of simulated PSD as device area scales up based on the RTSSIM and UNMF model. Simulation conditions are shown in Table 6-11.

Table 6-11 Conditions used for the simulated PSD in Figure 6-14.

Used parameters	1 Trap	5 Traps	9 Traps	16 Traps	25 Traps
W (μm)	0.6	0.6	0.6	0.6	0.6
L (μm)	0.6	2.4	4.8	10.0	11
N_A (cm^{-3})	3.5×10^{17}	3.5×10^{17}	3.5×10^{17}	3.5×10^{17}	3.5×10^{17}
V_{th} (V)	0.794	0.794	0.794	0.794	0.794
Slope of V_{th} vs. T (V/K)	2.0×10^{-3}	2.0×10^{-3}	2.0×10^{-3}	2.0×10^{-3}	2.0×10^{-3}
g_D (A/V)	3.27×10^{-5}	8.18×10^{-6}	4.09×10^{-6}	1.96×10^{-6}	1.78×10^{-6}
V_{GS} (V)	1.50	1.50	1.50	1.50	1.50
V_{DS} (V)	0.25	0.25	0.25	0.25	0.25
T (K)	295	295	295	295	295
N_{tA} (cm^{-2})	3.0×10^{8}	3.0×10^{8}	3.0×10^{8}	3.0×10^{8}	3.0×10^{8}
$\bar{x}_t$ (nm)	1.0	1.0	1.0	1.0	1.0
ΔE_B (eV)	0.20	0.20	0.20	0.20	0.20
$E_{Cox} - E_T$ (eV)	3.09	3.09	3.09	3.09	3.09
k_1 (V-s)	4.56×10^{-13}	4.56×10^{-13}	4.56×10^{-13}	4.56×10^{-13}	4.56×10^{-13}
k_2 (V-s)	-3.02×10^{-14}	-3.02×10^{-14}	-3.02×10^{-14}	-3.02×10^{-14}	-3.02×10^{-14}

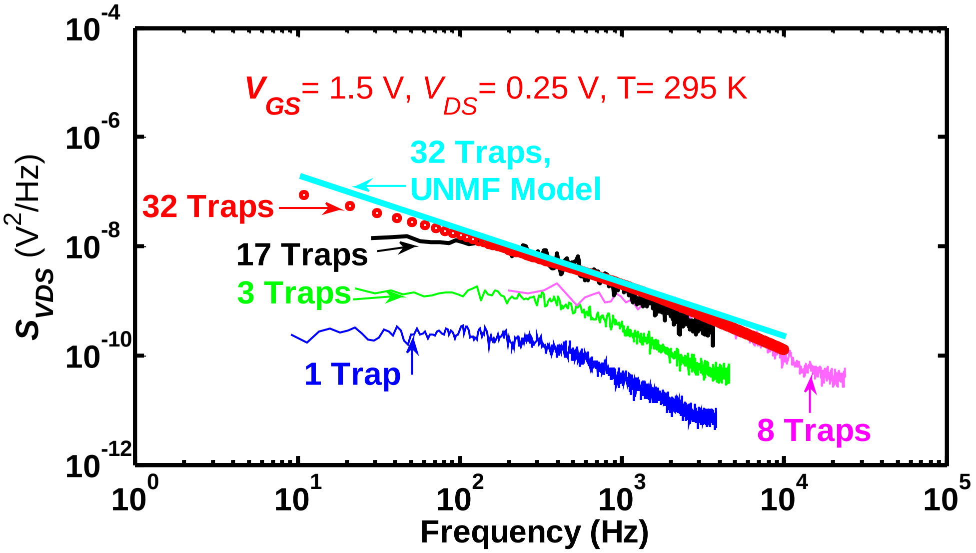

Figure 6-15 Simulated PSD for different number of active traps with fixed device area based on RTSSIM and UNMF model. Simulation conditions are shown in Table 6-12.

Table 6-12 Simulation conditions used to generate the PSD in Figure 6-15.

Used parameters	1 Trap	3 Traps	8 Traps	17 Traps	32 Traps
W (μm)	1.0	1.0	1.0	1.0	1.0
L (μm)	0.5	0.5	0.5	0.5	0.5
N_A (cm^{-3})	$1.0x10^{17}$	$1.0x10^{17}$	$1.0x10^{17}$	$1.0x10^{17}$	$1.0x10^{17}$
V_{th} (V)	0.553	0.553	0.553	0.553	0.553
Slope of V_{th} vs. T (V/K)	$1.26x10^{-3}$	$1.26x10^{-3}$	$1.26x10^{-3}$	$1.26x10^{-3}$	$1.26x10^{-3}$
Slope of g_D vs. V_{GS} (A/V^2)	$2.06x10^{-4}$	$2.06x10^{-4}$	$2.06x10^{-4}$	$2.06x10^{-4}$	$2.06x10^{-4}$
Intercept of g_D vs. V_{GS} (A/V)	$-1.97x10^{-4}$	$-1.97x10^{-4}$	$-1.97x10^{-4}$	$-1.97x10^{-4}$	$-1.97x10^{-4}$
V_{GS} (V)	1.50	1.50	1.50	1.50	1.50
V_{DS} (V)	0.25	0.25	0.25	0.25	0.25
T (K)	295	295	295	295	295
N_{tA} (cm^{-2})	$3.0x10^8$	$1.5x10^9$	$2.4x10^9$	$3.8x10^9$	$8.8x10^9$
$\bar{x}_t$ (nm)	1.0	1.0	1.0	1.0	1.0
ΔE_B (eV)	0.30	0.30	0.30	0.30	0.30
$E_{Cox} - E_T$ (eV)	3.09	3.09	3.09	3.09	3.09
k_1 (V-s)	$4.56x10^{-13}$	$4.56x10^{-13}$	$4.56x10^{-13}$	$4.56x10^{-13}$	$4.56x10^{-13}$
k_2 (V-s)	$-3.02x10^{-14}$	$-3.02x10^{-14}$	$-3.02x10^{-14}$	$-3.02x10^{-14}$	$-3.02x10^{-14}$

6.6 Summary and Conclusions

Random telegraph signals simulation tool was presented and shown to effectively predict and replicate the RTS in time and frequency domains. RTSSIM is constructed based on first-principles. It takes into account the Coulombic scattering effect and considers the non-uniformity in doping concentration in the channel and the non-uniformity in the trap distribution in the oxide. The newly developed RTS models incorporates the effect of both linear and saturation regions of operation in nMOSFETs. RTSSIM is fully scalable from single switching electron to ensemble 1/*f* noise. The RTSSIM generates the RTS in time domain based on the electrical properties that are associated with the identified trap(s). The PSD is evaluated from the generated RTS traces for each active trap as well as from the resultant RTS traces using Welch's PSD method (if total number of active traps <20). For 20 or more active traps, RTSSIM computes the total PSD based on the summation of the RTS Lorentzian spectra contributed from each trap without constructing the time domain RTS. RTSSIM shows over 92% accuracy in predicting the RTS and trap characteristics. The model also represents the first realistic simulation of multilevel RTS.

Chapter 7 Conclusions and Summary

A new RTS statistical model and its simulation tool are developed to predict and simulate the phenomenon of charging/discharging of trap(s) in the gate-oxide of nMOSFETs in time and frequency domains. We have presented a comprehensive, variable-temperature, single-to-multi-trap scalable RTS model and a simulation tool based on first principles, and supported by experimental data. We have investigated random telegraph signals on several sub-micron nMOSFETS from room temperature down to 80 K. Two-level and multi-level RTS due to correlated and uncorrelated traps were observed in the investigated nMOSFETs. RTS and trap characteristics were extracted from the gate-source voltage and temperature dependence such as: average capture times, average emission times, RTS amplitude, capture activation energy, emission energy, change in entropy, change in enthalpy, capture cross-section, capture cross-section prefactor, relaxation energy associated with the defect oxide, and trap energy level with respect to the SiO_2 conduction band-edge. The devices used in this work were provided by Texas Instruments Inc. The area of the investigated devices was ≤0.55 μm^2.

Analytical procedures were developed for extracting trap characteristics from the V_{GS} and temperature dependence of the average capture and emission times associated with the active trap(s). The average capture and emission times were extracted based on the transition from one level to others and the state of the trap whether empty or full. A multilevel RTS with envelope transitions was also observed due to the fast and slow traps. A MATLAB algorithm was developed to analyze the envelope transitions and separate the fluctuations due to each trap. The extracted average capture and emission times associated with the fast traps were several orders of magnitude less than the ones associated with the slow traps. The normalized trap locations with respect to T_{ox} for the fast and slow traps from the Si/SiO_2 interface ranged from 0.134 to 0.080. Capture activation energy associated with the fast and slow traps was on the average of 0.31 and 0.83 eV, accordingly. The high barrier energy may explain the long-time that takes the slow trap to capture and emit an electron from and to the channel. The extracted relaxation energy associated with the fast and slow traps was 1.24 and 3.19 eV, respectively. This results showed that the origin of the fast trap was due to unrelaxed neutral oxygen deficiency center. However, the origin of the slow trap could not be found. The V_{GS} and temperature dependence of capture cross-section for both traps was similar to the attributes of a neutral center where σ of a neutral center increases with the increase of temperature and shows a slight change with V_{GS}.

The predicted results based on the newly developed RTS model and its simulation tool were shown to agree with the experimentally obtained data. The reconstructed RTS traces had been related to the extracted electrical properties and location of the trap (capture activation energy, trap energy level in the SiO_2, screened scattering coefficients, and trap position in the oxide). To our knowledge, this is the first time an RTS simulation can predict RTS in time and frequency domains at variable V_{GS}, $V_{DS,}$ and temperatures from which the trap characteristics can be extracted. Amplitude of the RTS PSD and the corner frequency were shown for the measured and simulated RTS data to agree well. Simulated RTS on various channel widths and lengths had been provided. Results demonstrated that RTSSIM accurately quantifies device scalability and trap density in a simulated device. RTSSIM showed over 92% accuracy in predicting the RTS and trap characteristics.

The novelty of this work lies in the fact that four trap characteristics: relaxation energy, trap energy level in the oxide band-gap with respect to the SiO_2 conduction band-edge, capture activation energy, and capture cross-section are extracted from the measured RTS data and used together as identification markers to investigate the nature and origin of the gate oxide defects. RTSSIM interrelates the electrical properties of the identified traps to reconstruct RTS traces in time domain and evaluate the corresponding noise PSD as a function of V_{GS}, V_{DS}, and temperature. Smooth transition from RTS to $1/f$ noise was confirmed by checking the scalability of the model and agreement with the UNMF noise model. The estimated PSD according to the RTSSIM and UNMF model in large-area nMOSFETs show a good agreement.

Possible future work can be summarized as follows: (1) a comprehensive, variable-temperature, single-to-multi-trap scalable RTS model supported by experimental data on sub-micron pMOSFETs can be done and incorporated in the RTSSIM. (2) The effect of noise variability in highly scaled devices can be assimilated in the RTS model and its simulation tool. (3) High-k dielectric materials (HfO_2, ZrO_2, etc.) and its electrical properties can be embedded in the RTSSIM where user can be provided by different options of material properties that can be selected and simulated. (4) Integrating RTSSIM with circuit simulation such as SPICE to instantaneously monitor the effect of RTS on a circuit and take any precautionary measures during initial design cycle. Integrating RTSSIM with circuit simulation may allow some of the provided parameters to be directly inputted into the RTSSIM such as CV curve, doping profile, V_{th}, g_D, etc. without providing them manually.

Appendix A:

MATLAB Program Code to Analyze Complex RTS Due to Fast and Slow Oxide Traps

```
%-----------------------------------------------------------------
% This program is designed to run the analysis of RTS data due to the fast and slow traps.
The first section of the program converts all RTS data into digital values (0 and 1). Then,
from the pattern of these digitized values, we developed an algorithm to recognize the
overlapped levels where a function called "getrefineddata " handles this task. This function
can individually separate the RTS data due to the fast and slow trap without changing or
affecting the integrity of the RTS raw data. There are another two functions were used to
analyze this complex RTS which are “TrackTime” and “getAvgTime”. The three mentioned
functions are called from the main program. At the end of this main algorithm, all three
functions are listed with some comments and notes to ease the understanding of this code.
%-----------------------------------------------------------------
close force all
clear all
clc

G=10000;        % Gain of the preamplifier
tic
                % Upload the measured RTS data into the program
b1 = csvread(‘File name with full path extension,22);
t = b1(:,1);
v = b1(:,2);
v3=v/G;         % Real Value of Voltage
data=b1;
G=10000;        % gain of the preamplifier
t = data(:,1);  % assigned the measured time data to  variable t
v = data(:,2);  % assigned the measured RTS data to  variable v
v3=v/G;         % Real value of drain-source voltage fluctuations
                % Sampling frequency
sample_rate=length(v3)/(max(t)-min(t));
Delta_T=t(2,1)-t(1,1);
Time=zeros(length(v3),1);
for i=2:length(v3)

    t(i,1)=t(i-1,1)+Delta_T;
end

                 % Plot the raw RTS data
figure;
plot(t,v3);
title('RTS');
xlabel('Time (s)');
```

```
ylabel('\DeltaV_{DS} (V)')

% Plot the histogram of the raw RTS data, after number of bins is
% provided
Number_Bin_Noise=input('Number of Bins for Noise Histogram = ');
figure;
hist(v3,Number_Bin_Noise);
title('Noise')
title('(Raw) RTS Amplitude Histogram')
xlabel('\DeltaV_{DS} (V)');
ylabel('Frequency ');

% User interface where number of bins used for time events
% distribution due to the slow trap
NOB12S=input('Number of Bins for taw 0 = ');
NOB21S=input('Number of Bins for taw 1 = ');

% Set up limit of the upper and lower envelopes
L_Level_0 = input('Lower cut of Level 0 = ');
H_Level_0 = input('Higher cut of Level 0 = ');
L_Level_1 = input('lower cut of Level 1 = ');
H_Level_1 = input('Higher cut of Level 1 = ');

% This used to shift the fast trap data by certain amplitude which
% allows separation of RTS data due to the fast and slow traps
A1= input('The amplitude of the fast trap = ');
H_high=H_Level_1;
L_high=L_Level_1;
H_low=H_Level_0;
L_low=L_Level_0;
nrows=length(v);          % number of points which has been acquired
myState=zeros(nrows,1);   % create a matrix with number of elements
RTS_dig=zeros(nrows,1);   % equal to the number of acquired points
new_value=zeros(length(v3),1);
count=0;

% quick refinement on the RTS raw data, points out side the limit
% of each envelope will be shifted back to the level of the previous
% points
for i=2:length(v3)-1
    if(v3(i,1)>L_low && (v3(i,1)<H_low)||(v3(i,1) >L_high)&&...
            (v3(i,1) <H_high))
        new_value(i,1)=v3(i,1);
    else
        new_value(i,1)=v3(i-1,1);
    end
end

% Converting the real values of RTS data into digital values
% (000110).
```

```
for r=1:nrows

if((new_value(r,1)>=(L_Level_0))&&(new_value(r,1)<=(H_Level_0)))
        RTS_dig(r,1)=0;

else((new_value(r,1)>=L_Level_1)&&(new_value(r,1)<=(H_Level_1)))
        RTS_dig(r,1)=1;
    end
end
H2=H_high;
L2=L_high;
H1=H_low;
L1=L_low;
n=4;  % This sets the maximum number of points need to be
      refined,
      %if up to 4 points of 0's or 1's are found in series of the
%converted digital values e.g. if we have
%0000011111001111100000111100000, the expected refined values
are:
%0000011111111111100000000000000
%-----------------------------------------------------------------
% The getrefineddata function is used to extract the RTS data due
% to fast trap from the slow % trap. This function returns the
% following data:
%  1-RTS_dig_S:  Digitized RTS data due to the slow trap
%  2-RTS_RFBM: Extracted RTS data due to fast trap before is merged
%  3-RTS_RFAM: Extracted RTS data due to fast trap after is merged
%  4-RTS_RS: Extracted RTS data due to slow trap from the raw RTS
%     data
[RTS_dig_S,RTS_RFBM,RTS_RFAM,RTS_RS]=getrefineddata(new_value,...
                                    RTS_dig,L1,H1,L2,H2,A1,n);
RTS_dig=[];new_value=[];
Time=t(1:length(RTS_RFBM));
b=RTS_RS(RTS_RS~=L1);
D_ST=b(b~=L2);

figure;
hist(D_ST,Number_Bin_Noise);
title('RTS Amplitude Histogram for The Slow Trap')
xlabel('\DeltaV_{DS} (V)');
ylabel('Frequency ');

figure
plot(Time,RTS_RFBM)
title('RTS data for Fast Trap before is mearged')
xlabel('Time (s)');
ylabel('\DeltaV_{DS} (V)');

%% Run time analysis on the extracted RTS data due to fast trap
L_Level_0 = input('Lower cut of Level 0 = ');
```

```
H_Level_0 = input('Higher cut of Level 0 = ');
L_Level_1 = input('lower cut of Level 1 = ');
H_Level_1 = input('Higher cut of Level 1 = ');
NOB12F=input('Number of bins for fast trap, leve0 = ');
NOB21F=input('Number of bins for fast trap, level1 = ');
H2=H_high;
L2=L_high;
H1=H_low;
L1=L_low;

RTS_RFBM=RTS_RFBM';
for i=2:length(RTS_RFBM)-1

if(RTS_RFBM(i,1)>L_low&&(RTS_RFBM(i,1)<H_low)||(RTS_RFBM(i,1)...
   >L_high)&&                                       (RTS_RFBM(i,1)
<H_high))new_value(i,1)=RTS_RFBM(i,1);
    else
        new_value(i,1)=RTS_RFBM(i-1,1);
    end
end

RTS_digF=[];   % Digital values of RTS due to fast trap
for r=1:length(RTS_RFBM)-1

if((new_value(r,1)>=(L_Level_0))&&(new_value(r,1)<=(H_Level_0)))
       RTS_digF(r,1)=0;

elseif((new_value(r,1)>=L_Level_1)&&(new_value(r,1)<=(H_Level_1))
)
       RTS_digF(r,1)=1;
    else
       RTS_digF(r,1)=2;
    end
end

x=RTS_dig_S';  % Digital values of RTS due to slow trap

Ampl1=1;
Ampl2=2;
FS=sample_rate;

%----------------------------------------------------------------
% The TrackTime function is used to track the average times
% associated with a trap.
[taw12S,taw21S,taw23S,taw32S]=TrackTime(x,Ampl1,Ampl2,FS,NOB12S,N
O
                              B21S,NOB12F,NOB21F);
[taw12F,taw21F,taw23F,taw32F]=TrackTime(RTS_digF,Ampl1,Ampl2,FS,N
O
                              B12F,NOB21F,NOB12S,NOB21S);
```

```
% Plot the RTS data due to the fast and slow traps after separation
figure;
hist(RTS_RS,Number_Bin_Noise);
title('Refined RTS Amplitude Histogram of the Slow Trap')
xlabel('\DeltaV_{DS} (V)');
ylabel('Frequency ');

figure;
hist(RTS_RFAM,Number_Bin_Noise);
title('Refined RTS Amplitude Histogram of the Fast Trap')
xlabel('\DeltaV_{DS} (V)');
ylabel('Frequency ');

Time=t(1:length(RTS_RFAM));
figure
plot(Time,RTS_RFAM)
title('The Fast Trap Data after Mearged')
xlabel('Time (s)');
ylabel('\DeltaV_{DS} (V)');

Time=t(1:length(RTS_RS));
figure
plot(Time,RTS_RS)
title('The Slow Trap Data')
xlabel('Time (s)');
ylabel('\DeltaV_{DS} (V)');

Time=t(1:length(RTS_dig_S));
figure
plot(Time,RTS_dig_S)
title('Digital values of the slow trap')
xlabel('Time (s)');
ylabel('\DeltaV_{DS} (V)');

% List the extracted average times associated with each trap.
taw1slow_taw2slow_taw1fast_taw2fast=[taw12S  taw21S taw12F taw21F]
```

The associated programs that have been used along with the main algorithm for time analysis of RTS data due to the fast and slow traps

```
%*******************************************************************************************

function
[RTS_dig_S,RTS_RFBM,RTS_RFAM,RTS_RS]=getrefineddata(Data,state,..
.L1,H1,L2,H2,A1,n)
% Data         : the RTS raw data
% state        : the digital value of the RTS raw data
```

```
% L1           : lower level of the lower envelope
% H1           : Higher level of the lower envelope
% L2           : lower level of the upper envelope
% H2           : Higher level of the upper envelope

% initialization of some variables
RND=[];        % RND is the refined new data
NS=[];         % refined RTS data due to the slow trap
NIND0=[];      % index number where 0 is located
S=[];
ind0=[];
RD=[];
c1=0;
c2=0;
option1=0;
option2=0;
IND0=find(state==0);
IND1=find(state==1);
ind0=find(state==0);
if IND0(1)~=1 && IND0(1)-1<=n  % if RTS starts at higher level
                               % like 1111000
    option1=1;
    state([1:IND0(1)])=0;
    IND0=find( state==0);
    IND1=find( state==1);
    for j=1:n
    % This sets the number of points needs to be refined when
j=1,
   % the first point will be refined, when j=2, second point will
    % be refined etc.
        for i=1: length(IND0)-1
            if (IND0(i+1)-IND0(i))-j==1
    % Check where the transition occurs. This condition shows a
    % transition is realized.
                Temp_IND0=IND0(i);
                NIND0=[NIND0 Temp_IND0];% New refined
                for k=1:j
    % This will pick up the data at the edge of the transition
                    temp_RD=Data(i-1);
                    RD=[RD temp_RD];
                end
                for k=1:j
                    temp_IND0=IND0(i)+k;
                    NIND0=[NIND0 temp_IND0];
                end
            else
                temp_IND0=IND0(i);
                NIND0=[NIND0 temp_IND0];
            end  % end of if (IND0(i+1)-IND0(i))-j==1
        end      % end of for i=1: length(IND0)-1
```

```
        for ii=1:length(NIND0)-1
     % Check where the transition occurs, this conidian shows no
     % transition is realized.
            if (NIND0(ii+1)-NIND0(ii))==1
                NS=[NS 0];
            else
                NS=[NS 0];
                for jj=NIND0(ii)+1:NIND0(ii+1)-1
                    NS=[NS 1];
                end
            end % end of (NIND0(ii+1)-NIND0(ii))==1
        end % end of for ii=1:length(NIND0)-1

        if j<n  % This is to rest state between 0 and 1
            state=NS;
            IND0=find(state==0);
            IND1=find(state==1);
            state=[];
            NS=[];
            NIND0=[];
        else
            State=NS ;
           % This gives the final refinement due to the slow trap
        end
    end
else    % the condition of IND0(1)~=1 && IND0(1)-1<=n
        % if RTS starts at lower level such as 0000111000111000
    IND0=find( state==0);
    IND1=find( state==1);
    for j=1:n
        for i=1: length(IND0)-1
            if (IND0(i+1)-IND0(i))-j==1
                Temp_IND0=IND0(i);
                NIND0=[NIND0 Temp_IND0];
                for k=1:j
                    temp_IND0=IND0(i)+k;
                    NIND0=[NIND0 temp_IND0];
                end
            else
                temp_IND0=IND0(i);
                NIND0=[NIND0 temp_IND0];
            end
        end

        for ii=1:length(NIND0)-1
            if (NIND0(ii+1)-NIND0(ii))==1
                NS=[NS 0];
            else
                NS=[NS 0];
```

```
                for jj=NIND0(ii)+1:NIND0(ii+1)-1
                    NS=[NS 1];
                end
            end
        end

        if j<n          % This is to rest state
            state=NS;
            IND0=find(state==0);
            IND1=find(state==1);
            state=[];
            NS=[];
            NIND0=[];
        else
            State=NS;   % This gives the final refinement
        end
    end
end                       % end of IND0(1)~=1 && IND0(1)-1<=n
A=[];
if option1==1
    RTS_dig_S=State;      % digitized state of the slow trap
else

    for i=1:ind0(1)-1
        A=[A 1];
    end
    RTS_dig_S=horzcat(A,NS);
% included all digitized RTS data due to slow trap
end
% from the refined digital data of RTS due to the slow trap, we
% constructed the raw data of the RTS with the prober shift.
Datat_FT=[];
OIND0=find(RTS_dig_S==0);
OIND1=find(RTS_dig_S==1);
for i=1:(length(OIND0))-1
    temp_FDATA=Data(OIND0(i));
    Datat_FT=[Datat_FT temp_FDATA];
end
RTS_RFAM=[];
for i=1:(length(OIND1))-1
    temp_FDATA=Data(OIND1(i))-A1;
    RTS_RFAM=[RTS_RFAM temp_FDATA];
% RTS data due to the fast trap after it was stitched from the
% upper and lower envelopes.
end
RTS_RFBM=horzcat(Datat_FT,RTS_RFAM);
%----------------------------------------------------------------
% Preparing refined data for output
RTS_RS=[];   % extracted RTS data for slow trap from the raw data
NDFT=[];     % extracted RTS data for fast trap from the raw data
```

```
IND0ST=find(RTS_dig_S==0);
% Indices of 0 elements in the digitized RTS due to the fast trap
IND1ST=find(RTS_dig_S==1);
% Indices of 1 elements in the digitized RTS due to the fast trap
if (IND0ST(1))==1
    for i=1:length(IND0ST)-1
        if (IND0ST(i+1)-IND0ST(i))==1 && Data(IND0ST(i))<H1
            temp_data=Data(IND0ST(i));
            RTS_RS=[RTS_RS temp_data];
        elseif (IND0ST(i+1)-IND0ST(i))==1 && Data(i)>H1
            temp_data=L1;
            RTS_RS=[RTS_RS temp_data];
        elseif (IND0ST(i+1)-IND0ST(i))~=1
            for j=IND0ST(i)+1:IND0ST(i+1)-1
                if Data(j)>L2 && Data(j)<H2
                    temp_data=Data(j);
                    RTS_RS=[RTS_RS temp_data];
                else
                    temp_data=L2;
                    RTS_RS=[RTS_RS temp_data];
                end
            end
        end
    end
else
    for k=1:IND0ST(1)-1
        if Data(k)>L2 && Data(k)<H2
            temp_data=Data(k);
            RTS_RS=[RTS_RS temp_data];
        else
            temp_data=L2;
            RTS_RS=[RTS_RS temp_data];
        end
    end

    for i=1:length(IND0ST)-1
        if (IND0ST(i+1)-IND0ST(i))==1 && Data(IND0ST(i))<H1
            temp_data=Data(IND0ST(i));
            RTS_RS=[RTS_RS temp_data];
        elseif (IND0ST(i+1)-IND0ST(i))==1 && Data(IND0ST(i))>H1
            temp_data=L1;
            RTS_RS=[RTS_RS temp_data];
        elseif (IND0ST(i+1)-IND0ST(i))~=1
            for j=IND0ST(i)+1:IND0ST(i+1)-1
                if Data(j)>L2 && Data(j)<H2
                    temp_data=Data(j);
                    RTS_RS=[RTS_RS temp_data];
                else
                    temp_data=L2;
                    RTS_RS=[RTS_RS temp_data];
```

```
                end
            end
        end
    end %end of for loop of the second option for outputting data
end     % end of if statement (IND0ST(1))==1
end     % end of function


%*******************************************************************************************

function
[taw12,taw21,taw23,taw32]=TrackTime(Data,Amplitude1,Amplitude2,..
.

FS,Number_Of_Bin12,Number_Of_Bin21,Number_Of_Bin23,Number_Of_Bin3
2)

% This function extracts the average times associated with RTS
% levels based on the state of the trap and the transitions.
jmp12=Amplitude1;
jmp21=-jmp12;
jmp23=Amplitude2;
jmp32=-jmp23;
v3=Data;
L_Level_0 =-1;
H_Level_0 =.2;
L_Level_1 =.22;
H_Level_1 =1.3;
L_Level_2 =1.32
H_Level_2 =4
% Initialization of matrices
Time12=[];Time21=[];Time23=[];Time32=[];
startca=0;startcb=0;startea=0;starteb=0;
% This will save the index number where a transition is
% recognized
Pos21=[];Pos12=[];Pos23=[];Pos32=[];

% Extraction of average times from the digitized RTS data
for i=1:length(Data)-1
    if (Data(i+1)-Data(i))==jmp12 && Data(i+1)>H_Level_0 &&...
                            Data(i+1)<H_Level_1
        startca=startca;
% Set the capture time counter associated with trap A
        P12HB=i;
% Record index number of the higher limit of the Poisson process
% interval
        P12LB=i-startca;
% Record index number of the lower side of the Poisson process
& interval
        Pos12=[Pos12 P12LB P12HB];
```

```
        startea=0;
% Reset the emission time counter associated with trap A
        startca=0;
% Reset the capture time counter associated with trap A
        starteb=0;
% Reset the emission time counter associated with trap B
        startcb=startcb+1;
% Continue recording the capture time associated with trap B
        state=0; % set state to zero

% The rest of analysis follows the same analogy of the first part
    elseif (Data(i+1)-Data(i))==jmp21 &&  Data(i+1)<H_Level_0
        startea=startea;
        P21HB=i;
        P21LB=i-startea;
        Pos21=[Pos21 P21LB P21HB];
        startea=0;
        starteb=0;
        startca=0;
        startcb=startcb+1;
    elseif (Data(i+1)-Data(i))==jmp23 && Data(i+1)>L_Level_2
        startcb=startcb;
        P23HB=i;
        P23LB=i-startcb;
        Pos23=[Pos23 P23LB P23HB];
        starteb=0;
        startca=0;
        startcb=0;
        startea=startea+1;
    elseif (Data(i+1)-Data(i))==jmp32 &&  Data(i+1)<H_Level_1
                                &&Data(i+1)>L_Level_1
        starteb=starteb;
        P32HB=i;
        P32LB=i-starteb;
        Pos32=[Pos32 P32LB P32HB];
        starteb=0;
        startca=0;
        startcb=0;
        startea=startea+1;
        state=3;
    else
        startca=startca+1;
        startcb=startcb+1;
        startea=startea+1;
        starteb=starteb+1;
    end  % end of if (Data(i+1)-Data(i))==jmp12 &&...
         % Data(i+1)>H_Level_0 && Data(i+1)<H_Level_1
end      % end of for i=1:length(Data)-1

Pos12; % The indices number of Poisson process intervals
```

```
       % associated with the transition from level_1 to Level_2
Pos21;
Pos23
Pos32;

% Computing the duration time for each Poisson process intervals
L=length(Pos12);
if(rem(L,2)==0)
    for ii=1:2:length(Pos12)
        Time12=[Time12 length([v3(Pos12(ii):Pos12(ii+1))])/FS];
    end
else
    for ii=1:2:length(Pos12)-1
        Time12=[Time12 length([v3(Pos12(ii):Pos12(ii+1))])/FS];
    end
end

L=length(Pos21);
if(rem(L,2)==0)
    for ii=1:2:length(Pos21)
        Time21=[Time21 length([v3(Pos21(ii):Pos21(ii+1))])/FS];
    end
else
    for ii=1:2:length(Pos21)-1
        Time21=[Time21 length([v3(Pos21(ii):Pos21(ii+1))])/FS];
    end
end

L=length(Pos23);
if(rem(L,2)==0)
    for ii=1:2:length(Pos23)
        Time23=[Time23 length([v3(Pos23(ii):Pos23(ii+1))])/FS];
    end
else
    for ii=1:2:length(Pos23)-1
        Time23=[Time23 length([v3(Pos23(ii):Pos23(ii+1))])/FS];
    end
end

L=length(Pos32);
if(rem(L,2)==0)
    for ii=1:2:length(Pos32)
        Time32=[Time32 length([v3(Pos32(ii):Pos32(ii+1))])/FS];
    end
else
    for ii=1:2:length(Pos32)-1
        Time32=[Time32 length([v3(Pos32(ii):Pos32(ii+1))])/FS];
    end
end
% The average capture and emission times are computed using
```

```
% getAvgTime function. In this function we used equation 4_1 to
% compute the average times associated with each level.
% The algorithm of getAvgTime function is shown below.

if length(Time12)>1
    taw12=getAvgTime(Data,Time12,FS,Number_Of_Bin12);
else
    taw12=0;
end
if length(Time21)>1
    taw21=getAvgTime(Data,Time21,FS,Number_Of_Bin21);
else
    taw21=0;
end
if length(Time23)>1
    taw23=getAvgTime(Data,Time23,FS,Number_Of_Bin23);
else
    taw23=0;
end
if length(Time32)>1
    taw32=getAvgTime(Data,Time32,FS,Number_Of_Bin32);
else
    taw32=0;
end

end


%**************************************************************************************************

function taw=getAvgTime(Data,Array_average_time,FS,Number_Of_Bin)
%This function computes average time constants associated with each
%level using equation 4-1.
%Returns total bins were generated and its occurrence frequency
[hh,xout]=hist(Array_average_time,Number_Of_Bin);
numer_Of_bins=xout';
% Total bins used in the time events distribution
freq_Magnitude=hh';
% Frequency of time events in each bin
% Plot time events distribution as a function of histogram bin
% numbers
% Optimization of the total bin numbers used in the histogram
% of time events for RTS data
for i=20:5:200
    [HH,Xout]=hist(Array_average_time,i);
    Num_Bin=Xout';
    Freq_Mag=HH';
    for j=1:length(Num_Bin)
        Mul_Taw_With_frequen(j,1)=Num_Bin(j,1)*Freq_Mag(j,1);
        j=j+1;
```

```
    end
    t1=[1:length(Data)]/FS;
    Delta_T=t1(1,2)-t1(1,1);
    T=Delta_T;
    T=[T,(sum(Mul_Taw_With_frequen))/(sum(Freq_Mag))];

end

figure;
hist(Array_average_time,Number_Of_Bin);
showfit exp;
xlabel('Time (s) ');
ylabel('Frequency ');

for i=1:length(freq_Magnitude)
      Multib_taw_with_frequen(i,1)=numer_0f_bins(i,1)*freq_Magnit
      ude(i,1);
End
taw=(sum(Multib_taw_with_frequen))/(sum(freq_Magnitude));
%This is the extracted average time
end
```

This function is used to evaluate the PSD from the measured and simulated RTS data where thermal noise is considered .

```
S=floor(length(RTS_data)/16);
% RTS data is divided into 16 overlapped sections where each
% section has an equal number of elements.
[myPSD,f]=pwelch(RTS_data,hanning(S),Noverlap,w,FS);
% Hanning window is used in WPSD function where each section has S
% elements.
% Noverlap = S/2 is an integer smaller than length of a Hanning
% window.
% w=S is a vector of normalized frequency.
%Fs: sampling frequency extracted from measured RTS data or computed
% from average capture or emission times.
% f is the vector of frequency at which the PSD is evaluated.
PSD_R=4*kB*T*1/gd; %Thermal noise due to the channel conductance.
newf=f(1:end);
newMypsd=myPSD(1:end);
Tot_PSD=newMypsd+PSD_R; % total PSD
figure;
loglog(newf,Tot_PSD)
hold on
xdata = f(1:end);
ydata =Tot_PSD;
maxYdata=(max(ydata));
```

```
newYdata=ydata./maxYdata;
format long e
% fit the PSD data using least square curve fitting.
x = [-1;10]; % Initial guess
options=optimset('TolFun',1e-9);
VLB=[];VUB=[];
%keep the optimization for lower and upper boundaries to optimize
% for the best fitting result.
[c,RESNORM,F,EXITFLAG,OUTPUT,LAMBDA,JACOB] =...
    lsqcurvefit('myfun',x,xdata,newYdata,VLB,VUB);
% this function used to find the fitting parameters such as:
% corner frequency (f0) and the PSD magnitude (k)
myfit=(c(1)./(1+(xdata/c(2)).^2))*maxYdata;
plot(xdata,myfit,'r','LineWidth',2);
format shortEng
c(1); % the extracted PSD magnitude from the fitting curve
c(2); % the extracted f0 from the fitting curve
title(['V_{GS}',num2str(Vgs),' V',',  T=',num2str(T),...
    ' K',', With Thermal Noise']);
text(c(2), c(1)./(1+(C2/C2).^2)*maxYdata,['\leftarrow f_{0}
=',...
    num2str(C2),' Hz'],'FontSize',12);
xlabel('Frequency (Hz) ');
ylabel('\itS_{VDS}\rm (V^2/Hz)');
hold off
```

Appendix B:

Calculation of Probability of Electron transitions as a Function of Time

Probability of capturing an electron from the channel by a defect in the silicon dioxide is:

$$P_{01} = \frac{dt}{\bar{\tau}_c} \rightarrow \bar{\tau}_c = 10^{p}(1+e^{-E})\,. \tag{1}$$

Probability of emitting trapped electron from the defect site back to the channel is:

$$P_{10} = \frac{dt}{\bar{\tau}_e} \rightarrow \bar{\tau}_e = 10^{p}(1+e^{E})\,. \tag{2}$$

Probability of finding an electron free in the channel is:

$$P_{00} = \left(1-P_{01}\right) = \left(1-\frac{dt}{\bar{\tau}_c}\right). \tag{3}$$

Probability of finding a trapped electron by defect at the SiO_2 can be expressed as:

$$P_{11} = \left(1-P_{10}\right) = \left(1-\frac{dt}{\bar{\tau}_e}\right). \tag{4}$$

Probability of finding a trap active as a function of time is:

$$P_{01}(t+dt) = P_{01}(t) * P_{11}(dt) + P_{00}(t) * P_{01}(dt) \rightarrow P_{01}(t)\left(1-\frac{dt}{\bar{\tau}_e}\right) + \left(1-P_{01}(t)\right)\frac{dt}{\bar{\tau}_c}\,. \tag{5}$$

$$\therefore P_{01}(t+dt) - P_{01}(t) = \frac{dt}{\bar{\tau}_c} - P_{01}(t)\left(\frac{1}{\bar{\tau}_c}+\frac{1}{\bar{\tau}_e}\right)dt\,. \tag{6}$$

First order differential equation is solved to find $P_{01}\left(T\right)$:

$$\frac{\partial P_{01}(t)}{\partial t} + P_{01}(t) * \left(\frac{1}{\bar{\tau}_c}+\frac{1}{\bar{\tau}_e}\right) = \frac{1}{\bar{\tau}_c}\,. \tag{7}$$

Integrating factor $e^{\int 1/\bar{\tau}_c + 1/\bar{\tau}_e}$ is multiplied by both side of the equation:

$$\frac{\partial P_{01}(t)}{\partial t}\left[e^{\int \frac{1}{\bar{\tau}_c}+\frac{1}{\bar{\tau}_e}}\right] + P_{01}(t)\left(\frac{1}{\bar{\tau}_c}+\frac{1}{\bar{\tau}_e}\right)\left[e^{\int \frac{1}{\bar{\tau}_c}+\frac{1}{\bar{\tau}_e}}\right] = \frac{1}{\bar{\tau}_c}\left[e^{\int \frac{1}{\bar{\tau}_c}+\frac{1}{\bar{\tau}_e}}\right]. \tag{8}$$

$$\therefore P_{01}(t)e^{\left(\frac{1}{\overline{\tau}_e}+\frac{1}{\overline{\tau}_c}\right)t} = \left(\frac{\overline{\tau}_e}{\overline{\tau}_e+\overline{\tau}_c}\right)e^{\left(\frac{1}{\overline{\tau}_e}+\frac{1}{\overline{\tau}_c}\right)t} + c \ . \tag{9}$$

From the assumed condition, all traps are empty at time zero $P_{01}(t=0)=0$:

$$P_{01}(t=0)=0 \rightarrow c = -\frac{\overline{\tau}_e}{\overline{\tau}_e+\overline{\tau}_c}\,. \tag{10}$$

Thus, the probability of trap to be occupied as a function of time in terms of average capture and emission time constants is:

$$P_{01}(t) = \left(\frac{\overline{\tau}_e}{\overline{\tau}_e+\overline{\tau}_c}\right)e^{-\left(\frac{1}{\overline{\tau}_c}+\frac{1}{\overline{\tau}_e}\right)t} - \frac{\overline{\tau}_e}{\overline{\tau}_e+\overline{\tau}_c}\ . \tag{11}$$

Probability of occupied trap as a function of time is:

$$P_{11}(t+dt) = P_{11}(t) * P_{00}(dt) + P_{10}(t) * P_{01}(dt) \rightarrow P_{11}(t)\left(1-P_{10}(t)\right) + P_{10}(t)\frac{dt}{\overline{\tau}_c}\ . \tag{12}$$

$$\frac{\partial P_{11}(t)}{\partial t} + P_{11}(t)\left(\frac{1}{\overline{\tau}_e}+\frac{1}{\overline{\tau}_c}\right) = \frac{1}{\overline{\tau}_c}\ . \tag{13}$$

$$\frac{\partial P_{11}(t)}{\partial t}\left[e^{\int \frac{1}{\overline{\tau}_c}+\frac{1}{\overline{\tau}_e}}\right] + P_{11}(t)\left(\frac{1}{\overline{\tau}_c}+\frac{1}{\overline{\tau}_e}\right)\left[e^{\int \frac{1}{\overline{\tau}_c}+\frac{1}{\overline{\tau}_e}}\right] = \frac{1}{\overline{\tau}_c}\left[e^{\int \frac{1}{\overline{\tau}_c}+\frac{1}{\overline{\tau}_e}}\right]. \tag{14}$$

$$P_{11}(t)e^{\left(\frac{1}{\overline{\tau}_c}+\frac{1}{\overline{\tau}_e}\right)t} = \left(\frac{\tau_e}{\overline{\tau}_c+\overline{\tau}_e}\right)e^{\left(\frac{1}{\overline{\tau}_c}+\frac{1}{\overline{\tau}_e}\right)t} + c\ . \tag{15}$$

From the condition of all traps are empty at time zero, $P_{11}(t=0) = \left(1-P_{10}(t=0)\right) = 1$

$$P_{11}(t=0)=1 \rightarrow c = \frac{\overline{\tau}_c}{\overline{\tau}_e+\overline{\tau}_c}\,. \tag{16}$$

Hence, the probability of occupied trap as a function of time is:

$$P_{11}(t) = \left(\frac{\overline{\tau}_e}{\overline{\tau}_e+\overline{\tau}_c}\right)e^{-\left(\frac{1}{\overline{\tau}_e}+\frac{1}{\overline{\tau}_c}\right)t} + \frac{\overline{\tau}_c}{\overline{\tau}_e+\overline{\tau}_c}\,. \tag{17}$$

Appendix C:

RTSSIM Code

In this appendix, the functions used to construct the RTSSIM are shown in Table 1. In addition, code for some of the functions is shown here. Complete version of RTSSIM can be downloaded from the SRC website.

Table 1 Functions of the random telegraph signals simulation for both V_{GS} and V_{DS} modes

	V_{GS} dependence		V_{DS} dependence	
#	Function	# of lines	Function	# of lines
1	RTSSIM	17	getVDSDependence	1650
2	getVGSDependence	1110	getRTScalSingAcep_VdsDependence	379
3	getCV	86	outputRTSResul2tExcel_VDSD	900
4	getTraptype	330	getRTScalSingDonor_VDSDep	365
5	getxt	192	getRTSout2Excel_VDSD	70
6	getrangerror	21	getFlickNoisCalVDep	130
7	getOutputgraph2	47	getRTScal2Ldepnd_VDSDep	600
8	Mybuggy	3	outputRTSResutl_ML_VDSD_2Excel	100
9	getRTScalSingAcep	415		
10	getVthr	20		
11	getDIN3	127		
12	getDINSecond	100		
13	get1LARTS	164		
14	get3LAARTS	220		
15	getTimeB	161		
16	getTawSeperated	70		
17	getPSD	118		
18	myfun	4		
19	getPSD2Excel	60		
20	getPSD2Excel_VDSD	54		
21	getRTSout2Excel	70		
22	output2ExcelSA1	1238		
23	getSumTotalRTS	211		
24	getPSDML2	69		
25	getRTScalSingDonor	390		
26	getRTScal2Ldepnd	640		
27	output2ExcelMLB	1410		
28	getFinalRTSPlot	58		
29	getDopping	22		
30	getFlickNoisCal	210		
31	output2ExcelFlickerNoise	550		

```
clear all
close all force;
clc
tic

%%%%%%%%%%%%%%%%%%%%%%%%%%%%%%%%%%%%%%%%%%%%%%%%%%%%%%%%%%%%%%%%%
%   RTS simulation generates RTS traces in time domain from which
the PSD is evaluated. This program is built on several physical
mechanisms to replicate the phenomenon of charging/discharging a
trap in the gate oxide of a MOSFET. RTSSIM is capable of extracting
the RTS characteristics and the electrical properties of a trap.
RTSSIM has a friendly user interface environment where several input
choices are provided for parameters. RTSSIM also exports all
generated RTS data in time and frequency domains to MS Excel files.
In addition, RTSSIM transfers all RTS and extracted trap
characteristics to MS Excel files. Please refer to the RTSSIM manual
for more information on how to use the program and what kind of
information that a user needs to have prior to the simulation at
the level of simulated device and trap.

%%%%%%%%%%%%%%%%%%%%%%%%%%%%%%%%%%%%%%%%%%%%%%%%%%%%%%%%%%%%%%%%%
%   Authors: Mohamed Nour and Zeynep Celik Butler
%
%
%   Date: 05/15/2015
%
%   version 1.0
%
%
%
%
%
%   Mohamed Nour © April 2015
%
%
%   All rights are reserved
%
%%%%%%%%%%%%%%%%%%%%%%%%%%%%%%%%%%%%%%%%%%%%%%%%%%%%%%%%%%%%%%%%%
masage= msgbox('Random Telegraph Signals Simulation (RTSSIM)',...
    'Version 1');
pause (1)

prompt={'Simulation option'};

choice =questdlg('What would you like to run RTSSIM for?',...
    'Simulation option', ...
    'Vgs dependence','Vds dependence','No');
% Handle response
system('taskkill /F /IM EXCEL.EXE');
% This will assure to close all Excel.exe running in the background.
```

```
%Otherwise, there will be a problem when it output the data to excel
% files.
switch choice
    case 'Vgs dependence'
        Simulation_choise= 1;
        VGSdependence=getVGSDependence(Simulation_choise);
    case 'Vds dependence'
        Simulation_choise = 2;
        VDSdependence=getVDSDependence(Simulation_choise);
end
toc
close(masage)
```

```
function
[AQ_inv,BQ_inv,l_eff,Tox_eff]=getCV(Vth,l,W,N_f_device,...
                              N_device,W_cap,L_cap)
%================================================================
format long
q=1.602E-19;kB=8.617e-5; kB_j=1.3806E-23;  epsi=11.9; epsox=3.9;
eps0=8.85E-14;
[filename,path]=uigetfile('*.csv','Select the CSV file');
if isequal(filename,0)
    disp('File selected not to open a file')
else
end;
data =[];
CV_file = csvread(fullfile (path, filename),22);
cv_data = [data;CV_file];

%================================================================
%% Allocate imported array to column variable names
vgs_CV = cv_data(:, 1);
CV_data = cv_data(:, 2);
Qul_Fac = cv_data(:, 3);

CV_ov=CV_data(2);
CV_inv=max(CV_data);
% This will calculate the effective channel
% length for nMOS-cap.
L_eff=L_cap*(1-CV_ov/CV_inv);% for the nMOS-cap
l_eff=l*(1-CV_ov/CV_inv);    % for the nmos device
Tox_eff=(L_eff*W_cap*epsox*eps0*N_f_device*N_device)/(CV_inv-
CV_ov);

Area=L_eff*W_cap*N_f_device*N_device; % Total area of the MOS-cap
```

```
CV_sqcm=[];
for i=1:length(vgs_CV)        % Normalized calculated capacitance
    CV_sqcm(i)=CV_data(i)/(Area);
end
CV_min=CV_sqcm(2);
Corec_CV_sqcm=[];
for i=1:length(CV_sqcm)

    Corec_CV_sqcm(i)=CV_sqcm(i)-CV_min;

end

Delta_Vgs_CV=[];Avrg_corec_CV=[];
Max_corr=max(Corec_CV_sqcm);
index_max_cor=max(find(Corec_CV_sqcm==Max_corr));

for j=1:index_max_cor-1
    Delta_Vgs_CV(j)=vgs_CV(j+1)-vgs_CV(j);
    Avrg_corec_CV(j)=(Corec_CV_sqcm(j+1)+Corec_CV_sqcm(j))/2;

end
prod_VGS_Corec_CV=[];
for jj=1:index_max_cor-1
    prod_VGS_Corec_CV(jj)=Avrg_corec_CV(jj)*Delta_Vgs_CV(jj);
end
Bef_integ_Qinv=[0 prod_VGS_Corec_CV];
Qinv_sqcm=[];
for ii=1:length(prod_VGS_Corec_CV)-1

    Qinv_sqcm(ii)=Bef_integ_Qinv(ii+1)+Bef_integ_Qinv(ii);
end
Vth_index=find(vgs_CV==closest(vgs_CV,Vth));
 xt_ary=[];
vgs_CV_ary=[];Q_inv_ary=[];
Length_vgs=min(length(vgs_CV),length(Qinv_sqcm));
for i=Vth_index:Length_vgs
    vgs_CV_Ary=vgs_CV(i);
    vgs_CV_ary=[vgs_CV_ary vgs_CV_Ary];
    Q_inv_Ary=Qinv_sqcm(i);
    Q_inv_ary=[Q_inv_ary Q_inv_Ary];
end
 fiting_equation=polyfit(vgs_CV_ary,Q_inv_ary,1);
AQ_inv=fiting_equation(1)*100;
BQ_inv=fiting_equation(2)*100;

end
-----------------------------------------------------------------
```

```
function
Val_unVal=getrangerror(Reference_value_min,Reference_value_max,..
.
    Provided_value,parameter)
pv=Provided_value;
RF_Valumin=Reference_value_min;
RF_Valumax=Reference_value_max;

if pv>=RF_Valumin && pv<=RF_Valumax
    valid_pv=pv;
    Val_unVal=0;
else
 valid_pv=errordlg('Please check your value and keep it within
the range');
    Val_unVal=1;
    Mymasage=msgbox(['The correct range for ',parameter,'
is:',...
        ' [',num2str(RF_Valumin),' - ',num2str(RF_Valumax),']']);
    a=0;
    Mybuggy(magic(3));
% An intentional error to terminate the program

end

end

-----------------------------------------------------------------

 function [output1,output2,output3,output4,output5,...
                        output6]=getOutputgraph2(choise)
output1=[];output2=[];output3=[];output4=[];output5=[];output6=0;
for i=1:length(choise)
    output=choise(i);

    switch output
        case 1
            output1=1;
        case 2
            output2=2;

        case 3
            output3=3;

        case 4
            output4=4;

        case 5
            output5=5;
```

```
        otherwise
            output6=6;
    end
end
if isempty(output1)==1 || output6==6 ;
    output1=0;
end

if isempty(output2)==1 || output6==6;
    output2=0;
end

if isempty(output3)==1 || output6==6;
    output3=0;
end
if isempty(output4)==1 || output6==6;
    output4=0;
end
if isempty(output5)==1 || output6==6;
    output5=0;
end
if isempty(output6)==1;
    output6=0;
end

end

-----------------------------------------------------------------

 function z = Mybuggy(x)
n = length(x);
z = (1:n)./x;
-----------------------------------------------------------------

 function [VFB_aray,Vthr]=getVthr(VthRomm_Temp,T,Vthr_TD,NA,Tox)
            Vthr=[]; VFB_aray=[];
        for i=1:length(T)

            if i==1
                Vthr_temp=VthRomm_Temp+Vthr_TD*(T(1)-295);
            else
                Vthr_temp=New_Vthr+Vthr_TD*(T(i)-T(i-1));
            end
            Vthr=[Vthr Vthr_temp];
            New_Vthr=Vthr_temp;
        end
```

```
       for ii=1:length(Vthr)
           Vfb=getVFB(Vthr(ii),NA,Tox,T(ii))
           VFB_aray=[VFB_aray Vfb];
       end

end
-------------------------------------------------------


 function
[Taw_c,Taw_e,Amplitued,n_inv_v,V_ther,eta_T,D_ECT,Phis,...
    sigmao,E_relax,Delta_ECFB,mn,Nc,SR]=getDIN3(VGS,...
    VDS, Temp,NA,Width,Length,Tox,position_along_channel,...
    Threshold_voltage,VFB,xt,DEcox_ET,Delta_EB,K_1,K_2,A,B,...
    AQinv,BQinv,Trap_Type,NewC_inv,Cox_triangle)

format long e
%=================================================================
% This function calculates the average capture and emission times
% The foundation of RTS parameters are calculated here. The
output % of this function is fed into other RTSSIM functions.
%=================================================================
Vgs=VGS;
Vds=VDS;
T=Temp;
W=Width;
L=Length;
Tox=Tox;
Vthr=Threshold_voltage;
y=position_along_channel;
Del_Ecox_ET=DEcox_ET;
q=1.602E-19;kB=8.617e-5; kB_j=1.3806E-23;
Ev=0.0;h=6.626E-34; h_ev=4.135E-15;  m0=9.110E-31; % in kg
hprime=h/(2*pi);
Nco=2.90E19; % per cm3
pho=3.13; %VFB=-1.2;
ga=4; g=1; Ea_Ev=0.045;%in eV
epsi=11.9; epsox=3.9; eps0=8.85E-14;  % (F/cm)
vt=(kB_j*T)/q;
%=================================================================
mn=m0*(1.0533+0.00012*T); % electron mass as a function of
                          % temperature
mp=m0*(0.6135+0.00269*T-(3E-6)*T^2);
E_gap=1.166-((T^2)*4.730E-4)/(T+636);
% energy band gap as a function of temperature
Nc=2*((2*pi*mn*kB_j*T)/(h^2))^(3/2)*1E-6;
% State density around to the conduction band edge
Nv=2*(2*(pi*mp*kB_j*T)/(h^2))^(3/2)*1E-6;
% State density around to the valance band edge
ni=sqrt(Nc*Nv)*exp(-E_gap/(2*kB*T));% Intrinsic concentration
Vth=sqrt((8*kB_j*T)/(pi*mn))*100;   % Thermal velocity in cm
```

```
V_ther=Vth;
%==================================================================
% Majority carrier density as a function of temperature
po=(-1+sqrt(1+...

4*NA*(ga/Nv)*exp((Ea_Ev)/(kB*T))))/(2*(ga/Nv)*exp((Ea_Ev)/(kB*T))
);
Ef=kB*T*log(po/ni);
n0=(ni^2)/po;
Cox=((eps0*epsox)/Tox); %F/cm2

if AQinv~=0 && BQinv~=0
    Qinv=AQinv*Vgs+BQinv; %Ninv*q;
elseif AQinv==0 && BQinv==0 && NewC_inv==0
    Qinv=Cox*(Vgs-Vthr);
elseif AQinv==0 && BQinv==0 && NewC_inv~=0
    Qinv=Cox_triangle+NewC_inv*(Vgs-Vthr);
end

if Vgs<Vthr     % To check the device operation
    error('Device is simulated in cut-off region, please increase
Vgs')
end

Ninv=Qinv/q;
if (Vgs-Vthr)>VDS
    gd=abs(A*Vgs+B);   %Voltage dependence of channel conductance
                        %linear region
    mob=gd/((W/L)*Qinv);%Mobility in the linear region
    SR=((4*kB_j*T)/gd); %Thermal noise
elseif (Vgs-Vthr)<=VDS
    gd=abs(A*Vgs+B);   %Voltage dependence of channel conductance
                        %saturation region
    moblin=gd/((W/L)*Qinv); %Mobility in the linear region
    un=moblin;
    gm_sat=moblin*Cox*W/L*(Vgs-VFB-2*Ef-(q*po*epsi*eps0)...
        /(Cox^2)*(sqrt(1+2*(Cox^2)*(Vgs-VFB)/(q*po*epsi*eps0))-
1));
    u_sat=gm_sat/(Cox*(W/L)*(Vgs-Vthr));
    mob=u_sat;                % Mobility in the saturation region
    SR=((4*kB_j*T)/gd);       % Thermal noise
end

LD=((epsi*eps0*vt)/(q*po))^0.5;
a_c=(sqrt(2)*epsi*eps0*kB_j*T)/(LD*q^2);

syms phi                      % Solving for surface potential
phis0=solve(a_c*sqrt(phi/vt+exp(-phi/vt)-1+(ni/po)^2*...
```

```
    (exp(phi/vt)-phi/vt-1))-po*sqrt((2*epsi*eps0*phi)/(q*po))-
Ninv);

phiS=double(phis0)-(y*q/(L)*Vds);
N_v=n0*exp(phiS*q/(kB_j*T));
n_v=N_v;
n_inv_v=n_v;
Delta_ECFB=E_gap-E_gap/2+kB_j*T/q*log(po/ni);
Delta_ECFs=kB*T*(log(Nc/n0)-phiS/(kB*T));

eta=Nco*sqrt((8*kB_j)/(pi*mn))/100;
eta_T=eta;
RXT=xt/Tox;

% Ratio of average capture to emission times
RlnTc_Te=-(q/(kB_j*T))*(Del_Ecox_ET-Delta_ECFB-
pho+phiS+xt/Tox*(Vgs-...
    VFB-phiS));
kB_cm=1.3806E-19;
D_ECT=kB*T*((log((Nc*sqrt((8*kB_cm*T)/(pi*mn)))/(n_inv_v*V_ther))
-...
    RlnTc_Te));
DETF=real(kB*T*log(RlnTc_Te));
% Energy difference between trap and Fermi energy level
E_relax=real(D_ECT+2*Delta_EB+2*sqrt(Delta_EB*(Delta_EB+D_ECT)));
% Solve for relaxation energy
Xd=sqrt((2*epsi*eps0*phiS)/(q*po));
F_surf=(q*po*Xd)/(epsi*eps0);
hprim_ev=h_ev/(2*pi);
E_e=(hprime^2/(2*mn))^(1/3)*((9/8*pi*q*F_surf)^(2/3))*1/q;
sigmao=sqrt(E_e/E_relax)*(pi^2)/(2*exp(1))*(hprime^2/(2*mn*kB_j*T
));

taw_c=1/(sigmao*Vth*n_v)*exp(Delta_EB/(kB*T));
taw_e=1/(sigmao*sqrt(8*kB_cm*T/(pi*mn))*Nc)*exp((Delta_EB+D_ECT)/
...(kB*T));
cal_RTc_Te=taw_c./taw_e;
Phis=phiS;
alpha=K_1+K_2*log(Ninv*W*L);% Screened scattering coefficient
 if taw_c<500 && taw_e<500 && taw_c>1e-8 && taw_e>1e-8
    Taw_c=taw_c;
    Taw_e=taw_e;
else
    for i=1:5
        display(' ');
    end
    V_gs=VGS
    Temprature=T
    Tawc=taw_c
    Tawe=taw_e
```

```
    error('Average capture and emission times out of range,
please provide realistic values to RTSSIM')


end

if Trap_Type==1     % To differentiate between acceptor and donor
    Amplitued=Vds*abs(1/(W*L)*(1/Ninv+alpha*mob));
elseif Trap_Type==2
    Amplitued=Vds*abs(1/(W*L)*(1/Ninv-alpha*mob));
end

Avg_Taw=(Taw_c*Taw_e)/(Taw_c+Taw_e);
F0=1/(2*pi*Avg_Taw);
K=(4*(Amplitued^2)*(Avg_Taw^2))/(Taw_c+Taw_e);

end
 -----------------------------------------------------------------

function
[New_RTS,New_RMag_RTS]=get1LARTS(Number_trans,Freq_samp,Taw_c,...
    Taw_e, State0, State1,VGS,Trapnumber,output1,Temp,Ampli,...
    SetOrder,type,Simulation_mode,Direction)

% This function generates the RTS sample data based on Poisson
% distribution, the average capture and emission times that
% were calculated by getDIN3 function controls the Poisson
% statistics and the entire process of producing RTS samples.
% Calculating the average capture and emission times are important
% to reconstruct the RTS in time and frequency domains from which
% the trap characteristics are extracted.

T=Temp;
if Direction ==1
    Direc=', FM';
elseif Direction ==2
    Direc=', RM';
end
if SetOrder==1
    orderSet='_{First Set}';
elseif SetOrder==2
    orderSet='_{Second Set}';
end
if type==1% Setting the graph title to either SA, SD, % or a AA.
    tit='SA';
elseif type==2
    tit='SD';
elseif type==3
    tit='AA';
```

```
end
N=Number_trans;
taw_1=Taw_c;
taw_2=Taw_e;
i_MC=0;
Fs=Freq_samp;
FS=Freq_samp;
Sod=1;       % State of odd transition, when it goes from 0 to 1
Sev=1;       % State of even transition, when it goes from 1 to 0
countdow=0;
countdup=0;
countd3=0;
Time=0;
RTS=[];RMag_RTS=[];
c12=0;c21=0;c23=0;c32=0;
New_p23=[];New_p21=[];
rts11=[];rts12=[];
time=[];vod=0; vev=0;v3=0; New_p12=[];

for K=1:N    % K is number of transitions
    if  (rem(K,2)==0)
            % Transition form level 1 to level 0, even transition
        State= State1;
        sev=rand;
% generate random number from normal distribution between 0 and 1
        tev=-log(sev)*taw_2;
        vev=vev+tev;
% this is accumulative process to move to next point
        countdup=countdup+1;
% keep tracking of transition number when it goes to upper state
        Current_Num_sampev=ceil(vev*Fs);
% this is the number of events in each Poisson process
        New_curent_number_sampleev=Current_Num_sampev-Sev;
% subtract the current new sample from previous

Array_Num_Sampev=State*ones(1,New_curent_number_sampleev);
% this turns the generated sample into real RTS data
% when it is multiplied with the state and save it
        RTS=[RTS 1*Array_Num_Sampev];
% populating the RTS array
        RMag_RTS=[RMag_RTS 1*Array_Num_Sampev*Ampli];
% multiplying the populated RTS array with real magnitude of RTS
        Sev=Current_Num_sampev;
% Setting Sev to the current sample number where it will be
% subtracted latter from the new generated sample number
        Time=(New_curent_number_sampleev)/Fs;
% keep tracking time duration for each Poisson process. This is
% important to evaluate the probability when it comes to complex
% RTS.
        rts12=[rts12 State*Array_Num_Sampev];
```

```
        time=[time Time];
        c21=c21+1;
    else % This is exactly similar to the previous explanations,
         % except it generates sample data for level 0.
         % At time zero all traps are considered empty.
        State= State0;
        sod=rand;
        tod=-log(sod)*taw_1;
        vod=vod+tod;
        countdow=countdow+1;
        Current_Num_sampod=ceil(vod*Fs);
        New_curent_number_sampleod=Current_Num_sampod-Sod;

Array_Num_Sampeod=State*ones(1,New_curent_number_sampleod);
        RTS=[RTS State*Array_Num_Sampeod];
        RMag_RTS=[RMag_RTS State*Array_Num_Sampeod*Ampli];
        Sod=Current_Num_sampod;
        Time=(New_curent_number_sampleod)/Fs;
        rts11=[rts11 State*Array_Num_Sampeod];
        time=[time Time];
        c12=c12+1;
    end

    Time=0;
    p12=taw_1/(taw_1+taw_2)*(1-exp(-(1/taw_1+1/taw_2)*Time));
    New_p12=[New_p12 p12];
end

New_RTS1{1}=RTS;
RMag_RTS1{1}=RMag_RTS;
Vod=0;
Vev=0;
RTS=[];
RMag_RTS=[];

for jj=1:length(New_RTS1)
                        % Plot the RTS data in time domain
       if output1==1
        figure;
        t1{jj}=[1:length(New_RTS1{jj})]/Fs;
        plot(t1{jj},RMag_RTS1{jj})

        if Simulation_mode==1
            title(['RTS due to ',tit,orderSet,'-
',num2str(Trapnumber),...
                ', \itV_{GS}\rm= ',num2str(VGS),' V, T =
',num2str(T),...
                ' K',Direc]);
        else
```

```
            title(['RTS due to ',tit,orderSet,'-
',num2str(Trapnumber),...
                ', \itV_{DS}\rm= ',num2str(VGS),' V, T =
',num2str(T),...
                ' K',Direc]);
        end
        xlabel('Time(s)');
        ylabel('\DeltaV_{DS} (V)')
        xlim('auto');
        ylim('auto');
    else
        disp('User requested not to display RTS in time domain')
        t1{jj}=[1:length(New_RTS1{jj})]/Fs;
    end
end
%================================================================
New_t=t1{jj};
vd=1;
G=1/vd; % Normalized voltage
t3 = New_t';
v = New_RTS1{jj};
New_v=RMag_RTS1{jj};
v3=v/(G*vd)';
New_RTS=v;
New_RMag_RTS=New_v;
i_MC=i_MC+1;
end
----------------------------------------------------------------
 function
taw=getTawSeperated(Data,Array_average_time,FS,Number_Of_Bin,...
    Transition,VGS,Trapnumber,output2,Temp,SetOrder,typeTrap,...
    Simulation_mode,Direction)

if Direction ==1
    Direc=', FM';
elseif Direction ==2
    Direc=', RM';
end

if typeTrap==1% to set the graph title for either single acceptor
              % or single donor
    tit='SA';
elseif typeTrap==2
    tit='SD';
elseif typeTrap==3
    tit='AA';
end

if SetOrder==1
    orderSet='_{First Set}';
```

```
elseif SetOrder==2
    orderSet='_{Second Set}';
end
  % This will return the histogram of the Poisson events that
  % were generated from each level.
[hh,xout]=hist(Array_average_time,Number_Of_Bin);
numer_0f_bins=xout';  % Total bins
freq_Magnitude=hh';

for i=20:5:200
 % This will return total bins were generated and its frequency
    [HH,Xout]=hist(Array_average_time,i);
    Num_Bin=Xout';  % Total bins
    Freq_Mag=HH';
    for j=1:length(Num_Bin)
        Mul_Taw_With_frequen(j,1)=Num_Bin(j,1)*Freq_Mag(j,1);
        j=j+1;
    end
    t1=[1:length(Data)]/FS;
    Delta_T=t1(1,2)-t1(1,1);
    T=Delta_T;
    T=[T,(sum(Mul_Taw_With_frequen))/(sum(Freq_Mag))];

end

if output2==2

% Output the histogram for each level with the proper title and
% simulated trap number
    figure;
    hist(Array_average_time,Number_Of_Bin);
    showfit exp;
    if Simulation_mode==1
        title(['Histogram of a Poisson set of frequencies: ',...
            int2str(Transition),', ',tit,orderSet,'-',...
            num2str(Trapnumber),',  \itV_{GS}\rm =
',num2str(VGS),' V',...
            ', \itT\rm=',num2str(Temp),' K',Direc]);


    else
        title(['Histogram of a Poisson set of frequencies: ',...
            int2str(Transition),', ',tit,orderSet,'-',...
            num2str(Trapnumber),',  \itV_{DS}\rm =
',num2str(VGS),' V',...
            ', \itT\rm=',num2str(Temp),' K',Direc]);
    end

    xlabel('Time (s) ');
    ylabel('Frequency ');
```

```
else
    disp('User requested not to display hist graph Vs. time')
end

for i=1:length(freq_Magnitude)

Multib_taw_with_frequen(i,1)=numer_0f_bins(i,1)*freq_Magnitude(i,
1);
end
taw=(sum(Multib_taw_with_frequen))/(sum(freq_Magnitude));
end
-----------------------------------------------------------------
function F = myfun(c,f)
F = c(1)./(1+(f/c(2)).^2);
end
-----------------------------------------------------------------
function
Result_output=getPSD2Excel(inpVgs,T,Y,Comb_order,Trap_Num,...
    Direction)
vGS=inpVgs;
Tempre=T;
       % This function will transfer PSD data into MS Excel files
if Direction ==1
    Direc='FM';
elseif Direction ==2
    Direc='RM';
end

if Comb_order==1
    Trap_type='First_SA';
elseif Comb_order==2
    Trap_type='Second_SA';
elseif Comb_order==3
    Trap_type='First_SD';
elseif Comb_order==4
    Trap_type='Second_SD';
elseif Comb_order==5
    Trap_type='First_AA';
elseif Comb_order==6
    Trap_type='Second_AA';
elseif Comb_order==7
    Trap_type='Total_PSD';
end

Trapnumb=num2str(Trap_Num);
trapnumb=Trapnumb;
VGS=num2str(vGS,'%0.1f');
Temp=num2str(Tempre,'%0.1f');
Excel = actxserver ('Excel.Application');
```

```
CDIR=pwd; % This will return the current folder and the full path
          % name of the used file
File=fullfile(CDIR,'OutputPSD.xls');
% Assigning the full path name to File
if ~exist(File,'file')
    ExcelWorkbook = Excel.workbooks.Add;
    ExcelWorkbook.SaveAs(File,1);
    ExcelWorkbook.Close(false);
end
WB=invoke(Excel.Workbooks,'Open',File);
filename=File;

try
    WB.Worksheets.Item('Sheet2').Delete
catch
    ;
end

try
    WB.Worksheets.Item('Sheet3').Delete
catch
    ;
end

sheetname=sprintf('%s_%s_%s_T=%s_Vgs=%s',Direc,Trap_type,trapnumb
,Temp,VGS);
% Print sheet name for each bias and temperature condition
% as well as the simulation mode and simulated trap number
Varibale_name={'F (Hz)' 'Sv (V^2/Hz)'};
xlswrite2007(filename,Varibale_name, sheetname);
xlswrite2007(filename,Y,sheetname,'A2');
WS=Excel.sheets;
SN=WS.count;
WB.Worksheets.Item(SN).Range('A1:B1').Interior.ColorIndex = 6;
WB.Worksheets.Item(SN).Range('A1:B1').ColumnWidth=15;
WB.Worksheets.Item(SN).Range('A1:B10000').HorizontalAlignment = -
4108;
Excel.ActiveWorkbook.Save;
Excel.Quit
end
-----------------------------------------------------------------

function
Result_output=getPSD2Excel_VDSD(inpVgs,T,Y,Comb_order,Trap_Num,Di
rection)
vGS=inpVgs;
Tempre=T;
if Direction ==1
    Direc='FM';
```

```
elseif Direction ==2
    Direc='RM';
end

if Comb_order==1
    Trap_type='First_SA';
elseif Comb_order==2
    Trap_type='Second_SA';
elseif Comb_order==3
    Trap_type='First_SD';
elseif Comb_order==4
    Trap_type='Second_SD';
elseif Comb_order==5
    Trap_type='First_AA';
elseif Comb_order==6
    Trap_type='Second_AA';
elseif Comb_order==7
    Trap_type='Total_PSD';
end

Trapnumb=num2str(Trap_Num);
trapnumb=Trapnumb;
VGS=num2str(vGS,'%0.1f');
Temp=num2str(Tempre,'%0.1f');

Excel = actxserver ('Excel.Application');
CDIR=pwd;
File=fullfile(CDIR,'OutputPSD.xls');

if ~exist(File,'file')
    ExcelWorkbook = Excel.workbooks.Add;
    ExcelWorkbook.SaveAs(File,1);
    ExcelWorkbook.Close(false);
end
WB=invoke(Excel.Workbooks,'Open',File);

try
    WB.Worksheets.Item('Sheet2').Delete
catch
    ;
end

try
    WB.Worksheets.Item('Sheet3').Delete
catch
    ;
end

filename=File;
```

```
sheetname=sprintf('%s_%s_%s_T=%s_Vds=%s',Direc,Trap_type,trapnumb
,Temp,...
    VGS);
Varibale_name={'F (Hz)' 'Sv (V^2/Hz)'};
xlswrite2007(filename,Varibale_name, sheetname);
xlswrite2007(filename,Y,sheetname,'A2');
WS=Excel.sheets;
SN=WS.count;
WB.Worksheets.Item(SN).Range('A1:B1').Interior.ColorIndex = 6;
WB.Worksheets.Item(SN).Range('A1:B1').ColumnWidth=15;
WB.Worksheets.Item(SN).Range('A1:B10000').HorizontalAlignment = -
4108;
Excel.ActiveWorkbook.Save;
Excel.Quit
end
-----------------------------------------------------------------

function
result=getRTSout2Excel(inpVgs,T,RMagRTS_T,Fs,Comb_order,...
    Trap_Num,Direction)
vGS=inpVgs;
Tempre=T;
     % Output the RTS data in time domain to MS Excel file

if Direction ==1
    Direc='FM';
elseif Direction ==2
    Direc='RM';
end

if Comb_order==1
    Trap_type='First_SA';
elseif Comb_order==2
    Trap_type='Second_SA';
elseif Comb_order==3
    Trap_type='First_SD';
elseif Comb_order==4
    Trap_type='Second_SD';
elseif Comb_order==5
    Trap_type='First_AA';
elseif Comb_order==6
    Trap_type='Second_AA';
elseif Comb_order==7
    Trap_type='Total_PSD';
end

Trapnumb=num2str(Trap_Num);
trapnumb=Trapnumb;
Excel = actxserver ('Excel.Application');
CDIR=pwd;
```

```
File=fullfile(CDIR,'OutputRTSData.xls');
if ~exist(File,'file')
    ExcelWorkbook = Excel.workbooks.Add;
    ExcelWorkbook.SaveAs(File,1);
    ExcelWorkbook.Close(false);
end
WB=invoke(Excel.Workbooks,'Open',File);
filename=File;
try
    WB.Worksheets.Item('Sheet2').Delete;
catch

end
try
    WB.Worksheets.Item('Sheet3').Delete;
catch

end

for i=1:length(T)
    for ii=1:length(inpVgs)
        RTS_mat=(RMagRTS_T{i}{ii})';
        Time_mat=([1:length(RMagRTS_T{i}{ii})]/Fs{i}(ii))';
        HL=64000;% This will ensure the length of the data does
                 % not exceed 64000 pointes, since MS Excel 2007
                 % has a limit for maximum rows
        if length(RTS_mat)<HL
            Y=[ Time_mat,RTS_mat];
        else
            Y=[ Time_mat(1:HL), RTS_mat(1:HL)];
        end
        VGS=num2str(vGS(ii),'%0.1f');
        Temp=num2str(Tempre(i),'%0.1f');

sheetname=sprintf('%s_%s_%s_T=%s_Vgs=%s',Direc,Trap_type,...
            trapnumb,Temp,VGS);
        Varibale_name={'Time (s)' 'Voltage (V)'};
        xlswrite2007(filename,Varibale_name, sheetname);
        xlswrite2007(filename,Y,sheetname,'A2');
        WS=Excel.sheets;
        SN=WS.count;
        WB.Worksheets.Item(SN).Range('A1:B1').Interior.ColorIndex
= 6;
        WB.Worksheets.Item(SN).Range('A1:B1').ColumnWidth=15;

WB.Worksheets.Item(SN).Range('A1:B1000').HorizontalAlignment = -
4108;
    end
end
Excel.ActiveWorkbook.Save;
```

```
Excel.Quit
end
-----------------------------------------------------------------
function [mypsd]=getPSDML2(RTS_data,FS,T,inpVgs,tit,SR_mat,...
    Simulation_mode,Direction)

if Direction ==1
    Direc=', FM';
elseif Direction ==2
    Direc=', RM';
end

if tit==1
    Tit='PSD due to SA';
elseif tit==2
    Tit='PSD due to SA & SA';
elseif tit==3
    Tit='PSD due to SA & AA';
elseif tit==4
    Tit='PSD due to AA ';
elseif tit==5
    Tit='PSD due to AA & SA ';
elseif tit==6
    Tit='PSD due to AA & AA ';
elseif tit==7
    Tit='PSD due to SA & SD ';
elseif tit==8
    Tit='PSD due to AA & SD ';
elseif tit==9
    Tit='PSD due to SD & SA ';
elseif tit==10
    Tit='PSD due to SD & AA ';
elseif tit==11
    Tit='PSD due to SD & SD ';
elseif tit==12
    Tit='PSD based on the summation of the RTS';
elseif tit==13
    Tit='PSD due to SD & SD';
end
if Simulation_mode==1
    Tit2=', \itV_{GS}\rm= ';
elseif Simulation_mode==2
    Tit2=', \itV_{DS}\rm= ';
end

f0_calary=[];f0_calary2=[];
for i=1:length(RTS_data)

    for ii=1:length(RTS_data{i})
        w=floor(length(RTS_data{i}{ii})/20);
```

```
        [myPSD,f]=pwelch(RTS_data{i}{ii},hanning(w),w/3,w,FS);

        newf=f(4:end);
        newMypsd=myPSD(4:end);
        Tot_PSD=newMypsd+SR_mat{i}(ii);
        figure;
        plot(f(4:end),(Tot_PSD))
        title([Tit,Tit2,num2str(inpVgs(ii)),'V',',  T=',...
            num2str(T(i)),'K',', With Thermal Noise',Direc])
        xlabel('Frequency (Hz) ');
        ylabel('S_{v}(V^2/Hz)');
        set(gca, 'xscale', 'log');
        set(gca, 'yscale', 'log');
    end
end
mypsd='Done';
end
-----------------------------------------------------------------
 function
finalPlot=getFinalRTSPlot(RTS,T,inpVgs,tit,Simulation_mode,...
    Direction)
Fs=1E4;
if Direction ==1
    Direc=', FM';
elseif Direction ==2
    Direc=', RM';
end

if tit==1
    Tit='RTS due to SA';
elseif tit==2
    Tit='RTS due to SA & SA';
elseif tit==3
    Tit='RTS due to SA & AA';
elseif tit==4
    Tit='RTS due to AA ';
elseif tit==5
    Tit='RTS due to AA & SA ';
elseif tit==6
    Tit='RTS due to AA & AA ';
elseif tit==7
    Tit='RTS due to SA & SD ';
elseif tit==8
    Tit='RTS due to AA & SD ';
elseif tit==9
    Tit='RTS due to SD & SA ';
elseif tit==10
    Tit='RTS due to SD & AA ';
elseif tit==11
    Tit='RTS due to SD & SD ';
```

```
elseif tit==12
    Tit='Resultant RTS due to SA ';
elseif tit==13
    Tit='Resultant RTS due to SD ';
elseif tit==14
    Tit='Resultant RTS due to AA ';
end

if Simulation_mode==1
    Tit2=' at V_{GS}= ';
elseif Simulation_mode==2
    Tit2=' at V_{DS}= ';
end
for i=1:length(RTS)

    for ii=1:length(RTS{i})
        figure;
        t1=[1:length(RTS{i}{ii})]/Fs;
        plot(t1,RTS{i}{ii})
        title([Tit,Tit2,num2str(inpVgs(ii)),'V',', \itT\rm=',...
            num2str(T(i)),'K',Direc]);
        xlabel('Time(s)');
        ylabel('\Delta\itV_{DS}\rm (V)');
        xlim('auto');
        ylim('auto');

        finalPlot='ploting RTS due to multiple active traps is
completed';
    end
end
end
-----------------------------------------------------------------
function
Neff=getDopping(y,Substrate_dopping,Nhalo,channel_length,...
    Halo_length)
Nch=Substrate_dopping;
L=channel_length;
Lhalo=Halo_length;
pos=y/L;

if pos<L-Lhalo && pos>Lhalo
    Neff=Nch;
elseif pos<=Lhalo
    Neff=Nhalo;
else
    Neff=Nhalo;
end
end
```

References

[1] A. Ghetti, C. M. Compagnoni, F. Biancardi, A. L. Lacaita, S. Beltrami, L. Chiavarone, A. S. Spinelli, and A. Visconti, “Scaling trends for random telegraph noise in deca-nanometer flash memories,” *IEDM*, pp. 835-838, 2008.

[2] S. Realov, and K. L. Shepard, “Analysis of random telegraph noise in 45-nm CMOS using on-chip characterization system,” *IEEE Trans. Electron Dev.*, vol. 60, no. 5, pp. 1716 – 1722, 2013.

[3] M. H. Tsai, T. P. Ma, and T. B. Hook, “Channel length dependence of random telegraph signal in sub-micron MOSFET’s,” *IEEE Trans. Electron Dev.*, vol. 15, p. 504, 1994.

[4] C. Q. Wei, Y. Z. Xiong, X. Zhou, and L. Chan, “A technique for constructing RTS noise model based on statistical analysis”, *NSTI-Nanotech*, vol. 3, p. 885, 2008.

[5] A. G. Mahmutoglu, and A. Demir, “Modeling and analysis of nonstationary low – frequency noise in circuit simulators: enabling non Monte Carlo techniques,” *ICCAD* 14, p. 309, 2014.

[6] M. Jamal Deen, S. Majumder, O. Marinov, and M. M. El-Desouki, “Random telegraph signal noise in CMOS active pixel sensors,” *ICNF*, p. 208, 2011.

[7] V. Goiffon, P. Magnan, P. M. Gonthier, C. Virmontois, and M. Gaillardin, “Evidence of a novel source of random telegraph signals in CMOS image sensors,” *IEEE Electron Device Lett.* , vol. 32, p. 773, 2011.

[8] E. A. M. Klumperink, S. L. J. Gierkink, A. P. Van der Wel, and B. Nauta, “Reducing MOSFET 1/*f* noise and power consumption by switched biasing,” *IEEE J. Solid-State Circuits*., vol. 35, p. 994, 2000.

[9] G. I. Wirth, R. D. Silva, and R. Brederlow, “Statistical model for the circuit bandwidth dependence of low-frequency noise in deep-submicrometer MOSFETS,” *IEEE Trans. Electron Dev.*, vol. 54, no. 2, p. 340, 2007.

[10] E. Simoen, J. W. Lee, and C. Claeys, “Assessment of the impact of inelastic tunneling on the frequency-depth conversion from low-frequency noise spectra,” *IEEE Trans. Electron Dev.*, vol. 61, no. 2, p. 634, 2014.

[11] C. Leyris, F. Martinez, M. Valenza, A. Hoffmann, J. C. Vildeuil, and F. Roy, “Impact of random telegraph signal in CMOS image sensors for low-light levels,” *ESSCIRC*, p. 376, 2006.

[12] N. Zanolla, D. Siprak, M. Tiebout, P. Baumgartner, E. Sangiorgi, and C. Fiegna, “Reduction of RTS noise in small-area MOSFETs under switched bias conditions and forward substrate bias,” *IEEE Trans. Electron Dev.*, vol. 57, p. 119, 2010.

[13] T. Nagumo, K. Takeuchi, S. Yokogawa, K. Imai, and Y. Hayashi, “New analysis methods for comprehensive understanding of random telegraph noise,” *IEDM*, pp. 32.1.1-32.1.4, 2009.

[14] F. M. Puglisi, and P. Pavan, “RTN analysis with FHMM as a tool for multi-trap characterization in HfO_X RRAM,” *EDSSC*, p.1, 2013.

[15] H. Awano, H. Tsutsui, H. Ochi, and T. Sato, “Bayesian estimation of multi-trap RTN parameters using Markov chain Monte Carlo method,” *IEICE Trans. Fundamentals*, vol. E95-A, no. 12, pp. 2272 - 2283, 2012.

[16] R. D. Silva, L. C. Lamb, and G. I. Wirth, “Collective Poisson process with periodic rates: applications in physics from micro-to nanodevices,” *Phil. Trans. R. Soc. A*, vol. 369, p. 307, 2011.

[17] Y. Ye, C. C. Wang, and Y. Cao, “Simulation of random telegraph noise with 2-stage equivalent circuit,” *ICCAD*, pp. 709 – 713, 2010.

[18] Y. Son, T. Kang, S. Park, and H. Shin, “A simple model for capture and emission time constants of random telegraph signal noise,” *IEEE Trans. Nanotechnol.*, vol. 10, no. 6, p. 1352, 2011.

[19] T. Grasser, W. Goes, Y. Wimmer, F. Schanovsky, G. Rzepa, M. Waltl, K. Rott, H. Reisinger, V. V. Afanas’ev, A. Stesmans, A. M. El-Sayed, and A. L. Shluger, “On the microscopic structure of hole traps in pMOSFETs,” *IEDM*, p. 530, 2014.

[20] R. D. Silva, G. I. Wirth, and L. Brusamarello, “A novel and precise time domain description of MOSFET low frequency noise due to random telegraph signals,” *Int. J. Mod. Phys. B*, vol. 24, no. 30, pp. 5885-5894, 2010.

[21] Z. Çelik-Butler, and Y. Hsiang, “Spectral dependence of $1/f^{\gamma}$ noise on gate bias in N-MOSFETS,” *Solid-State Electron*., vol. 30, no. 4, pp. 419-423, 1987

[22] K. K. Hung, P. K. KO, C. Hu, and Y. C. Cheng, “A unified model for the flicker noise in metal-oxide-semiconductor field effect transistors,” *IEEE Trans. Electron Dev.*, vol. 37, no. 3, p. 654, 1990.

[23] G. Groeseneken, H. E. Maes, N. Beltran, and R. F. D. Keersmaecker, “A reliable approach to charge – pumping measuremntes in MOS transistors,” *IEEE Trans. Electron Dev.*, vol. ED-31, no. 1, pp. 42 - 53, 1984.

[24] F. Martinez, C. Leyris, G. Neau, M. Valenza, A. Hoffmann, J. C. Vildeuil, E. Vincent, F. Boeuf, T. Skotnicki, M. Bidaud, D. Barge, and B. Tavel, “Oxide traps characterization of 45 nm MOS transistors by gate current R.T.S. noise measurements,” *Microelectron. Eng.*, vol.80, p. 54, 2005.

[25] C. Leyris, F. Martinez, M. Valenza, A. Hoffmann, J C. Vildeuil, “Random telegraph signal: A sensitive and nondestructive tool for gate oxide single trap characterization,” *Microelectron. Reliab.,* vol.47, pp. 573 - 576, 2007.

[26] T. B. Tang, A. F. Murray, and S. Roy, “Methodology of statistical RTS noise analysis with charge-carrier trapping models,” *IEEE Trans. Circuits Syst.* I, *Reg. Papers*, vol. 57, no. 5, pp. 1062-1070, 2010.

[27] C. D. Motchenbacher, and J. A. Connelly, Low-noise electronic system design, *John Wiley & Sons, Inc*., 1993.

[28] W. M. Leach, “Fundamentals of low-noise analog circuit design,” *Proc. IEEE* , vol. 82, no. 10, p. 1515, 1994.

[29] C. Toumazou, G. Moschytz, and B. Gilbert, Trade-off in analog circuit design, New York, Kluwer Academic Publishers, 2002.

[30] J. B. Johnson, “Thermal Agitation of Electricity in Conductors,” *Phys. Rev*., vol. 32, pp. 97-109, 1928.

[31] H. Nyquist, “Thermal Agitation of Electric Charge in Conductors,” *Phys. Rev*., vol. 32, pp. 110-113, 1928.

[32] M. V. Haartman, and M. Ostling, low-frequency noise in advance MOS devices, Netherland, Springer, 2007.

[33] A. Gover, A. Nause, E. Dyunin, and M. Fedurin, “Beating the shot-noise limit,” *Nat. Phys.*, vol. 8, p. 877, 2012.

[34] G. D. Boreman, Basic electro-optics for electrical engineering, vol. TT31, Bellingham, Washington, The Society of Photo – Optical Instrumentation Engineers, 1998.

[35] J. Lee, G. Bosman, K. R. Green, and D. Ladwig, “Noise model of gate-leakage current in ultrathin oxide MOSFETs,” *IEEE Trans. Electron Dev.*, vol. 50, pp. 2499 - 2506, 2003.

[36] C. Fiegna, “Analysis of gate shot noise in MOSFETs with ultrathin gate oxides,” *IEEE Trans. Electron Dev.*, vol. 24, pp. 108-110, 2003.

[37] D. K. Schroder, *Semiconductor Material and Devices Characterization*, *John Wiley & Sons Inc*., 3rd edition, 2006.

[38] G. Ghibaudo, “On the theory of carrier number fluctuation in MOS devices,” *Solid State Electron*., vol. 32, pp. 563-565, 1989.

[39] O. R. D. Buisson, G. Ghibaudo, and J. Brini, “Model for drain current RTS amplitude in small-area MOS transistors,” *Solid State Electron.*, vol. 35, pp. 1273-1276, 1992.

[40] A. Asenov, R. Balasubramaniam, A. R. Brown, and J. H. Davies, “RTS amplitudes in decananometer MOSFETs: 3—D simulation study,” *IEEE Trans. Electron Dev.*, vol. 50, pp. 839 -845, 2003.

[41] K. K. Hung, P. K. Ko, C. Hu, Y. C. Cheng, “Random telegraph noise of deep-submicrometer MOSFET’s,” *IEEE Electron Device Lett.*, vol. 11, pp. 90-92, 1990.

[42] M. J. Kirton, and M. J. Uren, “Noise in solid-state microstructures: A new perspective on individual defects, interface states and low-frequency ($1/f$) noise,” *Adv. Phys.*, vol. 38, no. 4, pp. 367 - 468, 1989.

[43] Z. Shi, J.-P. Mieville, and M. Dutoit, “Random telegraph signals in deep submicron n-MOSFET's,” *IEEE Trans. Electron Devices* , vol. 41, pp. 1161-1168, 1994.

[44] B. V. Zeghbroeck. (2011). *Principles of semiconductor devices* [Online]. Available: http://ecee.colorado.edu/~bart/book/.

[45] P. M. Gonthier, V. Goiffon, and P. Magnan, “In-pixel source follower transistor RTS noise behavior under ionization radiation in CMOS image sensors,” *IEEE Trans. Electron Dev.*, vol. 59, p. 1686, 2012.

[46] S. L. Wu, H. F. Chiu, Y. S. Chang, and O. Cheng, “Defect properties of high-k/metal-gate metal–oxide–semiconductor field-effect transistors determined by characterization of random telegraph noise,” *Jpn. J. Appl. Phys.*, vol. 53, p. 035005-1, 2014.

[47] F. Gruneis, M. Nakao, Y. Mizutani, M. Yamamoto, M. Meesmann, T. Musha, “Further study on 1/f fluctuations observed in central single neurons during REM sleep,” *Biol. Cybern*, vol. 68, pp. 193-198, 1993.

[48] P. Bak, C. Tang, and K. Wiesenfeld, “Self – organized criticality: An explanation of 1/f noise,” *Phys. Rev. Lett.*, vol. 59, pp. 381 -384, 1987.

[49] R. T. Baillie, “Long memory processes and fractional integration in econometrics,” *J. Econometrics*, vol. 73, pp. 5-59, 1996.

[50] F. N. Hooge, T. G. M. Kleinpenning, and L. K. J. Vandamme, “Experimental studies on 1/*f* noise,” *Rep. Prog. Phys.*, vol. 44, pp. 479 - 532, 1981.

[51] C.-Y. Chen, “Low frequency noise in advanced CMOS technology,” Ph.D. dissertation, Dept. Elect. Eng., Stanford University, Stanford, CA, 2010

[52] A. P. Van Der Wel, E. A. M. Klumperink, J. S. Kolhatkar, E. Hoekstra, M. F. Snoeij, C. Salm, H. Wallinga, and B. Nauta, “Low-frequency noise phenomena in switched MOSFETs,” *IEEE J. Solid-State Circuits*, vol. 42, p. 540, 2007.

[53] I. Bloom, and Y. Nemirovsky, “1/f noise reduction of metal – oxide - semiconductor transistors by cycling from inversion to accumulation,” *Appl. Phys. Lett.*, vol. 58, p. 1664, 1991.

[54] B. Dierickx, and E. Simoen, “The decrease of random telegraph signal noise in metal- oxide - semicondutor field - effect transistors when cycled from inversion to accumulation,” *J. Appl. Phys.*, vol. 71, pp. 2028–2029, 1992.

[55] A. P. van der Wel, E. A. M. Klumperink, S. L. J. Gierkink, R. F. Wassenaar, and H. Wallinga, “MOSFET 1/f noise measurement under switched bias conditions,” *IEEE Electron Dev. Lett.*, vol. 21, no. 1, pp. 43–46, 2000.

[56] F. N. Hooge, “1/f noise is no surface effect,” *Physica*, vol. 29A, pp. 139–140, 1969.

[57] A. L. McWhorter, “1/f noise and related surface effects in Germanium,” Ph.D. dissertation, MIT, Cambridge, MA, 1955.

[58] J. Chang, A. A. Abidi, and C. R. Viswanathan, “Flicker noise in CMOS transistors from subthreshold to strong inversion at various temperatures,” *IEEE Trans. Electron Dev.*, vol. 41, pp. 1965–1971, 1994.

[59] G. Ghibaudo, O. Roux, C. Nguyen-Duc, F. Balestra, and J. Brini, “Improved analysis of low frequency noise in filed - effect MOS transistors,”*Phys. Stat. Sol*. A, vol. 124, pp. 571 – 581, 1991.

[60] R. Jayaraman, and C. G. Sodini, “A 1/*f* noise technique to extract the oxide trap density near the conduction band edge of silicon,” *IEEE Trans. Electron Dev.,* vol. 36, pp. 1773 – 1782, 1989.

[61] R. S. Muller, T. I. Kamins, and M. Chan, Device Electrons for integrated circuits, 3rd edition, John Wiley & Sons, Inc., 2003.

[62] F. N. Hooge, “1/*f* noise sources,” *IEEE Trans. Electron Dev.,* vol. 41, pp. 1926 – 1935, 1994.

[63] R. F. Pierret, and G. W. Neudeck, Advanced semiconductor fundamentals, 2nd ed., New Jersey, Prentice Hall.

[64] S. M. Sze,K. N. Kwok, Physics of semiconductor devices, 2nd ed., New Jersey, John Wiley and Sons Inc., 2007.

[65] G. Reimbold, “Modified 1/*f* trapping noise theory and experiments in MOS transistors biased from weak to strong inversion – influence of interface states,” ,” *IEEE Trans. Electron Dev.,* vol. ED-31, pp. 1190 - 1198, 1984.

[66] S. C. Sun, and J. D. Plummer, “Electron mobility in inversion and accumulation layers on thermally oxidized silicon surfaces,” *IEEE Trans. Electron Dev.,* vol. ED-27, pp. 1497, 1980.

[67] K. K. Hung, P. K. Ko, C. Hu, and Y. C. Cheng, “Flicker noise characteristics of advanced MOS technologies,” *IEDM*, pp. 34 -37, 1988.

[68] G. Wirth, and R. D. Silva, “Low-frequency noise spectrum cyclo - stationary random telegraph signals,” *Springer-Verlag*, pp. 435-441, 2008.

[69] J. Pavelka, J. Sikula, and M. Tacano, “RTS noise in Si MOSFETs and GAN/AlGaN HFETs,” *WSEAS Trans. Electron.*, vol. 4, no. 9, pp. 221-225, 2007.

[70] C. M. Compagnoni, R. Gusmeroli, A. S. Spinelli, A. L. Lacaita, M. Bonanomi, and A. Visconti, “Statistical model for random telegraph noise in flash memories,” *IEEE Trans. Electron Dev.*, vol. 55, pp. 388-395, 2008.

[71] A. P. Van Der Wel, E. A. M. Klumperink, L. K. J. Vandamme, and B. Nauta, “Modeling random telegraph noise under switched bias conditions using cyclostationary RTS noise,” *IEEE Trans. Electron Dev.*, vol. 50, pp. 1378 -1384, 2003.

[72] L. K. J. Vandamme, D. Sodini, and Z. Gingl, “On the anomalous behavior of the relative amplitude of RTS noise,” *Solid State Electron*., vol. 42, pp. 901 – 905, 1998.

[73] D. Lopez, S. Haendler, C. Leyris, G. Bidal, and G. Ghibaudo, “Low-frequency noise investigation and noise variability analysis in High-*k* metal gate 32-nm CMOS transistors,” *IEEE Trans. Electron Dev.*, vol. 58, pp. 2310 -2316, 2011.

[74] N. Tega, H. Miki, Z. Ren, C. P. D’Emic, Y. Zhu, D. J. Frank, J. Cai, M. A. Guillorn, D.-G. Park, W. Haensch, and K. Torii, "Reduction of random telegraph noise in high-κ/metal-gate stacks for 22 nm generation FETs," *IEDM,* pp. 32.4.1-32.4.4, 2009.

[75] K. V. Aadithya, A. Demir, S. Venugopalan, and J. Roychowdhury, “Accurate prediction of random telegraph noise effects in SRAMs and DRAMs*,” IEEE Trans. Comput.-Aided Design Integr. Circuits Syst.,* vol. 32, pp. 73-86, 2013.

[76] H. D. Xiong, W. Wang, Q. Li, C. A. Richter, J. S. Suehle, W.-Ki Hong, T. Lee, and D. M. Fleetwood, “Random telegraph signals in n-type ZnO nanowire field effect transistors at low temperature,” *Appl. Phys. Lett*., vol. 91, p. 053107, 2007.

[77] D. H. Cobden, and M. J. Uren, “Random telegraph signals from liquid helium to room temperature,” *Microelectron. Eng.*, vol. 22, pp. 163-170, 1993.

[78] LakeShore User’s Manual Model 330 Autotuning Temperature Controller, Rev. 1.3, Westerville, OH, 2000.

[79] Z. Celik-Butler, P. Vasina, and N. V. Amarasinghe, “A method for locating the position of oxide traps for random telegraph signals in submicron MOSFETs,” *IEEE Trans. Electron Dev.*, vol. 47, pp. 646-648, 2000.

[80] M. Zhong-Fa, Z. Peng, W. Yong, L. Wei-Hua, Z. Yi-Qi, and D. Lei, “Accurate extraction of trap depth responsible for RTS noise in nano-MOSFETs,” *Chin. Phys. B*, vol. 19, no. 3, p. 037201-1, 2010.

[81] H. Lee, Y. Yoon, S. Cho, and H. Shin, “Accurate Extraction of the trap depth from RTS noise data by including poly depletion effect and surface potential variation in MOSFETs,” *IEICE Trans. Electron*., vol. E90-C, no. 5, pp. 968-972, 2007.

[82] B. G. Streetman, and S. Banerjee, Solid state electronic devices, 4th ed., Upper Saddle River , NJ, Prentice Hall Inc., 2000.

[83] A. Palma, A. Godoy, J. A. Jimenez-Tejada, J. E. Carceller, and J. A. Lopez-Villanueva, “Quantum two-dimensional calculation of time constants of random

telegraph signals in metal-oxide-semiconductor structures;" *Phys. Rev. B*, vol. 56, p. 9565, 1997.

[84] D. Veksler, G. Bersuker, S. Rumyantsev, M. Shur, H. Park, C. Young, K. Y. Lim, W. Taylor, and R. Jammy, "Understanding noise measurements in MOSFETs: the role of traps structural relaxation," *IRPS* 10, p. 2B.4.1, 2010.

[85] P. Restle, and A. Gnudi, "Internal probing of submicron FETs and photoemission using individual oxide traps," *IBM J. Res. Develop*., vol. 34, no. 2/3, pp. 227-242, 1990.

[86] D. Kang, J. Kim, D. Lee, B.-G. Park, J. D. Lee, and H. Shin, "Extraction of vertical, lateral locations and energies of hot-electrons-induced traps through the random telegraph noise," *Jpn. J. Appl. Phys.*, vol. 48, no. p. 04C034-1, 2009.

[87] D. A. Buchanan, M. V. Fischetti, and D. J. DiMaria, "Coulombic and neutral trapping centers in silicon dioxide," *Phys. Rev. B*, vol. 43, no. 2, p. 1471, 1991.

[88] Y. Taur, and T. H. Ning, "Fundamental of modern VLSI Devices," *Cambridge University Press*, 1998.

[89] D. J. DiMaria, in *The Physics of SiO_2 and its Interfaces,* S. T. Pantelides (ed.), 160-178, New York, Pergamon Press Inc. 1978.

[90] A. L. Shluger, and K. P. McKenna, "Models of oxygen vacancy defects involved in degradation of gate dielectrics," *IRPS*, p. 5A.1.1, 2013.

[91] A. V. Kimmel, P. V. Sushko, A. L. Shluger, and G. Bersuker, "Positive and negative oxygen vacancies in amorphous silica," *ECST*, vol. 19, no. 2, p. 3, 2009.

[92] D. Vuillaume, and A. Bravaix, "Charging and discharging properties of electron traps created by hotcarrier injections in gate oxide of nchannel metal oxide semiconductor filed effect transistor," *J. Appl. Phys.*, vol. 73, p. 2559, 1993.

[93] N. V. Amarasinghe, Z. Çelik-Butler, and A. Keshavarz, "Extraction of oxide trap properties using temperature dependence of random telegraph signals in submicron metal–oxide–semiconductor field-effect transistors," *J. Appl. Phys.*,vol. 89, pp. 5526-5532, 2001.

[94] D. H. Cobden, M. J. Uren, and M. J. Kirton, "Entropy measurements on slow Si/SiO_2 interface states," *Appl. Phys. Lett*., vol. 56, p. 1245, 1990.

[95] N. V. Amarasinghe, "Random telegraph signals in submicron MOSFETS," Ph.D. dissertation, Dept. Elect. Eng., SMU, Dallas, TX, 2001.

[96] B. I. Fuks, "Fluctuation slow surface traps," *J. Exp. Thero. Phys.* vol. 102, pp. 555-576, August, 1992.

[97] O. Engstrom, B. Raeissi, and J. Piscator, "Vibronic nature of hafnium oxide/silicon interface states investigated by capacitance frequency spectroscopy," *J. Appl. Phys*. vol. 103, p. 104101. 2008.

[98] E. G. Seebauer, and M. C. Kratzer, "Charged point defects in semiconductors," *Mater. Sci. Eng*., vol. R-55, pp. 57-149, 2006.

[99] O. Engstrom, and H. G. Grimmeiss, "Vibronic states of silicon-silicon dioxide interface traps," Semicond. Sci. Technol., vol. 4, pp. 1106-1115, 1989.

[100] R. Salh, "Defect related luminescence in silicon dioxide network," in *Crystalline Si Prop. & Uses*, S. Basu (ed.) InTech, 2011, pp. 135–72.

[101] V. B. Sulimov, P. V. Sushko, A. H. Edwards, A. L. Shluger, and A. M. Stoneham, "Asymmetry and long-range character of lattice deformation by neutral oxygen vacancy in α-quartz," *Phys. Rev.* B, vol. 66, p. 024108-1, 2002.

[102] P. V. Sushko, S. Mukhopadhyay, A. M. Stoneham, and A. L. Shluger, "Oxygen vacancies in amorphous silica: structure and distribution of properties," *Microelectron. Eng.*, vol. 80, pp. 292-295, 2005.

[103] MD. I. Mahmud, "Investigation of degradation in advanced analog MOS technologies," Ph.D. dissertation, Dept. Elect. Eng., UTA, Arlington, TX, 2013.

[104] T. R. Oldham, F. B. McLean, "Total Ionizing dose effects in MOS oxides and devices," *IEEE Trans. Nuclear Scie.*, vol. 50, pp. 483-499, 2003.

[105] N. H. Hamid, A. F. Murray, and S. Roy, "Time-domain modeling of low-frequency noise in deep-submicrometer MOSFET," *IEEE Trans. Circuits Syst. I, Reg. Papers*, vol. 55, no. 1, pp. 245, 2008.

[106] Z. Y. Lu, C. J. Nicklaw, D. M. Fleetwood, R. D. Schrimpf, and S. T. Pantelides, "Structure, properties, and dynamics of oxygen vacancies in amorphous SiO_2*," Phys. Rev. Lett*., vol. 89, pp. 285505-1- 285505-4, 2002.

[107] V. J. Kappor, and W. D. Brown, Silicon nitride and silicon dioxide thin insulator films, Pennington, New Jersey, The Electrochemical Society, Inc. 1997.

[108] R. Perera, A. Ikeda, R. Hattori, and Y. Kuroki, "Trap assisted leakage current conduction in thin silicon oxynitride films grown by rapid thermal oxidation combined microwave excited plasma nitridation combined microwave excited plasma nitridation," *Microelectron. Eng.,* 65, pp. 357-370, 2003.

[109] E. Suzuki, D. K. Schroder, Y. Hayashi, "Carrier conduction in ultrathin nitrided oxide films", *J. Appl. Phys.* vol. 60, pp. 3616–3621, 1986.

[110] S. Fleischer, P.T. Lai, Y.C. Cheng, “A new method for extracting the trap energy in insulators,” *J. Appl. Phys.*, vol. 73, pp. 3348–3351, 1993.

[111] X. R. Cheng, Y.C. Cheng, B.Y. Liu, “Nitridation-enhanced conductivity behavior and current transport mechanism in thin thermally nitrided SiO_2,” *J. Appl. Phys.*, vol. 63, pp.797–802, 1988.

[112] A. Alkauskas, A. Pasquarello, “ Alignment of hydrogen–related defect levels at the Si–SiO_2 interface,” *Physica* B, pp. 546–549, 2007.

[113] S. N. Rashkeev, D. M. Fleetwood, R. D. Schrimpf, and S. T. Pantelides, “Dual behavior of H+ at Si–SiO_2 interfaces: Mobility versus trapping,” *Appl. Phys. Lett*., vol. 81, p. 1839, 2002.

[114] W. Goes, M Karner, V. Sverdlov, and T. Grasser, “Charging and discharging of oxide defects in reliability issues,” *IEEE Trans. Device Mater. Rel.*, vol. 8, p. 491, 2008.

[115] A. C. Pineda, and S. P. Karna, “Electronic structure theory of radiation–induced defects in Si/SiO_2,” *HPCERC*, pp. 1–39, 2000.

[116] M. Boero, A. Pasquarello, J. Sarnthein, and R. Car, “Structure and hyperfine parameters of E'_1 centers in α-quartz and in vitreous SiO_2,” *Phys. Rev. Lett.*, vol. 78, p. 887, 1997.

[117] N. L. Anderson, “Structural, thermodynamic, electronic, and magnetic, characterization of point defect in amorphous silica,” Ph.D. dissertation, School of Materials Engineering., Purdue University, West Lafayette, IN, 2012.

[118] G. I. Wirth, J. Koh, R. de Silva, R. Thewes, and R. Brederlow, “Modeling of statistical low-frequency noise of deep-submicrometer MOSFETs,” *IEEE Trans. Electron Dev.*, vol. 52, no. 7, pp. 1576–1588, 2005.

[119] K. Takeuchi, T. Nagumo, S. Yokogawa, K. Imai, and Y. Hayashi, “Single – charge - based modeling of transistor characteristics fluctuations based on statistical measurement of RTN amplitude,” in *Proc. Symp.VLSI Technol.*, p. 54, 2009.

[120] M. Nour, Z. Çelik-Butler, A. Sonnet, F. C. Hou, and S. Tang, “Random telegraph signals originating from unrelaxed neutral oxygen vacancy centers in SiO_2,” *Electron. Lett*., vol. 51, no. 20, pp. 1610-1611, 2015.

[121] K. S. Ralls, W. J. Skocpol, L. D. Jackel, R. E. Howard, L. A. Fetter, R. W. Epworth, and D. M. Tennant, “Discrete resistance switching in submicrometer silicon layers: individual interface traps and low-frequency (1/*f* ?) noise,” *Phys. Rev. Lett*., vol. 52, no. 3, pp. 228-231, 1984.

[122] C. H. Henry, and D. V. Lang, “Nonradiative capture and recombination by multiphonon emission in GaAs and GaP,” *Phys. Rev. B*, vol. 15, no. 2, p. 989, 1977.

[123] P. D. Welch, “The use of fast Fourier transform for the estimation of power spectra: A method based on time averaging over short, modified periodograms,” *IEEE Trans. Audio Electroacoust*., vol. 15, p. 70, 1967.

[124] H. Schmid, “How to use the FFT and Matlab’s pwelch function for signal and noise simulations and measurements,” *Institute of Microelectronics* (*IME*), pp.1-13, 2012.

[125] Y. Higashi, N. Momo, H. Sasaki, H. S. Momose, T. Ohguro, Y. Mitani, T. Ishihara and K. Matsuzawa, “ Unified transient and frequency domain noise simulation for random telegraph noise and flicker noise using a physics-based model,” *IEEE Trans. Electron Dev.*, vol. 61, no. 12, pp. 4197-4203, 2014.

[126] G. Wirth, D. Vasileska, N. Ashraf, L. Brusamarello, R. D. Giustina, P. Srinivasan, “Compact modeling and simulation of random telegraph noise under non-stationary conditions in the presence of random dopants,” *Microelectron. Reliab*., vol. 52, pp. 2955-61, 2012.

[127] K. R. Farmer, C. T. Rogers, and R. A. Buhrman, “Localized-state interactions in metal-oxide-semiconductor tunnel diodes,” *Phys. Rev. Lett.*, vol. 58, no. 21, pp. 2255-, 1987.

[128] M. Nour, M. Iqbal-Mahmud, Z. Çelik-Butler, D. Basu, S. Tang, F-C. Hou, R. Wise, “Variability of random telegraph noise in analog MOS transistors,” in *Proc. ICNF*, pp. 1-4, 2013.

[129] K. Kandiah, M. O. Deighton, and F. B. Whiting, “A physical model for random telegraph signal currents in semiconductor devices,” *J. Appl. Phys.*, vol. 66, no. 2, pp. 937-948, 1989.

[130] S. Miller, and D. Childers, Probability and random processes, 2nd ed., Waltham, MA, Academic Press, 2012.

Biographical Information

Mohamed Nour attended The University of Texas at Arlington and received the PhD degree in electrical engineering in 2015. He received the B.S. degree in electrical and computer engineering from Oklahoma State University in 2002 and the MBA from University of Phoenix in 2008. He won the engineering academic excellence award from the UTA College of Engineering for 2015. He also received Best in Session award for TECHCON 2014 in Austin, Texas. In addition, he won The UTA Graduate Studies Dissertation Fellowship for summer 2015. His objectives are to continue investigating and modeling random telegraph signals and reliability issues in MOSFETs, memory devices, nanotube, BJT, FINFET, and to improve the random telegraph signals simulation tool.